ornl

ORNL-6943

OAK RIDGE NATIONAL LABORATORY

LOCKHEED MARTIN

Fossil Energy Program Annual Progress Report for April 1997 Through March 1998

R. R. Judkins
Program Manager

Fossil Energy Program

MANAGED AND OPERATED BY
LOCKHEED MARTIN ENERGY RESEARCH CORPORATION
FOR THE UNITED STATES
DEPARTMENT OF ENERGY

ORNL-27 (3-96)

DISCLAIMER

Portions of this document may be illegible in electronic image products. Images are produced from the best available original document.

ORNL-6943

Fossil Energy Program

Fossil Energy Program Annual Progress Report for April 1997 Through March 1998

R. R. Judkins
Program Manager

July 1998

Prepared for the
DOE Office of Fossil Energy
(AA, AB, AC, AW, AZ, SA)

Prepared by the
OAK RIDGE NATIONAL LABORATORY
Oak Ridge, Tennessee 37831-6285
Managed by
LOCKHEED MARTIN ENERGY RESEARCH CORP.
for the
U.S. DEPARTMENT OF ENERGY
under Contract DE-AC05-96OR22464

CONTENTS

FOSSIL ENERGY PROGRAM ANNUAL PROGRESS REPORT FOR APRIL 1997 THROUGH MARCH 1998[1]

R. R. Judkins, Program Manager

ABSTRACT

This report covers progress made during the period April 1, 1997, through March 31, 1998, for research and development projects that contribute to the advancement of fossil energy technologies. Projects on the Fossil Energy Program are supported by the DOE Office of Fossil Energy, the DOE Federal Energy Technology Center, the DOE Fossil Energy Clean Coal Technology Program, the DOE National Petroleum Technology Office, and the DOE Fossil Energy Office of Strategic Petroleum Reserve.

INTRODUCTION

The Oak Ridge National Laboratory (ORNL) Fossil Energy Program research and development activities, performed for the Department of Energy (DOE) Assistant Secretary for Fossil Energy, cover the areas of coal, clean coal technology, gas, petroleum, and support to the Strategic Petroleum Reserve (SPR).

An important part of the Fossil Energy Program is technical management of all activities on the DOE Fossil Energy Advanced Research and Technology Development (AR&TD) Materials Program. The AR&TD Materials Program involves research at other DOE and government laboratories, at universities, and at industrial organizations.

MATERIALS RESEARCH AND DEVELOPMENT

Materials research and development activities at ORNL include development of ceramic composites for high temperature applications; new alloys with unique mechanical properties for advanced fossil energy systems; development of functional materials, such as ceramic filters, ceramic membranes, solid oxide fuel cell materials, and carbon materials; and corrosion research to

[1]Research sponsored by the U.S. Department of Energy, Office of Fossil Energy, under contract DE-AC05-96OR22464 with Lockheed Martin Energy Research Corp.

understand the behavior of materials in coal processing environments. Transfer of technology developed on this program is enhanced through interactions with industry and by joint research programs with interested end-users.

ENVIRONMENTAL ANALYSIS SUPPORT

Activities in environmental analysis support include assistance to the Federal Energy Technology Center at Morgantown, West Virginia, and Pittsburgh in reviewing and preparing documents required by the National Environmental Policy Act for projects selected for the Clean Coal Technology Program and for the Low Emission Boiler System (LEBS) Program. An important activity was the preparation of an environmental impact statement (EIS) for a new coal-fired LEBS technology for electric power generation at the proof-of-concept scale adjacent to the Turris Coal Company's existing underground coal mine near Elkhart, Illinois. Another important activity was the initiation of an EIS for a new circulating fluidized bed combustor fueled by coal and petroleum coke to repower an existing steam turbine at Jacksonville Electric Authority's Northside Generating Station in Jacksonville, Florida.

BIOPROCESSING RESEARCH

Work on the Fossil Energy Bioprocessing Research Program includes fundamental research for coal applications, with emphasis on advanced reactor design for conversion of coal synthesis gas to liquid fuels, and investigates the manner in which bioprocessing may contribute to CO_2 mitigation options. In addition, the program includes studies on the removal of heteroatoms from heavy oils, renewable hydrogen production, and remediation of oil containing soils. All activities apply biological approaches that allow the utilization of our nation's fossil energy reserve in an economical and environmentally more benign manner.

FOSSIL FUEL SUPPLIES MODELING AND RESEARCH

The fossil fuel supplies modeling and research effort is focused on two areas: SPR planning and management, and transportation fuels and efficiency. Topics include new SPR oil valuation models, updating models for SPR risk analysis, and fill-draw planning.

OIL AND GAS PRODUCTION

Research in oil and gas production involves measurements of wax points in crude oils and petroleum fluids; research on the thermodynamics of brine/oil/rock interfaces and their influence on enhanced oil production in waterfloods; evaluation of the hydrocarbon potential of a part of the Appalachian basin; application of nuclear fuel reprocessing technology to the separation of petroleum and water downhole in an oil well; application of global optimization methods to residual statics in seismic imaging; and the use of neural networks in oil field parameter estimation.

MATERIALS RESEARCH AND DEVELOPMENT

R. R. Judkins

Materials research and development activities at Oak Ridge National Laboratory include development of ceramic composites for high temperature applications; new alloys with unique mechanical properties for advanced fossil energy systems; development of functional materials, such as ceramic filters, ceramic membranes, solid oxide fuel cell materials, and carbon materials; and corrosion research to understand the behavior of materials in coal processing environments. Transfer of technology developed on this program is enhanced through interactions with industry and by joint research programs with interested end-users.

DEVELOPMENT OF A SCALED-UP CVI SYSTEM FOR TUBULAR GEOMETRIES

T. M. Besmann and J. C. McLaughlin
Metals and Ceramics Division
Oak Ridge National Laboratory
P.O. Box 2008, Oak Ridge, TN 37831-6063
e-mail: tmb@ornl.gov

K. J. Probst and T. J. Anderson
Department of Chemical Engineering
University of Florida
Gainesville, FL 32611

T. L. Starr
Department of Materials Science and Engineering
Georgia Institute of Technology
Atlanta, GA 30332-0245

Silicon carbide-based heat exchanger tubes are of interest to energy production and conversion systems due to their excellent high temperature properties. Fiber-reinforced SiC is of particular importance for these applications since it is substantially tougher than monolithic SiC, and therefore more damage and thermal shock tolerant. This paper reviews a program to develop a scaled-up system for the chemical vapor infiltration of tubular shapes of fiber-reinforced SiC. The efforts include producing a unique furnace design, extensive process and system modeling, and experimental efforts to demonstrate tube fabrication.

INTRODUCTION

Fiber-reinforced SiC-matrix composites are candidates for numerous high temperature applications. These composites possess high-temperature strength, high thermal conductivity, thermal shock and creep resistance, and damage tolerance. However, in the current commercial isothermal, isobaric chemical vapor infiltration process, thick-walled parts are difficult to densify. A leading alternative process is forced chemical vapor infiltration (FCVI) (1, 2). In FCVI, a thermal gradient is developed along the preform thickness by heating the preform exterior and cooling the interior. The reactant gases are constrained to flow from the cooled interior to the heated exterior. These gases react at the fiber surfaces throughout the preform volume and deposit the ceramic matrix. In the case of SiC deposited from chlorosilanes, the resulting effluent by-product HCl gas has a poisoning effect on the deposition rate. This poisoning combined with the reactant depletion through the preform thickness inhibits the matrix deposition rate. However,

since the gases are forced toward the heated preform exterior, the higher temperatures support faster deposition rates due to the Arrhenius behavior of the deposition reaction. Therefore, the SiC deposition is controlled by counterbalance of thermal gradient and reactant depletion.

In the current work, emphasis is on the development of composites with tubular geometries. In order to demonstrate the fabrication of a prototypical tube, the efforts have centered on component diameters approaching 64 mm with a 6.4 mm wall thickness. Therefore, a unique furnace system was designed and constructed to facilitate the FCVI of such tubes with lengths of 350 mm. Supporting the developmental effort has been extensive process modeling that has successfully described and aided the optimization of the FCVI of composite plates (3,4).

MODELING

In a preliminary effort, GTCVI, a three-dimensional finite volume model, has been used to simulate the CVI of composite tubes (5). The model calculations are performed in cylindrical geometry due to its ease of use and symmetry. The FCVI experimental reactor configuration modeled is shown in Figure 1. The preform exterior is radiatively heated by a graphite coating chamber and its interior cooled with a water-cooled line. The methyltrichlorosilane (MTS) and hydrogen mixture is injected inside the preform and infiltrates through the thickness, exhausting at atmospheric pressure. Ceramic fiberboard disks seal the preform ends. Graphite felt insulation is placed on both sides of the preform to reduce axial heat loss.

The reactor configuration shown in Figure 1 is discretized into a two-dimensional array of finite volume elements. Neglect of the θ-direction reduces the cylindrical discretization to only radial and axial components. The preform itself is discretized into four radial and 29 axial volume elements. The preform is 370 mm in length and 6.4 mm in thickness with an inside diameter of 51 mm, and has a 40% Nextel™ 312 (Al/Si/B oxide) fiber volume.

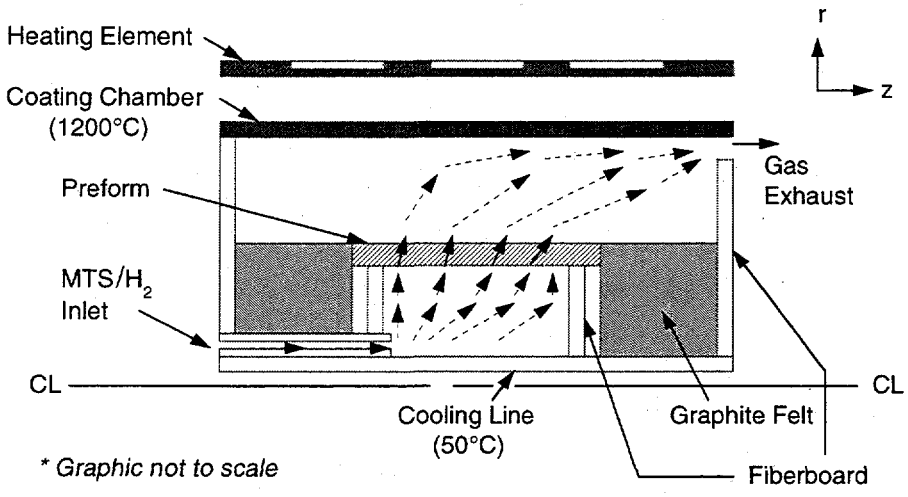

Figure 1: The FCVI experimental reactor configuration.

In the model, the thermal conductivities for the graphite, graphite felt, stainless steel, and ceramic fiberboard are functions of temperature. The gas mixture heat capacity, viscosity, thermal conductivity, and binary diffusivities of MTS and HCl in hydrogen are also functions of temperature. The thermal conductivity, permeability, effective diffusivity, and surface area of the preform are functions of theoretical density.

Several key boundary conditions are applied to the model. A parabolic temperature profile is imposed along the length of the graphite coating chamber. The coating chamber temperature is 1200°C at the mid-line and 1000°C at the ends. These temperature values describe the thermal profile seen experimentally. A constant temperature of 50°C is assumed along the centerline of the water-cooled line. Both total molar flux and MTS mole fraction are specified at the hydrogen/MTS inlet. Atmospheric pressure is fixed at the gas exhaust and the ends of the domain are specified as adiabatic.

The modeling results presented in this paper investigate three key parameters that influence the FCVI process: graphite coating chamber temperature; molar feed ratio of hydrogen to MTS, and total flow. The temperature range is 1100°C to 1200°C, the hydrogen/MTS molar feed ratio range is 5 to 10, and the total flow range is 3 to 9 *l*/min.

Figures 2-4 show the effects of FCVI parameters on the transient theoretical density. The baseline FCVI parameters used are given in Table 1.

Table 1: Baseline FCVI parameters used in the modeling results.

Coating Chamber Mid-Line Temperature	1200°C
Hydrogen/MTS Molar Feed Ratio	5
Total Molar Flow	6 *l*/min

It is seen that at a given time, increasing the coating chamber mid-line temperature, reducing the molar feed ratio, and increasing the total flow result in higher theoretical densities.

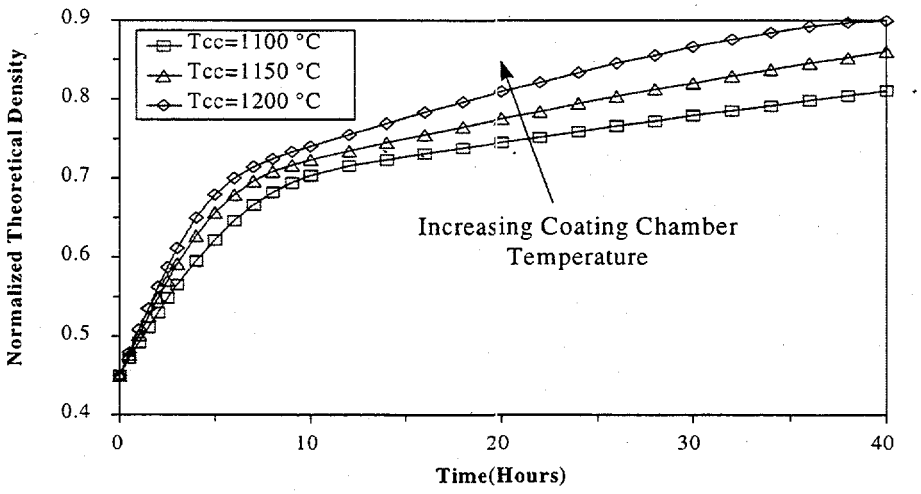

Figure 2: Coating chamber mid-line temperature effect on theoretical density.

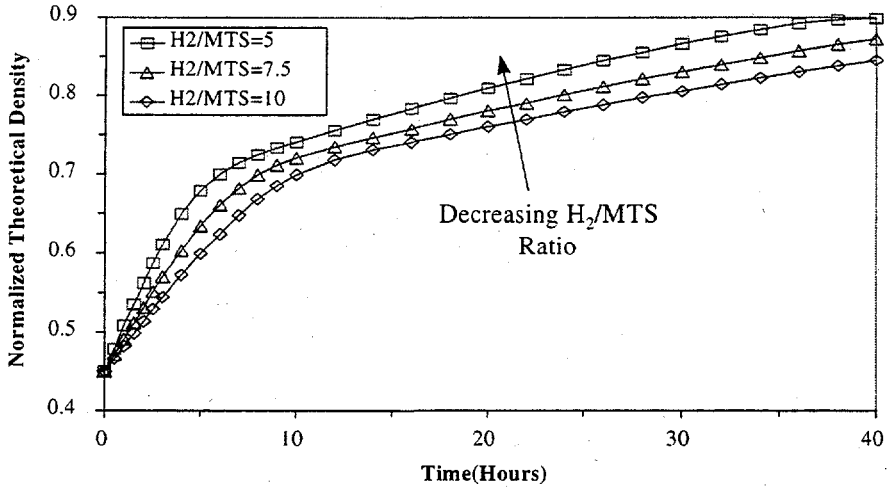

Figure 3: Hydrogen/MTS molar feed ratio effect on theoretical density.

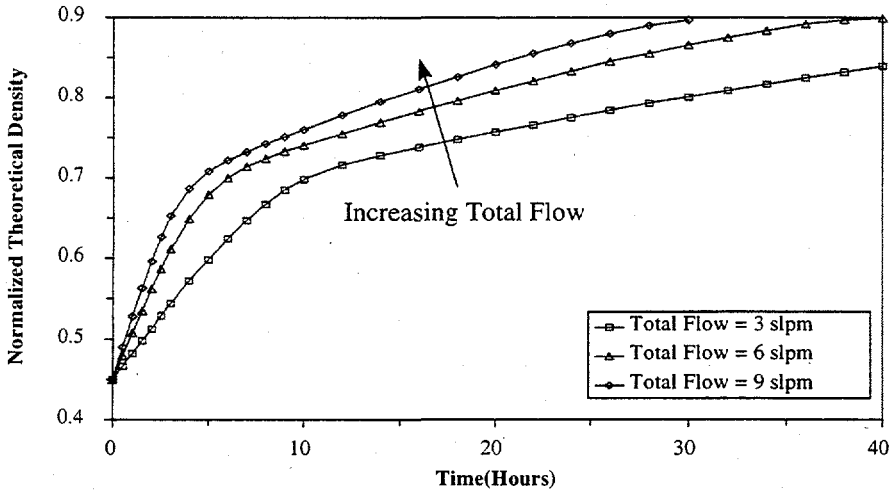

Figure 4: Total flow effect on theoretical density.

The initial temperature profile produced by the model is displayed in Figure 5. The radial temperature gradient is quite uniform along the preform length with a higher radial gradient in the tubular preform region directly above the gas inlet. No axial temperature gradient is seen along the preform length. Both preform ends are at higher temperatures with little radial temperature gradient. This result is from both the graphite felt placed outside the preform ends and the adiabatic boundary condition assumed at the domain ends.

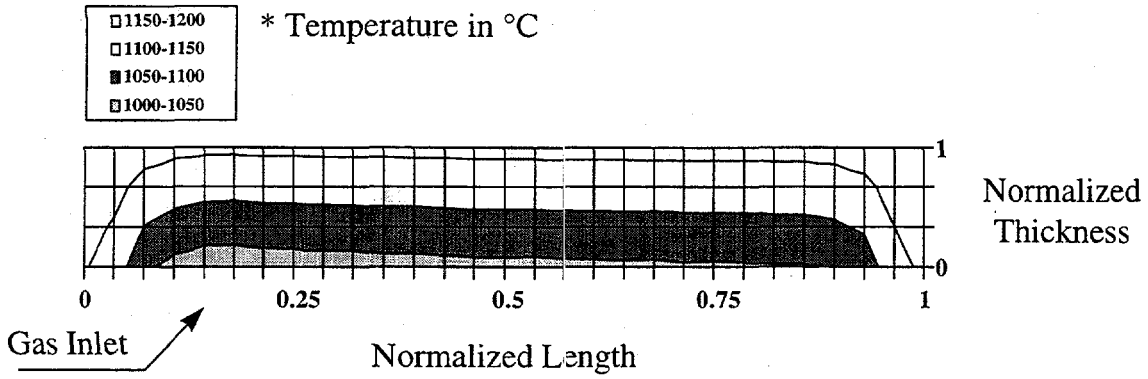

Figure 5: Initial temperature profile of the tubular preform.

Figure 6 shows the transient radial temperature gradient profile. Naturally, the temperature gradient is largest at the start of infiltration since the preform thermal conductivity consists only of the Nextel™ fiber. The transient radial temperature gradient decreases with time. Infiltration proceeds and silicon carbide matrix is deposited throughout the tubular fibrous preform. The matrix addition increases the preform thermal conductivity and reduces the radial temperature gradient given a constant radial heat flux.

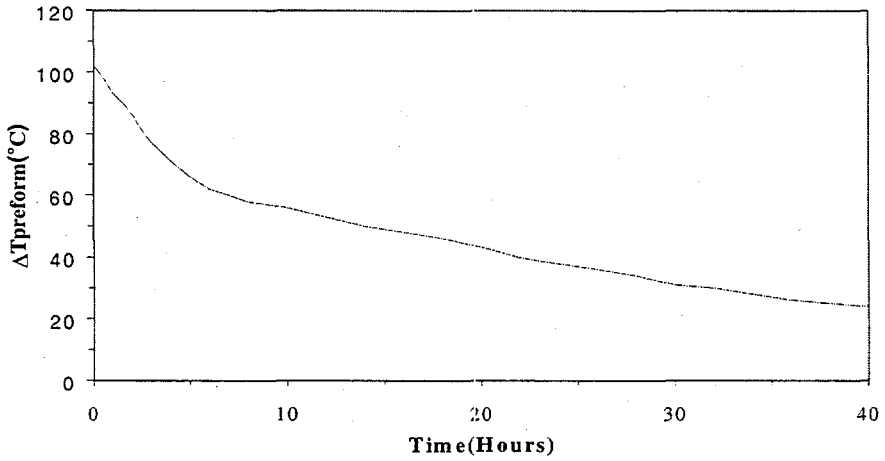

Figure 6: The transient temperature gradient profile.

EXPERIMENT

Several tubular preforms have been infiltrated by FCVI. These preforms were made up of concentric layers of Nextel™ 312 fibrous tubular sleeves. The preforms were rigidized by resin impregnation and curing, which enables the preforms to be fixtured inside the furnace. Preform fiber volumes between 34% and 50% were achieved with the tubular preform fabrication techniques utilized.

The FCVI conditions used were a hydrogen flow of 5 *l*/min, an hydrogen/MTS molar feed ratio of 5, a coating chamber mid-line temperature of 1200°C, and a cooling line temperature of 50°C. The infiltration was conducted for a specified time or until a 70-kPa backpressure was realized in the preform interior.

Figure 7 displays an individual Nextel™ 312 tubular sleeve, an uninfiltrated, fibrous tubular preform, and an infiltrated, dense composite tube. The preform dimensions, fiber volumes, infiltration times, and theoretical densities for each FCVI-fabricated composite tube are presented in Table 2. For each composite tube, the estimated experimental theoretical density is compared to the model prediction at the given infiltration time.

Figure 8 shows computerized tomographic (CT) images taken from specimen CVI 1103. These images show a finite SiC overcoat thickness on the tube interior. This overcoat is a result of FCVI processing near full-density. Both the fiber mass and total composite mass are used in the theoretical density estimation. However, the SiC overcoat mass must be estimated and subtracted from the total mass. Overcoat thickness measurements obtained from the CT images helped estimate the theoretical density of the composite tube.

Figures 9 and 10 show CT images of specimens CVI 1132 and CVI 1173. These images show well-infiltrated regions and some undesired porosity through the preform thickness. It is noted that the preform thickness at the tapered inlet end of CVI 1132 is thicker than in the remaining tube. The observed porosity in these CT images is from the preform channels that occur at fiber tow intersections. CVI 1173 appears denser than CVI 1132. This agrees with the experimental density estimates presented in Table 2.

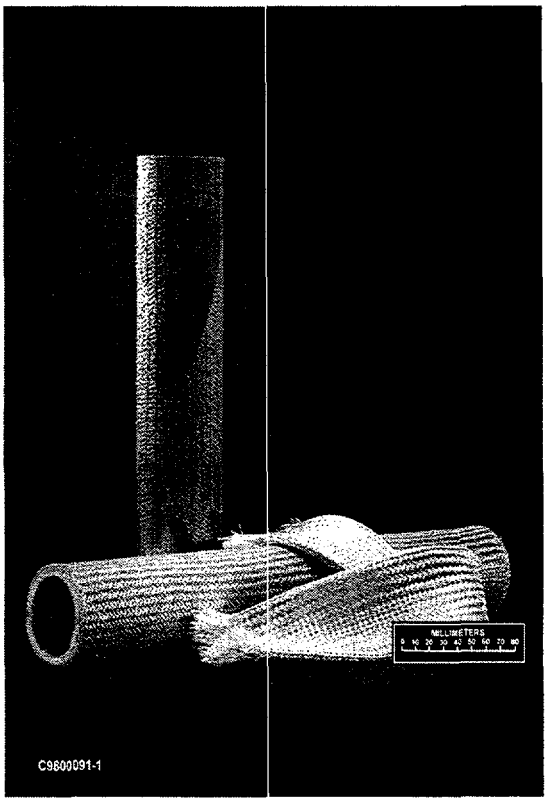

Figure 7: An uninfiltrated, fibrous tubular preform, dense composite tube, and Nextel™312 tubular sleeve.

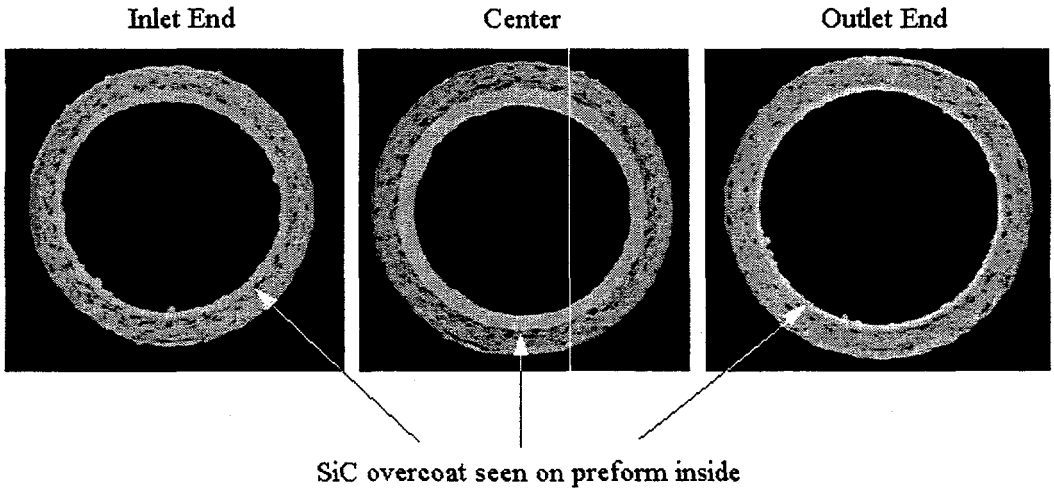

Figure 8: CT Images of CVI 1103 clearly show the SiC overcoat.

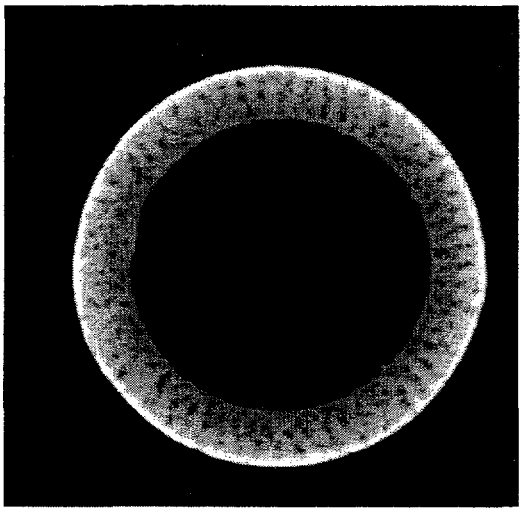

5.1 cm from Inlet End

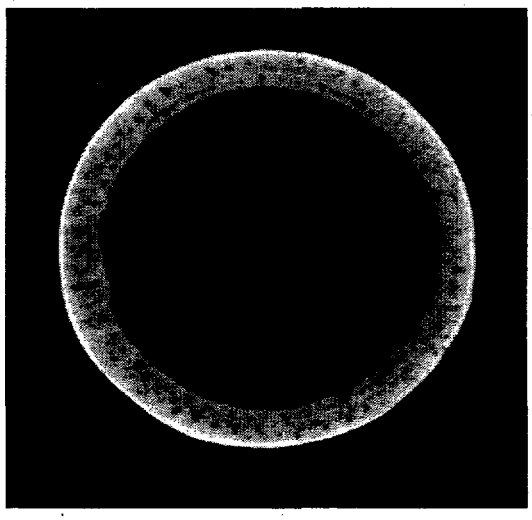

5.7 cm from Outlet End

Figure 9: CT Images of CVI 1132.

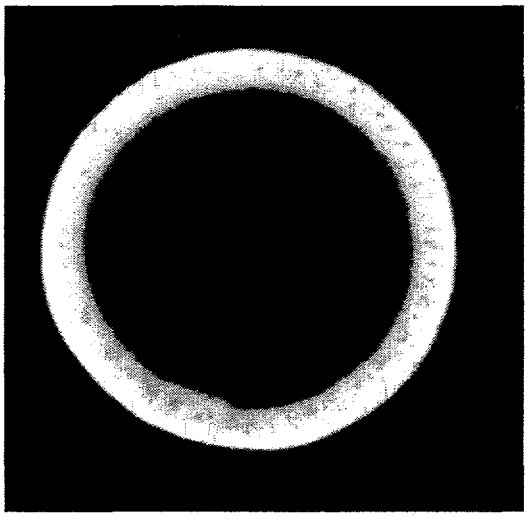

5.7 cm from Inlet End

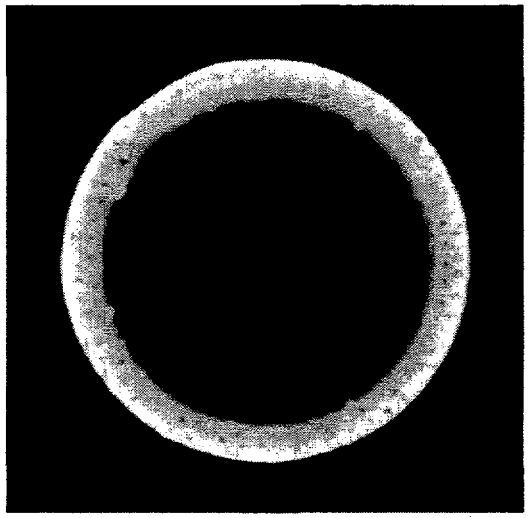

5.7 cm from Outlet End

Figure 10: CT Images of CVI 1173.

Table 2: Summary of FCVI-fabricated composite tubes.

Tube Identification	CVI 1103	CVI 1132	CVI 1173
Inside Diameter	48 mm	51 mm	51 mm
Taper ID	N/A	44 mm	N/A
Thickness	6.4 mm	5.1 mm	4.8 mm
Taper Thickness	N/A	8.3 mm	N/A
Fiber Volume	34.6%	43.7%	49.8%
Infiltration Time	24 Hours	28 Hours	24 Hours
Theoretical Density (Exp.)	79.9%	75.1%	86.6%
Theoretical Density (Mod.)	81%	81%	79%

CONCLUSIONS

FCVI modeling efforts for tubular geometries have demonstrated infiltration conditions necessary to achieve dense composite tubes. Increasing the coating chamber mid-line temperature, decreasing the hydrogen/MTS molar feed ratio, and increasing the total flow will reduce infiltration time and yield higher theoretical densities at a given time.

Application of the model infiltration conditions has indicated that dense composite tubes can be fabricated by FCVI. Experimental composite tube theoretical densities between 75% and 87% have been realized. At the corresponding infiltration times, reasonable theoretical density agreement between the model and experiment is seen. Future efforts focus on model validation through comparison with experiment. Theoretical density variation at intermediate infiltration times will be compared to model prediction.

ACKNOWLEDGEMENTS

The comments and suggestions of J. T. Klett and S. D. Nunn are gratefully acknowledged. W. Ellingson, D. Koehl, and W. Simpson are acknowledged for the computerized tomography imaging. This research was supported by the U. S. Department of Energy, Office of Fossil Energy, Advanced Research and Technology Development Materials Program under contract DE-AC05-96OR22464 with Lockheed Martin Energy Research Corporation.

REFERENCES

1. W. J. Lackey and A. J. Caputo, *U. S. Patent No. 4,580,524* (April 8, 1986).

2. T.M. Besmann, B.W. Sheldon, R.A. Lowden, and D.P. Stinton, *Science* **253**, 1104 (1991).

3. T.M. Besmann, in *Proc. High Temperature Matrix Composites II, Ceramic Transactions,* A. G. Evans and R. Naslain, Editors, **58**, p. 1, American Ceramic Society, Westerville, OH (1995).

4. W.M. Matlin, D.P. Stinton, T.M. Besmann, and P.K. Liaw, in *Ceramic Matrix Composites - Advanced High-Temperature Structural Materials*, R.A. Lowden, M.K. Ferber, J.R. Hellman, K.K. Chawla, and S.G. DiPietro, Editors, **365,** p. 309, Materials Research Society, Pittsburgh, PA (1995).

5. T.L. Starr, *Finite-Volume Model for Chemical Vapor Infiltration Incorporating Radiant Heat Transfer*, Oak Ridge National Laboratory ORNL/Sub/19X-55901 (1995).

OXIDATION-RESISTANT COATINGS FOR CMC COMPONENTS

Virginie M. Vaubert and David P. Stinton
Oak Ridge National Laboratory
P.O. Box 2008, Bldg. 4515, MS-6063
Oak Ridge, TN 37831-6063

Deidre A. Hirschfeld
Department of Materials & Metallurgical Engineering
159 Jones Hall
New Mexico Tech
Socorro, NM 87801

ABSTRACT

Corrosion resistant $Ca_{0.6}Mg_{0.4}Zr_4(PO_4)_6$ (CMZP) coatings and $Ca_{0.5}Sr_{0.5}Zr_4(PO_4)_6$ (CS-50) coatings for fiber-reinforced SiC-matrix composite heat exchanger tubes have been developed. Aqueous slurries of both oxides were prepared with very high solids loading. One coating process consisted of dipping the samples in the slip. A tape casting or doctor-blade process has also been created that produced relatively thin and dense coatings covering large areas. A drying and sintering schedule, involving a pre-sintering sequence was developed and coatings exhibiting very few cracks were produced.

INTRODUCTION

This work was aimed at developing a new coating process for protecting materials operating at elevated temperatures and in corrosive environments for long periods of time. Specific applications are for components such as heat exchanger tubes and hot-gas filters. The necessity of operating in a high temperature and highly corrosive environment suggests the use of ceramic materials in these applications; however monolithic ceramics are brittle and exhibit very low toughness. These undesirable features limit the reliability, damage tolerance, and durability of monolithics and make them unsuitable for many fossil energy applications. Emphasis has thus been placed on the development of ceramic matrices reinforced with strong ceramic fibers. Such ceramic matrix composites (CMC's) combine the temperature stability of monolithic ceramics with the non-brittle, tough behavior characteristic of metals.

The corrosion of fibers and matrix materials in the presence of alkali species[1, 2] is a major problem in certain fossil energy applications, such as hot-gas filters and heat exchangers. The alkali species, mainly sodium compounds, are by-products from the combustion of fossil fuels. Therefore, corrosion/oxidation resistant coatings for the exterior of CMC components are needed for durability and reliability in such environments.

In the past several years, a new ceramic family has been developed based on the crystal structure of sodium zirconium phosphate $NaZr_2(PO_4)_3$ (NZP)[3,4]. From this family $Ca_{0.6}Mg_{0.4}Zr_4(PO_4)_6$ (CMZP)[5] and $Ca_{0.5}Sr_{0.5}Zr_4(PO_4)_6$ (CS-50)[6] have been developed. Both have a near-zero thermal expansion coefficient, low thermal conductivity and thermal stability up to 1500°C, which make them excellent candidates for high temperature applications. Additionally, these oxides have shown great promise for operating in an alkali environment. CMZP coatings produced by sol-gel synthesis techniques on silicon carbide and silicon nitride provided protection to alkali exposure at 1000°C [7, 8, 9]. The interaction between plasma-spray CS-50 coatings as well as bulk CS-50 and sodium sulfite at high temperature has been studied and CS-50 remained intact after exposure [10, 11]. The goal of this study is to develop a protective coating of these two NZP candidates. Processing techniques focused on two cost-effective, water-based slurry-coating methods: a slurry dipping process and a doctor-blade coating process.

EXPERIMENTAL PROCEDURE: COATING PROCESS

Specimen preparation

Nicalon fiber-reinforced SiC matrix composites prepared by chemical vapor infiltration by the Ceramic Surface Systems Group at Oak Ridge National Laboratory (ORNL) were used in this study. Flat samples as well as hollow circular samples cut from "heat exchanger tubes" were machined to the appropriate size and surface treated. The impact of an intermediate oxide layer on the coating quality was evaluated. Some specimens were heated to 1000° C for four hours. In order to prepare a thicker oxide layer, some samples were washed in acetone, dried, washed in HF followed by rinsing and drying, calcined at 1200°C, washed in HCl and finally rinsed and dried. The bonding mechanism between the coating and the substrate appears to be mostly mechanical interlocking. The fibers and woven pattern of the composite offer a very textured surface that provides good locking sites for the coating. To further improve the infiltration of the

slurry into the crevices, the effort focused on improving the wettability of the substrate and the slurry. Therefore, the surface tension of untreated and oxidized monolithic SiC was measured with water in an environmental chamber. Surface oxidation of monolithic SiC improved its wettability since contact measurements varied from 55° for untreated samples to 40° for oxidized specimens. Oxidizing the substrate surface prior to applying the coating appeared very beneficial to the coating quality. In order to reduce the use of harmful chemicals in the coating process, a heating oxidation process was chosen over a chemical oxidation process. Additionally, some samples presenting large smooth areas where most fibers were completely embedded in the matrix exhibited poor coating adhesion. Roughening of the surface with 60-grit sandpaper before oxidation improved coating adherence.

Powder and slip preparation

Powder preparation

CMZP powder was prepared at Virginia Polytechnic Institute and State University and New Mexico Tech by a proprietary method and was screened to 100-mesh. The powder was then fully crystallized by heating it to 1200°C for 4 hr. CS-50 powder was obtained from LoTEC Inc. (Salt Lake city, UT). The powder was fully calcined with an average particle size of 10 μm.

Particle size distribution is important and should be optimized to obtain a high quality coating. Maximizing the solids loading will increase contact between particles and reduce the amount of water removal during drying. A solids loading of 33 vol % was initially used for coatings with a goal of reaching 55 to 60 vol% solids loading. A small and narrow particle size distribution allows higher solids loading; thus milling trials were performed to optimize powder size distribution. The desired particle size and distribution was reached after 48 hr. of wet milling with a pearled zirconia media. The particle size analysis was completed at ORNL using a Horiba LA-700 particle size measurement device. A mean particle size below a micron was obtained for CS-50 and CMZP. The particle size distribution is very narrow with a standard deviation of 0.25 μm for both powders.

Slip composition

A proprietary CMZP slip composition was adjusted to obtain the best rheology for dip coating. Dolapix PC 21 (Zschimmer and Schwartz, Lahnstein Germany) replaced the original dispersant. CS-50 slurry was also prepared according to a proprietary composition.

The powder was gradually added to the slurry to obtain the highest powder-to-water ratios. Currently, solids loadings of 60% were obtained for CMZP and 63 % for CS-50. The slurry was then used in the doctor-blade coating process by adding binders, Methocel (Dow Corning) or polyvinyl alcohol (PVA, grade 75-15, Dupont), and plasticizers such as polyethylene glycol (PEG, ME Science). The gel-like slurry was sprayed easily on the substrate and the casting process was improved. Binders and plasticizers are usually added in larger quantities for tape casting than in common slip casting processes [12, 13]. Different amounts of ZnO (Me, Science) were added to the slurry as a sintering aid. The effect of ZnO on the sintering behavior of NZP materials has been studied [14, 5, 15] and it was concluded that in the presence of a sintering aid (e.g., ZnO, MgO, Nb_2O_5) a liquid phase is created and promotes the sintering reaction. It has been shown that for CMZP, Ca^{2+} and Mg^{2+} dissolve in a liquid phase of $Zn_3(PO_4)_6$ that forms around 1000°C. In order to reduce the amount of coating cracking during densification, it was believed that the coating should behave more like a glaze. Therefore, the amounts of ZnO additions as well as particle size and sintering temperature have been optimized to obtain the highest amounts of liquid phase.

Aging of the slurry by milling proved detrimental to the coating quality. As the viscosity increased, the pH decreased causing the slurry to become less stable and to flocculate. Milling of the slurry must be limited to a maximum of 48 hr.

Coefficient of Thermal Expansion Adjustment

Cracks and more specifically debonding at the interface between the coating and the substrate are typical of coefficient of thermal expansion (CTE) mismatch between the different materials. Matching the CTE of the coating to that of the substrate without detrimentally affecting the properties of the material was investigated. Mixtures of CS-50 with a CTE of ~3.0x10-6/°C and 4% Y_2O_3 stabilized ZrO_2 (Tosoh Soda) with a CTE of ~10x10-6/°C have been prepared [16] to match the CTE of SiC ceramic matrix composite of ~4.5x10-6/°C. No reaction between CS-50

and 4 wt% Y_2O_3-stabilized ZrO_2 has been detected. A very similar evaluation is being performed with CMZP. Cold pressed samples of mixtures of CMZP and 4 wt% Y_2O_3-stabilized ZrO_2 have been prepared, sintered at 1300 °C for 8 hr and analyzed by X-ray diffraction. No reaction between CMZP and 4 wt% Y_2O_3-stabilized ZrO_2 additive has been found.

Coating deposition

Dipping process

Slurry coatings were applied to composite rings by manually dipping the samples in the CMZP or CS-50 solution (Fig. 1). The samples were only dipped once since it appeared that multiple dipping leads to thick and non-uniform coatings, which cracked in the thickest regions. Since most flaws appeared in the regions of non-uniform thickness it is anticipated that mechanical dipping the samples will yield higher quality coatings. Increasing withdrawal rate might also limit the formation of drops at the bottom of the specimen. Further improvements in the process will include mechanical dipping with variable rate.

Doctor-blade process

The second slurry coating to be evaluated was obtained with doctor-blade coating process also known as tape casting (Fig. 2). Tape casting is mostly used in the electronics industry [17, 18, 19]. This process was chosen for evaluation since it provides thin, large and uniformly dense coatings. The use of a blade to level the coating allows an increase in the viscosity and the density of the slurry, which reduces shrinkage stresses. Additionally, coating thickness is precisely controlled.

The coating process is very simple and consists of covering the surface of the specimen with the slurry, leveling the coating with a doctor-blade, drying the specimen in a controlled environment and finally sintering the samples at a very closely monitored rate. The quality of the coating is influenced by many different factors, which were optimized as part of this program. Slurries were initially prepared as if for slipcasting then adjusted for tape casting. A low viscosity slurry flowed off the substrate; while a thick slurry cracked during processing. The slurry rheology was modified to suit tape casting by adding Methocel as a binder.

Drying and sintering

After coating, the samples were kept at 80 % humidity for 48 h and in ambient humidity for the same amount of time. The samples were then slowly heated at 0.5 °C/ min. up to 600 °C for 4 hr., to enable binder burnout. The samples were crack-free after this treatment. The specimens were ramped at 1°C/ min. up to 1200°C, soaked for 1 min and cooled at the same rate down to room temperature. The same heating schedule was performed a second time, with a soaking time of 24 hr. at 1200°C. Stresses and deformations occurring during heating and cooling were less destructive with a pre-sintering stage.

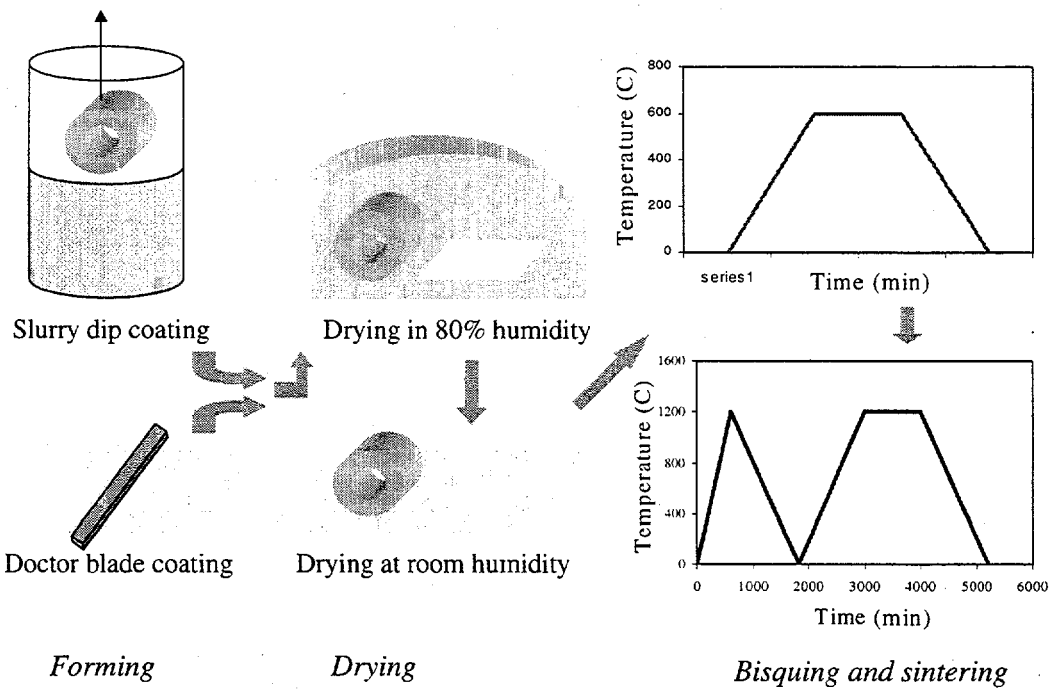

Figure 1: Coating deposition, drying and sintering process

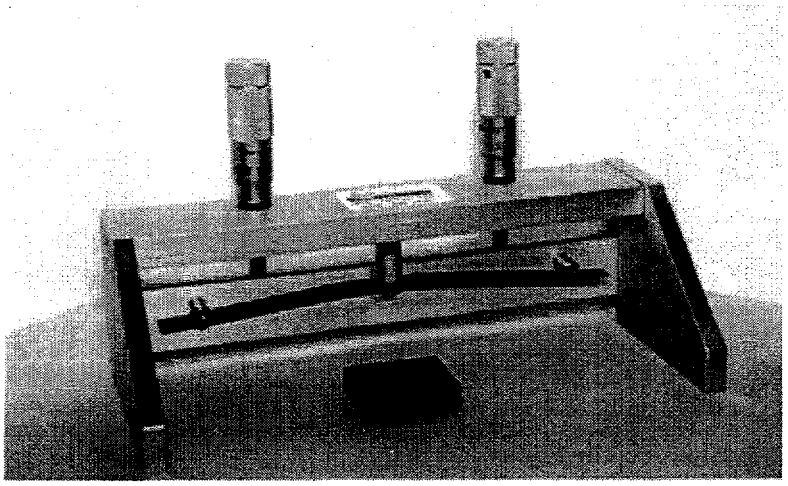

Figure 2: doctor blade apparatus

RESULTS: COATING QUALITY

Characterization of the samples

Visual evaluation of the coating

Good quality coatings exhibiting very few cracks and a smooth surface were obtained and are shown in Figure 3 and Figure 4.

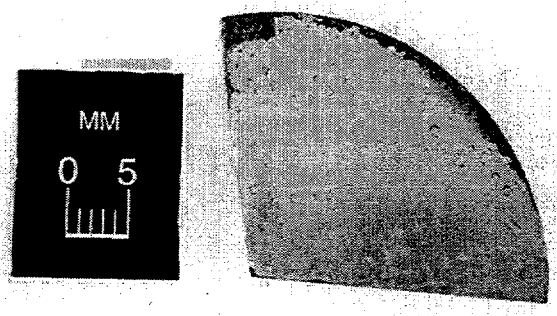

Figure 3: SiC/SiC coated with CMZP (doctor-blade process)

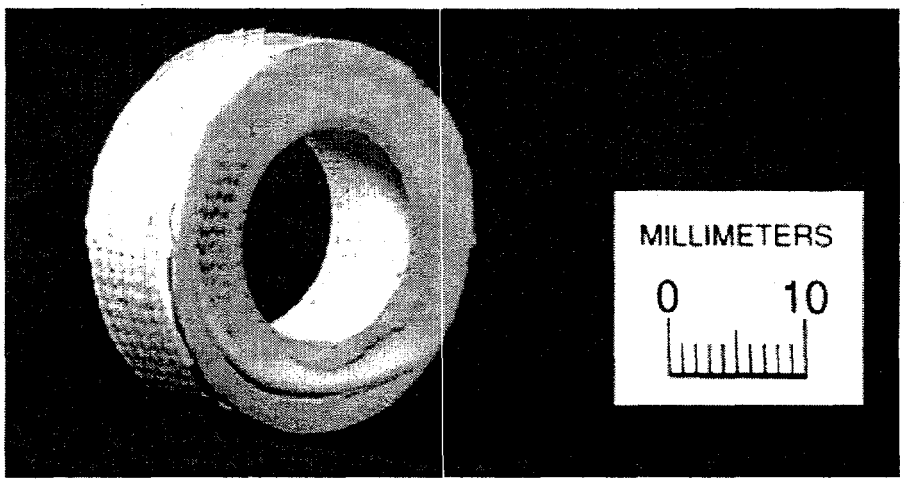

Figure 4: Example of CS50 coatings

X-ray diffraction

Determination of the phases present on the coating surface was determined before and after corrosion by standard X-ray diffraction (XRD) using a Scintag PADV diffractometer, which utilizes CuK_{α} radiation with a Peltier-cooled solid state detector. The coatings' diffraction patterns were compared with the reference powder diffraction patterns to determine the existence of new phases. No new phases have been detected on the X-ray of the coatings, indicating that no new crystalline compounds have been created.

Microscopy

Samples were embedded in epoxy resin, cut with a diamond saw and polished. Characterization of the coating/composite interface was first performed with an optical microscope, Nikon 4X, then with a scanning electron microscope (SEM) Hitachi S800. Pictures of different CS50 and CMZP coatings are seen in Figure 5 and Figure 6.

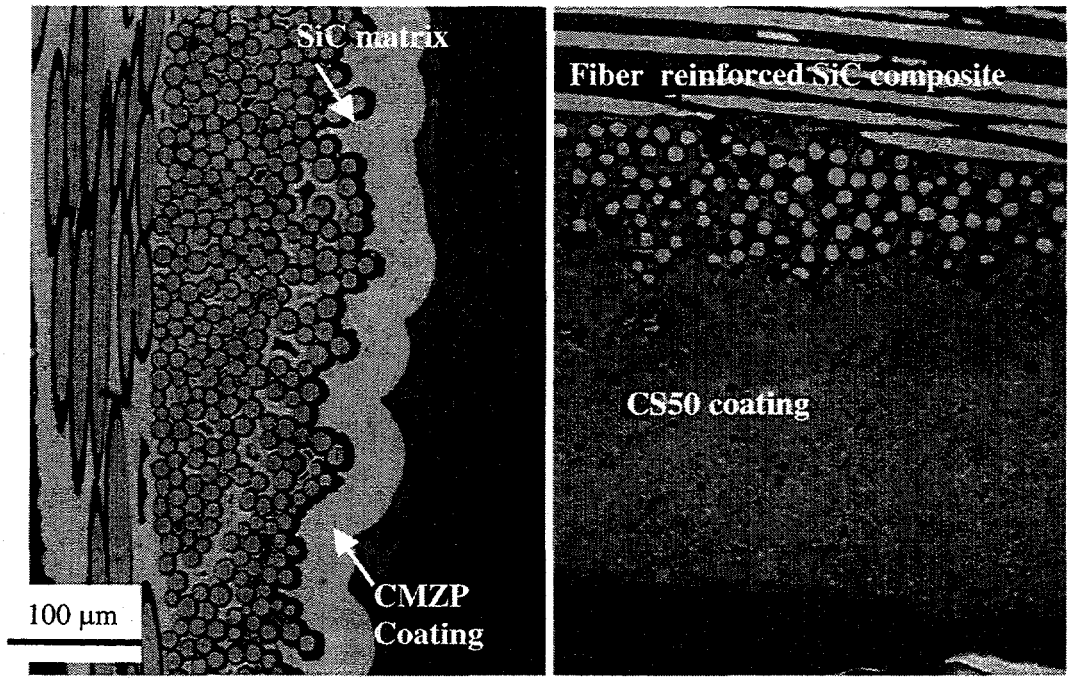

Figure 5: Optical micrographs of CS50 and CMZP coatings

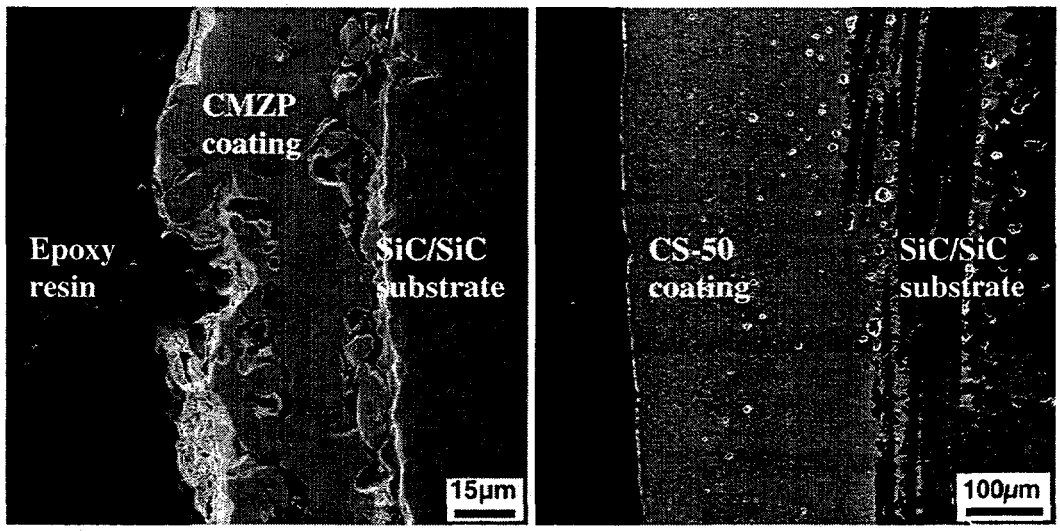

Figure 6: Scanning electron micrographs of CS50 and CMZP coatings

Corrosion resistance of the coatings

Experimental procedure

The surface of SiC oxidizes at high temperature to SiO_2. The silica layer is responsible for the oxidation resistance of the material. There have been excellent reviews of the oxidation of SiC and Si_3N_4 [1, 2] and it has been shown that the protective silica layer, when in contact with molten sodium salts, reacts to form a sodium silicate liquid, resulting in an increase in the oxidation rate. Several types of corrosion studies have been evaluated; (a) burner rig corrosion test [20], (b) application of a thin film of a sodium sulfite or sodium carbonate and heating the coated specimen to the desired temperature [21], and (c) partial or complete immersion of the specimen in a crucible containing the molten alkali melt. A thin film procedure was performed for this evaluation. A total of five specimens were used; 2 coated with CS-50, one coated with CMZP and 2 reference composites. The samples were carefully measured and weighed. Then the specimens were washed in an ultrasonic cleaner in acetone followed by distilled water. The samples were dried overnight in an oven at 60°C. The sodium sulfate loading was performed by heating the specimen on a hot plate at 90°C and by dispensing drops of saturated Na_2SO_4 solution. The samples were left to dry for an hour, weighed and more sodium sulfate was added until the loading reached 8 mg/cm^2. The samples were then heated in an Astro furnace at 1000°C for 100 hr. with O_2 at 200 cm^3/min flowing over them. The specimens were then weighed, washed in hot distilled water for two hours to dissolve any residual salt and sodium sulfate and then weighed again. Phases present on the sample surfaces were determined before and after corrosion by standard XRD. Some samples were then cut, polished using kerosene as a lubricant and observed with a SEM (Hitachi S800) to determine any microstructure transformation. An energy dispersive X-ray analysis (EDX) was also used to evaluate the penetration depth of sodium compounds.

No major weight loss has been observed for both coated and reference samples after exposure. The samples used during the study were very porous and it appears that the sodium sulfate flowed inside the samples. Thus, the surface loading must have been much lower than 8 mg/cm^2. No sign of degradation was found on the coated samples, but a white deposit was visible on both non-corroded composites. No sign of microstructure degradation was observed during

microscopic evaluation of the polished samples. Samples were then broken and observed with a SEM. Pictures of non-coated Nextel fiber-reinforced SiC matrix composite before and after corrosion are presented respectively in Figure 7 and in Figure 8. The corroded non-coated samples present a very glassy phase, indicating a degradation of the SiC matrix. SEM micrographs of corroded, coated (CS50) samples are presented for two different samples in Figure 9 and in Figure 10. Very little degradation of the composite was found for either sample. EDX results are presented in Figure 11. Sodium was detected in the CS50 coating, but not in the composite, indicting that most of the sodium was trapped in the coating, preventing the degradation of the substrate.

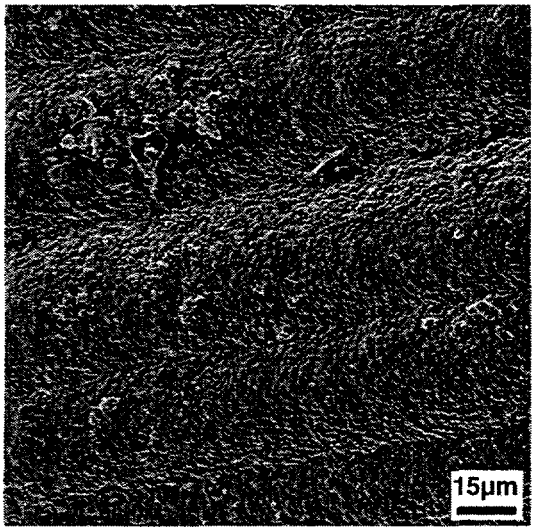

Figure 7: Non-corroded SiC composite

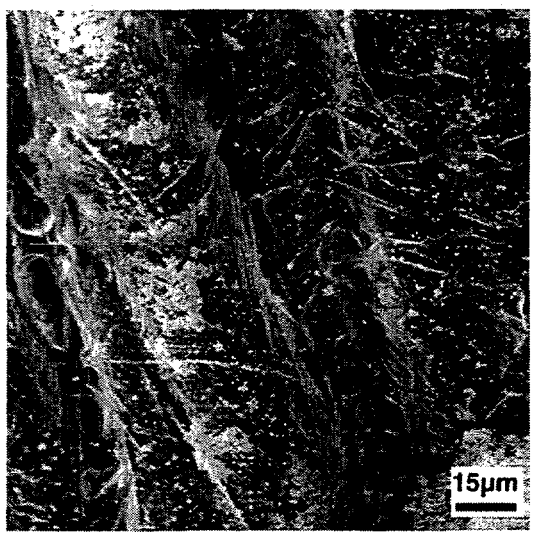

Figure 8: Corroded SiC composite

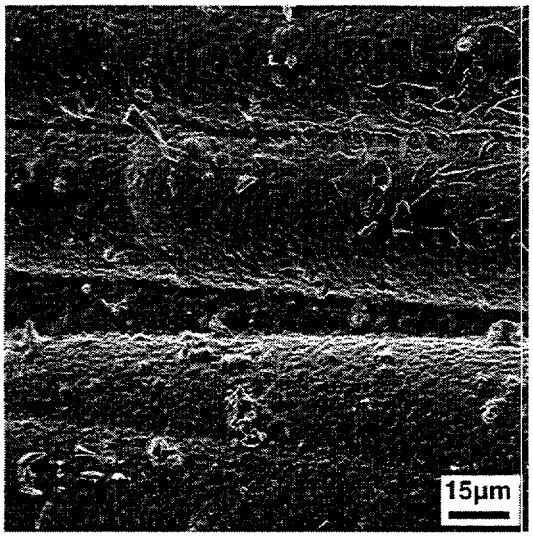

Figure 9: Corroded/ Coated SiC sample A

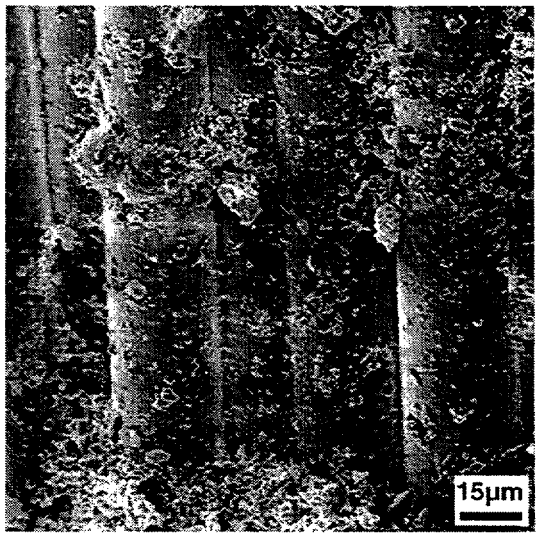

Figure 10: Corroded/ Coated SiC sample B

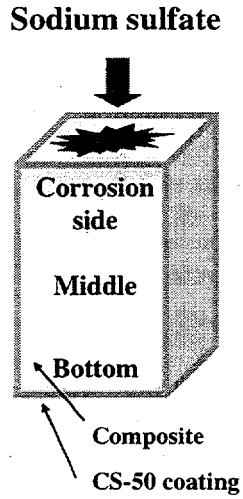

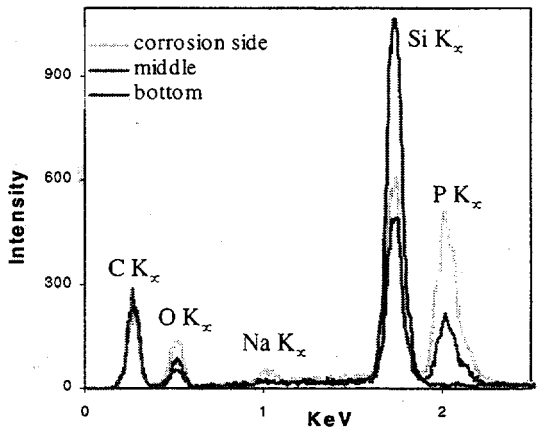

Figure 11: Energy Dispersive X rays were taken in different regions in the CS-50 coating close to the corroded side, in the middle and in the coating at the bottom

CONCLUSIONS

A good quality, relatively inexpensive coating process for putting oxide protective coatings on SiC/SiC has been developed and an understanding of the most critical factors controlling the process has been determined. The glaze like behavior of both NZP materials obtained with ZnO

additions was shown to be beneficial to the quality of the coating. Corrosion resistance of the coating is very encouraging and further improvements in the coating quality should make NZP coatings even more efficient in terms of corrosion protection.

ACKNOWLEDGMENTS

This work was supported by the Advanced Research and Technology Development Materials Program of the Office of Fossil Energy, U.S. Department of Energy under contract DE-AC05-96OR22464 with Lockheed Martin Energy Research Corporation. We would like to thank Carolyn Angel for the photography work, Tom Geer for the metallography work, John Stuecker for the processing of CMZP powder at New Mexico Tech and LoTEC, Inc. for providing us with CS-50 powder. We would also like to thank Claudia Walls for her help and advice during coating processing.

REFERENCES

[1] N. S. Jacobson, "Corrosion of Silicon-Based Ceramics in Combustion Environments", *Journal of the American Ceramic Society*, **76**, [1], 3-28, 1993

[2] G. R. Pickrell, T. Sun, J. J. Brown, "High temperature Corrosion of SiC and Si_3N_4", *Fuel processing technology*, **44**, 213-236, 1995

[3] L. O. Hagman and P. Kierkegaard, "The Crystal Structure of $NaMe_2^{IV}(PO_4)_3$; Me^{IV}=Ge, Ti, Zr", *Acta Chemica Scandinavice*, **22**, 1822-1832, 1968

[4] R. Roy, D.K. Agrawal, J. Alamo and R.A. Roy, "[CTP]: A New Structural Family of Near Zero Expansion Ceramics," *Materials Research Bulletin*, **19**, 471-77, 1984

[5] T. K. Li, D. A. Hirschfeld, S. VanAken, Y. P. Yang and J. J. Brown, "The Synthesis, Sintering, and Thermal Properties of $Ca_{0.6}Mg_{0.4}Zr_4(PO_4)_6$ (CMZP) Ceramics, *Journal of the Materials Research Society*, **8**, 2954-67, 1993

[6] S. Y. Limaye, D. K. Agrawal, and H. A. McKinstry, "Synthesis and Thermal Expansion of $MZr_4(PO_4)_6$, (M=Mg, Ca, Sr, Ba)", *Journal of the American Ceramic Society*, **70**, C232-36, 1987

[7] M. Kang, "Alkali/Steam Corrosion Resistance of Commercial SiC Products Coated with Sol-Gel Deposited Mg-Doped Al2TiO5 and $Ca_{0.6}Mg_{0.4}Zr_4(PO_4)_6$" Masters Thesis, VPI&SU, 1994

[8] T. K. Li, D. A. Hirschfeld, and J. J. Brown, "Thin Film Coatings of $Ca_{0.6}Mg_{0.4}Zr_4(PO_4)_6$ (CMZP) ceramics" *Journal of the Materials Research Society*, 9, 2004-18, 1994

[9] T. K. Li, D. A. Hirschfeld, and J. J. Brown, "Alkali Corrosion Resistant Coatings and Ceramic Foams Having Superfine Open Cell Structure and Method of Processing", U.S. Patent No. 5,268,199 Granted December 1993.

[10] W. Y. Lee, K. M. Cooley, C. C. Berndt, D. L. Joslin and D. P. Stinton, "High-Temperature Chemical Stability of Plasma-sprayed $Ca_{0.5}Sr_{0.5}Zr_4P_6O_{24}$ Coatings on Nicalon/SiC Ceramic Matrix Composite and Ni-based Superalloy Subtrates", *Journal of the American Ceramic Society*, **79**, [10], 2759-62, 1996

[11] W. Y. Lee, D. P. Stinton, and Debra L. Joslin, "Interaction of low-expansion NZP Ceramics with Na_2SO_4 at 1000°C," *Journal of the American Ceramic Society*, **79**, [2], 484-486, 1996

[12] N. R. Gurak, P. L. Josty, and R. J. Thompson, "Properties and Uses of Synthetic Polymers as Binders in Advanced Ceramics Processing", *Ceramic Bulletin*, **66**, [10], 1987

[13] J. J. Thompson, "Forming Thin Ceramics", *Ceramic Bulletin*, **42**, [9], 1963

[14] D. K. Agrawal and V.S. Stubican, "Synthesis and sintering of $Ca_{0.5}Zr_2P_3O_{12}$- A Low Thermal Expansion Material", *Materials Research Bulletin*, **20**, 99-106, 1985

[15] J. R. Clarcke, "The Sintering Effects of Time, Temperature and ZnO Additions on $Ca_{0.6}Mg_{0.4}Zr_4(PO_4)_6$ [CMZP] Ceramics", M.S. Thesis, Materials Science and Engineering, Virginia Polytechnic Institute and State University, Blacksburg, VA, 1996

[16] D. P. Stinton, D. M. Kupp, and R. L. Martin, "Corrosion-Resistant Coating Development", *Proceedings of the Twelfth Annual Conference on Fossil Energy Materials* (in press).

[17] R. E. Mistler, "Tape/Casting", Ceramics and Glasses, Engineered Materials Handbook Volume 4, ASM international, 161-165

[18] R. E. Mistler, "Tape Casting: The basic Process for Meeting the Needs of the Electronics Industry", *Ceramic Bulletin*, **69**, [6], 1990

[19] R. E. Mistler, R. B. Runk, and D. J. Shanefield, "Ceramic Fabrication Before Firing", G. Y. Onoda and L. L. Henc. Wiley, N.Y., 411-418

[20] D. S. Fox and J. L. Smialek, "Burner Rig Hot Corrosion of Silicon Carbide and Silicon Nitride." *Journal of the American Ceramic Society*, **73**, (2], 303-311, 1990

[21] N. S. Jacobson, J. L. Smialek, "Hot Corrosion of Sintered α-SiC at 1000°C.", *Journal of the American Ceramic Society*, **68**, (8], 432-39, 1985

CORROSION-RESISTANT INTERFACE COATINGS FOR NICALON®/SIC COMPOSITES

R. A. Lowden, J. J. Henry, K. L. More, H. T. Lin, and P. F. Tortorelli
Oak Ridge National Laboratory
P.O. Box 2008
Oak Ridge, Tennessee

Boron nitride continues to be of significant interest for use as fiber coating for controlling interfacial properties in advanced fiber-reinforced ceramic composites. It possesses all of the positive attributes of carbon; however, it exhibits improved oxidation resistance at elevated temperatures. Composites with properties comparable to those with carbonaceous interlayers have been produced, and enhanced oxidation resistance has been observed. Although BN has proven to be a useful fiber coating, the relationships between composition, microstructure, processing, and performance are not fully understood. Boron nitride, deposited on fibrous preforms employing chemical vapor deposition, is being characterized, and composites fabricated and tested. The effects of processing conditions and contaminants on the properties, microstructure, and oxidation behavior of boron nitride interface layers in Nicalon®/SiC composites are being evaluated. Oxygen contamination in BN interlayers has been shown to react with the fibers and matrix, degrading composite mechanical properties. Oxygen in the BN also accelerates the corrosion process. Carbon added during layer deposition had little effect on composite mechanical properties; however, oxidation resistance was diminished. It is hoped that the results of these studies will provide guidance for the optimization of BN and other interlayers for controlling interface properties in ceramic composites for use in elevated temperature applications.

INTRODUCTION

Typically, fiber coatings or "interlayers" are used to protect the reinforcements in ceramic composites from chemical attack during processing and to control interfacial forces. An interlayer must be thermochemically compatible with the fibers and matrix, control stresses and frictional forces within the composite, and be environmentally stable. Carbon, whether intentionally deposited on the fibers prior to consolidation[1-3] or formed serendipitously during processing,[4] is the

most commonly used interlayer in ceramic composites today. Carbon fiber coatings protect the reinforcements during processing, and control bonding and friction at the fiber-matrix interface. Exceptional room- and elevated-temperature mechanical properties have been measured, and thus ceramic composites are prime candidates for use in many advanced elevated-temperature applications.

A highly-oriented graphite layer has been shown to perform well in Nicalon® fiber reinforced SiC matrix composites.[5,6] The graphitic carbon coating protects the fibers during processing and controls the forces acting at the fiber-matrix interface. The presence of the carbon interlayer alters the compressive stresses at the interface and thus the properties of the composites. The poor oxidation resistance of carbon, however, is well known, as is the fact that any disturbance at the fiber-matrix interface can have a profound effect on the properties of a composite. Carbon begins to oxidize at temperatures around 400°C and oxidation is rapid in air at temperatures above 900°C.[7] It has been shown that the oxidation of Nicalon®/SiC composites begins by attack of the carbon interface coating at exposed fiber ends.[8] Once the carbon is removed along the entire fiber length, the matrix and fiber oxidize to form a silica layer that eventually bonds the components together, resulting in brittle behavior.

In order to improve the elevated temperature stability of fiber-reinforced ceramic matrix composites, boron-containing replacements for carbon fiber coatings are being examined. Hexagonal boron nitride is a leading candidate for it possesses a structure and mechanical properties similar to those of graphitic carbon, but exhibits improved oxidation resistance.[9,10] Hexagonal BN has been used successfully as an interlayer in a variety of ceramic/ceramic composites.[11,12] Nicalon®/SiC composites with polycrystalline BN interlayers, deposited using boron trichloride (BCl_3), ammonia (NH_3), and hydrogen (H_2) gas mixtures exhibited flexure strengths comparable to analogous specimens with a graphitic carbon interlayer.[11] The composites with the BN interlayers showed improved short-term oxidation resistance; however, toughness was diminished after a 24 h exposure in air at 1000°C. The decrease in toughness was caused by the decomposition of the fiber and chemical changes at the coating-fiber interface. It was found that oxygen contamination in the as-deposited BN layers caused the fibers to decompose, which led to a decrease in reinforcement strength and a loss of toughness.

Recent efforts have been devoted to the examination of the effects of contaminants on the properties, microstructure and environmental stability of boron nitride interface coatings for composites with silicon carbide matrices and reinforcements. Many factors influence the

properties and performance of BN fiber coatings. For example, the crystallinity of a BN coating appears to be significant when oxidation resistance is a concern. [9,10] Pyrolytic, polycrystalline BN coatings deposited using the aforementioned gas mixtures but at temperatures above 1400°C, exhibit good oxidation to 1300°C in dry air.[9] Amorphous BN coatings deposited at lower temperatures oxidize more rapidly, and at lower temperatures than the polycrystalline materials.[10] It is believed that amorphous BN layers typically contain a higher density of unstable or active oxidation sites, and are generally not stoichiometric. Low temperature BN deposits also typically contain oxygen, and these materials have been shown to decompose at room temperature.

Contaminants such as oxygen have a detrimental effect on the environmental stability of BN. To assess this phenomenon, BN fiber coatings with differing levels of oxygen contamination, < 2 and ~ 20 atomic % oxygen, were deposited on Nicalon® fabric preforms from gas mixtures containing BCl_3, NH_3, and H_2. The coated preforms were densified with a silicon carbide matrix employing the FCVI process.[13] In collaboration with participants of the CFCC Program's Supporting Technologies Task, the corrosion behavior and stability of the Nicalon®/SiC composites with oxygen-contaminated BN interface layers were evaluated.

Carbon is also commonly found in chemically vapor deposited BN interface layers. There are various sources of carbon contamination, such as graphite furnace components, preform fixtures, and heating elements. As with oxygen, carbon may also be detrimental to the stability of BN interlayers, and therefore the effects of carbon contamination on the processing, microstructure, and performance of BN fiber coatings were also examined. Methane, CH_4, was added to the BCl_3, NH_3, and H_2 gas mixture during fiber coating to simulate carbon contamination. Nicalon®/SiC composites were fabricated, tested, and characterized to examine carbon-contamination of BN fiber coatings.

EXPERIMENTAL PROCEDURE

(1) Composite Fabrication

Fibrous preforms were fabricated by stacking multiple layers of ceramic-grade Nicalon® plain-weave fabric rotated in a 0 ± 30° sequence within the cavity of a graphite holder. The layers were hand compressed to produce a preform with a nominal fiber loading of 40 vol. % and were held in place by a perforated graphite lid pinned to the holder. The polyvinylacetate cloth sizing

was removed through multiple washings with acetone. The nominal size of the fibrous preforms was 45 mm in diameter and 12.5 mm thick.

Preforms were next coated with the boron nitride interface layers. The coatings were deposited using a forced-flow, isothermal chemical vapor infiltration approach from gas mixtures containing boron trichloride (BCl_3), ammonia (NH_3), and hydrogen (H_2), a preform temperature of 1100°C, and a reactor pressure of ≈ 5 kPa. The ratio of boron to nitrogen in the reactant gas mixture was held constant at unity, and reactant flows and concentrations were modified to produce: (i) deposition rates similar to those for the standard graphitic carbon layer, (ii) microstructures comparable to those of graphitic carbon, and (iii) a uniform layer throughout the preform. Layer deposition time was then varied to control coating thickness. The final thicknesses of the interface layers were calculated from preform weight gains.

The high concentration of oxygen in the coatings was attributed to leaks in the furnace and gas distribution systems, and contamination of the reactants. In order to produce fiber coatings with minimal oxygen levels, the furnace and gas handling systems were completely refurbished, and reactants replaced. The integrity of the systems was verified through careful leak checks and frequent inspections.

Methane, CH_4, was added to the BCl_3, NH_3, and H_2 gas mixture to simulate carbon contamination. As before, the coatings were deposited using a forced-flow, isothermal chemical vapor infiltration approach, a preform temperature of 1100°C, and a reactor pressure of ≈ 5 kPa. The methane flow was varied to examine different levels of contamination and hydrogen flow was adjusted to maintain a constant total gas flow of 550 sccm. Deposition time was held constant at 2h. A summary of the methane additions to the deposition of the BN fiber coatings is given in Table 1.

Table 1. Gas Flows and Strengths for Nicalon®/SiC Composites with Carbon-Doped BN Interlayers

Dopant	**Gas Flows* BCl_3:NH_3:CH_4 (sccm)**	**As-Fab. Flexure Strength (MPa)**	**Oxidized Flexure Strength (MPa)**
None	25:25:0	365 ±	341 ±
Carbon	25:25:50	321 ±	305 ±
	25:25:100	293 ±	283 ±
	25:25:250	285 ±	254 ±
	25:25:500	177 ±	201 ±

* Hydrogen included to maintain total gas flow of 550 sccm.

The preforms were densified with silicon carbide using the forced-flow, thermal-gradient chemical vapor infiltration (FCVI) process.[13] The SiC matrix was produced by the decomposition of methyltrichlorosilane (CH_3SiCl_3 or MTS) in hydrogen at a hot-surface temperature of 1473 K and atmospheric pressure. The preforms were infiltrated with SiC to a maximum of 85 to 90 % of theoretical density in ~ 20 h.

(2) Testing and Characterization

Test bars were cut from the composite samples parallel to the 0° orientation of the top layer of cloth using a diamond saw, and tensile and compression surfaces were ground parallel to the long axis of the specimen. The average dimensions of the specimens were 2.5 x 3 x 40 mm and all specimens were measured and weighed to determine densities. Half of the specimens with the carbon-contaminated BN interlayers were oxidized in static air at 950°C for 24 hours.

Room-temperature flexure strengths for as-fabricated and heat-treated composites were measured in four-point bending. A support span of 25 mm and a loading span of 6 mm were used with a crosshead speed of 0.50 mm/min. The load was applied perpendicular to the layers of cloth. Load-displacement curves were recorded to examine the fracture process and determine the loads for ultimate strength calculations. Some of the flexure specimens were used in the stress-rupture

tests, and for thermogravimetric analysis. Details concerning the testing of the composites utilizing these techniques are given elsewhere.[14]

The composition and microstructure of the BN interlayers were examined using transmission electron microscopy. Specimens were prepared such that the area for analysis contained a quantity of fibers oriented perpendicular to the surface. The specimens were mechanically ground, polished, dimpled, and ion-milled to perforation using standard techniques. Microstructural characterization was conducted on a high-resolution transmission electron microscope (HRTEM). The BN layers were also analyzed by parallel electron loss spectroscopy (PEELS), conducted at 100 kV using a transmission electron microscope with a field emission gun in the diffraction mode (image coupled).

RESULTS AND DISCUSSION

It was evident that oxygen contamination of the BN fiber coating exacerbated the oxidation of the fiber and matrix, and accelerated degradation of the composite. The properties of composites containing BN interlayers with a high concentration of oxygen (~ 20 atomic %) were severely degraded upon exposure to an oxidizing environments. Stress rupture tests, conducted in air at 600 and 950 °C, showed significant differences in the performance of the composites with BN interlayers having varying levels of oxygen contamination. The results of the 600°C tests are graphically depicted in Figure 1. The composites with the higher oxygen content exhibited much shorter times to failure than those with the lower level of contamination.

Microstructural characterization of the composites after the stressed oxidation revealed no interaction between constituents, or oxidation thereof, for composites with the BN layer containing almost no oxygen (< 2 atomic % - Fig. 2). In contrast, both the matrix and reinforcement were oxidized in the composites with the high oxygen-content BN interlayer. The degree of oxidation intensified with increased temperature. In some cases, quantities of borosilicate glass and voids were found at the interlayer-fiber boundary, indicating significant decomposition of both the reinforcement and coating. It is thus concluded that oxygen contamination must be minimized or eliminated to produce stable composites with BN interlayers and SiC-containing constituents.

A summary of the results for the methane additions is given in Table 1 and graphically depicted in Fig. 3. The addition of methane diminished room temperature flexure strength,

which decreased further with increased CH_4 concentration. Although the as-fabricated strengths were lower than for composites with "uncontaminated" interlayers, the 24-h heat treatments in air at 950°C did not appear to substantially degrade the strength or toughness of the composites. Initial examination of the coatings employing TEM showed, however, the layers to be porous with highly disturbed microstructures (Fig. 4). It appeared that the addition of methane not only contaminated the BN with carbon but also disrupted the deposition process. These significant changes in interface coating microstructure likely result in differences in interlayer and interfacial properties, thus composite behavior, properties, and stability. As with oxygen, it appears that carbon contamination must be minimized to produce desired mechanical properties and ensure the stability of composites with BN interlayers.

CONCLUSIONS

Many factors influence the properties and performance of BN fiber coatings. Contaminants such as oxygen and carbon have proven to be detrimental to the environmental stability of BN. At elevated temperatures, oxygen present in the BN layer reacts with the fibers and matrix, degrading composite properties. The oxygen contamination in the BN appears to accelerate the corrosion process when composites are exposed to an oxidizing environment. Methane additions to the deposition process not only contaminated the BN with carbon but also disrupted the deposition process. These significant changes in interface coating microstructure likely result in differences in interlayer and interfacial properties, and thus diminish composite properties and stability. It can be concluded that contamination of the BN interlayer must be minimized or eliminated to produce stable composites with the given fiber coating and SiC-containing constituents.

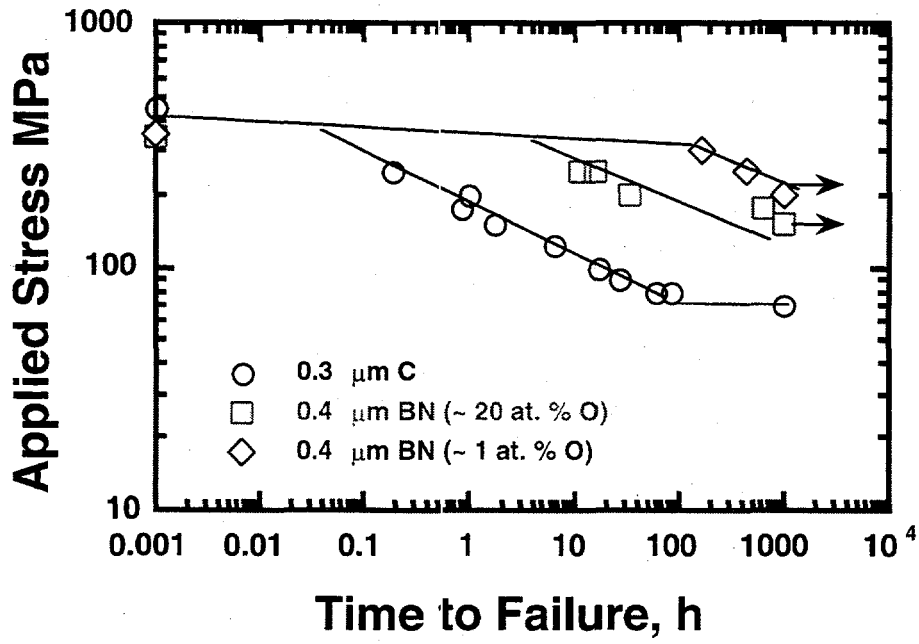

Figure 1. Four-point stress rupture tests of Nicalon®/SiC composites conducted in air at 600°C. (H.T. Lin, ORNL)

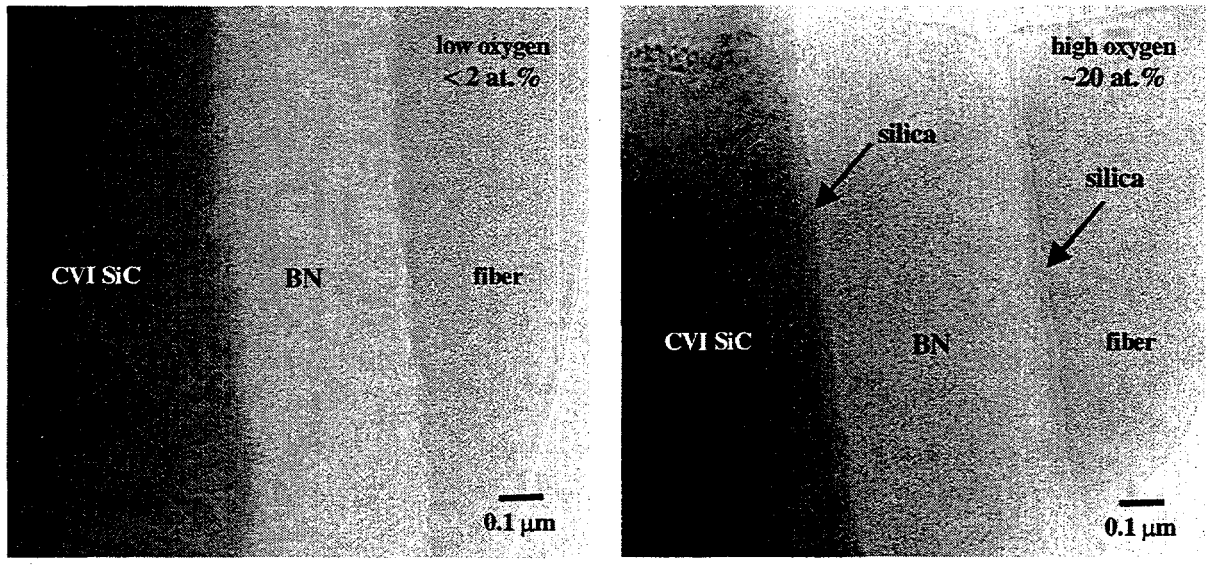

Figure 2. Transmission electron micrograph of Nicalon®/SiC composites with BN interlayers after oxidation at 600°C in air. (K. L. More, ORNL)

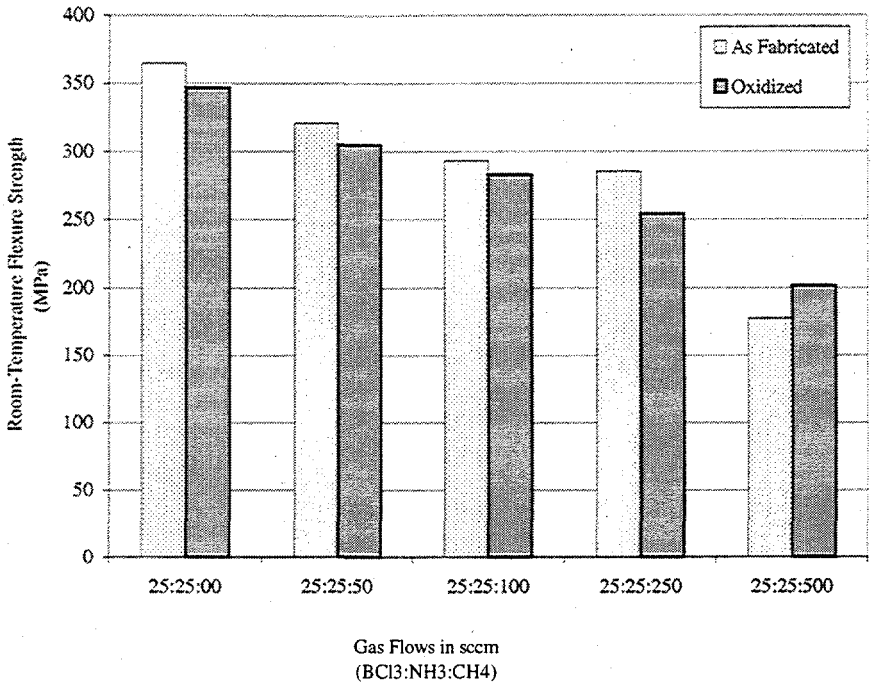

Figure 3. Room-temperature flexure strength of Nicalon®/SiC composites with carbon contaminated BN interface coatings.

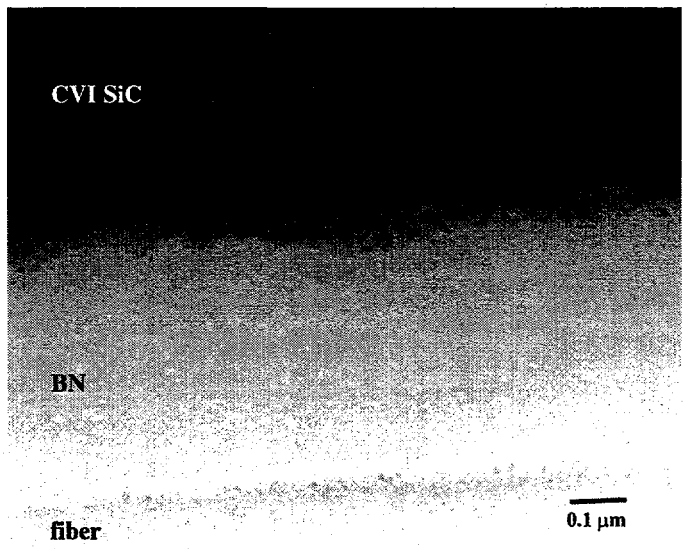

Figure 4. Transmission electron micrograph of carbon-contaminated BN fiber coating in a Nicalon®/SiC composite. (K.L. More, ORNL)

ACKNOWLEDGEMENTS

This project is being conducted in collaboration with the Supporting Technologies Task of the CFCC Program. Special thanks to K. L. More, H.T. Lin, Pete Tortorelli, Edgar Lara-Curzio, and the others involved in the testing and characterization of fiber-reinforced ceramic composites.

REFERENCES

1. R. A. Lowden, "Fiber Coatings and the Mechanical Properties of a Fiber-Reinforced Ceramic Composite," pp. 619-630 in *Ceramic Transactions*, Vol. 19, Advanced Composite Materials, ed. by Michael D. Sacks, The American Ceramic Society, Westerville, Ohio (1991).

2. Fretty, N. and M. Boussuge, "Relationship Between High-Temperature Development of Fiber-Matrix Interfaces and the Mechanical Behavior of SiC-SiC Composites," *Composites Science and Technology* **37**, 177-189 (1990).

3. Kmetz, M. A., Laliberte, J. M., and Suib, S. L., "Synthesis, Characterization, and Tensile Strength of CVI C/SiC, SiC/B_4C, and C/B_4C Composites," *Ceram. Eng. Sci. Proc.* **13**[9-10], 743-751 (1992).

4. J. J. Brennan, "Interfacial Characterization of Glass and Glass-Ceramic Matrix/Nicalon SiC Fiber Composites," pp. 549-560 in *MRS Proceedings, Vol. 20, Tailoring Multiphase and Composite Ceramics,* ed. R. E. Tressler et al., Plenum Publishing Corporation (1986).

5. R. A. Lowden, *Characterization and Control of the Fiber-Matrix Interface in Ceramic Matrix Composites*, ORNL/TM-11039, March 1989.

6. R. A. Lowden, "Fiber Coatings and the Mechanical Properties of a Fiber-Reinforced Ceramic Composite," pp. 619-630 in *Ceramic Transactions*, Vol. 19, Advanced Composite Materials, ed. by Michael D. Sacks, The American Ceramic Society, Westerville, Ohio (1991).

7. Hove, J. E., and W. C. Riley, "Graphite," pp. 14-76 in *Ceramics for Advanced Technologies*, John Wiley and Sons, New York, New York (1965).

8. James, R. D., R. A. Lowden, and K. L. More, "The Effects of Oxidation and Corrosion on the Properties of Nicalon®/SiC Composites," pp. 925-935 in *Ceramic Transactions*, Vol. 19, Advanced Composite Materials, ed. by Michael D. Sacks, The American Ceramic Society, Westerville, Ohio (1991).

9. Archer, N. J., "The Preparation and Properties of Pyrolytic Boron Nitride," pp. 167-181 in *High Temperature Chemistry of Inorganic and Ceramic Materials*, Special Publication No. 30, Edited by F. P. Glasser and P. E. Potter, The Chemical Society, London (1976).

10. Matsuda, T., "Stability to Moisture for Chemically Vapour-Deposited Boron Nitride," *J. Mater. Sci.* **24**, 2353-2358 (1989).

11. R. A. Lowden, K. L. More, O. J. Schwarz, and N. L. Vaughn, "Improved Fiber Coatings for Nicalon/SiC Composites," pp. 345-352 in the Proceedings of HT-CMC1, High Temperature Ceramic Matrix Composites, edited by R. Naslain, J. Lamon, and D. Doumeingts, Woodhead Publishing Limited: Cambridge (1993).

12. O. Dugne, et. al., "AES, XPS, amd TEM Characterization of Boron Nitride Deposited Under Chemical Vapor Infiltration (CVI) Conditions," *Journal de Physique*, Colloque C5, Supplement au n-5, Tome 50, 333-341, (1989).

13. D. P. Stinton, A. J. Caputo, and R. A. Lowden, "Synthesis of Fiber-Reinforced SiC Composites by Chemical Vapor Infiltration," *Ceram. Bull* **65** [2] 347-50 (1986).

14. H. T. Lin, P. F. Becher, and C. H. Hsueh, Time-Dependent Behavior, *Continuous Fiber Ceramic Composites Program Task 2 Bimonthly Progress Report for October-December 1997*, Compiled by M. Rawlins, R. A. Lowden and M. A. Karnitz.

GAS SEPARATION AND ADSORPTION STUDIES ON CARBON FIBER COMPOSITE MOLECULAR SIEVES

T. D. Burchell

INTRODUCTION

This research activity is directed toward the development of porous activated carbon fiber composite materials, which are manufactured from pitch based carbon fibers using a slurry molding process initially developed at Oak Ridge for the space program [1]. The material, known as a carbon fiber composite molecular sieves (CFCMS) will find wide application in the field of gas separations and storage, or as a catalyst support [2]. In previous years we have explored different methods of activation (development of the microporous texture) and demonstrated the ability of the material to preferentially adsorb certain gasses from a gas mixture [2-4].

DISCUSSION OF CURRENT ACTIVITIES

In the current reporting period we have directed our efforts toward the construction and preliminary use of a gas flow loop that will allow gas separation experiments to be conducted under field relevant conditions of temperature and pressure. Moreover, in our studies of the adsorption behavior of CFCMF we have examined the adsorption of water, and the role of surface functional groups in increasing hydrophilicity.

The Gas Flow Loop

A schematic drawing of the gas flow loop is shown in Figure 1. A premixed gas is circulated at pressures up to 1000 psi around the flow loop and passes through a water bath, allowing the gas temperature to be raised to temperature of 100°C or less. A side stream is led from the loop and passes through the adsorption cell, which is housed in a pressure vessel. The vessel internal space is filled with an inert gas at the same pressure as the flow loop. The adsorption cell (Figure 2) contains a large piece of activated CFCMS which is electrically insulated from the stainless steel cell wall. Copper head ring connectors are attached at each end of the CFCMS and electrical connections are led out of the cell and pressure vessel to a low voltage (0-8 V) power supply. The loop and cell are instrumented to allow the gas pressure, temperature and flow rates in the loop and adsorption cell

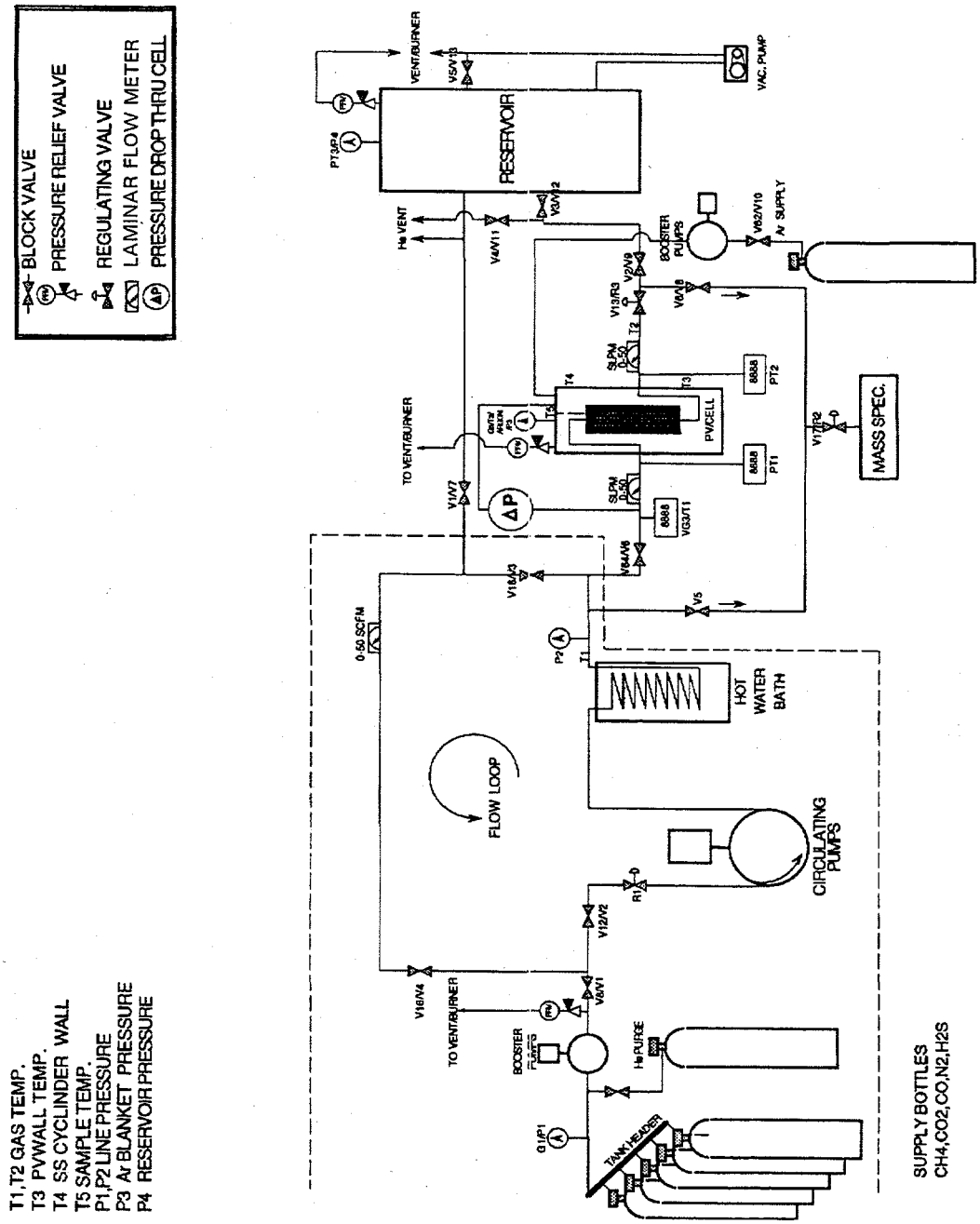

Figure 1. Schematic diagram of the Gas Flow Loop.

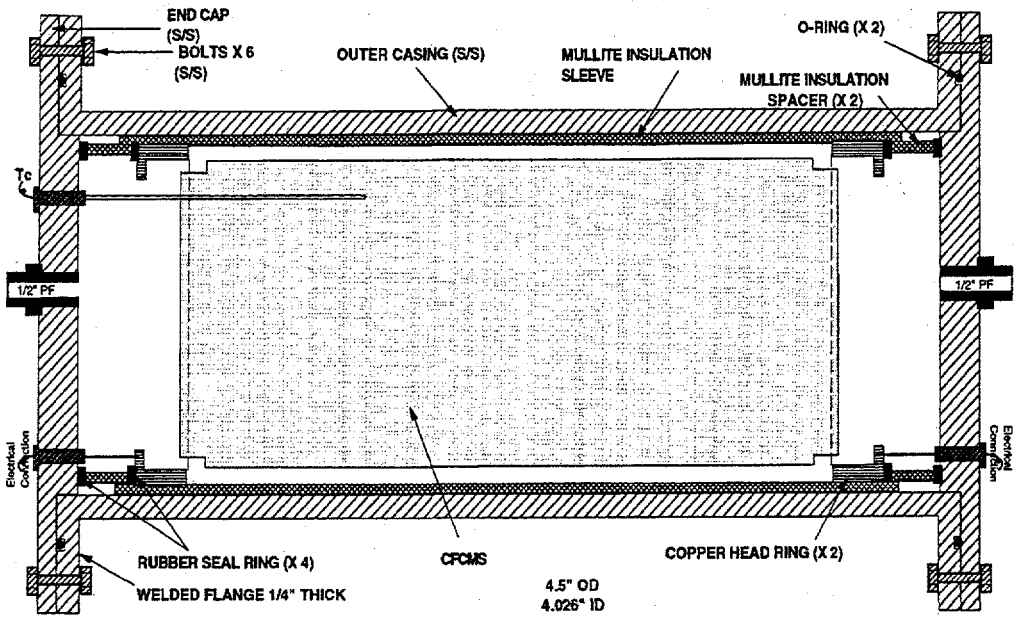

Figure 2. Schematic illustration of the Gas Flow Loop Adsorption Cell.

to be monitored and recorded. A sample of the cell outlet gas is led to a mass spectrometer so that breakthough of the adsorbed gas may be detected.

Initial trials of the gas flow loop have been successful. The loop has been pressure tested and trouble shooting has been completed. The Electrical Swing Adsorption (ESA) sub-system of the loop has been tested and the ability to heat the large CFCMS sample (9.5 cm diameter × 25 cm length) to temperatures exceeding 100°C demonstrated. Figure 3 shows the voltage-current relationship for the CFCMS sample in our ESA cell. The CFCMS attained a temperature in the ESA cell of 130°C when the applied voltage was 8V and the current was 20A.

Some problems were encountered when running at high pressures (P>200 psi). The exhaust gas stream must combust prior to being vented through the building exhaust system. The available burner and exhaust ducts cannot handle the high volume/velocity that results from high pressure operation. To remedy this situation the gas flow loop will be retro-fitted with two 200 gallon accumulator vessels which will run at low pressure (<200 psi). The accumulated exhaust gas can then be bled to the burner at lower pressure/velocity.

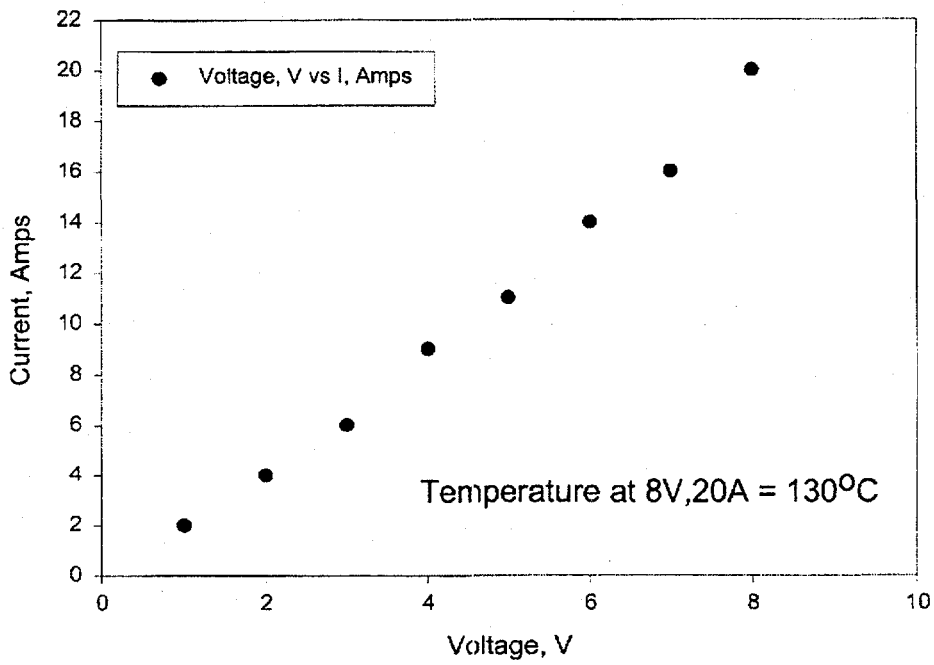

Figure 3. The current-voltage characteristics for a large CFCMS sample (95 mm dia. × 250 mm len.) measured in gas flow loop separation cell.

The Adsorption of Water on CFCMS

A microbalance study has been conducted to assess the ability of CFCMS to adsorb water from gas streams. Water vapor must be removed from natural gas prior to its entry to the pipeline distribution system. Moreover, there are numerous instances where drying gas streams prior to processing is required. Carbon materials are normally hydrophobic. However, it has long been known that water adsorption will occur if functional groups are added to the micropore surfaces. Consequently, a series of CFCMS samples were activated to develop large micropore volumes and then soaked at 200°C for 2 hours in flowing oxygen. Details of the samples' microporosity are given in Table 1 below.

Table 1. Micropore characterization data for CFCMS samples

Sample Number	Burn-off (%)	BET Surface Area (m^2/g)	DR Micropore Volume (cm^3/g)	DR Micropore Width (nm)
SMS 1-1	50.3	1886	0.68	2.2
SMS 1-2	50.3	2247	0.81	2.2
SMS 2-1	56.8	2144	0.75	2.3
SMS 2-2	56.8	2289	0.81	2.4
SMS 3-1	30.2	1271	0.48	1.9
SMS 3-2	30.2	1364	0.52	1.9
SMS 4-1	0	99	0.031	1.8
SMS 4-2	0	74	0.026	1.8

Each of the four CFCMS specimens reported in Table 1 was sampled in two places and the microporosity characterized. Subsequent to characterization, the CFCMS specimen was cut into two, and one half of each specimen exposed to flowing oxygen at 200°C for 2 hours. Samples from the treated and untreated CFCMS specimens were then placed in a microbalance and exposed to He saturated with water vapor at 18°C to determine their adsorption capacity. Water vapor adsorption measurements have been completed for samples, SMS 1 and SMS 3, in the oxygen treated and untreated conditions. Tests on the remaining samples are ongoing. The mass gains due to water vapor adsorption are reported in Table 2.

Several significant observations can be made from the data in Table 2. First, the amount of water adsorbed on the O_2 treated carbon is an order of magnitude greater than that adsorbed on the untreated carbon, demonstrating the role of surface functional groups in the water adsorption process. Second, the amount of water adsorbed is seen to increase with each cycle. This is especially noticeable in the untreated case. The reasons for this are unclear at the present time, but may be due to irreversible pore expansion during adsorption, or the creation of additional adsorptive sites in the micropores. In a collaborative effort with colleagues in the U.K. the nature of these surface functional groups is being determined.

Table 2. Moisture uptake data for CFCMS in the activated and oxygen treated conditions

Adsorption cycle #	Mass gain due to moisture adsorption (%)			
	Sample SMS-1		Sample SMS-3	
	Activated	Activated & O_2 treated	Activated	Activated & O_2 treated
1	0.75	21	0.5	24
2	0.9	31	1.5	27
3	2.1	34	6.5	31
Mean	1.25	29	3	27

ACKNOWLEDGMENTS

This work was supported by the Advanced Research and Technology Development Materials Program of the Office of Fossil Energy, U.S. Department of Energy under contract DE-AC05-96OR22464 with Lockheed Martin Energy Research Corp.

REFERENCES

1. Wei, G.C. and Robbins, JM. *Ceramic Bulletin,* **64** No. 5 (1985), pp. 691-699.

2. Burchell, T.D., Judkins, R.R., Rogers, M.R. and Williams, A.M. *CARBON,* **35** No. 9 (1997), pp. 1279-1294.

3. Burchell, T.D. and Judkins, R.R. *Energy Convers. Mgmt.* **37** Nos 6-8 (1996), pp.947-954.

4. Burchell, T.D. and Judkins, R.R. *Energy Convers. Mgmt.* **38** Suppl., (1997), pp.S99-S104.

DEVELOPMENT OF A MODIFIED 310 STAINLESS STEEL

R. W. Swindeman and D. A. Canonico*

INTRODUCTION

Because of their relatively low cost, good strength, fabricability, and corrosion resistance, austenitic stainless steels are widely used for high-temperature structural applications. Many 300 series stainless steels are Code-approved for pressure containment to 815°C and several specialty steels have been developed for construction of components operating above 815°C. Generally, steels containing at least 20% chromium are needed for adequate corrosion resistance above 650°C. The addition of strong carbide formers has significantly improved the load bearing capacity of the 20 to 25%Cr-bearing stainless steels, and the temperature range of their potential usage extends from 650 to 925°C. The purpose of the research on modified 310 and 20Cr-25NiNb stainless steels is to examine their behavior over a broad range of applications and to compare the performance of these stainless steels to higher alloys.

The potential uses of the stainless steels for fossil energy application were identified earlier and included superheater tubing in advanced steam cycle boilers, structural components for fluidized bed combustors, structural components for hot gas cleanup systems, and anchors for refractory liners (1). Criteria for design with these materials for service above 815°C were also reviewed (2).

DISCUSSION OF CURRENT ACTIVITIES

During the past year, activities included the procurement and characterization testing of tubing of modified 310 and 20Cr25NiNb stainless steels, the continuation of long-time creep testing of base metals, and the completion of fatigue and crack growth testing of the stainless steels and HR 120, the testing of alternate superheater tubing in various thermal-mechanical conditions.

---

* ABB-Combustion Engineering, Chattanooga, TN

Steels for low emission boilers

To address issues related to the selection of materials in the boiler, research was undertaken through a CRADA with ABB-Combustion Engineering to evaluate candidate tubing and piping materials. Issues include the relative merits of an all-ferritic steel system, the performance of dissimilar metal welds, the effect of cold work on the performance of stabilized and nonstabilized stainless steels, the relative performance advanced austenitic stainless steel tubing, and techniques of assessing damage due to excursions of temperature or pressure.

To assess damage accumulation methods, T91 tubing was removed from the superheater of a power boiler after exposure for more than 16 years (3). Examination revealed slight oxide wedging at dissimilar metal welds between T91 and the austenitic filler metal, minor type IV cracking under a stainless steel lug welded to T91, coarsening of the metallurgical structure, and slight cracking in the 321 stainless steel at dissimilar metal welds. The tensile strength and ductility of the T91 exceeded the requirements for the materials specification (ASME SA-213), but a loss was observed in the short-time creep strength that was similar to losses found after thermal aging for long times. These short-time data are compared to the database for T91 in Fig. 1.

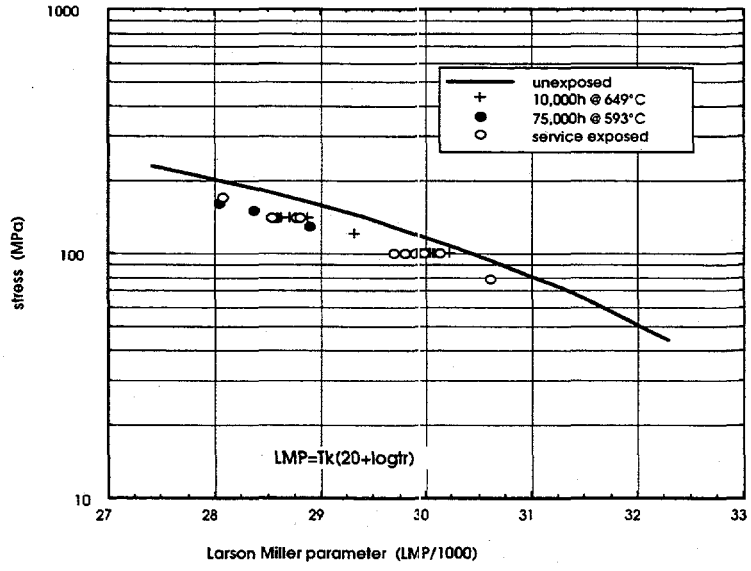

Fig. 1. Comparison of short-time stress-rupture data for T91 superheater tubing exposed 140,000 h in a power boiler to the stress rupture database for uniaxial test coupons.

Testing of 310TaN, 310HCbN, and 20Cr25NiNb stainless steels continued for times beyond 10,000 h. All steels exhibited excellent strengths at temperatures of interest to the LEB. The 20Cr25NiNb stainless steel was found to approach the strength level of the HT-UPS steels developed for the advanced steam cycle applications (4).

Steels for Service at 760°C and Above

The long-time testing of 310TaN stainless steel approached 50,000 h at 871°C (1600°F). Over the temperature range of testing 600 to 1038°C, the steel exhibited a fairly uniform behavioral pattern with no indication of structural instability. The modified 25Cr20NiNb stainless steel was found to have excellent creep strength and ductility to times well beyond 10,000 h. Slightly stronger than the 310TaN stainless steel, the 25Cr20NiNb steel was observed to have excellent weldability and good resistance to embrittlement. This stainless steel was judged to be a good alternative to the 310TaN stainless steel for service at 815°C and above. The two advanced stainless steels were estimated to be a least twice the strength of 310S stainless steel, and the 310TaN stainless steel was found be stronger than most other stainless steels used above 815°C, including 310HCbN, 253MA, RA85H, and the 20Cr-32Ni-Ti-Al (alloy 811) stainless steels (5). A comparison of strength levels at 10,000 h is provided in Fig. 2.

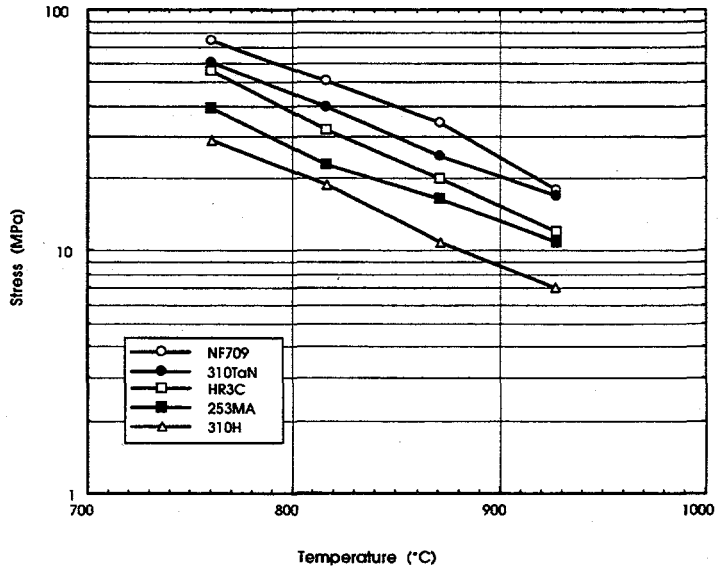

Fig. 2. Comparison of stress to produce rupture in 10,000 h for several stainless steels.

The high Cr-Ni alloy HR120 was selected for the tubesheet in the Westinghouse hot gas cleanup vessel at Wilsonville, and its usage in such an application requires good low cycle fatigue and crack growth resistance. Material from the Wilsonville tubesheet was supplied to ORNL for evaluation. The creep crack growth behavior was evaluated to 927°C (6).

SUMMARY

Studies show that advanced ferritic stainless steels degrade during service at elevated temperature, while advanced austentic stainless steels retain their strength. Studies of the 310TaN and 20Cr-25NiNb stainless steels show that these steels offer good strength and long-time stability properties at temperature below 760°C and could replace standard 300 series stainless steels and some specialty stainless steels for non-pressure-bearing service at 760°C and above.

REFERENCES

1. R. W. Swindeman, *The Potential of Modified 310 Stainless Steel for Advanced Fossil Energy Application*, ORNL/TM-12057, March 1992.

2. R. W. Swindeman and D. L. Marriott, "Criteria for Design with Structural Materials in Combined-Cycle Application above 815°C, " *J. Engineering for Gas Turbines and Power*, 116, 352-59 (April, 1994).

3. R. W. Swindeman, V. K. Sikka, P. J. Maziasz, and D. A. Canonico, "Evaluation of T91 after 130,000 Hours in Service," paper submitted for publication in the proceedings of the 1998 ASME Pressure Vessels and Piping Conference. San Diego, CA, July 21 to 26, 1998.

4. P. J. Maziasz, Developing an Austenitic Stainless Steel for Improved Performance in Fossil Power Facilities," *J. Met.* **41**, 14-20.

5. R. W. Swindeman, "Stainless Steels with Improved Strength for Service at 760°C and Above," paper submitted for publication in the proceedings of the 1998 ASME Pressure Vessels and Piping Conference, San Diego, CA, July 21 to 26, 1998.

6. W. Ren and R. W. Swindeman, "Time-Dependent Crack Growth Behavior of a Nitrogen Strengthened Ni-Fe-Cr-Nb-N Alloy 120," paper submitted for publication in the proceedings of the 1998 ASME Pressure Vessels and Piping Conference, San Diego, CA, July 21 to 26, 1998.

ADVANCED STAINLESS STEELS FOR RECUPERATOR APPLICATIONS

R. W. Swindeman, P. J. Maziasz, B. A. Pint
M. Fitzpatrick*, J. P. Montague*, A. Metcalfe*, and J. H. Grubb**

INTRODUCTION

Work on advanced austenitic stainless steels for superheaters has shown that the application of basic concepts of alloy design and fabrication technology can be effectively used to improve the performance of stainless steels, provided that the target properties are well-defined. These principals are being brought to bear on the objective of improving the performance of recuperators for simple cycle advanced turbine systems. A CRADA with the Solar Turbines, Inc. for this purpose has two goals. The first goal is to enhance the strength of 347 stainless steel foil to permit extension the operating life for existing recuperator designs for temperatures to 650°C. The second goal is to develop a stainless steel with improved strength and oxidation resistance that will permit an increase in the operating temperature of recuperator materials to near 704°C.

DISCUSSION OF CURRENT ACTIVITIES

Techniques to produce fine-grained 347 stainless steel foil with good oxidation resistance and mechanical strength were developed, and evaluations were undertaken in the temperature range of 677 to 732°C. The evaluation included four laboratory heats and one commercial heat, and each heat was examined in three thermal-mechanical conditions. The creep rates varied by more than two orders of magnitude. It was found that the fabrication schedule for standard 347 stainless steel could be optimized to meet the strength requirements of goal 1. A comparison of the creep behavior of the optimized condition with the standard condition is shown in Fig. 1 for 347 stainless steel at 732°C and 48.3 MPa. Based on these findings, a commercial heat is being produced to the modified processing schedule.

---

* Solar Turbines, Inc., San Diego, CA

** Allegheny Ludlum Technical Center, Brackenridge, PA

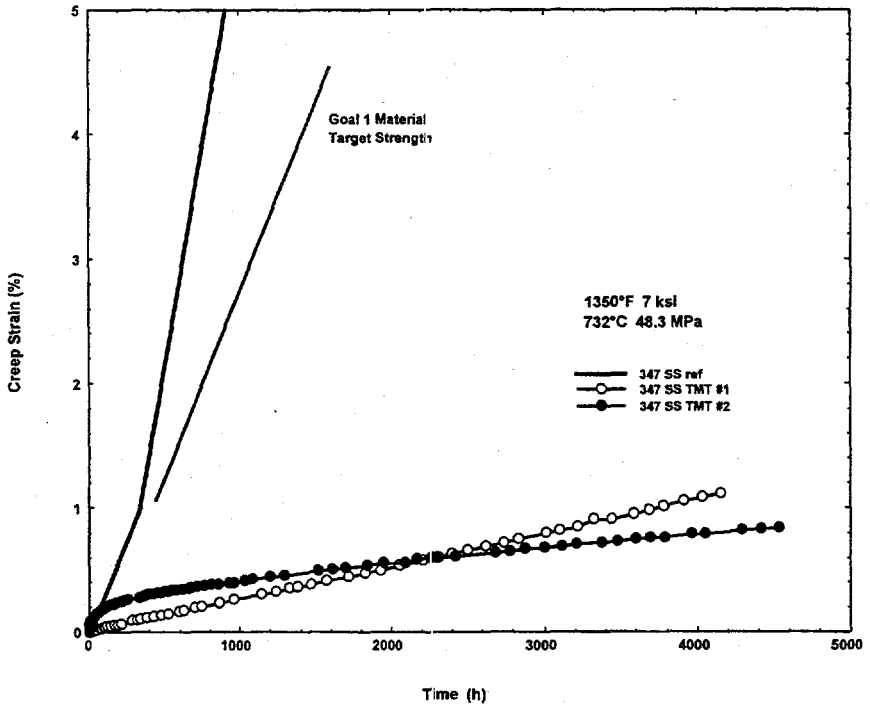

Fig. 1. Comparison of creep curves for 347 stainless steel at 732°C and 48.3 MPa in the standard and optimized processed condition to meet goal 1.

Exploratory creep testing was begun of alternate materials to meet goal 2. Steels such as 253MA and 310HCbN were examined but were eliminated due to poor strength. Three steels, 310TaN, modified 20Cr25NiNb, and modified 347 stainless steels, were found to be promising, and long-time creep testing was begun. Creep data at 704°C and 75.8 MPa are compared in Fig. 2. Here, it may be seen that the 20Cr-25NiNb stainless steel exhibited creep hardening to long times with no indication of tertiary creep. The creep rates approached that required for the goal 2 application. The modified 347 stainless steel exhibited low initial creep rates, but accelerated to a steady creep rate slightly above the requirement for goal 2. Some additional optimization of the fabrication schedules may be needed, but the initial results are encouraging.

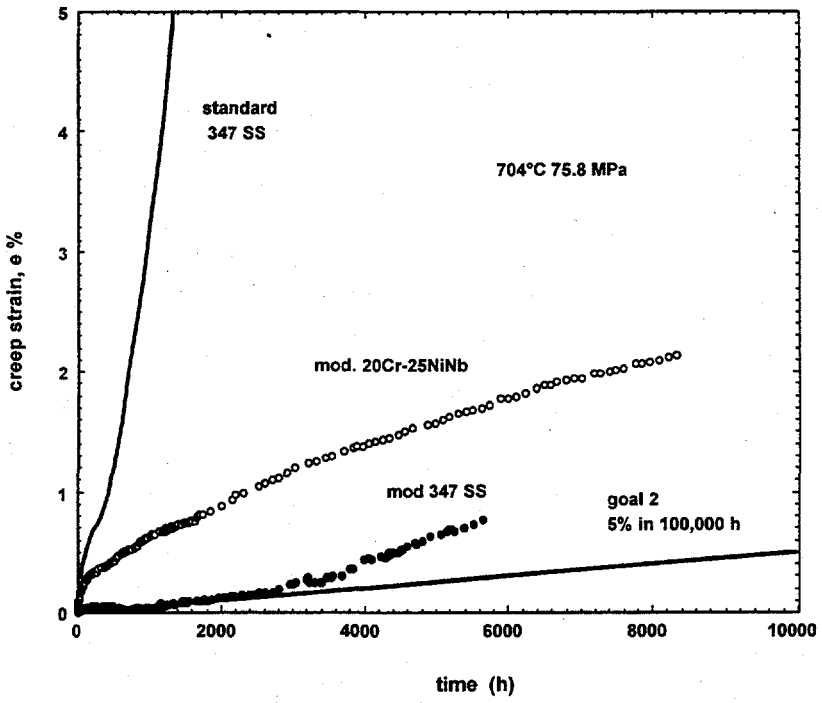

Fig. 2. Comparison of creep curves for 347 stainless steel at 704°C and 75.8 MPa in the standard and optimized processed condition to meet goal 2.

SUMMARY

Experimental work was undertaken to develop improved materials for construction of advanced recuperators for simple cycle gas turbines. Initial results were encouraging.

WELD OVERLAY CLADDING WITH IRON ALUMINIDES

G.M. Goodwin

Oak Ridge National Laboratory

ABSTRACT

We are continuing the development of iron aluminide filler metals and cladding techniques for overlay of aluminide compositions on various substrates. Recent efforts have emphasized the wire arc cladding process as a technique for potential commercial application. The process has the advantages of high deposition rate and low cost, and is made possible by the availability of the aluminum-cored, iron-sheathed composite filler metals developed in this program.

Optical metallography and electron microprobe analyses of wire arc sprayed coatings on steel substrates show a tightly adherent deposit with a mixed microstructure consisting of high and low aluminum phases and a distribution of thin layers of aluminum oxide, from which the coating derives its excellent resistance to cracking and spalling. Deposits on 3-in diameter carbon steel boiler tubes have survived over one year of exposure to 800 degrees F and 30 thermal cycles to room temperature with no evidence of degradation.

In order to characterize the performance of wire arc coatings in a simulated coal gas environment, a new specimen design has been developed which can be used in the standard isothermal test facility. The specimen is cylindrical with hemispherical ends, which permits coating of the entire surface with uniform thickness.

Clad specimens have been prepared for environmental testing in-house and at outside facilities.

INTRODUCTION

To utilize the excellent properties of alloys based on the Fe_3Al nominal composition, we are continuing to develop welding filler metals, processes, and procedures aimed at introducing these alloys into commercial service.

Due to the difficulties involved with joining monolithic sections of these materials, recent activities have emphasized overlay cladding using conventional gas metal arc and gas tungsten arc welding processes, as well as wire arc cladding, a thermal spray technique. All three of these approaches are made possible by the availability of iron-sheathed, aluminum-cored composite filler metal developed in this program.

FILLER METAL DEVELOPMENT

We have developed and now have available a family of filler metal compositions spanning a range of aluminum contents from less than 8 to greater than 26 weight % (see table I). These aluminum-cored, iron-sheathed composite wires are 1.6-mm diameter, in spooled form, and thus can be used with automatic wire feeders in a variety of welding and cladding processes (1,2). The actual deposit composition can be modified as desired by control of dilution, deposition rate, and other welding parameters.

Table I. Composition of Filler Metals

Heat	Weight %	Al	Cr	C	Zr	Mo
Stoody I	Aim, all weld metal	20	7	0.1	0.25	0.25
	Actual, all weld metal	21.8	7.3	0.06	0.40	NA[a]
	Actual, clad deposit[b]	12.6	6.0	0.08	0.20	0.44
Stoody II	Aim, all weld metal	20	–	0.1	0.25	0.25
	Actual, all weld metal	21.5	–	0.08	0.25	NA
	Actual, clad deposit	12.6	–	0.1	0.12	0.4
Stoody III	Aim, all weld metal	12	–	0.1	0.25	0.25
	Actual, all weld metal	12.5	–	0.06	0.4	NA
	Actual, clad deposit	7.6	–	0.07	0.32	0.4
Stoody IV	Aim, all weld metal	26	–	0.1	0.25	0.35
	Actual, all weld metal	26.5	–	0.08	0.6	NA
	Actual, clad deposit	14.1	–	0.09	0.32	0.4

[a]NA–Not Analyzed.
[b]Single layer gas metal arc on 25.4-mm thick type 2-1/4 Cr–1 Mo steel.

WIRE ARC CLADDING[1]

Wire arc cladding, also known as arc spraying, is being investigated as an alternative to conventional gas tungsten arc or gas metal arc weld cladding. A primary advantage of this technique is that it avoids the cold cracking problems inherent with fusion welding techniques. The process is shown schematically in figure 1, from (3).

Basically, an arc is struck between two independently fed wires, and compressed gas is used to detach molten droplets from the arc zone and propel them to the substrate. It is a high velocity, high deposition rate process, with droplet temperatures high enough to assure good bond strength. Figure 2a and b show an overall view and cross-section of 3-in (76-mm) OD carbon steel boiler tube clad with the Stoody II composite filler wire (see table I). Spray parameters were 100 amperes DCV, 30 volts, and 90 psi air pressure. As seen in the figure, the coating is heterogeneous but sound. The chemical analysis of the coating is shown in table II. Note that other than the major elements Fe and Al, there is little impurity content in the deposit, it having essentially the same composition as the undiluted, all weld metal deposit applied by fusion welding. It is particularly interesting that the overall oxygen content of the deposit is only 0.34 weight %, even though the entire process is conducted in air. Other test deposits were produced in dry nitrogen, and the oxygen levels remained essentially constant, indicating that most of the oxygen pickup occurs after the droplets have left the arc zone.

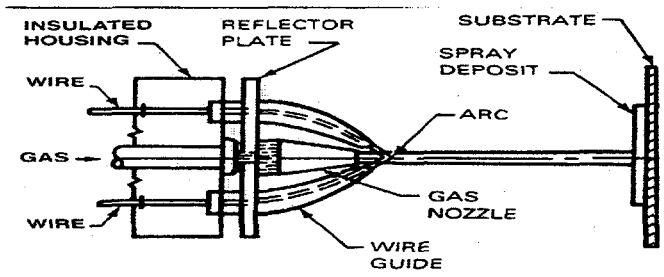

Figure 1. Schematic of Wire Arc Process.

[1]This task is being performed in collaboration with E. A. Franco-Ferreira of the Engineering Technology Division.

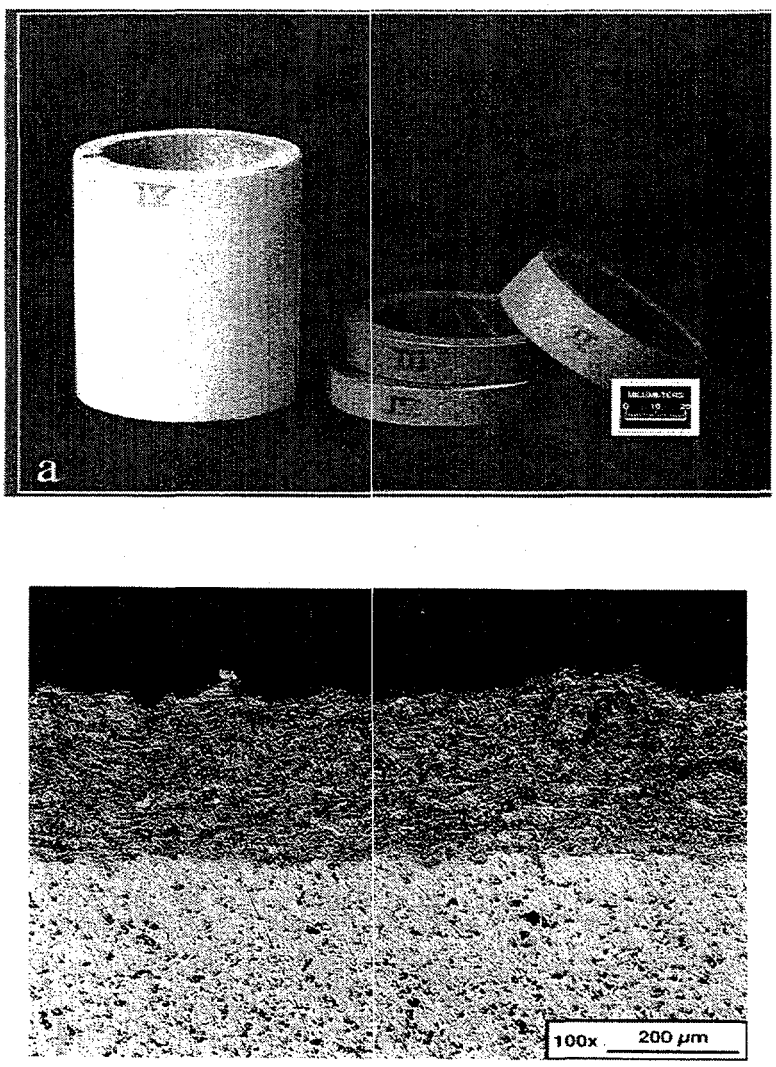

Figure 2. Boiler Tube Coated by Wire Arc Cladding,
(a) Overall, and (b) Microstructure.

Table II. Composition (weight %) of Wire Arc Deposit

Fe	78.2
Al	21.3
C	0.011
Mn	0.03
S	0.002
Si	0.03
Ni	0.01
Cr	0.02
Mo	0.02
Cu	0.03
N	0.05
O	0.34

Electron microprobe analyses of the clad deposit are summarized in figure 3a through e. Figure 3a shows the normal image, 3b the backscattered electron image, and 3c, d, and e, element maps for Fe, Al, and O, respectively. Note that the deposit is heterogeneous, with limited mixing of the iron and aluminum components, and that many of the discrete regions are coated with high oxygen layers, which may explain the excellent resistance of this composite structure to thermal cycling, *i.e.*, it behaves like a cermet.

Ring samples of wire arc clad 3-in (76-mm) OD carbon steel boiler tubes produced with three different wire compositions (Stoody II, III, and IV, see table I) have survived aging for over one year at 800 degrees F with over 30 thermal cycles to room temperature without any evidence of cracking, spalling, or any other degradation. Samples have also been prepared for testing in the ORNL isothermal simulated coal gas test facility. The new design specimens are 0.5-in (12.7-mm) diameter cylinders with 0.5-in (12.7-mm) straight length and hemispherical ends, which permits cladding of the entire surface with a uniform thickness.

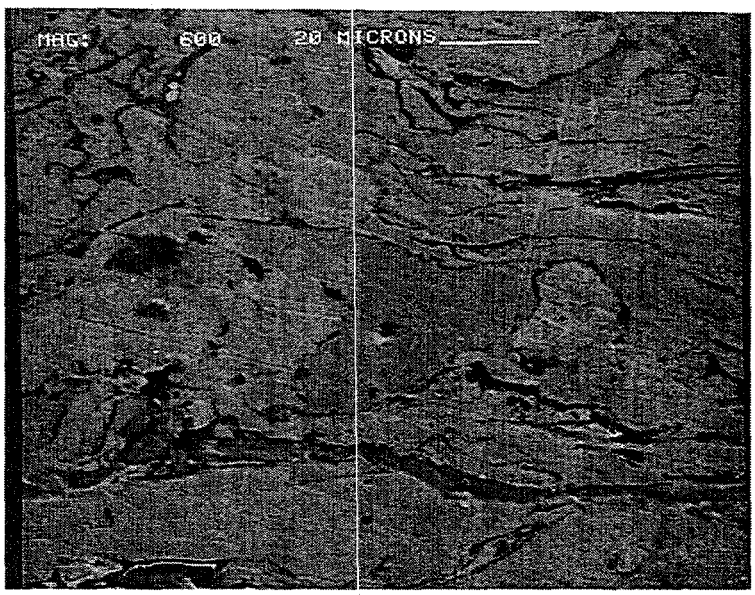

Figure 3a. Electron Microprobe Analyses of Wire Arc Clad Deposit, Normal Image.

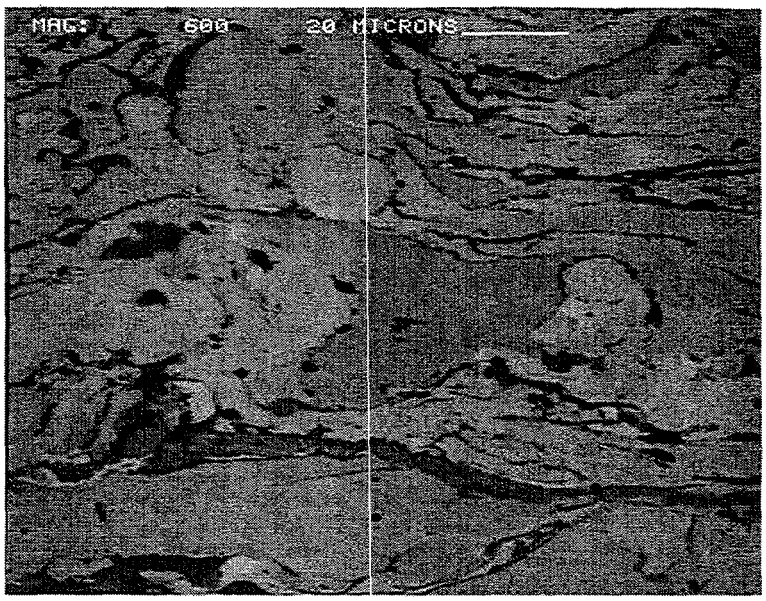

Figure 3b. Wire Arc Clad Deposit, Backscattered Electron Image.

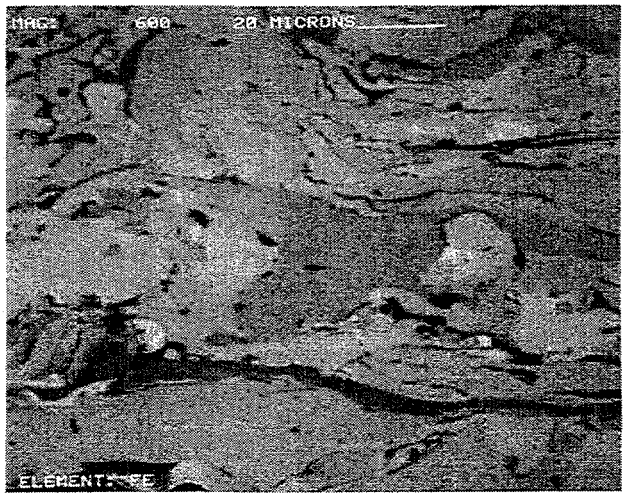

Figure 3c. Wire Arc Clad Deposit, Element Map for Fe.

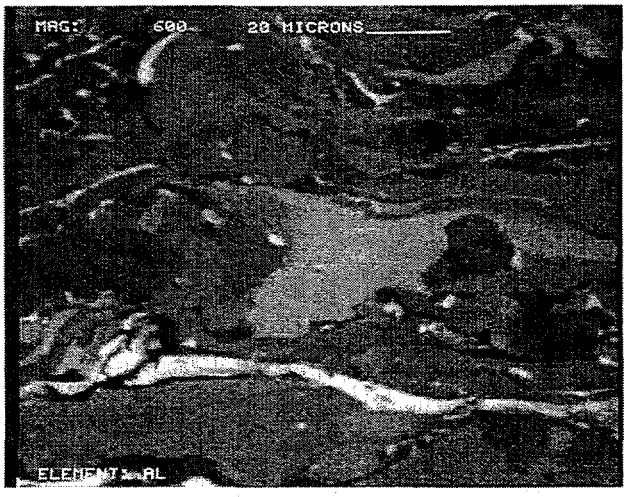

Figure 3d. Wire Arc Clad Deposit, Element Map For Al.

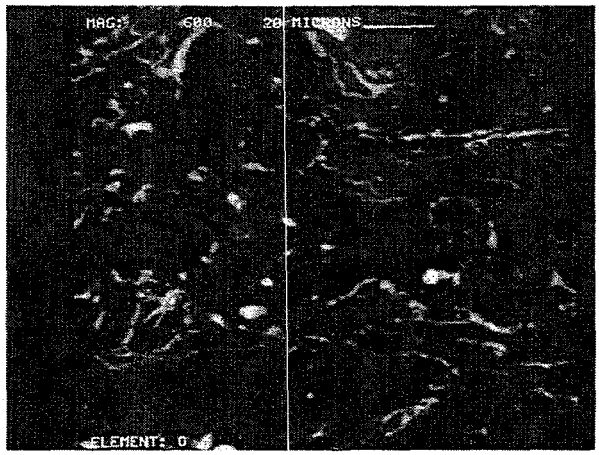

Figure 3e. Wire Arc Clad Deposit, Element Map for O.

REFERENCES

1. G.M. Goodwin, "*Weld Overlay Cladding with Iron Aluminides,*" Proceedings of the Tenth Annual Conference on Fossil Energy Materials, ORNL/FMP-96/1, Oak Ridge National Laboratory, August 1996.

2. G.M. Goodwin, *"Weld Overlay Cladding with Iron Aluminides,"* Proceedings of the Eleventh Annual Conference on Fossil Energy Materials, ORNL/FMP-97/1, Oak Ridge National Laboratory, December 1997.

3. Welding Handbook, **2**, Eighth Ed., pp 872-74, American Welding Society, Miami, FL, 1991.

ODS IRON ALLOYS

I. G. Wright, C. G. McKamey, E. K. Ohriner, and B. A. Pint

INTRODUCTION

The various processes that will form part of a Vision 21 powerplant [1] will be honed to operate at maximum efficiency in order to accomplish the overall efficiency goal of such plants of 65 percent. Such processes will likely involve gasification of coal, cleanup of the hot product gas stream, separation of the gas into fuel and product synthesis streams, combustion of the fuel gas, reaction of the synthesis gas, and cleanup of effluent streams. The components of such plants will have requirements for materials to operate at increased temperatures, necessitating increased high-temperature strength capabilities and improved resistance to degradation in the environments encountered, which will range from oxidizing to sulfidizing to carburizing. These components will include pressure containment vessels, tubing, valves, filters, and gas and steam turbine parts.

The strongest available ASME Boiler Code-certified alloys have usable strength to approximately 900°C but, since these are typically austenitic Fe-Ni-Cr-based alloys, they have relatively low thermal conductivity and are susceptible to environmental attack, particularly in sulfidizing and carburizing environments. The ferritic ODS alloys based on Fe-Cr-Al have the potential for application at higher temperatures than the modified conventionally-strengthened alloys in which the strengthening mechanisms degrade as the precipitated phases become less stable with increasing temperature. Oxide dispersion-strengthened alloys can provide creep strength up to approximately 90 percent of the alloy melting temperature (which is 1480°C for FeCrAls). The use of ODS alloys is currently limited to a few niche applications, partly because they are relatively expensive to produce, and partly because design and fabrication using ODS alloys require the implementation of procedures that are different from those used with conventional wrought alloys. Nevertheless, the potential of ODS-FeCrAl alloys has been demonstrated with the construction and operation of an externally-fired heat exchanger of harp design, made from 4 m long, 2.5 cm diam. tubes, to heating air to 1100°C in a closed-cycle demonstration plant [2].

Compared to ODS-FeCrAl alloys, ODS-Fe_3Al has potential advantages of superior sulfidation and carburization resistance, longer oxidation-limited lifetimes, lower density, and potentially lower cost, provided that adequate creep strength can be developed through the incorporation of oxide dispersion strengthening. Hence, the goal of this program is to determine the potential for improving the high-temperature strength of Fe_3Al by ODS processing, to ensure that the inherent high-temperature environmental resistance is not impaired, and to expedite the use of this (and other ODS alloys) to overcome some of the materials-limited barriers identified in the advanced coal conversion and utilization processes required in Vision 21 power plants.

DISCUSSION OF CURRENT ACTIVITIES

Recrystallization

Recrystallization experiments on three variants of ODS-Fe_3Al reported earlier [last year] found that one alloy, PMWY2 [Fe-28Al-2Cr-0.0015Zr (at.%) + 0.3 cation% Y_2O_3], could be recrystallized to form very large, elongated grains at temperatures of 1200°C and higher, whereas PMWY1 did not recrystallize below 1300°C, and PMWY3 did not recrystallize under any of the conditions studied. The three alloys were made from the same starting alloy powders, but different gaseous environments were used in the high-energy milling processing [3]. The bulk of the subsequent studies have used alloy PMWY2.

The microstructures of PMWY2 recrystallized at 1200°C contained a few non-recrystallized grains, which resulted in elongated, fine-grained regions amidst otherwise very large grains which had large length to diameter ratios—essentially archetypal ODS alloy grain structures. It appeared that the population of these non-recrystallized features decreased with increasing time at temperature, and with increasing temperature. A further concern was the appearance of pores in the alloy after recrystallization. Two types of pores were found: large pores associated with regions of non-recrystallized grains, and finer pores which were visible in the unetched alloy, and which assumed a characteristic shape after etching. With increasing temperature it appeared that the size of the (finer) pores increased, while their number decreased. Figure 1 is an attempt to illustrate this behavior with data obtained by automated image analysis of specimens subjected to different recrystallization treatments. Note the rapid increase in size (and decrease in number) of

the pores from 1300 to 1350°C suggested in Fig. 1a. Figure 1b illustrates the finding that the size of the smallest pores remained essentially constant under the conditions studied, while the size of the largest pores increased by a factor of ten in the temperature range 1300 to 1350°C. As a compromise between minimizing the size of the porosity present as well as the number of unrecrystallized grains, the procedure adopted for the preparation of mechanical test specimens was the B9 schedule: rapid heat up from 1100 to 1275°C, 1 h at 1275°C, and rapid cool to 800°C with furnace cooling from 800°C.

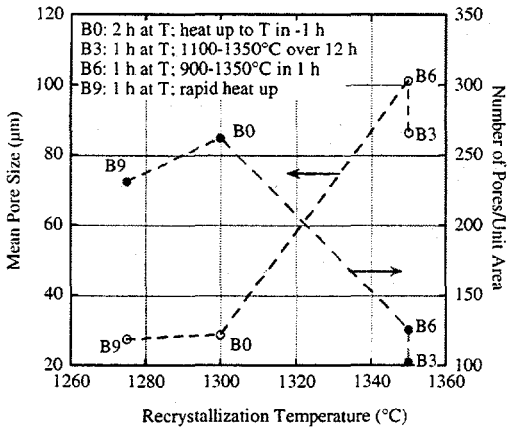

(a) Effect of temperature on pore size and number

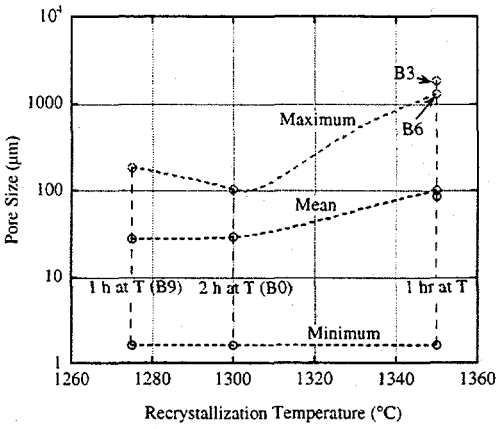

(b) Effect of temperature on mean pore size

Fig. 1. Changes in pores size and number as a function of recrystallization temperature

In a companion study [4], the available experience on the sources and types of defects and their effects on alloy properties is being examined for information to help devise routes to minimize the formation of pores, and to eliminate the non-recrystallized grains. Significant advances in this area were made during the processing of ODS alloys as part of a European collaborative (COST) program [2].

Creep Tests

Round specimens with a gauge diameter of approximately 3 mm and a gauge length of 17.8 mm were machined from extruded and recrystallized ODS-Fe_3Al bars. These specimens were creep-rupture tested in air at temperatures of 980-1075°C and at stresses of 34-48 MPa

(5-7 ksi), using a 20:1 lever arm ratio in a dead-load type creep machine. The results for specimens heat treated by the indicated schedules are summarized in Table I, which also repeats data reported earlier for specimens recrystallized to schedule B0. The first two specimens were heat treated using schedule B3, and were set up for testing at 980°C/34 MPa and 1075°C/48 MPa, respectively. However, during initial loading of the weights onto the load pan, both specimens failed immediately with large elongations to failure, as indicated in Table I. Metallography and scanning electron microscopy of the specimen ruptured at 1075°C showed it to contain numerous creep cavities (Figs. 2 and 3). These cavities were observed throughout the gauge length and were elongated proportionately as one approached the fracture. The presence of cavities at long distances from the fracture, combined with the lack of strength of the specimens, suggested that these cavities were present before testing. Optical metallography of the

Table I. Creep-rupture properties of ODS-Fe_3Al alloy PMWY2

Recrystallization Temp. (°C)/Time (h)	Test Conditions		Creep Properties	
	Temp. (°C)	Stress (MPa)	Life (h)	Elong. (%)
1350/1*	980	34	0	12.8
1350/1*	1075	48	0	• 20
1300/2**	980	48	68.35	1.7
1300/2**	1075	48	8.3	3.1
1300/1†	980	34-41	250	0.2
1275/1††	1075	34.5	205.3	<<1.0

* schedule B3: 1100 to 1350°C over 12 h

** schedule B0: heated to 1300°C over 2 h

† schedule B8: 900 to 1300°C in 1h

†† schedule B9: rapidly heated to 1275°C

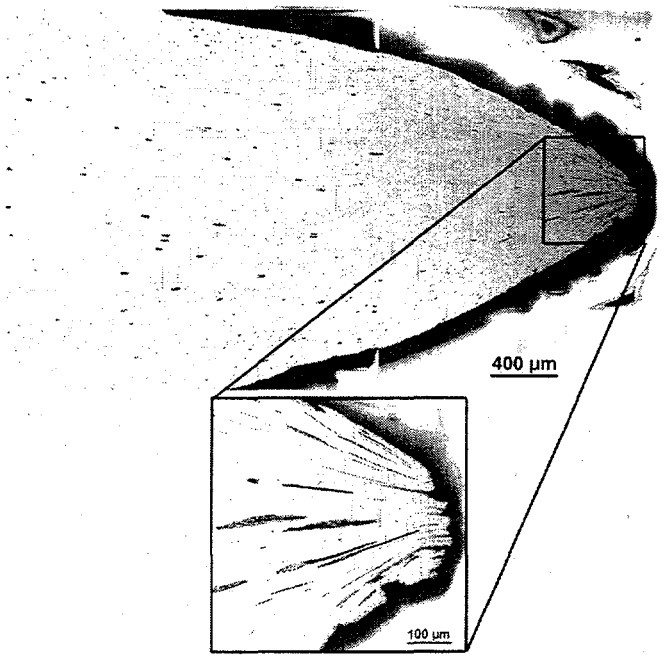

Fig. 2. Optical micrograph showing elongated creep cavities in specimen recrystallized to schedule B3 creep tested at 1075°C under a stress of 48 MPa. The specimen failed immediately on application of the stress, with approximately 20% elongation.

shoulder region (outside of the gauge region) of the PMWY2 (B3) specimen confirmed the presence of the cavities in the as-heat-treated specimens, as well as fine needle-shaped features (see Fig. 4).

Creep-rupture tests of the specimens from the B8 and B9 heat treatment schedules were more successful. As shown in Table I, these specimens survived for over 200 h when tested at temperatures of 980-1075°C under stresses of 34-41 MPa (5-6 ksi). However, even though their fracture surfaces were covered with shallow dimples typical of microvoid coalescence (see Fig. 5), they exhibited virtually no ductility nor any evidence during the creep test of progressing through the normal creep stages. Instead, they held the stress for 200-250 h and then fractured without warning. The reason for this behavior, and why these specimens should act so differently from the other specimens is under investigation. The creep behavior of these B8 and B9 specimens is encouraging, as shown by the comparison of these results with those of Fe_3Al-based alloys and a typical ferritic and an austenitic steel in Fig. 6. Also shown are creep data for three commercial ODS-FeCrAl alloys: INCO's MA956 [5], Plansee's PM2000 [6], and the Dour

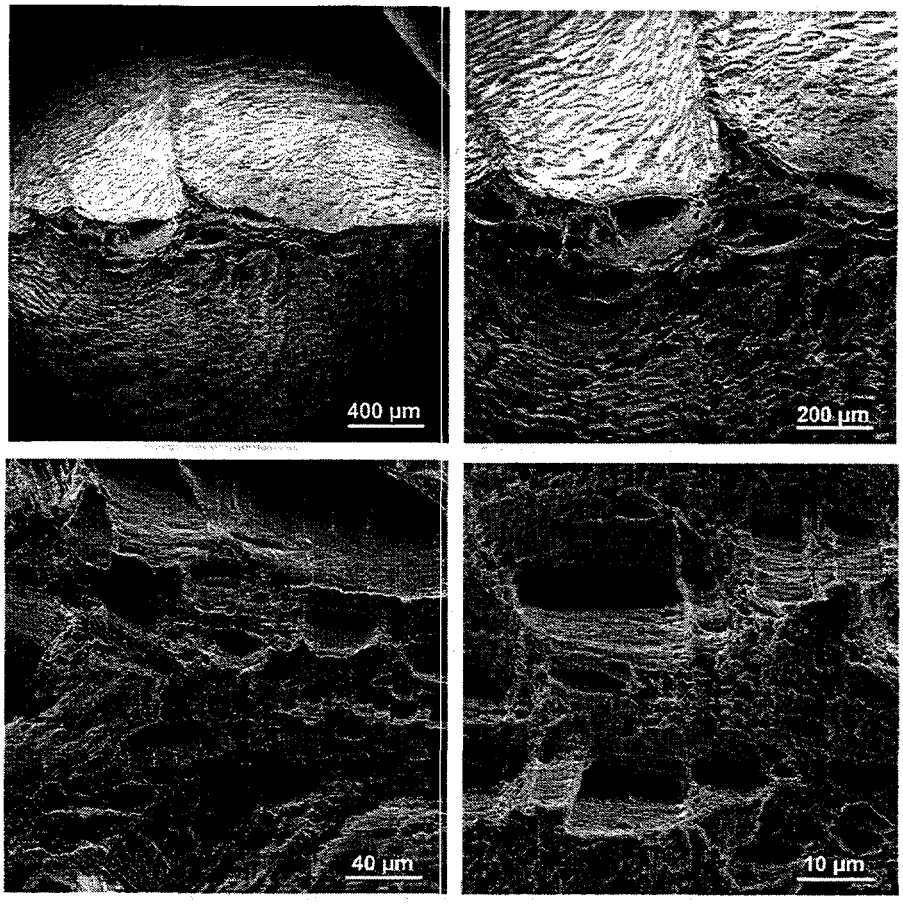

Fig. 3. Scanning electron micrographs of the creep fracture in the B3 specimen creep tested at 1075°C under a stress of 48 MPa.

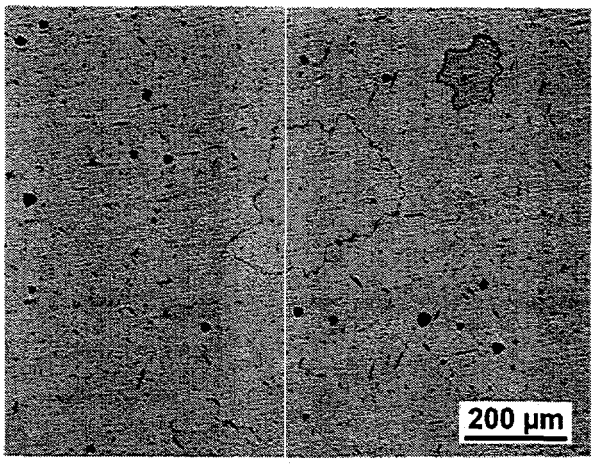

Fig. 4. Optical micrograph showing cavities in PMWY2 produced by recrystallizing at 1350°C, with a 12 h heat up from 1100°C (schedule B3).

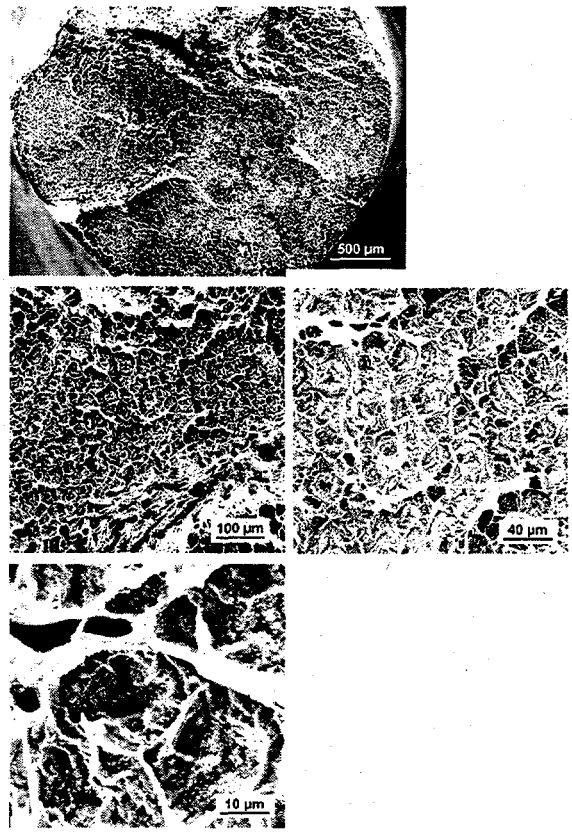

Fig. 5. Scanning electron micrographs of the creep fracture in specimen PMWY2 (B8) creep tested at 980°C at 34-41 MPa. The specimen had a creep life of 250 h, but elongated only 0.2%.

Metal alloy ODM751 [7]. Clearly, given the presence of defects such as pores and non-recrystallized grains in the ODS Fe_3Al which most likely degrade its creep performance, the high-temperature creep strength of the alloy is a significant improvement on the non-ODS iron aluminides and the typical ferritic and austenitic steels, and approaches the level achieved by the developed ODS-FeCrAl alloys.

Specimens taken from the grip ends of creep specimens recrystallized using schedules B0 and B3 were prepared for examination by transmission electron microscopy (TEM). The B0 specimen was found to contain a distribution of small, round particles which appeared to be

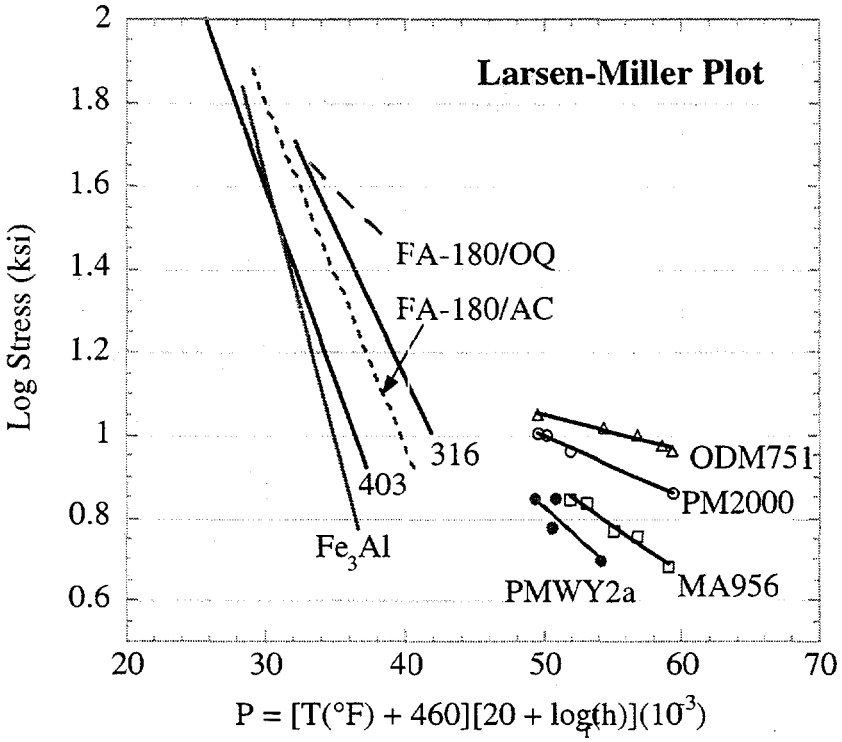

Fig. 6. Larsen-Miller plot showing a comparison of the creep properties of ODS-Fe_3Al with those of other iron aluminides, typical steels, and commercial ODS-FeCrAl alloys.

yttria in the size range of approximately 250 to 500 nm, together with fewer, larger particles which appeared to be alumina; there were also some small, rod-shaped features which also appeared to be yttria. These features are illustrated in Fig. 7. The equivalent observations on the B3 specimen (Fig. 8) indicated significantly fewer small, round yttria particles, although the larger particles still appeared to be essentially alumina; there was a suggestion that these particles may contain a low level of yttrium. The number of rod-shaped yttria particles also was increased compared to the B0 specimen. Extensive work elsewhere [4] on the change in composition, shape and size of the yttria dispersion as a function of the processing of other ODS alloys has shown the formation of various classes of compounds between Y_2O_3 and Al_2O_3 as a function of time and temperature, but did not report agglomeration of the yttria dispersoid or any associated drastic loss in creep strength.

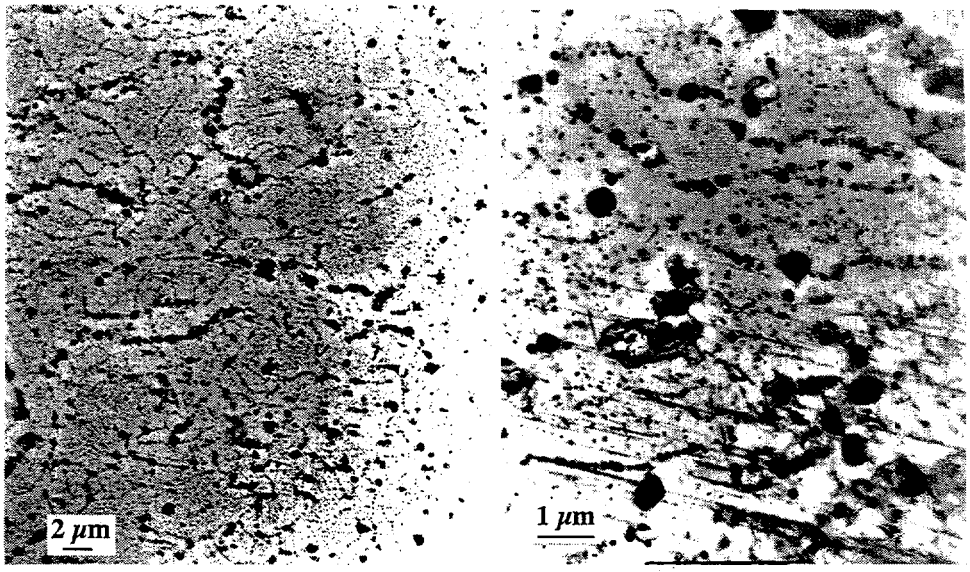

Fig. 7. Transmission electron micrographs of PMWY2 after recrystallization schedule B0

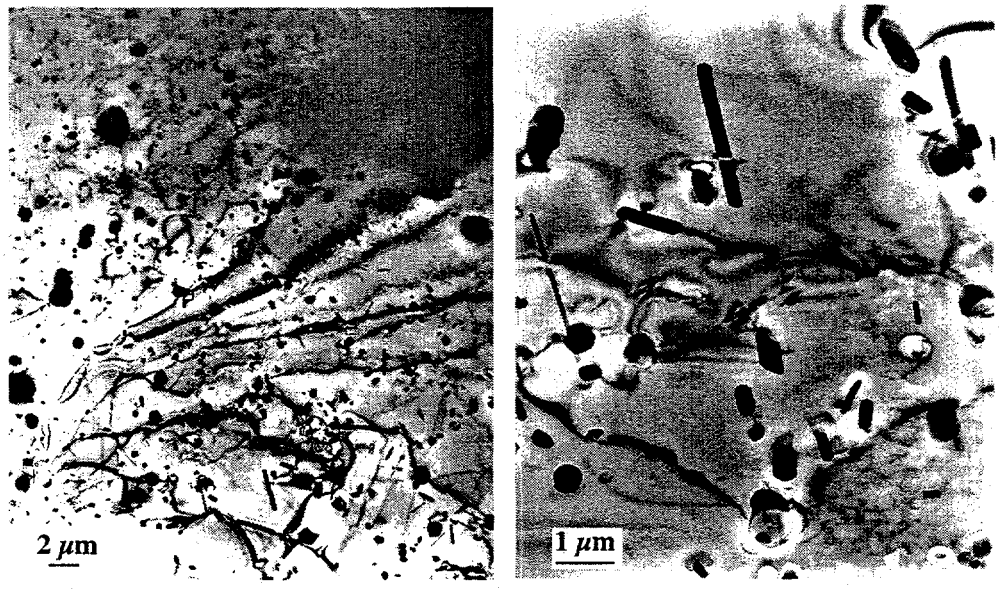

Fig. 8. Transmission electron micrographs of PMWY2 after recrystallization schedule B3

Room temperature tensile tests were also conducted in air at a strain rate of 10^{-3}/s, with the results shown in Table II. One specimen was recrystallized according to schedule B9 (similar to B0, which gave good high-temperature creep strength), and the other to B3, which resulted in very low creep strength. The data in Table II show no apparent difference in the room-temperature tensile strength for these two specimens, in contrast to the high-temperature creep behavior. Both failed at surface flaws, as shown in the scanning electron fractograph of the PMWY2 (B3) specimen in Fig. 9. Comparison with the tensile data for other iron aluminides listed in Table II shows the PMWY2 alloy to have significantly higher yield and rupture strengths but lower elongation at fracture. The alloy also has lower yield strength but higher rupture strength than the commercial ODS FeCrAl alloy PM2000; however, the elongation of the commercial alloy was significantly higher.

Table II. Room-temperature tensile properties of Fe_3Al alloys

Alloy	Recrystallization Temp. (°C)/Time (h)	Tensile Properties		
		Yield Stress (MPa)	Fracture Stress (MPa)	Elongation (%)
PMWY2	1350/1*	794	1059	2.7
PMWY2	1300/1†	796	1167	3.7
FAS		394	679	9
FAS-3Y		643	959	2.4
FA-129		380	900	15
FA-180		620	900	8
PM2000		872	890	13

PMWY2 = Fe-28Al-2Cr-0.015Zr (at.%) + 0.2 cation% Y_2O_3
FAS = Fe-28Al-2Cr-0.05B (at.%)
FAS-3Y = Fe-28Al-2Cr-0.05B (at.%) + 0.2 cation% Y_2O_3
FA-129 = Fe-28Al-5Cr-0.5Nb-0.2C (at.%)
FA-180 = Fe-28Al-5Cr-0.5Nb-0.8Mo-0.025Zr-0.05C-0.005B (at.%)
AISI 316 = Fe-13Ni-17Cr-2Mn-2.5Mo-1Si-0.08C (wt%)
AISI 403 = Fe-12Cr-1Mn-1Si-0.15C (wt%)
PM2000 = Fe-20Cr-5.5Al-0.5Ti-0.5Y_2O_3 (wt%)
* schedule B3: heated from 1100 to 1350°C over 12 h
† schedule B9: heated from 900 to 1300°C in 1h

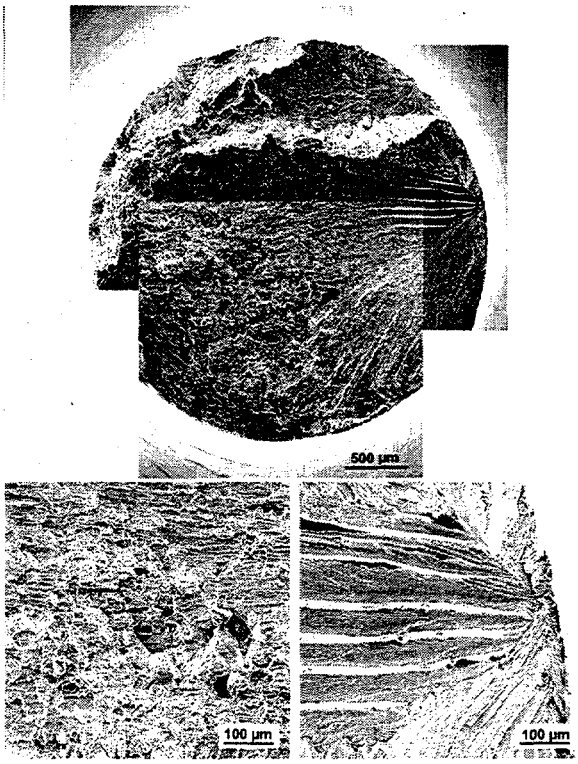

Fig. 9. Scanning electron fractographs of the PMWY2 (B3) specimen fractured in tension at room temperature.

Oxidation Lifetime Tests

Data for use in estimating the high-temperature oxidation lifetimes of the recrystallized ODS-Fe_3Al alloy (PMWY2) and of the commercial ODS FeCrAl alloys MA956, ODM751, and PM2000 were generated in long-term furnace tests. Data also were generated for Kanthal APM, which is nominally not an ODS alloy, but which has a composition similar to the commercial ODS-FeCrAl alloys and is used as a standard for comparison of oxidation behavior. In these tests individual specimens were exposed in lidded, pre-baked alumina crucibles so that the total oxygen uptake by the alloys (including that in any spalled oxide) could be measured. Exposures were made at 1000, 1100, 1200, and 1300°C for times to 4,000 h, and the specimens were removed for weighing every 100 h. Some of the data are from single specimens, and some are from duplicate or triplicate specimens; further specimens are in the process of being exposed to

supplement the single specimen cases. The oxidation-limited lifetimes of each alloy at each temperature were calculated following the approach described by DeVan et al. [8] and Quadakkers et al. [9], where the end-of-life criterion is taken as the point at which a protective alumina layer can no longer be maintained, and the alloy experiences the onset of rapid, breakaway oxidation. In that approach, the oxidation rate (k) and rate law index (n) parameters derived from the measured oxidation data are used, together with values of the initial aluminum concentration in the alloy (C_o) and the concentration at which breakaway oxidation is observed (C_b). One problem with this approach is that the calculated oxidation lives are extremely sensitive to the value of the oxidation rate exponent (n). This parameter is typically derived from log-log plots of weight gain and time, and can be significantly influenced by the short-time data points. Hence, for the purpose of this work which is to provide a common basis for comparison, all the specimens were assumed to have oxidized according to a parabolic rate law (i.e., $n = 0.5$). The results of these calculations, based on a tube wall thickness of 2.5 mm (0.1 in), are summarized in Fig. 10. Note that the 1000°C data for ODS-Fe_3Al alloy are for the earlier version of the alloy made at ORNL (FAS3Y); the PMWY2 version typically has shown improved

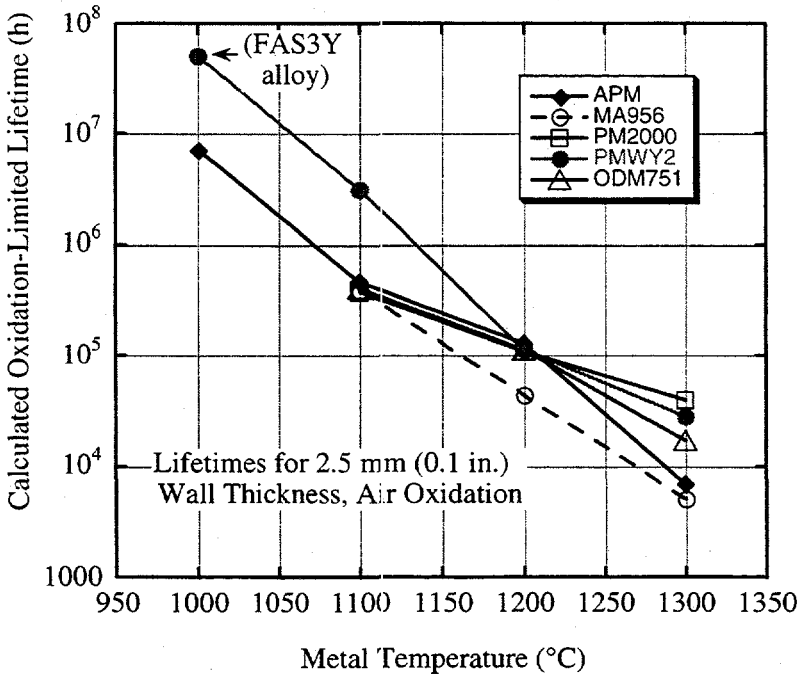

Fig. 10. Comparative oxidation-limited lifetimes for ODS-Fe_3Al and commercial ODS-FeCrAl alloys in air.

resistance to scale spallation, and hence would be expected to have a longer lifetime. Note also that a wall thickness of 2.5 mm is quite practical for these alloys for service at temperatures around 1100°C in externally-fired heat exchangers; tubes of ODM751 of this thickness were successfully demonstrated in a heat exchanger constructed in a European program [2].

Clearly, the ODS-Fe_3Al alloy with its much larger reservoir of aluminum has the potential for a longer oxidation-limited lifetime than the ODS-FeCrAl alloys. Even though the ODS-Fe_3Al alloy undergoes a greater degree of scale loss by spallation than the ODS-FeCrAls, much of this potential is realized at 1000 and 1100°C, which is the most likely range of service temperatures. The calculated lifetimes for the PMWY2 alloy at 1200 and 1300°C are similar to those of the best of the commercial ODS-FeCrAls, which suggests that over-temperature situations should not cause any surprise acceleration in alloy degradation. Studies are continuing to determine the causes of the difference in susceptibility to scale spallation between the ODS-Fe_3Al alloys and ODS-FeCrAls.

SUMMARY AND CONCLUSIONS

Work on the ODS-Fe_3Al alloy has progressed to the point where useful creep strength can be developed (in rod stock) at temperatures not attainable by other iron aluminides or by conventional ferritic and austenitic steels. Although there remain some problems with defects in the alloys following the recrystallization step, which probably detract from the mechanical properties of the alloy, the longitudinal creep strength-temperature capability is approaching that of the developed, commercial ODS-FeCrAl alloys. Improved understanding of the recrystallization characteristics and the generation of microstructural defects, and how to eliminate them, is needed to fully develop the high-temperature strength of this and of ODS alloys in general. Incremental improvements have been made in the resistance of the alloy to scale spallation to the extent that some of the potential for a longer oxidation-limited lifetime than competing alumina scale-forming alloys may be realized at 1000 and 1100°C. An improved understanding of the root cause of the difference in oxide scale spallation behavior on ODS-Fe_3Al and ODS-FeCrAl alloys is needed to provide guidance on routes to maximize the oxidation-governed lifetime.

REFERENCES

1. "Federal Energy Research and Development for the Challenges of the Twenty-First Century," Report of the Energy research and development panel of the President's Committee of Advisors on Science and Technology (PCAST), Nov. 1997.
2. F. Starr, A. E. White, and B. Kazimierzak , "Pressurized Heat Exchangers for 1100°C Operation Using ODS Alloys," Pp. 1393-1412 in *Materials for Advanced Power Engineering, 1994*, D. Coutsouradis, et al., Eds., Kluwer Academic Publishers (1994).
3. I. G. Wright, B. A. Pint, P. F. Tortorelli, and C. G. McKamey, "Development of ODS-Fe_3Al Alloys," Proc. Tenth Ann. Conf. on Fossil Energy Materials, ORNL Report No. ORNL/FMP-96/1, CONF-9605167 (1996), pp. 359-371.
4. A. R. Jones and D. M. Jaeger, "Reduction in Defect Content of ODS Alloys," Proc. Twelfth Ann. Conf. on Fossil Energy Materials, Knoxville, Tennessee, May 1998.
5. J. J. Fischer, J. J. deBarbadillo, and M. J. Shaw, "MA Alloys for Industrial Applications," pp. 79-87 in *Structural Applications of Mechanical Alloying*, F. H. Froes and J. J. deBarbadillo, Eds., ASM International (1990).
6. Materials Data Sheet: ODS Superalloy PM2000, Metallwerk Plansee GmbH/Lechbruch, Feb 1993.
7. Private communivcation, R. Hurst, Joint Reseach Centre, Petten, The Netherlands, with I. G. Wright, June 1996.
8. J. H. DeVan, P. F. Tortorelli, M. J. Bennett, pp. 309-320 in Proc. Eighth Annual Conference on Fossil Energy Materials, Oak Ridge, Tennessee, CONF-9405143; ORNL/FMP-94/1 (1994).
9. W. J. Quadakkers, and K. Bongartz, Werkstoffe u. Korrosion, **45,** 232 (1994).

PROCESSING OF OXIDE-DISPERSION-STRENGTHENED Fe_3Al-BASED ALLOY TUBE*

V. K. Sikka, I. G. Wright, and B. D. Kad†
Metals and Ceramics Division
Oak Ridge National Laboratory
P.O. Box 2008
Oak Ridge, Tennessee 37831

ABSTRACT

The development of Fe-Al alloys has been under way at the Oak Ridge National Laboratory (ORNL) over the last several years. The aluminum content of the Fe-Al alloys ranged from 8.5 to 16 wt %. The Fe-Al alloy with 8.5 wt % Al is a low-aluminum content, iron aluminide alloy; this ORNL-patented composition is known as FAPY. The Fe-Al alloy, based on 16 wt % Al, has an ordered structure; this alloy has excellent sulfidation resistance and is designated as FAS. This alloy also contains 2% Cr. The FAS alloy has exceptional corrosion properties at temperatures ≥ 600°C. The FAS alloy with Y_2O_3 dispersion is one of the avenues being pursued to achieve an increase in strength. The FAS powder with Y_2O_3 dispersion became available during this year. The oxide-dispersion-strengthened (ODS) Fe_3Al-based FAS alloy powder (PMWY-2) was consolidated into solid bar and tube by the hot-extrusion method. The solid bars were extruded at 900, 1000, and 1100°C. The tubing was extruded at 1000°C. The solid bars were rolled to sheet to produce test bars. Metallography was conducted on solid bars, sheet, and tube. A 1200°C/1-h treatment of the sheet resulted in an extremely large coarse grain structure. Sheet specimens of the coarse grained microstructure were creep tested at 1000, 1050, and 1100°C. The creep data were compared with the results on the baseline material without the oxide dispersion. The ODS FAS powder (PMWY-2) can be consolidated to full density by the hot-extrusion process at temperatures as low as 900°C and an area reduction ratio of 9.8:1. A 1200°C treatment for 1 h resulted in secondary recrystallization and grain growth. Preliminary creep data demonstrate that the ODS FAS material can result in the high-temperature creep properties comparable to that of the commercial alloy, MA-956.

*Research sponsored by the U.S. Department of Energy, Office of Fossil Energy, Advanced Research and Technology Development Materials Program [DOE/FE AA 15 10 10 0, Work Breakdown Structure Element ORNL-2(H)] under contract DE-AC05-96OR22464 with Lockheed Martin Energy Research Corp.

†University of California-San Diego, Department of AMES, 1801-EBU1, 9500 Gilman Drive, LaJolla, CA 92093-0411.

INTRODUCTION

The Fe_3Al-based alloys, developed at the Oak Ridge National Laboratory (ORNL), have been documented[1-3] to show excellent resistance to high-temperature oxidation and sulfidation. The specific Fe_3Al-based alloy with exceptional sulfidation properties is designated as FAS. The nominal composition of this alloy is given in Table 1. The FAS alloy is highly desirable for many applications for its corrosion properties at temperatures ≥ 600°C. However, it is the same temperature range where FAS alloy has limited high-temperature mechanical (tensile and creep) properties. The oxide dispersion strengthening (ODS) using Y_2O_3 particles is one of the approaches being pursued at ORNL to strengthen the FAS alloy for temperatures ≥ 600°C. The purpose of this paper is to describe the processing, microstructure, and properties of an ODS FAS composition known as PMWY-2.

Table 1. Chemical composition of FAS alloy

Element	Percent	
	Weight	Atomic
Al	15.9	28.0
Cr	2.2	2.0
B	0.01	0.04
Fe	*a*	*a*

[a]Balance.

EXPERIMENTAL DETAILS

The hot extrusion was used as a primary method for the consolidation of ODS powder. Because of the limited supply of powder, extrusions were carried out in 51-mm (2-in.) -diam carbon steel billets. Each of the carbon steel cans measured 51-mm OD × 6.4-mm wall × 125-mm length (2-in. × 0.25-in. × 5-in.). The cans were filled with powder, evacuated, and sealed. A total of three cans were prepared for direct consolidation of powder into solid bar. The extrusion number, temperature, reduction ratio, and tonnage are listed in Table 2. All of the extrusions were of excellent quality, and a section of each was used for microstructural analysis. Both longitudinal and transverse sections were examined. The transverse sections were also characterized for their uniformity by microhardness profiles.

For the tube fabrication, an 89-mm (3.5-in.) can was used with a 25.4-mm (1-in.) -diam carbon steel core. The annular space between the can's inner diameter and the core bar's outer diameter was filled with the ODS powder, evacuated, sealed, and extruded through a 25-mm (1-in.) -diam die at a temperature of 1000°C (considered as optimum

Table 2. Extrusion data for consolidation of oxide-dispersion-strengthened FAS powder

Extrusion		Die size		Area reduction ratio	Tonnage
Number	Temperature (°C)	(mm)	(in.)		
5016[a]	900	16.3	(0.64)	9.8:1	266
5014[a]	1000	12.7	(5)	16.0:1	290
5013[a]	1100	12.7	(5)	16.0:1	180
5030[b]	1000	25.4	(1)	12.25:1	532

[a]51-mm (2-in.) billets for solid extrusion.
[b]88.9-mm (3.5-in.) billet for tube extrusion.

extrusion temperature, based on solid extrusions). The cored extrusion was of good quality, and a section of the extrusion was used for the longitudinal and transverse metallography and microhardness characterization.

The carbon steel core and the steel on the outside of the extruded bar were machined to obtain the tubing of the ODS FAS material.

In order to determine mechanical properties, it was decided to roll 51-mm (2-in.) -long pieces of bars from the solid extrusion to 0.76-mm (30-mil) -thick sheet. The rolling process consisted of: (1) hot-roll the section at the extrusion temperature to a sheet of 2.54 mm (100 mil) thickness. The steel can was left on during the rolling process. At 2.54 mm (100 mil) thickness, the carbon steel was removed by sand blasting followed by acid cleaning in 10% HNO_3/H_2O solution. Acid-cleaned sheets were of good quality for each of the three extrusion temperatures. (2) the second step was to roll the sheets at 650°C (a temperature commonly used for the base FAS alloy). At this rolling temperature, extensive cracking was observed. (3) The trial was repeated except that the carbon steel was removed without acid etching. (The acid was believed to have charged the sheets with hydrogen.) The rolling temperature was increased to 900°C, but with only limited success. It was realized that chilling of the thin sheet by large rolls might have been responsible for the extensive cracking. At this stage, the carbon steel was removed mechanically from a sample, and a sheet was rolled at 1000°C. The sample was rolled in a stainless steel cover to minimize chilling by the rolls. This process yielded a small section of sheet that was 0.76 mm (30 mil) thick. Three test bars were punched from the sheet for creep testing. The three test bars and a small blank produced during punching were given a 1-h treatment at 1200°C in vacuum. The treatment was chosen based on results reported by Wright.[4] The annealed blank was used for microstructural characterization.

The heat-treated sheet specimens were creep tested in air at 1000°C and 69 MPa (10 ksi), 1050°C and 34.5 MPa (5 ksi), and 1100°C and 14 MPa (2 ksi).

RESULTS

The microstructure of a solid bar extrusion of ODS FAS extruded at 900°C to an area reduction ratio of 9.8:1 is shown in Figs. 1 and 2. The unetched transverse sections from the nose and tail of the extrusion were essentially the same and were free of any microporosity, Fig. 1(*a,b*). The etched sections, Fig. 2(*a-d*), revealed the microstructure to be extremely fine. The longitudinal section showed an elongated grain structure. The transverse section, Fig. 2(*c*), also showed the presence of inclusions. The comparison of transverse and longitudinal sections indicates an elongated grain structure in the longitudinal direction, Fig. 2(*a-d*).

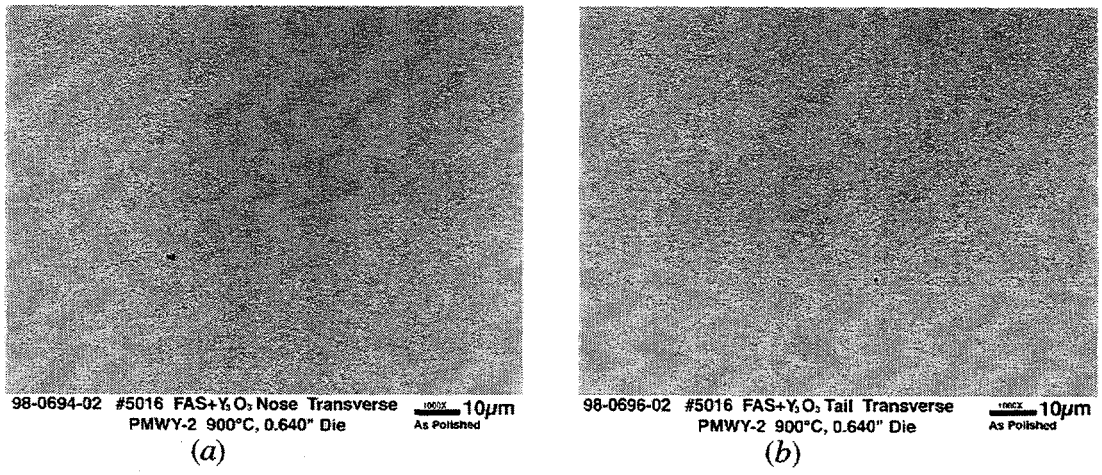

Fig. 1. Transverse section of nose (*a*) and tail (*b*) of solid extrusion of oxide-dispersion-strengthened FAS alloy powder (PMWY-2) at 900°C.

The microstructure of a solid bar extrusion of ODS FAS extruded at 1000°C to an area reduction of 16:1 is shown in Figs. 3 and 4. The unetched transverse sections from the nose and tail of the extrusion were essentially the same and similar to that for extrusion at 900°C. No porosity was observed. Some indications of precipitates are evident in the nose section, Fig. 3(*a*). The etched sections in Fig. 4(*a-d*) show elongated grains in the longitudinal direction. The nonuniformity of microstructure for extrusion at 1000°C is similar to that observed for extrusion at 900°C.

The microstructure of a solid bar extrusion of ODS FAS extruded at 1100°C to an area reduction of 16:1 is shown in Figs. 5 and 6. The unetched nose and tail sections show the presence of precipitates, Fig. 5(*a,b*). The etched sections, Fig. 6(*a-d*), still show the elongated grains in the longitudinal direction for extrusion at 1100°C, similar to the structure observed for extrusions at 1000 and 900°C.

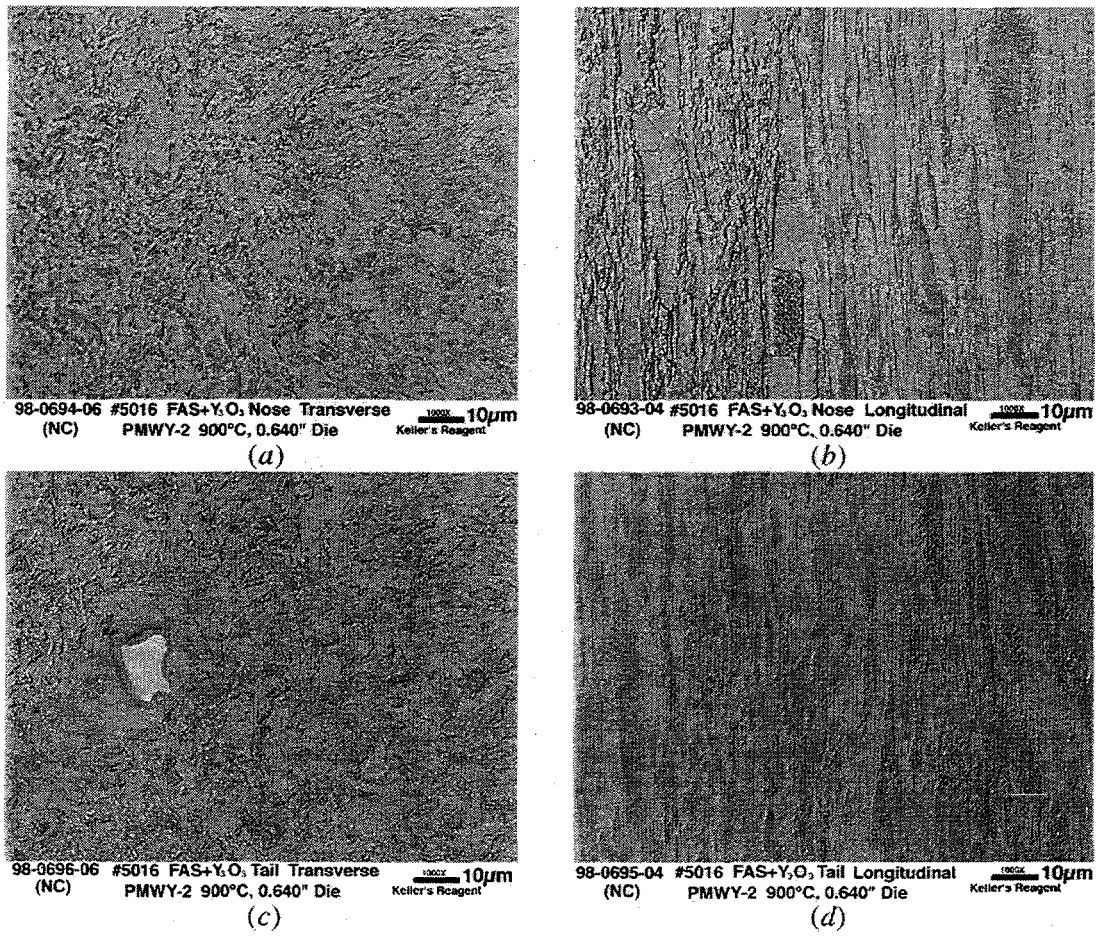

Fig. 2. Transverse and longitudinal sections of nose (*a*) and(*b*) and tail (*c*) and (*d*) of solid extrusion of oxide-dispersion-strengthened FAS powder (PMWY-2) at 900°C.

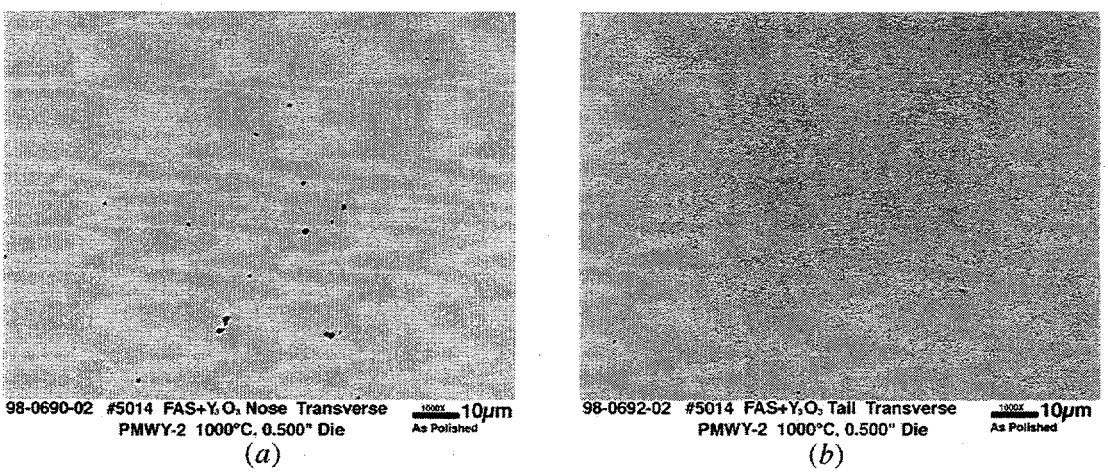

Fig. 3. Transverse section of nose (*a*) and tail (*b*) of solid extrusion of oxide-dispersion-strengthened FAS powder (PMWY-2) at 1000°C.

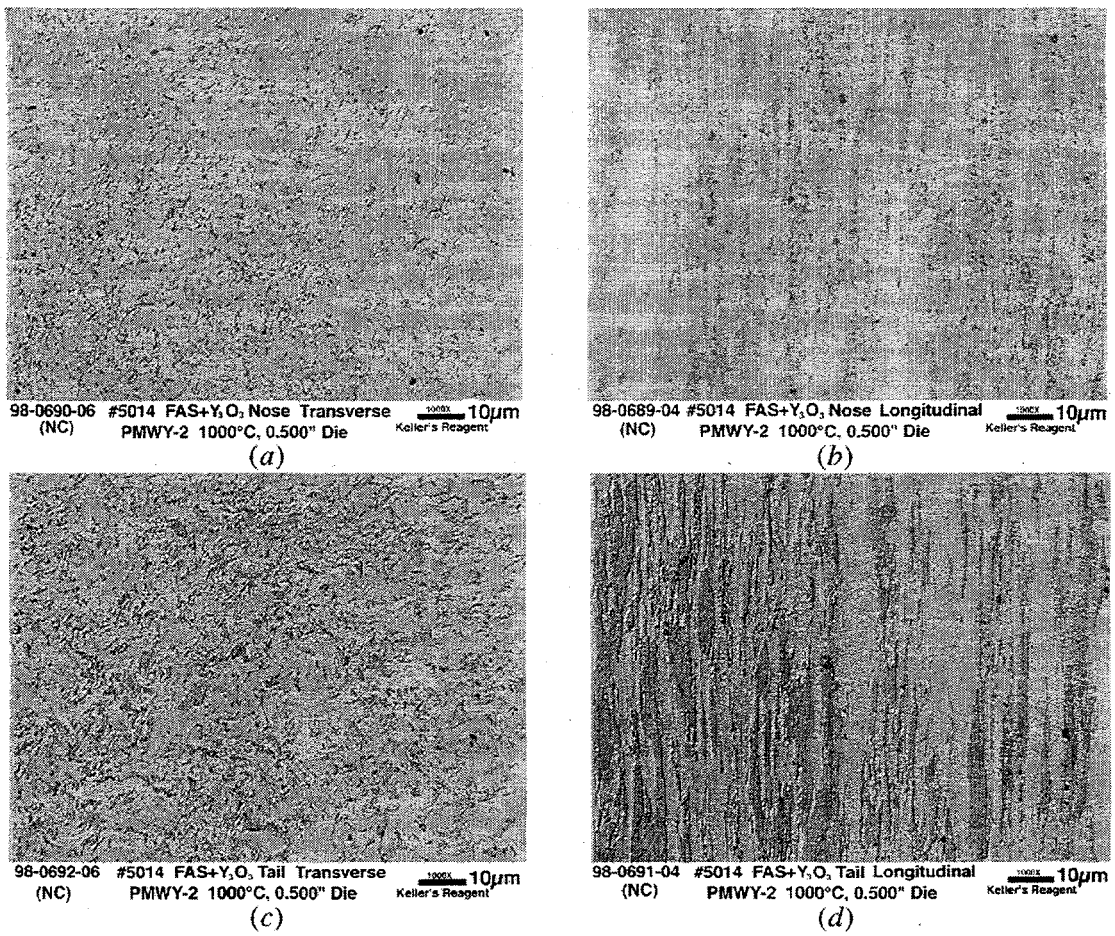

Fig. 4. Transverse and longitudinal sections of nose (*a*) and (*b*) and tail (*c*) and (*d*) of solid extrusion of oxide-dispersion-strengthened FAS powder (PMWY-2) at 1000°C.

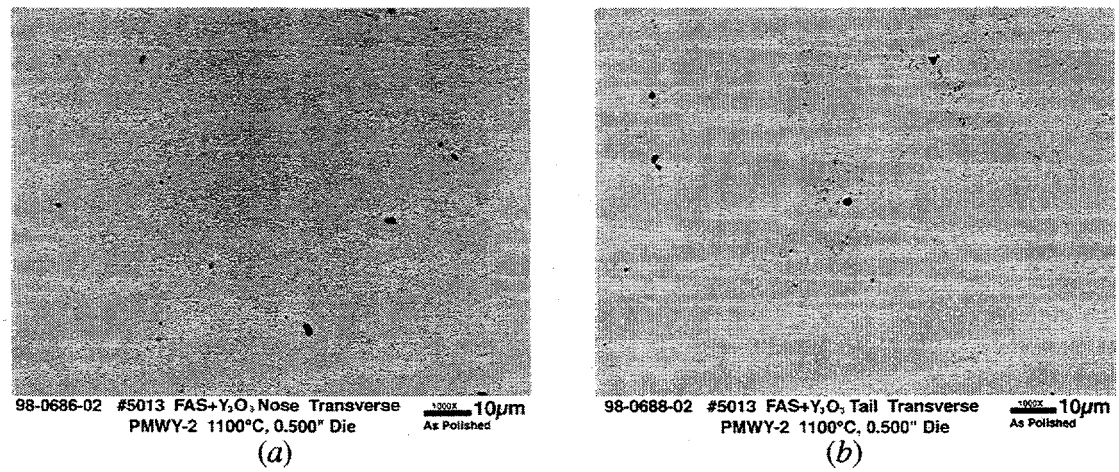

Fig. 5. Transverse section of nose (*a*) and tail (*b*) of solid extrusion of oxide-dispersion-strengthened FAS powder (PMWY-2) at 1100°C.

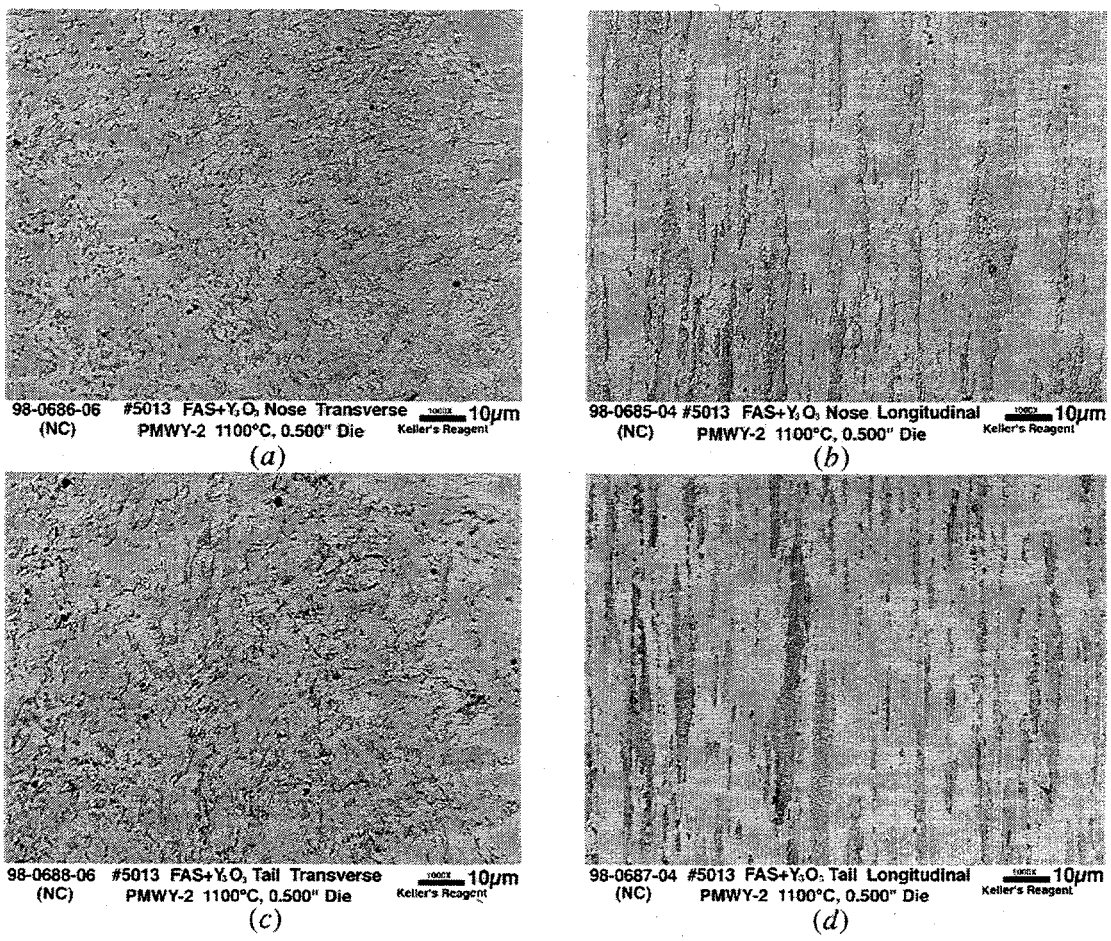

Fig. 6. Transverse and longitudinal sections of nose (*a*) and (*b*) and tail (*c*) and (*d*) of solid extrusion of oxide-dispersion-strengthened FAS powder (PMWY-2) at 1100°C.

The microhardness traverse for the transverse sections of solid extrusions at 900, 1000, and 1100°C are compared in Fig. 7. Some variation in hardness was observed across the section for each extrusion temperature. More importantly, the average hardness decreased with the increasing extrusion temperature (change in hardness from 532 to 465 HV for an increase in extrusion temperature from 900 to 1100°C). This decrease in hardness is presumably the result of an increase in grain size with increasing extrusion temperature.

Photomicrographs of the sheet specimen (extruded and rolled at 1000°C) after a 1200°C treatment in vacuum for 1 h are shown in Fig. 8 which clearly shows the secondary recrystallization and extensive grain coarsening. Such a grain size is essential in order to achieve the very high-temperature creep strength properties of the ODS alloys. The other important requirement for high-temperature strength is the retention of very fine Y_2O_3 dispersion within the matrix. The microhardness transverse for the coarse-grained sheet is also included in Fig. 7 for comparison. The lower hardness for the coarse-grained

Fig. 7. Comparison of the microhardness for the transverse section of solid extrusions at 900, 1000, and 1100°C.

microstructure is consistent with the observed trend of decreasing hardness with increasing extrusion temperature. The creep data obtained on the sheet specimens with a 1200°C

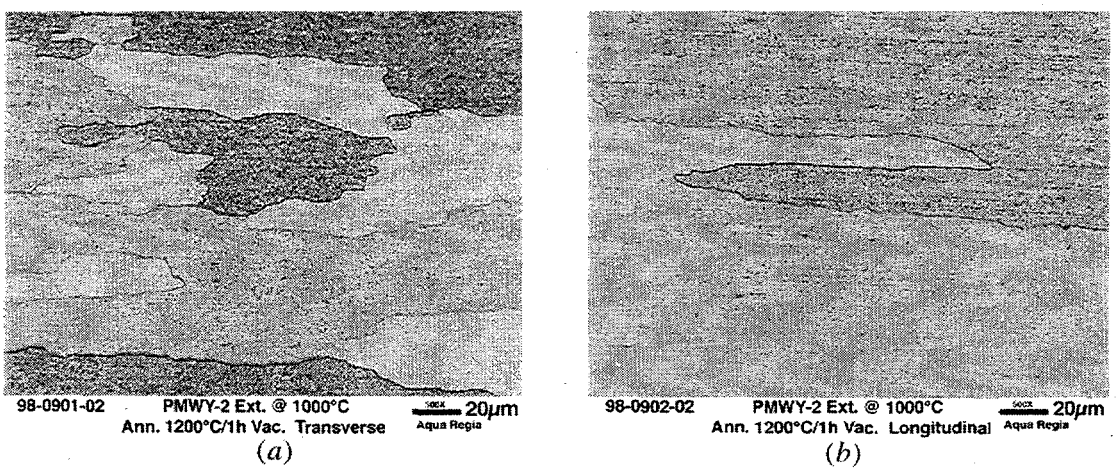

(*a*) (*b*)

Fig. 8. Photomicrographs of 0.76-mm (30-mil) -thick sheet rolled at 1000°C from 1000°C extrusion and annealed at 1200°C for one hour in vacuum: (*a*) transverse and (*b*) longitudinal.

treatment are compared in Fig. 9 with the baseline data for Fe_3Al alloys FAS, FAL, and FA-129. The figure also includes the creep data on ODS material prepared by a proprietary process developed by Hoskins Manufacturing Company[5] (Hamburg, Michigan). A limited amount of creep data on ODS FAS material processed previously is also included in Fig. 9. Data in this figure demonstrate that the ODS FAS material (PMWY-2) consolidated by hot-extrusion followed by a 1200°C/1-h treatment can approach high-temperature creep properties similar to those of commercial ODS alloy MA-956.

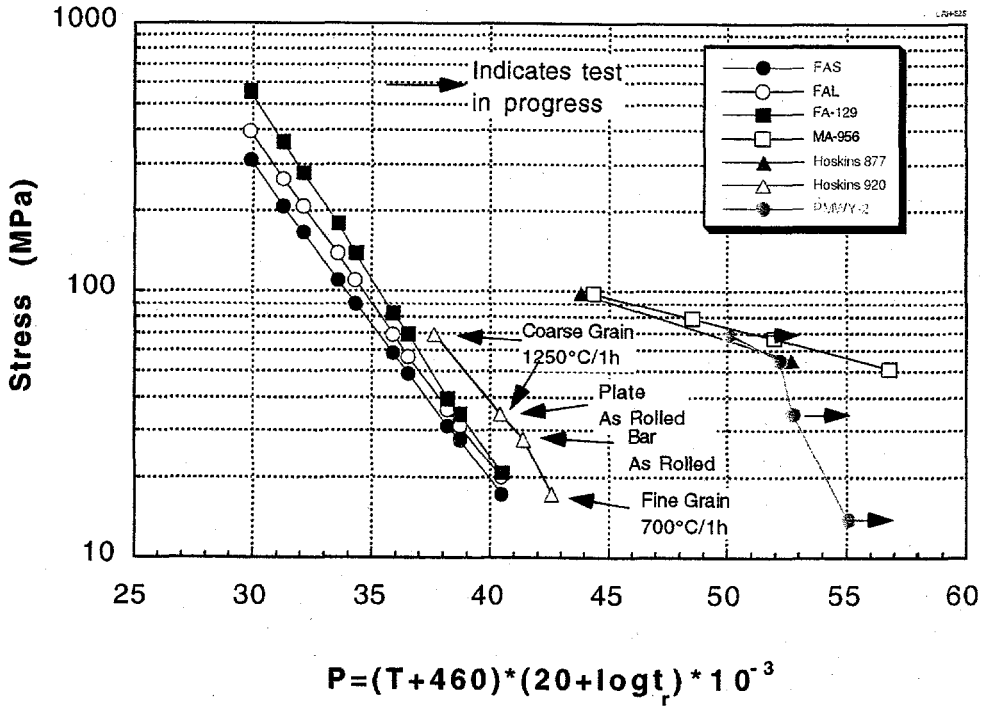

Fig. 9. Comparison of creep data obtained on sheet specimens with 1200°C treatment with the baseline data for Fe_3Al-based alloys FAS, FAL, and FA-129.

FUTURE WORK

Additional creep tests are required on the sheet specimens to demonstrate the temperature range of high creep strength for the ODS alloy. The creep tests are needed on specimens taken from the extruded tube. Such specimens will provide creep results without the secondary processing that occurred in the preparation of sheet specimens, which is going to be the situation in actual application of ODS alloy tubes. Fabrication of thicker wall tube, typical of application [6.3-mm (0.25-in.) wall] is required. Additional lower cost (other than having to machine the carbon steel core) method(s) for the production of tubing is needed. Tensile ductility and toughness properties are needed at both ambient and high temperatures.

SUMMARY AND CONCLUSIONS

The oxide-dispersion-strengthened (ODS) Fe$_3$Al-based FAS alloy powder (PMWY-2) was consolidated into solid bar and tube by the hot-extrusion method. The solid bars were extruded at 900, 1000, and 1100°C. The tubing was extruded at 1000°C. The solid bars were rolled to sheet to produce test bars. Metallography was conducted on solid bars, sheet, and tube. A 1200°C/1-h treatment of the sheet resulted in an extremely large coarse grain structure. Sheet specimens of the coarse grained microstructure were creep tested at 1000, 1050, and 1100°C. The creep data were compared with the results on the baseline material without the oxide dispersion. The following conclusions are possible:

1. The ODS FAS powder (PMWY-2) can be consolidated to full density by the hot-extrusion process at temperatures as low as 900°C and an area reduction ratio of 9.8:1.
2. A 1200°C treatment for 1 h can result in secondary recrystallization and extensive grain growth.
3. Preliminary creep data demonstrate that the ODS FAS material can result in the desired high-temperature properties.
4. Additional work is needed in several areas (listed above).

REFERENCES

1. K. Natesan and P. F. Tortorelli, *International Symposium on Nickel and Iron Aluminides: Processing, Properties, and Applications*, eds., S. C. Deevi, V. K. Sikka, P. J. Maziasz, and R. W. Cahn, (Materials Park, OH: ASM International, 1997), pp. 265-82.
2. P. F. Tortorelli and J. H. Devan, *Oxidation and Corrosion of Intermetallic Alloys*, eds., G. Welsch and P. D. Desai, (West Lafayette, IN: Purdue University, 1996), pp. 267-321 .
3. K. Natesan, *Proc. Sixth Annual Conference on Fossil Energy Materials*, ORNL/FMP-92/1 (1992), p. 271.
4. R. N. Wright, Idaho National Engineering and Environmental Laboratory, Private communication, April 1998.
5. V. K. Sikka, C. R. Howell, F. Hall, and J. Valykeo, *Proc. Eleventh Annual Conference on Fossil Energy Materials*, ORNL/FMP-97/1 (1997), p. 313.

ULTRAHIGH TEMPERATURE INTERMETALLIC ALLOYS

M.P. Brady, J.H. Zhu, C.T. Liu, P.F. Tortorelli, J.L. Wright, and C.A. Carmichael
Metals and Ceramics Division
Oak Ridge National Laboratory
Oak Ridge, TN 37831-6115 USA

INTRODUCTION

The objective of this work is to develop high-strength, oxidation- and corrosion-resistant intermetallic alloys for use as hot components in advanced fossil energy conversion and combustion systems that meet the 65% efficiency goal of the Vision 21 Concept. The successful development of these alloys is expected to allow improvement in thermal efficiency primarily through decreased cooling requirements in advanced gas turbines. Initially targeted applications include components such as vanes, seals, and nozzles. However, these materials may also find other uses as wear-resistant parts in coal handling systems (for example nozzles), drill bits for oil/gas wells, valve guides in diesel engines, and interconnects in solid oxide fuel cells.

The development efforts have focused on two-phase, in-situ composite alloys of the type Cr-Cr_2X, where Cr_2X is a Cr-based refractory Laves phase compound. Toughness and oxidation resistance are provided by a soft Cr_{ss} (solid solution) matrix. The Cr_2X Laves phase acts as a reinforcement to the Cr_{ss} matrix in order to provide high temperature strength. Recently, we identified a promising new class of alloys based on the Cr-Cr_2Ta system[1,2] (Fig. 1), with melting points in the 1600-1700°C (2912-3092°F) range[3]. Preliminary evaluation suggested that the Cr-Cr_2Ta based alloys possess superior mechanical properties and oxidation resistance to the Cr-Cr_2Nb and Cr-Cr_2Zr alloys previously developed in this program[3]. This report presents an overview of current Cr-Cr_2Ta alloy development objectives and performance.

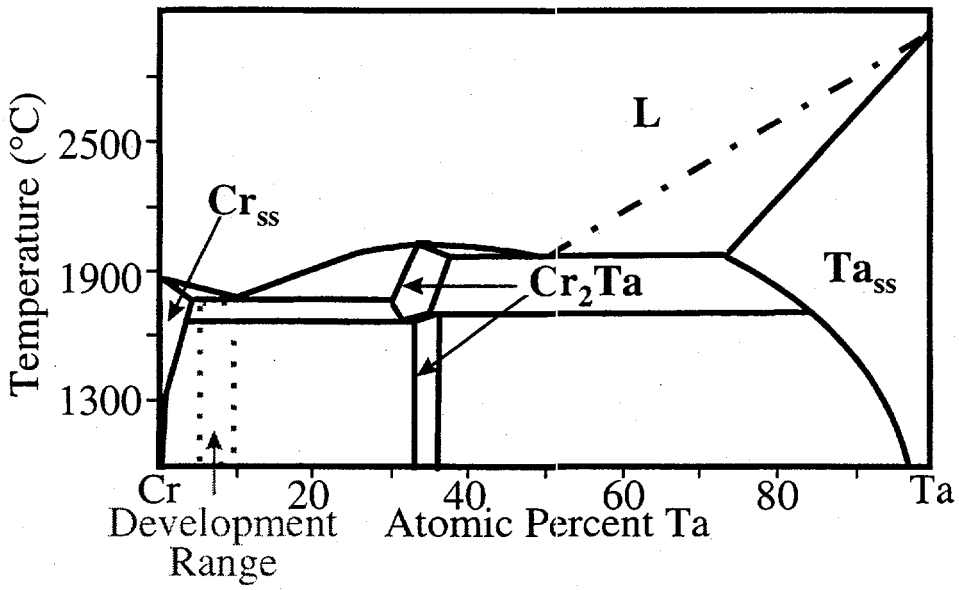

Fig. 1- Schematic binary Cr-Ta phase diagram[1,2].

DISCUSSION OF CURRENT ACTIVITIES

Three properties are key to the initial development of the two phase Cr-Cr_2Ta based alloys: room temperature fracture toughness, high temperature strength, and high temperature oxidation resistance. The target mechanical properties are room temperature fracture toughness ≥ 15-20 MPa$\sqrt{m}$ (1.1 MPa$\sqrt{m}$ = 1 ksi$\sqrt{in.}$) and 345 MPa (50 ksi) tensile fracture strength at 1200°C (2192°F). Oxidation kinetics in the range of commercial chromia (Cr_2O_3) forming alloys is the goal for temperatures up to about 900-1000°C (1652-1832°F). At higher temperatures, where chromia scale volatility is significant[4], the goal is noncatastrophic oxidation behavior of the bare substrate alloy such that use of a protective coating is a reasonable protection approach (i.e., local coating failure would not result in immediate component loss).

Alloy Preparation and Processing

Alloys based on the Cr-Cr_2Ta system weighing 400-500 g were prepared by arc melting and drop casting in a copper mold (2.5 cm diam x 7.6 cm long) preheated to 200°C (392°F). Small 40-60 g

castings were also prepared by arc melting and drop casting in a chilled copper mold. High-purity chromium and other metal chips were used as charge materials. The alloys were easily cast and showed no evidence of cracking. After heat treatment, the larger 400-500 g alloy ingots were clad inside Mo billets and hot extruded at 1480°C (2696°F) and an extrusion ratio of 4:1. The hot-extruded material was then heat treated and used for tensile specimens. The small 40-60 g castings were used as-cast and/or after heat treatment to provide specimens for oxidation exposures and room temperature fracture toughness evaluation. The development range is based on Cr-(6-10)Ta atomic percent, at.% (Fig. 1). Detailed alloy compositions are not reported due to patent considerations, and are denoted in the report by the letter "X" followed by a number.

Room Temperature Fracture Toughness

Chevron notched three-point bend samples approximately 3 mm x 4 mm x (20-25) mm were used to evaluate fracture toughness at room temperature. A modulus of 250 GPa (36 ksi) was estimated for the Cr-Cr_2Ta based alloys. A modulus of 300 GPa (43 ksi) was used for the Cr-(0-0.1X10) alloys. Details of this technique are provided in ref. 5.

Current Cr-Cr_2Ta based alloys have a room temperature fracture toughness in the 10-12 MPa$\sqrt{m}$ range, with one alloy test sample exhibiting a toughness of 12.8 MPa$\sqrt{m}$ (Table 1). This represents significant progress beyond the 7-8 MPa$\sqrt{m}$ room temperature fracture toughness exhibited by the best Cr-Cr_2Nb based alloys previously developed under this initiative[6]. However, it is still short of the goal levels of 15-20 MPa$\sqrt{m}$.

Room temperature fracture toughness of several binary Cr-Ta and microalloyed Cr alloys are shown in Table 2. A comparison of Table 1 with Table 2 reveals that the alloy additions to the Cr-(8-10)Ta base have not significantly increased room temperature fracture toughness. The binary Cr-(8-10)Ta alloys exhibit room temperature fracture toughness values in the 9-10 MPa$\sqrt{m}$ range, only slightly below the 10-12 MPa$\sqrt{m}$ range achieved with further alloying. (It should be noted the alloying strategy adopted thus far has proven effective in improving high temperature strength and oxidation resistance).

Table 1- Room temperature fracture toughness of selected Cr-Cr_2Ta based alloys.

Alloy No.	Composition (At.%)	Microstructure	Condition and Heat Treatment	Fracture Toughness (MPa√m) Best	Average (#)
CN144	Cr-8Ta-5X1-0.5X3-0.011X8	Hypoeutectic	extruded,1200°C	**11.0**	**11.0 (1)**
			cast, 1000°C	10.2	8.3 (2)
			cast, 1200°C	8.3	7.9 (2)
CN145	Cr-10Ta-5X1-0.5X3-0.011X8	Hypereutectic	cast, 1000°C	8.7	6.0 (2)
			cast, 1200°C	**12.8**	**11.1 (2)**
CN147	Cr-9.5Ta-5X1-0.5X3-0.011X8	Eutectic	cast, 1200°C	**11.7**	**10.7 (4)**

Table 2- Room temperature fracture toughness of selected binary Cr-Ta and Cr alloys.

Composition (At.%)	Microstructure	Condition and Heat Treatment	Fracture Toughness (MPa√m) Best	Average (#)
Binary Cr-Ta				
Cr-8Ta	Hypoeutectic	cast, 1000°C	10.4	9.8 (3)
Cr-11Ta	Hypereutectic	cast, 1000°C	9.8	9.7(2)
Cr-9.8Ta	≈ Eutectic	cast, 1000°C	9.0	9.4 (2)
Cr Matrix				
Pure Cr	Cr	cast, 1000°C	**16.1**	**15.2 (2)**
Cr-0.1X10		cast, 1000°C	**34**	**22.3 (3)**

Alloying for further improvement in room temperature fracture toughness will focus on two key areas: the Cr_{ss} phase and the Cr_{ss}/Laves phase interface. Pure Cr (200 O and 25 N weight parts per million) processed under similar conditions to the Cr-Cr_2Ta based alloys exhibits a room temperature fracture toughness of only 15-16 MPa√m (Table 2). Microalloying additions to improve the toughness of Cr are currently under evaluation. For example, the addition of 0.1at.% of X10 was recently found to increase the room temperature fracture toughness to level of 34 MPa√m in one test sample (Table 2).

Manipulation of the Cr_{ss}/Laves phase interface is the second route under consideration to further improve toughness. Understanding of processing/composition/microstructure relationships in the Cr-Ta system, including phase equilibria studies to determine the eutectic composition, has been achieved. Microstructures consisting of a fine dispersion of Laves particles in the Cr_{ss} matrix or lamellar Cr_{ss}/Laves eutectic structures can now be produced (Fig. 2). Very preliminary results suggest that the lamellar eutectic structures (Fig. 2a) may exhibit greater room temperature fracture toughness than the fine dispersed structures (Fig. 2b). Future work will concentrate on confirming and optimizing this effect through adjustments of microstructural parameters such as lamellar spacing and lamellar colony grain size.

Tensile Properties

Button-type tensile specimens with gage dimensions 0.31 cm diam x 0.97-1.3 cm long were cut from hot-extruded material by electro-discharge machining, followed by grinding and polishing with "0" Emery paper. The tensile specimens were tested in an Instron Testing Machine at room temperature and 800°C (1472°F) in air, and at 1200°C (2192°F) in vacuum (crosshead speed of approximately 0.25 cm/minute). The tensile properties are summarized in Tables 3-5.

At room temperature, no macroscopic yielding prior to fracture was observed. However, tensile fracture strengths in excess of 700 MPa (100 ksi) were achieved (Table 3). At 800°C in air, tensile elongations on the order of 1% were observed in several alloys, with yield strengths of around 900 MPa (130 ksi) (Table 4). This suggests that the ductile to brittle transition temperature (DBTT) was just under 800°C (1472°F). At 1200°C (2192°F), elongations were generally in the 20-30% range, with several alloys exhibiting tensile fracture strengths in excess of 345 MPa (50 ksi) (Table 5). Thus, the Cr-Cr_2Ta based alloys meet the high temperature strength goals of the program.

a)

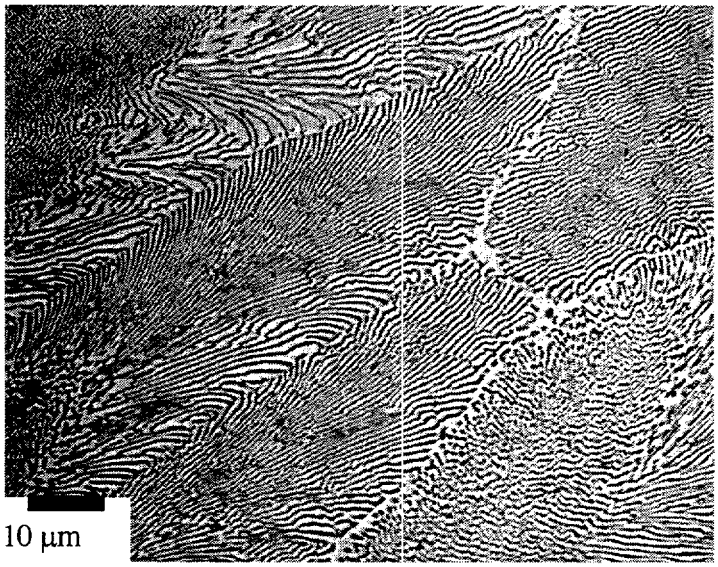

b)

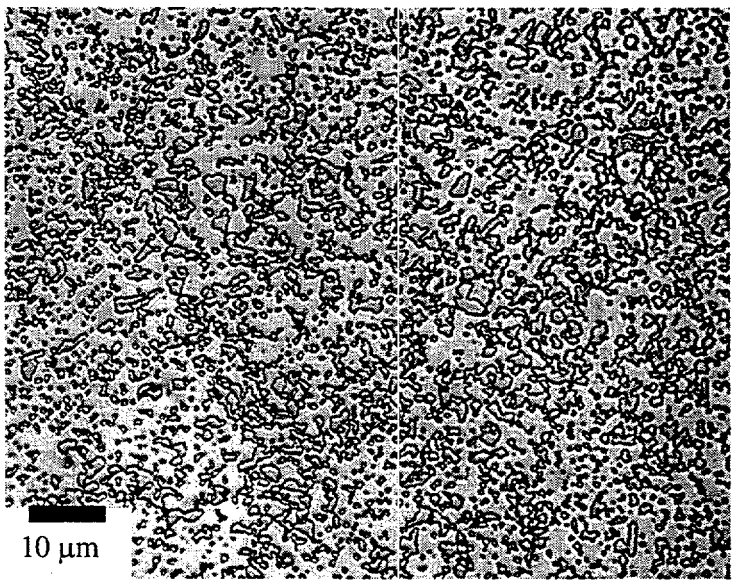

Fig. 2- Possible microstructures for Cr-Cr_2Ta based alloys (light microscopy). a) lamellar eutectic b) Cr_2Ta Laves particles dispersed in a Cr_{ss} matrix.

Table 3- Room temperature tensile properties.

Alloy No.	Composition Cr-8Ta-0.5X3 Base (At.%)	Yield Strength ksi (MPa)	Fracture Strength ksi (MPa)	Elongation %
CN130	5X1	>104 (717)	**104 (717)**	*
CN132	5X1-3X2-.05X6	>71 (489)	71 (489)	*
CN133	2.5X1-3X2	>101 (696)	**101 (696)**	*
CN136	6.5X1-0.5X6	>87 (600)	87 (600)	*
CN137	6.5X1-0.05X6-0.022X8	>92 (634)	92 (634)	*
CN144	5X1-0.011X8	>104 (717)	**104 (717)**	*
CN146	8X7-0.011X8	>80 (552)	80 (552)	*

*Fracture Prior to Macroscopic Yielding

Table 4- 800°C (1472°C) tensile properties.

Alloy No.	Composition Cr-8Ta-0.5X3 Base (At.%)	Yield Strength ksi (MPa)	Fracture Strength ksi (MPa)	Elongation %
CN130	5X1	120 (827)	120 (827)	0.8
CN132	5X1-3X2-.05X6	**134 (924)**	**137 (944)**	**1.2**
CN133	2.5X1-3X2	>69 (476)	69 (476)	*
CN136	6.5X1-0.5X6	>118 (813)	**118 (813)**	*
CN137	6.5X1-0.05X6-0.022X8	**128 (882)**	**131 (903)**	**0.9**
CN144	5X1-0.011X8	**130 (896)**	**133 (917)**	**1.0**
CN146	8X7-0.011X8	>116 (800)	116 (800)	*

*Fracture Prior to Macroscopic Yielding

Table 5- 1200°C (2192°F) tensile properties.

Alloy No.	Composition Cr-8Ta-0.5X3 Base (At.%)	Yield Strength ksi (MPa)	Fracture Strength ksi (MPa)	Elongation %
CN130	5X1	37 (255)	45 (310)	16.6
CN132	5X1-3X2-.05X6	42 (290)	**51 (352)**	18.5
CN133	2.5X1-3X2	30 (207)	36 (248)	22.0
CN136	6.5X1-0.5X6	46 (317)	**56 (386)**	14.3
CN137	6.5X1-0.05X6-0.022X8	37 (255)	45 (310)	28.1
CN144	5X1-0.011X8	37 (255)	46 (317)	39.0
CN146	8X7-0.011X8	30 (206)	36 (248)	25.8

High Temperature Oxidation

The development effort focused on optimization of chromia scale growth kinetics on Cr-Cr_2Ta based alloys through microalloying, with an emphasis on reactive element (RE) additions. A series of alloys based on Cr-8Ta-5X1 with microalloying additions in the 0.05 to 1 at.% range was selected for evaluation. Disk shaped oxidation specimens of 8-13 mm in diameter and 1 mm thickness were sectioned from as-cast and/or heat treated material and polished to a 600 grit finish using SiC paper. Evaluation of oxidation was performed by thermogravimetric analysis (TGA) at 950°C (1742°F) in dry air for 168 h and short term cyclic oxidation screening at 1100°C (2012°F) . The 1100°C (2012°F) screening was performed in a tube furnace open to room air. The samples were placed in a covered alumina crucible and inserted/removed from the furnace at temperature after intervals of 1, 4, 10, 30, 48, and 120 h of cumulative exposure. Significant chromia volatility occurred as evidenced by green stains on the underside of the alumina crucible lid.

At 950°C (1742°F) in air, RE modified Cr-8Ta alloys exhibited a 2-7 fold decrease in the rate of oxidation relative to binary Cr-8Ta (Fig. 3). No isothermal scale cracking was observed during a 168 h isothermal exposure and the scale remained adherent on cooling. This behavior is in contrast to binary Cr-8Ta, which exhibited a relatively low rate of oxidation but suffered from isothermal scale cracking and scale spallation on cooling to room temperature. The best RE modified Cr-8Ta based alloy oxidized within the range defined at the high end by Waspalloy,[7] a commercial chromia-forming superalloy, and at the low end by MA754,[8] a Y_2O_3 dispersed Ni-Cr alloy (1000°C data) which is among the most oxidation resistant chromia-forming alloys (Fig. 3). It should be noted that the oxidation kinetics of the RE modified Cr-8Ta based alloys were not parabolic, although the rate of oxidation did decrease with time.

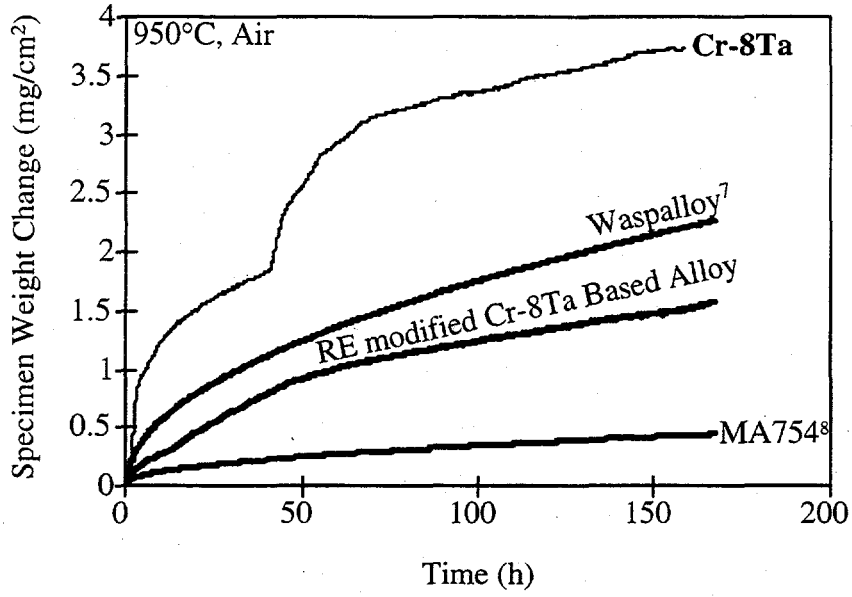

Fig. 3-TGA data at 950°C in dry air.

The microalloying additions were also successful at reducing the rate of oxidation at 1100°C (2012°F). The alloys generally exhibited a 3-5 fold decrease in the rate of oxidation and no scale spallation during the short term 1100°C (2012°F) cyclic oxidation screening test. The most recent RE modified Cr-8Ta based alloy exhibited a 50 fold decrease in the rate of oxidation as compared with Cr-8Ta-5X1 (Fig. 4), although it should be noted that this result has not yet been repeated.

Overall, microalloying of the Cr-Cr_2Ta based alloys was successful in reducing the rate of oxidation and in improving scale adherence, although further composition optimization is needed. The short term (< 200 h) behavior was in the target goal range of chromia-forming oxidation kinetics below 900-1000°C (1652-1832°F) and noncatastrophic oxidation at 1100°C (2012°F). Although the behavior thus far is promising, longer term exposures (>1000 h) are needed (and planned) before an assessment can be made as to the oxidation performance of the microalloyed Cr-Cr_2Ta based alloys. Of particular concern is the possibility of oxygen/nitrogen embrittlement of the alloys. Preliminary results suggest that the chromia scale formed on the Cr-

Cr_2Ta based alloys can provide some protection from embrittlement, but obviously only if the scale remains adherent.

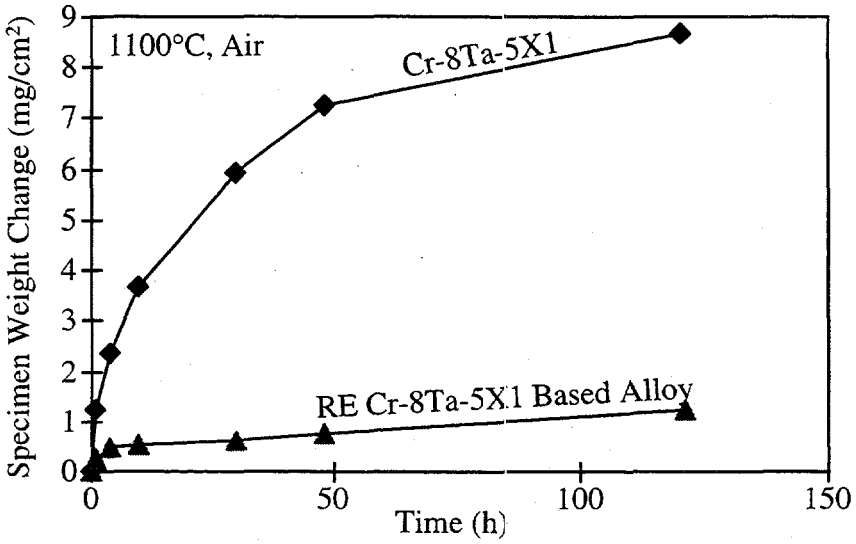

Fig. 4- Cyclic oxidation data at 1100°C in air.

SUMMARY AND FUTURE WORK

The room temperature fracture toughness and high temperature strength and oxidation resistance of a series of developmental Cr-Cr_2Ta based alloys were evaluated. The developmental goal of 345 MPa (50 ksi) tensile fracture strength at 1200°C (2192°F) was met. Significant improvement in room temperature fracture toughness over previously developed Cr-Cr_2Nb based alloys was achieved, with the Cr-Cr_2Ta based alloys exhibiting toughness in the 10-12 MPa$\sqrt{m}$ range as compared with 7-8 MPa$\sqrt{m}$ for Cr-Cr_2Nb. Although short of the goal of 15-20 MPa$\sqrt{m}$, further improvements are thought possible through microalloying of the Cr_{ss} phase and manipulation of the Cr_{ss}/Laves phase interface. Microalloying with reactive elements successfully reduced the rate of chromia scale formation during short term 950°C (1742°F) and 1100°C (2012°F) exposures in air. Long-term oxidation studies and optimization of microalloying levels are planned.

REFERENCES

1. M. Venkatraman and J.P. Neumann, in Binary Alloy Phase Diagrams,Vol. 1, T.B. Massalaski, J.L. Murray, L.H. Bennett, and H. Baker eds., ASM, p. 867 (1986).

2. J.H. Zhu and C.T. Liu, unpublished research (1997).

3. M.P. Brady, J.H. Zhu, C.T.Liu, P.F. Tortorelli, J.L. Wright, C.A. Carmichael, and L. R. Walker, *in Proc. of the Eleventh Annual Conference on Fossil Energy Materials*, R.R. Judkins (comp.), U. S. Department of Energy, p. 195 (December 1997).

4. P. Kofstad, High-Temperature Corrosion, Elsevier, London, 1988.

5. J.H. Schneibel, C.A. Carmichael, E.D. Specht, and R. Subramanian, Intermetallics, 5, p. 61 (1997).

6. C. T. Liu, P. F. Tortorelli, J. A. Horton, D. S. Easton, J. H. Schneibel, L. Heatherly, C. A Carmichael, M. Howell, and J. L. Wright, in *Proc. Ninth Annual Conf. Fossil Energy Materials*, N. C. Cole and R. R. Judkins (comp.), U. S. Department of Energy, p. 415 (August 1995).

7. J.H. Chen, P.M. Rogers, and J.A. Little, Oxidation of Metals, Nos. 5/6, p. 381 (1997).

8. B.A. Pint and L. Hobbs, unpublished research (1990).

ACKNOWLEDGMENTS

This research was sponsored by the Fossil Energy Advanced Research and Technology Development (AR&TD) Materials Program, U S. Department of Energy, under contract DE-AC05-96OR22464 with Lockheed Martin Energy Research Corporation.

PROCESSING AND PROPERTIES OF MOLYBDENUM SILICIDE INTERMETALLICS CONTAINING BORON

J. H. Schneibel, C. T. Liu, L. Heatherly, Jr., and C. A. Carmichael

INTRODUCTION

The objective of this task is to develop new-generation corrosion-resistant Mo-Si alloys for use as hot components in advanced fossil energy combustion and conversion systems. The successful development of Mo-Si alloys is expected to improve the thermal efficiency and performance of fossil energy conversion systems through an increased operating temperature, and to increase the service life of hot components exposed to corrosive environments at temperatures as high as 1600°C. While $MoSi_2$ is highly oxidation resistant at elevated temperatures, it is extremely brittle at ambient temperatures and has poor creep resistance at elevated temperatures. Molybdenum compounds with lower Si contents, such as Mo_5Si_3 are potentially less brittle and exhibit higher strengths at elevated temperatures, but do not have the required oxidation resistance. Boron additions appear to resolve the oxidation problem. As early as 1957, Nowotny et al.[1] pointed out that boron-containing silicides possess high oxidation resistance due to the formation of borosilicate glasses. Based on Nowotny et al.'s work, boron-containing molybdenum silicides based on Mo_5Si_3 were recently developed at Ames Laboratory.[2-4] These silicides consist of approximately 25 vol.% of Mo_3Si, 50 vol.% Mo_5Si_3 (T1), and 25 vol.% Mo_5SiB_2 (T2). A typical composition, which is indicated in Fig. 1, is Mo-26.7Si-7.3B, at. % (compositions will always be given in at. %). This alloy has an oxidation resistance comparable to that of $MoSi_2$, and it does not appear to show catastrophic oxidation ("pest reaction") at intermediate temperatures such as 800°C.[4] Also, its creep strength is superior to that of $MoSi_2$. Another class of Mo-Si-B alloys of interest are those developed by Berczik,[5,6] which consist of α-Mo, Mo_3Si, and Mo_5SiB_2 (T2). These types of alloys have also been studied recently by Perepezko and co-workers.[7-9] While their oxidation resistance is inferior to that of the Mo_3Si-T1-T2 alloys, it is likely that it can be improved by minimizing the α-Mo volume fraction, by suitable alloying additions, and/or silicide coatings. The main advantage of the Mo-Mo_3Si-T2 alloys is that they do not consist exclusively of brittle phases. This suggests that fracture toughnesses higher than those for the Mo_3Si-T1-T2 alloys can be achieved.

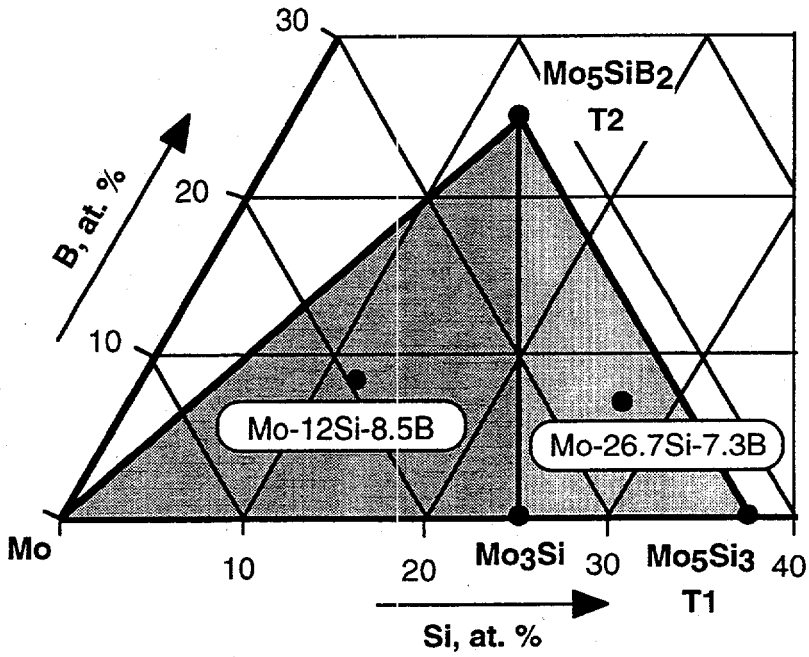

Figure 1: Schematic section of the ternary Mo-Si-B phase diagram showing the phases and alloy compositions of interest.

The present work describes our experience with the processing of these two classes of Mo-Si-B materials. Microstructural information as well as mechanical property measurements will be presented.

RESULTS AND DISCUSSION

Processing and mechanical properties of Mo-26.7Si-7.3B

A Mo-26.7Si-7.3B extrusion carried out at 1800°C in FY 97 was unsuccessful, probably due to the formation of liquid phases. Therefore, an extrusion of this composition was repeated at 1700°C. Ingots were arc-melted from commercially pure elements and drop-cast into 25 mm diameter MgO molds. The MgO molds resulted in slow cooling, thus minimizing macrocracking. Several ingots prepared in this manner were put into a Mo-can with an outer diameter of appr. 50 mm, sealed by electron-beam welding, and extruded at 1700°C with an area reduction of 1:4. However, only about 200 mm of rod was extruded before the maximum capacity of the die assembly was reached, at which point the extrusion process had to be discontinued. The extruded material showed profuse cracking. It is concluded that extrusion of cast material with the above composition

is very difficult, because extremely high loads and stresses are required at "low" temperatures such as 1700°C, whereas partial liquid phase formation occurs at high temperatures such as 1800°C.

Another processing option is powder metallurgy (PM). Previous work seemed to indicate that hot-pressing of $MoSi_2$, Mo, and B powders resulted in incomplete densification.[10,11] A more detailed analysis showed, however, that the dark spherical features (with typical sizes of 2 μm) seen in scanning electron micrographs were not cavities, but instead glass particles containing primarily Si and O. Since then, additional powder-metallurgical processing has been carried out. In order to reduce surface area and oxygen content, coarse elemental powders (> 100 μm) were blended in an Ar glove box and hot-pressed in graphite dies at temperatures ranging from 1600 to 1700°C and pressures of about 50 MPa. Even after annealing at 1700°C, homogenization was not achieved and microcracks were often observed. SiO_2 inclusions were occasionally seen. In another PM experiment, mixtures of elemental Mo, Si, and B powders with sizes < 45 μm were blended in an Ar glove box, filled into Nb cans, outgassed at 400°C in vacuum, sealed by electron-beam welding, and hot isostatically pressed (HIPed) at 1650°C and 200 MPa. Again, SiO_2 inclusions were seen. Similar to the coarse powders, full equilibration was not achieved, since particles consisting primarily of Mo were seen (Fig. 2). The distribution of the phases was quite inhomogeneous. For example, coarse Mo particles were surrounded by fine T2 particles. However, only occasional microcracking was seen. Improved PM processing is in progress.

Three-point flexure specimens with a cross section of 3x4 mm were tested with a span of 20 mm and a crosshead speed of 10 μm/s. The fracture strengths σ_f were evaluated as $1.5xP_f/(wt^2)$, where P_f is the load at which fracture occurs, w is the specimen width, and t the specimen thickness. The fracture strengths of the PM materials are listed in Table 1. They are significantly higher than those for the corresponding cast materials, which are only on the order of 100 MPa.[10,11]

Instead of elemental powders, prealloyed powders obtained by breaking up a casting into -325 mesh powder was also HIPed (1600°C/200 MPa). This material was more homogeneous than the material made from elemental powders and had a slightly higher room temperature strength (see Table 1).

Table 1. Room temperature flexure strengths of PM Mo-26.7Si-7.3B

Processing	Flexure Strengths, MPa
HIPing from elemental powders (476-2HI)	199, 194
HIPing from prealloyed powder (459F)	220, 211, 235

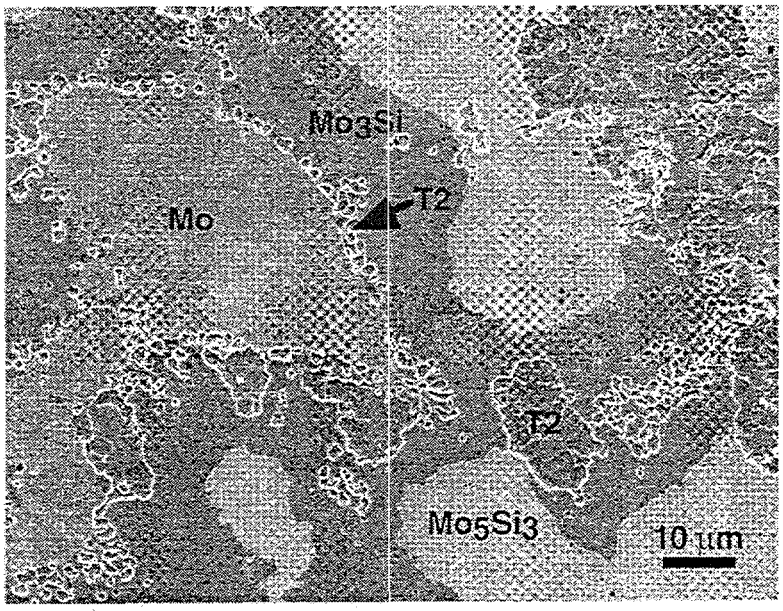

Figure 2: SEM micrograph of polished and etched (Murakami's etch) Mo-26.7Si-7.3B HIPed from elemental powders.

Cast Mo-12Si-8.5B

Figure 3 is an SEM micrograph of cast and annealed (1 day/1600°C/vacuum) Mo-12Si-8.5B. The different phases were identified by energy dispersive spectroscopy and several phase particles are annotated. The T2 phase appears etched, the α-Mo phase is the brightest phase, and the third phase is Mo_3Si. The α-Mo occurs discontinuously in a brittle matrix of Mo_3Si and T2.

The strength of Mo-12Si-8.5B was examined by 3-point flexure tests. As would be expected from the microstructure in Fig. 3, no plastic deformation was noted prior to fracture. The measured flexure strengths are summarized in Table 2. The strength is lowest for the as-cast condition. An anneal for 1 day at 1600°C in vacuum appears to increase the strength slightly. One possible reason for this might be a reduction of the concentration of Si and B in the α-Mo phase. This reduction might increase the ductility of the Mo and reduce the flaw sensitivity of the material. Since the ductile-to-brittle transition temperature of Mo and its alloys is usually above room temperature,[12] two tests were carried out at 500°C in air. The significantly higher strength at 500°C is consistent with improved mechanical properties of the α-Mo phase at 500°C, as compared to room temperature. The specimens darkened during the testing, which lasted approximately 1 h at 500°C. However, they showed no evidence for a pest reaction.

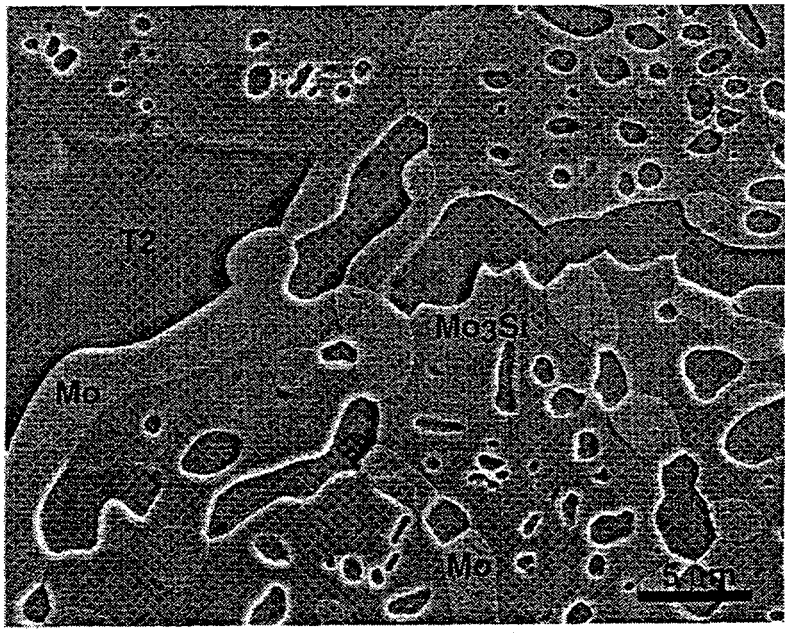

Figure 3: SEM micrograph of cast and annealed (1 day/1600°C/vacuum) Mo-12Si-8.5B, after polishing followed by etching with Murakami 's etch.

Table 2. Three-point flexure strengths of cast Mo-12Si-8.5B (at. %)

Specimen	Condition	Temp, C	Flexure
531#1	as-cast	20	457
531#2	as-cast	20	455
531-A1#1	1d/1600C/Vac	20	484
531-A1#2	1d/1600C/Vac	20	539
531-A2#1	1d/1600C/Vac	500	722
531-A2#2	1d/1600C/Vac	500	697

Room temperature fracture toughnesses were measured by determining the energy dissipated during the controlled 3-point fracture of chevron-notched specimens. Similar to the flexure specimens, a cross section of 3x4 mm, a span of 20 mm, and a crosshead speed of 10 µm/s were employed. During the testing, crack nucleation started at the apex of a triangle with a height of about 2 mm and a base of about 3 mm (see schematic of cross section in Fig. 4).

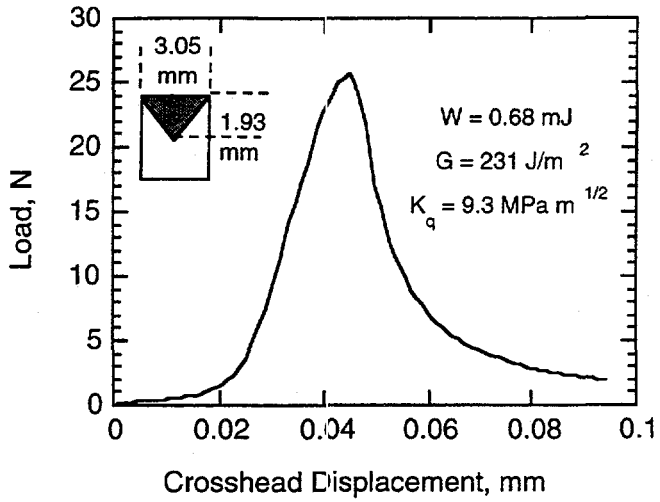

Figure 4: Load-displacement curve obtained during the controlled fracture of a chevron-notched specimen of Mo-12Si-8.5B annealed for 1 day at 1600°C in vacuum.

Figure 4 shows a typical load-displacement plot. Integration of this curve provided the absorbed energy W. The fracture toughness was determined either as G=W/(2A), where A is the area of the triangle through which the crack propagated, or as $K_q=(G\times E')^{1/2}$, where $E'=E/(1-\nu^2)$ is the plane strain Young's modulus and ν is Poisson's ratio. By ultrasonic techniques, the room temperature elastic constants were found to be E=327 GPa and ν=0.29. The density was found to be 9.32 Mg/m^3 by He pycnometry. The fracture toughnesses evaluated in this manner are shown in Table 3. The as-cast Mo-12Si-8.5B had a value on the order of 7 MPa $m^{1/2}$. Annealing for 1 day at 1600°C in vacuum improved the fracture toughness to values of 9 to 10 MPa $m^{1/2}$. This suggests that the 1600°C anneal increased the toughening contribution of the α-Mo phase. This finding is in agreement with the increased flexure strength after a 1600°C anneal, since a higher toughness of the α-Mo phase is likely to reduce the flaw sensitivity of the flexure specimens and will thus increase the flexure strength. There is also some indication that the fracture toughness at 500°C may be higher than that at room temperature. However, the increase may be within the error of the testing technique and needs verification.

Table 3. Fracture toughness of Mo-12Si-8.5B (at. %)

Specimen Number	Processing	Temp., °C	A, mm^2	W, mJ	G, J/m^2	K_q MPa $m^{1/2}$
531#3	as-cast	20	3.02	0.4179	138.4	7.2
531#4	as-cast	20	2.75	0.3927	142.8	7.3
531-A1#3	1d/1600°C/Vac	20	2.94	0.6800	231.0	9.3
531-A1#4	1d/1600°C/Vac	20	2.88	0.7750	269.5	10.0
531-A2#3	1d/1600°C/Vac	500	2.62	0.7087	271.0	10.0
531-A2#4	1d/1600°C/Vac	500C	2.93	1.0599	361.7	11.6

Figure 5 shows a fracture surface of annealed Mo-12Si-8.5B. This particular image shows α-Mo particles in a matrix of T2. In other micrographs, Mo_3Si was found as well. Similar to the cross section in Fig. 3, the α-Mo forms inclusions in a brittle matrix. Figure 5 shows some evidence for debonding at the Mo-T2 interfaces. Limited ductility of the α-Mo particles is also seen.

The fracture toughnesses of Mo-12Si-8.5B alloys exceeds those of most engineering ceramics. However, in view of the high volume fraction of the α-Mo phase (approximately 40%), higher fracture toughnesses might be expected. It is hoped that further improvements may be achieved by lowering the ductile-to-brittle transition temperature of the α-Mo by suitable alloying additions. Also, processing resulting in a microstructure consisting of T2 and Mo_3Si particles in a matrix (or "binder") of Mo is likely to be more effective with regard to the mechanical properties. The oxidation behavior of these alloys will be examined as well.

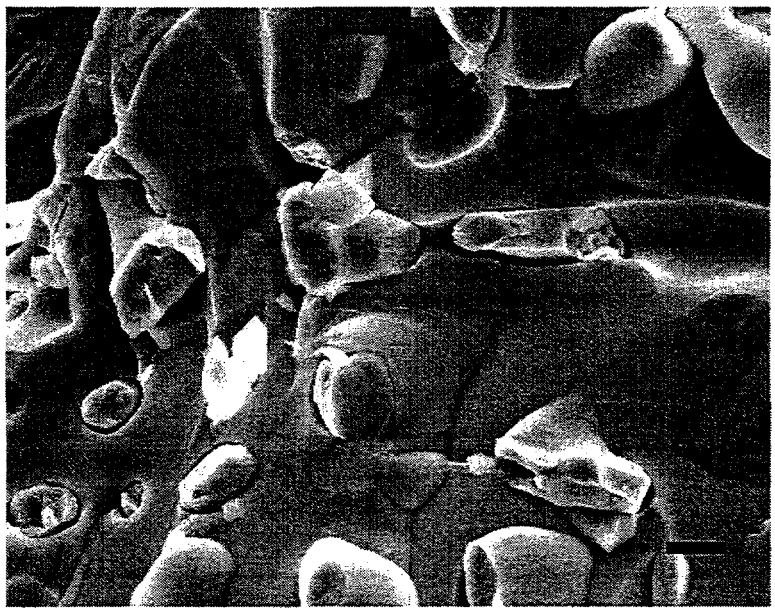

Figure 5: Fracture surface of Mo-12Si-8.5B. Prior to fracture, the material was annealed for 1 day at 1600°C in vacuum.

ACKNOWLEDGMENTS

This research was sponsored by the Fossil Energy Advanced Research and Technology Development (AR&TD) Materials Program, U.S. Department of Energy, under contract DE-AC05-96OR22464 with Lockheed Martin Energy Research Corporation.

REFERENCES

1. H. Nowotny, E. Kimakopoulou, and H. Kudielka, "Untersuchungen in den Dreistoffsystemen: Molybdän-Silizium-Bor, Wolfram-Silizium-Bor und in dem System: VSi_2-$TaSi_2$," Mh. Chem. 88 (1957) 180.
2. A. J. Thom, M. K. Meyer, Y. Kim, and M. Akinc, "Evaluation of $A_5Si_3Z_x$ Intermetallics for Use as High Temperature Structural Materials," in "Processing and Fabrication of Advanced Materials III, V. A. Ravi et al., eds., TMS, 1994, p. 413.
3. M. K. Meyer, M. J. Kramer, and M. Akinca [sic], "Compressive Creep Behavior of Mo_5Si_3 with the Addition of Boron," Intermetallics 4 (1996) 273.
4. M. Meyer, M. Kramer, and M. Akinc, "Boron-Doped Molybdenum Silicides," Adv. Mater. 8 (1996) 85.
5. D. M. Berczik, United States Patent 5,595,616 (1997), "Method for enhancing the oxidation resistance of a molybdenum alloy, and a method of making a molybdenum alloy."
6. D. M. Berczik, United States Patent 5,693,156 (1997) "Oxidation Resistant Molybdenum Alloy."
7. J. H. Perepezko, C. A. Nunes, S.-H. Yi, and D. J. Thoma, "Phase Stability in Processing of High Temperature Intermetallic Alloys," MRS Symposium Proceedings Vol. 460, C. C. Koch et al., eds., 1996, pp. 3-14
8. C. A. Nunes, R. Sakidja, and J. H. Perepezko, "Phase Stability in High Temperature Mo-rich Mo-B-Si Alloys, in "Structural Intermetallics 1997," eds. M. V. Nathal et al., TMS, 1997, pp. 831-839.
9. R. Sakidja, H. Sieber, and J. H. Perepezko, "Microstructural Development of Mo-rich Mo-B-Si Alloys, to be published in proceedings of "Molybdenum & Molybdenum Alloys," San Antonio, TX, TMS, 1998.

10. J. H. Schneibel, C. T. Liu, L. Heatherly, J. L. Wright, and C. A. Carmichael, Proc. 11th Annual Conference on Fossil Energy Materials, R. R. Judkins, ed., Knoxville, TN, 1997, pp. 367-378.

11. J. H. Schneibel, C. T. Liu, L. Heatherly, and M. J. Kramer, "Assessment of Processing Routes and Strength of a 3-Phase Molybdenum Boron Silicide (Mo_5Si_3-Mo_5SiB_2-Mo_3Si), Scr. Mater. 38 (1998) 1169.

12. T. E. Tietz and J. W. Wilson, "Behavior and Properties of Refractory Metals," Stanford University Press, Stanford, CA, 1965.

IRON-ALUMINIDE FILTERS FOR IGCCs AND PFBCs

P. F. Tortorelli, E. Lara-Curzio, C. G. McKamey, I. G. Wright, and R. R. Judkins

Oak Ridge National Laboratory
Oak Ridge, Tennessee, U. S. A.

INTRODUCTION

Hot-gas filtration is a key enabling technology with respect to advanced coal-based power plants based on the Integrated Gasification Combined Cycle (IGCC) and pressurized fluidized bed combustors (PFBC). The use of filters to remove particles from hot gases produced by coal gasification or combustion is vital to achieving the efficiency and emission goals of these systems as they protect the gas turbine and other downstream components from degradation by erosion and erosion/corrosion. Consequently, reliability and durability of the hot-gas filtering devices are of special importance.

Materials used in hot-gas filters are required to withstand prolonged exposure to corrosive, high-temperature gaseous environments as well as to condensable vapors and solid species, some of which may have the potential for localized interaction with the filter material after extended times. The gas streams may be oxidizing (PFBCs) or reducing, in which the sulfur species are largely in the form of H_2S (in the case of the product gas from IGCC processes or from carbonizers). Degradation of metallic filter elements has been observed as an environmental effect under oxidation, sulfidation, and/or carburization conditions and acts as a driving force for the development of ceramic hot-gas filters, particularly for the higher temperatures associated with advanced gasification and combustion designs. However, iron aluminides can also be considered for such applications because of their good to exceptional high-temperature corrosion resistance in a variety of sulfur-bearing environments relevant to coal-derived energy production systems.[1-11] In most cases, the results from these laboratory studies have been directly compared to austenitic stainless steels (particularly type 310). With respect to such alloys, iron aluminides with greater than about 20 at.% Al show exceptional corrosion resistance in coal-gasification environments (high p_{S_2}, low p_{O_2}), and sulfur present as H_2S).[1,3,5-11] While the relative differences

in corrosion resistance between these iron aluminides and stainless steels are not as pronounced as in the gasification environment, Fe_3Al and its alloy modifications also show better corrosion behavior under some coal-combustion-gas conditions (high p_{O_2}, low p_{S_2}, and sulfur as SO_2)[2,4,7,8] and in the presence of $CaSO_4$ and circulating-PFBC-type ash deposits[4,7] up to at least 900°C. Therefore, because of their good to exceptional high-temperature corrosion resistance in such environments, Fe_3Al-based alloys may offer distinct temperature and reliability advantages as materials of construction for hot-gas filters used in advanced coal plants. Consequently, the potential of iron aluminides for these applications is being examined through metallurgical and mechanical evaluation of dense and porous Fe_3Al-based alloys exposed under environmental conditions appropriate to IGCCs and PFBCs.

DISCUSSION OF CURRENT ACTIVITIES

EXPERIMENTAL PROCEDURES

Cylindrical sintered metal filter elements of Fe-28 at.% Al-5% Cr-0.1% Zr (FAS-Zr) were fabricated by Pall Corporation (Cortland, NY) from water-atomized alloy powder produced by Ametek, Inc. (Eighty Four, PA). Two of the four filter elements used to provide specimens for this study, IA-191 and IA-141, were preoxidized (at Pall) for 7 h at 800 and 1000°C, respectively. O-ring specimens were cut from IA-141 and IA-191 as well as from the two as-fabricated cylinders (IA-187 and IA-188). Some of the o-rings from each of the four elements were further divided into eight sections along their circumference. Specimens were exposed to flowing air or air + SO_2 at (approximately 100 cm/min, ambient pressure) at temperatures up to 900°C. Weight changes were measured before and after exposure or continuously at temperature using a recording microbalance. Post-exposure characterization consisted of microstructural analysis by optical and scanning electron microscopy and energy dispersive x-ray analysis (EDS) and mechanical testing of o-rings by internal pressurization to determine tangential (hoop) stress-strain behavior.

The internal pressurization tests were conducted at ambient air and temperature by subjecting an incompressible rubber insert to axial compression at a constant displacement rate of 2 mm/min. The o-ring specimens had a nominal inner diameter of 56 mm and wall thickness of 2 mm and were either 12.2 or 25.4 mm long. The machined edges of the specimens were dry-sanded to a smooth finish using 400 grit silicon carbide sand paper.

Because of the interest in the determination of the mechanical properties of iron-aluminide and ceramic filters at elevated temperatures, part of the present work has been devoted to the design and demonstration of an approach that would allow the determination of the tangential strength of tubular components at temperatures up to 900°C. The principle of operation is based on the radial displacement of a set of eight wedges driven by the vertical displacement of a prismatic conical wedge. Schematics of the device and assembly are shown in Fig. 1.

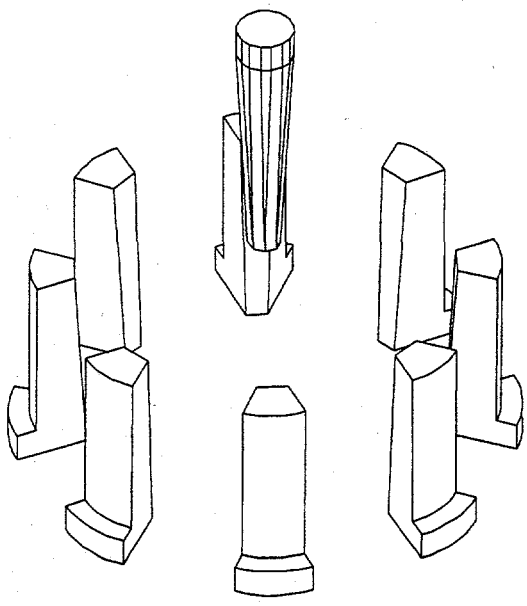

Fig. 1. Schematic of mechanical wedge mechanism.

RESULTS AND DISCUSSION

AS-FABRICATED MATERIALS

The as-fabricated materials contained numerous oxide particles on pore surfaces and at the boundaries of agglomerated powder particles (see Fig. 2). Qualitative analysis by EDS showed that these particles were most likely alumina and zirconia. These stable oxides are formed during the water atomization process used to produce the starting powder.

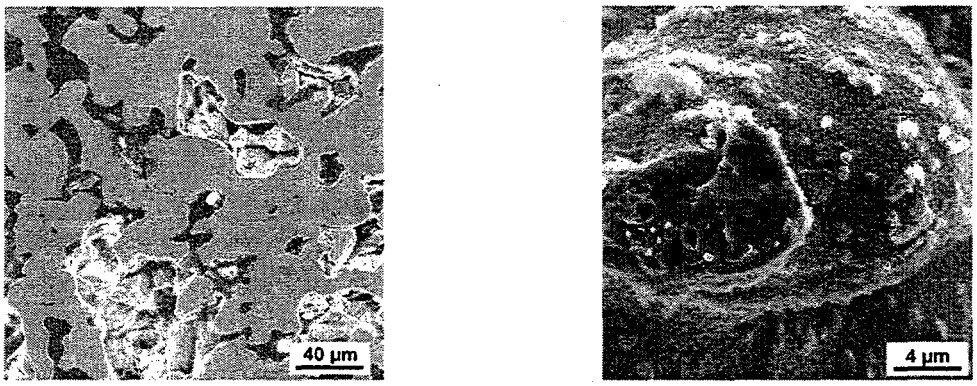

(a) (b)

Fig. 2. As-fabricated FAS-Zr filter material. Oxide particles are found on pore surfaces (a) and at the boundaries of agglomerated powder particles (b).

Determination of the room-temperature tangential stress - tangential strain curves using the rubber-insert internal pressurization approach showed that the porous iron aluminide had reasonable strengths (see, for example, Fig. 3). The average hoop strengths for o-rings cut from two as-fabricated filter elements (IA-187, IA-188) were 112.1 and 112.3 MPa, respectively. As typified by the behavior shown in Fig. 3, the stress-strain curves exhibited a linear regime, a yield point, and a non-linear region up to failure. Loading/reloading experiments demonstrated that the yield point was associated with the onset of plastic deformation. The slope of the linear regions (Young's modulus) was typically between 25 and 35 GPa. Microscopy of the ruptured o-rings showed that the failure occurred transgranularly through fully sintered material and that the transgranular fracture surfaces were free of oxide particles (Fig. 4). As such, the fracture surfaces were typical of what is observed for ductile failure of fully dense iron aluminide and, when allowance is made for the reduced load-bearing area, the measured strengths appear to be consistent with those measured for similar dense alloys.[3]

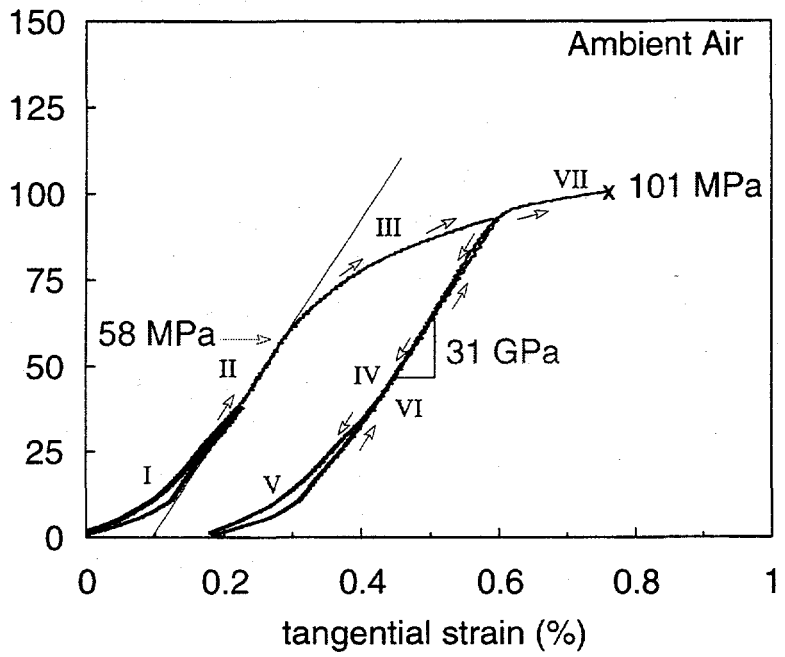

Fig. 3. Stress-strain curve for as-fabricated FAS-Zr filter material.

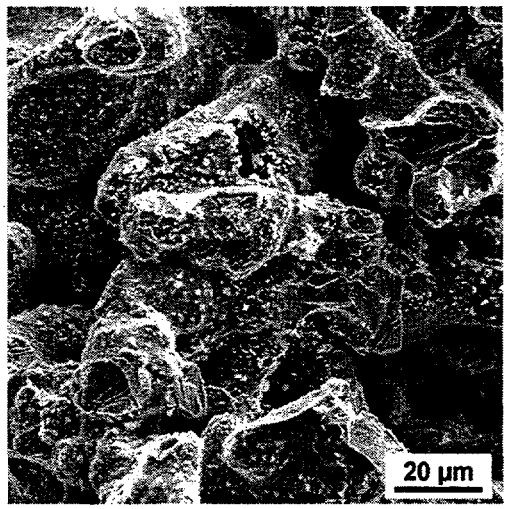

Fig. 4. Fracture surfaces of as-fabricated FAS-Zr filter material showing transgranular failure through fully sintered material. Note lack of oxide particles on fracture surfaces.

PREOXIDIZED MATERIAL

Preoxidation at 1000°C for 7 h resulted in an increase of the hoop strength of the FAS-Zr filter material (IA-141), while a 800°C treatment (IA-191) had no influence. This effect of preoxidation is illustrated in Fig. 5, which compares the hoop strength of preoxidized o-rings to that of as-fabricated specimens (IA-187 and IA-188). The error bars in Fig. 5 are the bounds to the highest and lowest tangential strength values from 3, 3, 2 and 2 tests for specimens from tubes IA-187, IA-188, IA-141 and IA-191, respectively. As discussed below, one possible reason for the higher strength of the specimens preoxidzed at 1000°C may be related to some densification of the material during the thermal treatment.

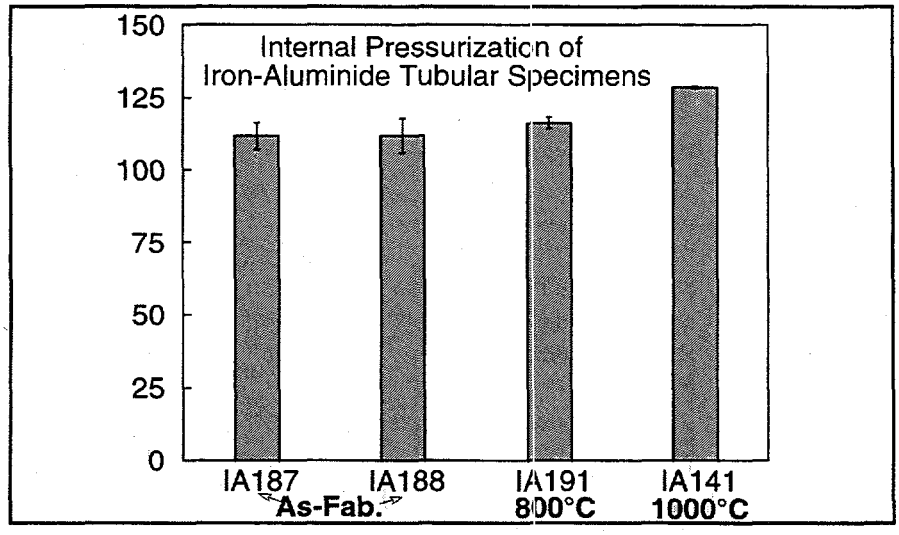

Fig. 5. Hoop strength of as-fabricated and preoxidized FAS-Zr.

EFFECTS OF CORROSION

Gravimetric Results

Thermogravimetric analysis showed that, upon exposure to high-temperature gaseous environments, porous iron-aluminide displayed a rapid initial weight gain followed by a much

more gradual mass increase with time. Examples of this behavior are shown by the microbalance traces in Figs. 6 and 7. This type of kinetic behavior is typical of most systems that form a protective oxide layer during exposure (in this case, alumina) and is normally observed for iron aluminides.[5.12] However, the percent weight changes of the porous filter material are always much higher than what would be measured for a companion fully dense Fe_3Al alloy because of the much greater exposed surface areas in the former case. This difference is illustrated in Fig. 6. Based on this surface area effect, the present results are not inconsistent with prior observations of good high-temperature corrosion resistance of iron aluminides in gaseous environments typically experienced by hot-gas filters used for IGCC and advanced PFBCs.

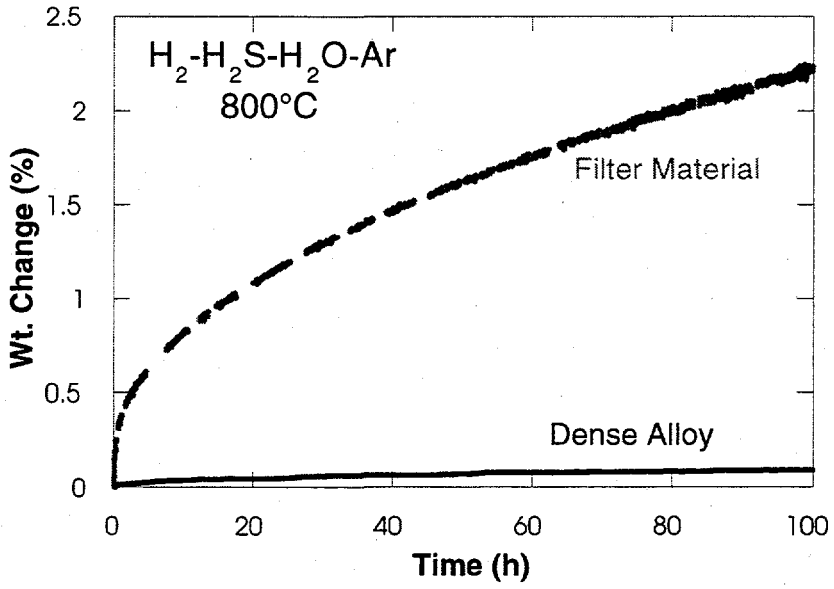

Fig. 6. Weight change versus time for FAS alloy exposed to H_2-H_2S-H_2O at 800°C.

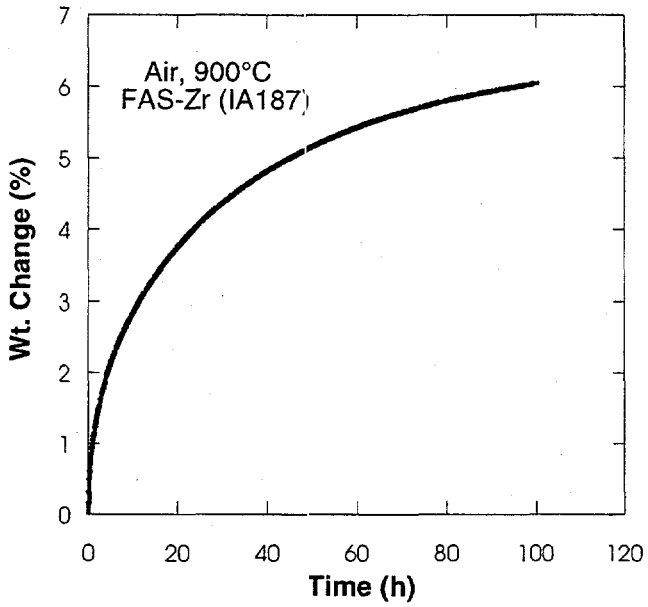

Fig. 7. Weight change versus time for as-fabricated FAS-Zr filter material exposed to air at 900°C.

Porous o-ring specimens exposed in a furnace to simulated combustion environments (flowing air or air + 1 vol% SO_2) showed weight changes consistent with what was measured in the microbalance experiments (compare Fig. 7 with the data in the first row of Table 1). The presence of SO_2 did not degrade corrosion resistance at 800 or 900°C. In fact, these gravimetric measurements indicated that, at 900°C, measured corrosion weight gains were actually higher in air than in air + 1% SO_2. This is somewhat surprising as previous work with dense iron aluminides has shown that the presence of SO_2 had a small negative effective on high-temperature oxidation resistance[2,8,13] and, therefore, the present observed trend will need to be examined in more detail.

The Pall preoxidation treatments reduced the subsequent effect of the air + SO_2 environment on mass gain of the FAS-Zr filter materials (Table 1). Referring to the thermogravimetric data shown in Fig. 7, much of the weight gain of these porous specimens occurs within the first few hours of exposure. Therefore, a preoxidation step of 7 h clearly should result in a reduced weight gain upon subsequent exposure to an oxidizing environment if the protective alumina

scale formed during this treatment remains adherent. Based on the results shown in Table 1, this preoxidation treatment was effective in this regard and bodes well for its use for protection in more aggressive environments, where the surface alumina can still provide protection but any potential problems with its nucleation and initial growth are avoided.

Table 1. Weight changes of O-rings of FAS-Zr filter material exposed for 100 h

Material Condition	**Environment**	**% Wt. Change**
	900°C	
as-fabricated	Air	5.2 ± 0.0
as-fabricated	Air + 1% SO_2	3.9 ± 0.2
7 h at 800°C	Air + 1% SO_2	2.3
7 h at 1000°C	Air + 1% SO_2	0.9
	800°C	
as-fabricated	Air	3.5 ± 0.8
as-fabricated	Air + 1% SO_2	3.1
7 h at 800°C	Air + 1% SO_2	1.9
7 h at 1000°C	Air + 1% SO_2	0.2

O-ring Strength

Initial results from experiments to determine the effect of 100-h exposures in air and air + 1% SO_2 on the mechanical behavior of the FAS-Zr filter material indicated that the hoop strength increased by as much as 10% after these treatments (Fig. 8). This finding is consistent with the above results for the evaluation of preoxidzed specimens tubes that were exposed at 800°C and 1000°C in air for 7 h. Comparison of Figs. 5 and 8 shows that, while the 800°C exposures had essentially no effect on hoop strength, higher-temperature treatments (100 h at 900°C or 7 h at 1000°C) resulted in a small, but significant, strength increase. At the same time, it appears that the specimens became "stiffer" after exposures (Fig. 8) and that the degree of

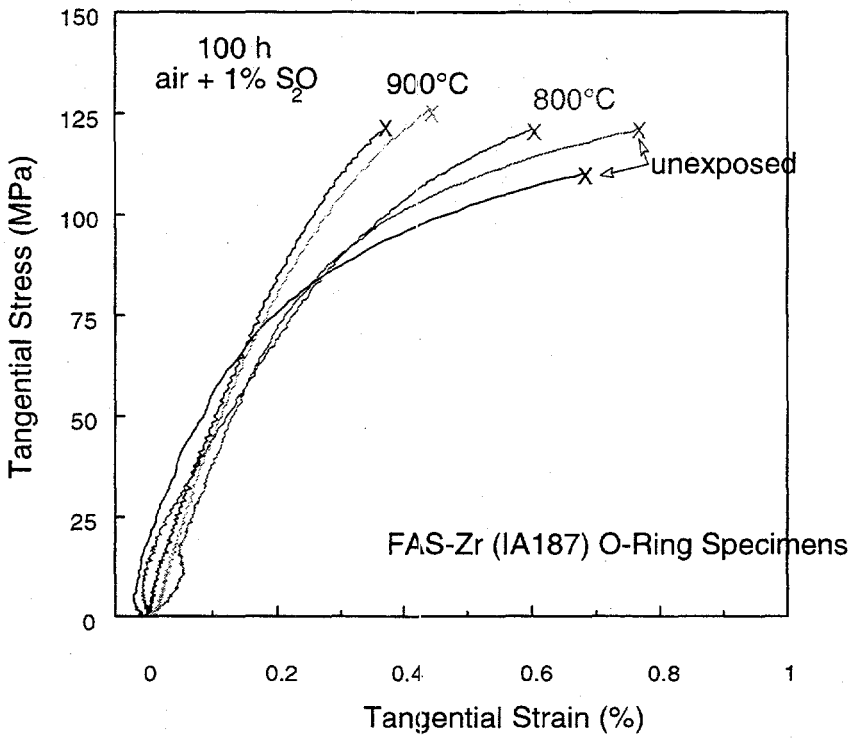

Fig. 8. Stress-strain curves for as-fabricated FAS-Zr filter material in the unexposed condition and after 100-h exposures in air + 1% SO_2 at the indicated temperatures.

stiffening was proportional to the treatment temperature (although the strain measurements are less reliable than those of load).

The observed increase in strength must be considered preliminary pending further testing (these findings are derived from only two measurements) and microstructural analysis, but it is interesting to speculate that such an effect may possibly be explained by an increase in density of the porous bodies during high-temperature exposure. Indeed, there is also some indication from the gravimetric data that some densification may be occurring. Specifically, examination of the thermogravimetric curve in Fig. 7 reveals that the kinetics are sub-parabolic at longer times: $n < 0.5$ where $\bullet w = (k \bullet t)^n$ and •w, k, and t are the total weight change per unit area, the associated rate constant, and the exposure time, respectively. This is shown in Fig. 9, which plots the weight change data of Fig. 7 versus •t; after approximately 20 h at 900°C, the weight change data negatively deviates from a •t dependence. Such behavior could be explained by a decrease in the

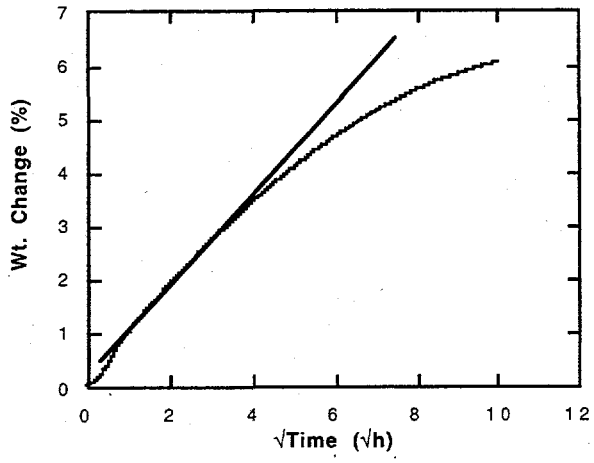

Fig. 9. Wt. change versus •time for FAS-Zr filter material exposed to air at 900°C.

effective surface area (densification) over the course of the experiment. There was not sufficient corrosion observed to explain this densification as being from some closure of pores by accumulation of reaction products in them.

DEVELOPMENT OF A SLIDING WEDGE INTERNAL PRESSURIZATION TECHNIQUE

Because of the interest in the determination of the mechanical properties of filter materials at elevated temperatures, some effort has been dedicated to the design and demonstration of an approach that would allow the determination of the tangential strength of tubular components up to 900°C while avoiding some of the technical problems associated with the use of gases or molten glass for high-temperature internal pressurization.[14,15] The principle of operation of this mechanism is based on the radial displacement of a set of eight wedges driven by the vertical displacement of a prismatic conical wedge (Fig. 1).

Preliminary experiments conducted on clear extruded acrylic o-rings have demonstrated the viability of the sliding wedge approach. Clear extruded acrylic was chosen for the demonstration experiments because it is made with reproducible mechanical properties and tubes of it are very inexpensive and readily available with uniform dimensions. This material is therefore very

appropriate for use in verifying the reproducibility of the data measured by this technique. Figure 10 shows the resulting load versus cross-head and radial displacement curves from four internal pressurization tests. These results serve to demonstrate the uniformity in the properties of the acrylic specimens and the reproducibility of the test results obtained with the mechanical wedge mechanism.

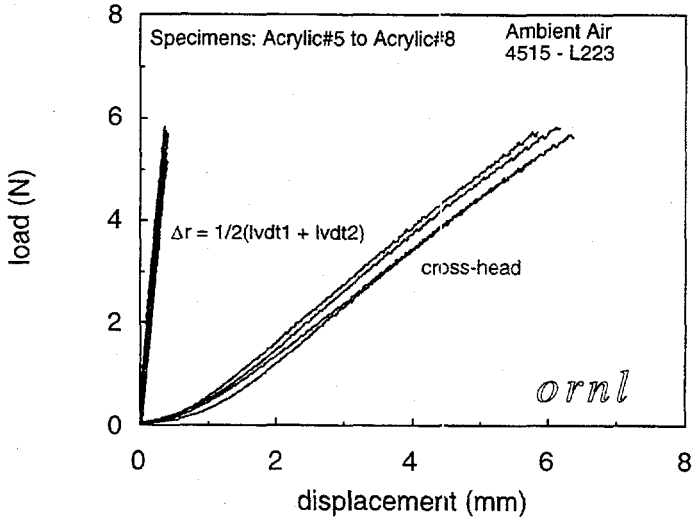

Fig. 10. Load versus cross-head and radial displacement curves obtained from the internal pressurization of four different extruded clear acrylic O-ring specimens using the mechanical wedge mechanism.

To investigate the degree of strain uniformity, the tangential strain on the outer surface of o-ring specimens subjected to internal pressurization with the mechanical wedge mechanism was monitored using adhesively bonded strain gauges and two linear variable differential transducers (LVDTs) positioned on opposite sides of the specimen. One strain gauge was placed at the same spot where one LVDT was contacting the specimen at a location aligned at the middle of one wedge. The other strain gauge was positioned on the outer surface of the specimen in-between two wedges. Figure 11 shows a comparison of the tangential strain measurements using the

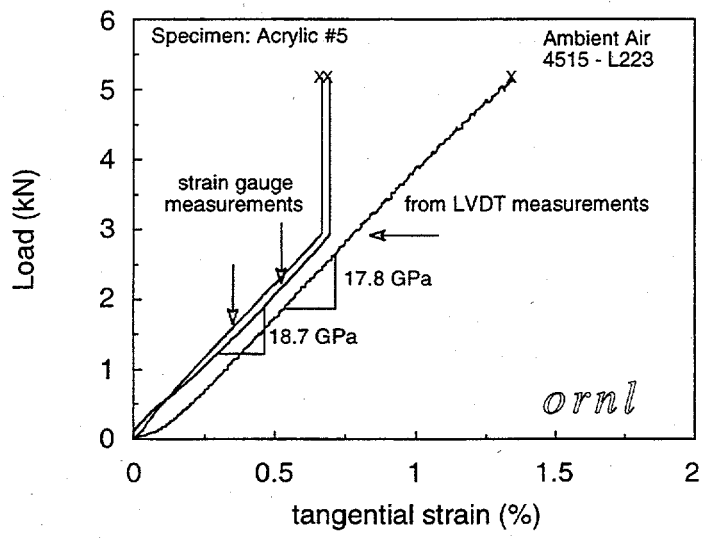

Fig. 11. Load versus tangential strain from the internal pressurization of acrylic O-rings using the mechanical wedge mechanism. Tangential strains were recorded using both adhesively bonded strain gauges and two LVDTs.

strain gauges and the LVDTs. Although there are small deviations among the three tangential strain readings at the start of the test, the slope of the curves obtained by the strain gauges and by the LVDTs are nearly identical afterwards. The discrepancies at the start of the test are attributed to slack in the load train.

At this time, the results obtained from the internal pressurization of tubular specimens using the mechanical wedge mechanism are presented in terms of axial load. This is because numerical simulations are necessary to quantify the effect of friction between the wedges in order to relate the axial load to the tangential stress in the specimen. To facilitate the analysis of frictional effects, tests have been conducted either with or without a Teflon layer between the eight radial wedges and the axial one. These conditions represent the two limiting cases, namely one of maximum friction for the sliding of stainless steel against stainless steel, and one of very low friction for the sliding of two stainless steel bodies with a Teflon interface. Plots of load

versus radial and cross-head displacement obtained with and without a Teflon interlayer demonstrated that, as expected, lower loads are required to induce failure of the acrylic specimens when using the interlayer. The axial displacements were different and larger cross-head displacements were obtained when using a Teflon interface as a result of less friction. However, regardless of the use of a Teflon interlayer, the radial displacement (tangential strain) at failure was the same.

SUMMARY

Experiments with porous iron-aluminide filter materials fabricated by Pall Corporation showed good potential high-temperature corrosion resistance in air, air + SO_2, and H_2S-containing environments. As-fabricated iron-aluminide filter materials have a significant amount of incorporated alumina and zirconia, but their strength and failure are characteristic of typical Fe_3Al alloy behavior. Preoxidation at 800 and 1000°C for 7 h or 100-h exposures in air and air + SO_2 at 800 and 900°C had little effect on hoop strength apart from a possible increase in load at failure due to densification at the higher temperatures. Preliminary results showed that a method for internal pressurization of o-rings based on a sliding wedge mechanism holds promise for application to high-temperature testing.

ACKNOWLEDGMENTS

The authors thank M. Howell and T. Parham for experimental support. This research was sponsored by the U S. Department of Energy, Office of Fossil Energy, through the Advanced Research and Technology Development (AR&TD) Materials Program and the Federal Energy Technology Center (Morgantown) under contract DE-AC05-96OR22464 with Lockheed Martin Energy Research Corporation.

REFERENCES

1. J. H. DeVan, pp. 107-115 in *Oxidation of High-Temperature Intermetallics*, T. Grobstein and J. Doychak (eds.), TMS, 1989.

2. W. H. Lee and R. Y. Lin, pp. 475-486 in *Fourth Annual Conf. Fossil Energy Materials*, R. R. Judkins and D. N. Braski (eds.), U. S. Department of Energy, May, 1990.

3. C. G. McKamey, J. H. DeVan, P. F. Tortorelli, and V. K. Sikka, J. Mater. Res. 6 (1991) 1779-1805.

4. K. Natesan, pp. 271-82 in *Sixth Fossil Energy Materials Conf.*, N. C. Cole and R. R. Judkins (eds.), U. S. Department of Energy, 1992.

5. J. H. DeVan and P. F. Tortorelli, "Oxidation/Sulfidation of Iron-Aluminum Alloys," *Mater. at High Temp.* 11 (1993) 30-35.

6. P. F. Tortorelli and J. H. DeVan, pp. 257-270 in Processing, Properties, and Applications of Iron Aluminides, J. H. Schneibel and M. A. Crimp, Editors, The Minerals, Metals, and Materials Society, Warrendale, PA, 1994.

7. F. Gesmundo *et al.*, pp. 1657-1667 in Materials for Advanced Power Engineering, D. Cousouradis et al., Editors, Kluwer Academic Publishers, 1994.

8. K. Natesan and R. N. Johnson, pp. 591-599 in Heat-Resistant Materials II, K. Natesan, P. Ganesan, and G. Lai, Editors, ASM International, Materials Park, OH, 1995.

9. K. Natesan and P. F. Tortorelli, pp. 265-280 in International Symposium on Nickel and Iron Aluminides: Processing, Properties, and Applications, S. C. Deevi, *et al.*, Editors, ASM International, Materials Park, OH, 1997.

10. J. L. Blough and W. W. Seitz, pp. 357-366 in *Eleventh Fossil Energy Materials Conf.*, R. R. Judkins (ed.), U. S. Department of Energy, 1997.

11. S. R. J. Saunders *et al.*, Mater. Sci. Forum 251-254 (1997) 583-589.

12. P. F. Tortorelli and J. H. DeVan, Mater. Sci. and Eng. A153 (1992) 573-577.

13. P. F. Tortorelli, Oak Ridge National Laboratory, unpublished results, 1997.

14. D. L. Shelleman, O. M. Jadaan, J. C. Conway, and J. J. Mecholsky, J. Testing and Evaluation 19 (1991) 192-200.

15. L. Chuck and G. A. Graves, *Proc. Symposium on Thermal and Mechanical Test Methods and Behavior of Ceramic Composites,* Cocoa Beach Florida, 1996.

HIGH-TEMPERATURE CORROSION BEHAVIOR OF IRON-ALUMINIDE ALLOYS AND COATINGS

P. F. Tortorelli, B. A. Pint, and I. G. Wright

Oak Ridge National Laboratory
Oak Ridge, Tennessee, U. S. A.

INTRODUCTION

Because of their good high-temperature corrosion resistance,[1-3] iron aluminides have a number of potential applications in future efficient fossil-fuel-based energy systems. These possible applications include hot-gas filters, syngas duct work, heat exchangers, parts of desulfurization units, and protective coatings for low-NO_x boiler waterwalls. Because of these uses, the oxidation/sulfidation resistance of iron aluminides based on Fe_3Al appears to extend to temperatures well above those at which these alloys have adequate mechanical strength.[1,2] Consequently, in addition to alloying and processing modifications for improved creep resistance of wrought material, this strength limitation is being mitigated by development of oxide-dispersion-strengthened (ODS) iron aluminides[4,5] and by evaluation of Fe_3Al alloy compositions as coatings or claddings on higher-strength, less corrosion-resistant materials.[6-10] As part of these efforts, the high-temperature corrosion of iron-aluminide weld overlays and ingot-processed alloys based on Fe_3Al are being characterized. Recent oxidation results for ODS Fe_3Al can be found elsewhere.[5]

DISCUSSION OF CURRENT ACTIVITIES

OXIDATION OF Fe_3Al ALLOYS

The long-term oxidation performance of ingot-processed Fe-28% Al-(2-5)% Cr alloys was characterized for cyclic exposures in air at 1000 and 1100°C to optimize the concentration and type of minor alloying elements (referred to as reactive elements or REs) that improve the adhesion of the protective alumina scale to the alloy substrate. (All compositions are in at.%.)

Most of the alloys of the present study were based on Fe-28% Al-2% Cr (FASN) and contained approximately 0.1% of a RE. They are designated as FASX, where X is the chemical symbol for the specific alloying element. In addition, an iron aluminide containing Fe-28% Al-5% Cr-0.1% Zr (FAL) was included. For comparison, an ingot-processed Fe-18%Cr-10%Al alloy (FCAN) and a commercial ZrO_2-dispersed (0.05% Zr) Fe-20% Cr-10% Al composition (Kanthal alloy APM) were also oxidized. The APM alloy is used as the benchmark for oxidation resistance as it typically displays low scale-growth and spallation rates at high temperatures under both isothermal and thermally cycled conditions.[11]

The cyclic oxidation studies were conducted by exposing specimens in covered pre-annealed alumina crucibles in order to catch all spalled oxide. This experimental technique allows the measurement of the total weight gain (specimen + spalled oxide) which is equivalent to the metal wastage rate. Under these conditions, the FASN alloy consistently showed rapid weight gain kinetics under cyclic oxidation conditions, while the presence of Hf, Y, or Zr in this base composition substantially improved performance of the iron aluminides (Figs. 1 and 2). At 1000°C (Fig. 1), there was little differentiation among the various RE-doped alloys over 5000 h of exposure and FAL and FASZr matched the performance of the benchmark APM alloy. These findings confirm the preliminary, shorter-term 1000°C results reported previously.[10] At 1100°C, RE additions of Y or Hf to FAS improved oxidation resistance relative to the undoped composition (FASN), but only the FASZr alloy displayed a cyclic oxidation resistance comparable to that of APM (Fig. 2). As such, however, this is the best performance of an iron aluminide at 1100°C to date.[10]

As indicated in Figs. 1 and 2, FASN consistently showed rapid weight gain kinetics under cyclic oxidation conditions at 1000 and 1100°C. Its performance was much worse than that of an undoped FeCrAl (FCAN, Fig. 1) and is believed to be due to some nitridation that occurs because of the inability of FAS to maintain a protective alumina coating during thermal cycling in the absence of a RE alloying addition. This speculation is based on the results of a series of 96-h experiments that were conducted with Fe-28%Al-5%Cr (FA186) and FAL (Fe-28%Al-5%Cr-0.1%Zr) in a variety of gas mixtures in order to examine the effects of water vapor and nitrogen on the development of protective alumina on iron aluminides. These results are described in more detail elsewhere;[12] the salient findings applicable to the present discussion were that (1) the undoped alloy (FA186) showed twice the weight gain in air compared to Ar-O_2 or O_2 and (2) the addition of Zr to this alloy (resulting in FAL) consistently reduced the weight

gains observed so that there was no appreciable difference among the results for the three different gas environments (see Table 1). The large weight gains associated with FASN (Figs. 1 and 2) are consistent with the nitridation effect suggested by the work with FA186 and FAL.[12] In the absence of a RE, the FAS cannot a maintain a protective alumina scale during exposure in

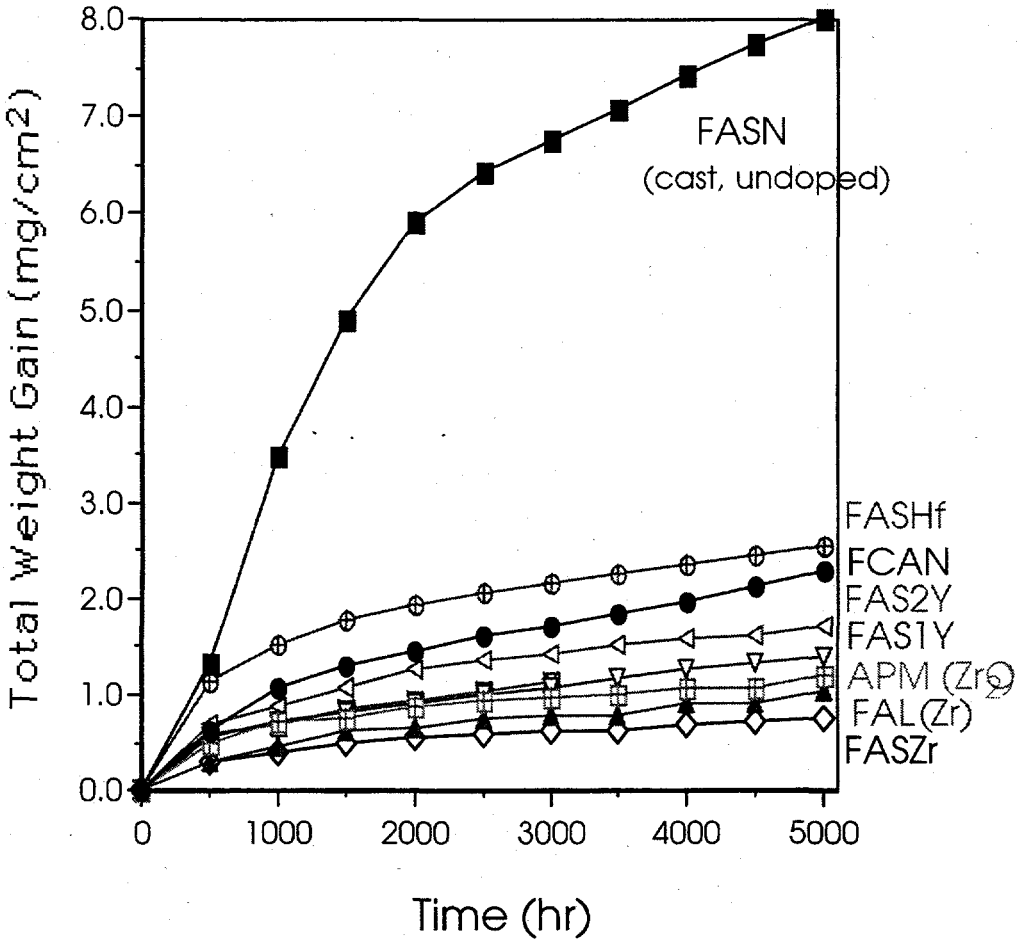

Fig 1. Total weight gain (specimen + spall) for 500-h cycles at 1000°C in laboratory air.

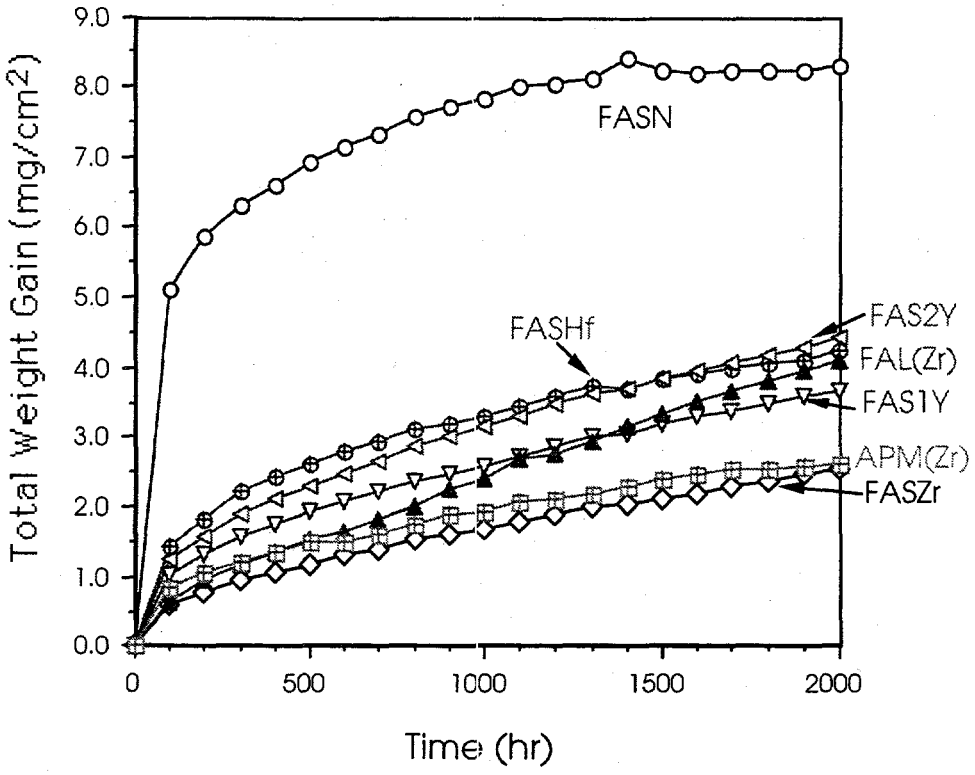

Fig. 2. Total weight gain (specimen + spall) for 100-h cycles at 1100°C in laboratory air.

Table 1. Weight gains of iron aluminides after 96 h in specified environment

Gas Environment	1000°C FA-186	1000°C FAL	1100°C FA-186	1100°C FAL
dry air	1.03	0.35	4.56	0.34
wet air	1.12	0.34	4.50	0.32
dry O_2	0.55	0.27	1.63	0.39
wet O_2	0.53	0.30	2.08	0.40
Ar-20% O_2	0.47	0.22	1.25	0.39

air and its weight gains could well be exacerbated by nitridation – obviously to a much greater degree than FCAN, which must be somewhat protected from reaction with nitrogen by a partially adherent oxide scale. These results again indicate the importance of RE dopants in assuring the long-term corrosion resistance of iron aluminides.

It has been shown previously that an optimal RE concentration is needed to maximize the oxidation resistance of iron aluminides.[13,14] Such observations are consistent with the present

result that FAS2Y (0.6% Y) showed a higher weight gain than FAS1Y with ~ 0.1% Y (Fig. 2) and therefore appears to be overdoped with respect to its RE concentration. This higher level of Y in the as-cast FAS2Y resulted in a blocky metallic Y-rich phase (Fe_xY) that was preferentially oxidized. At 1200°C, this resulted in fairly high weight gains after 10 100-h oxidation cycles (Fig. 3). Interestingly, as also shown in Fig. 3, a specimen obtained from the same alloy after subsequent rolling showed significantly lower weight gains during oxidation. Presumably, the rolling refined and dispersed the Fe_xY such that this phase became more effective as a source of RE and thus led to improved scale adhesion. In contrast, there was essentially no difference between the cyclic oxidation behavior of as-cast and rolled FASZr, which contained a relatively low concentration (~ 0.1%) of Zr (Fig. 3). Although requiring further study, this observed effect of deformation processing on the oxidation resistance of RE-containing iron aluminides, if verified, may have important implications for minimizing the detrimental effects associated with overdoping. An appropriate deformation schedule could be used to expand the effective concentration range of REs for improved oxidation resistance of wrought iron aluminides.

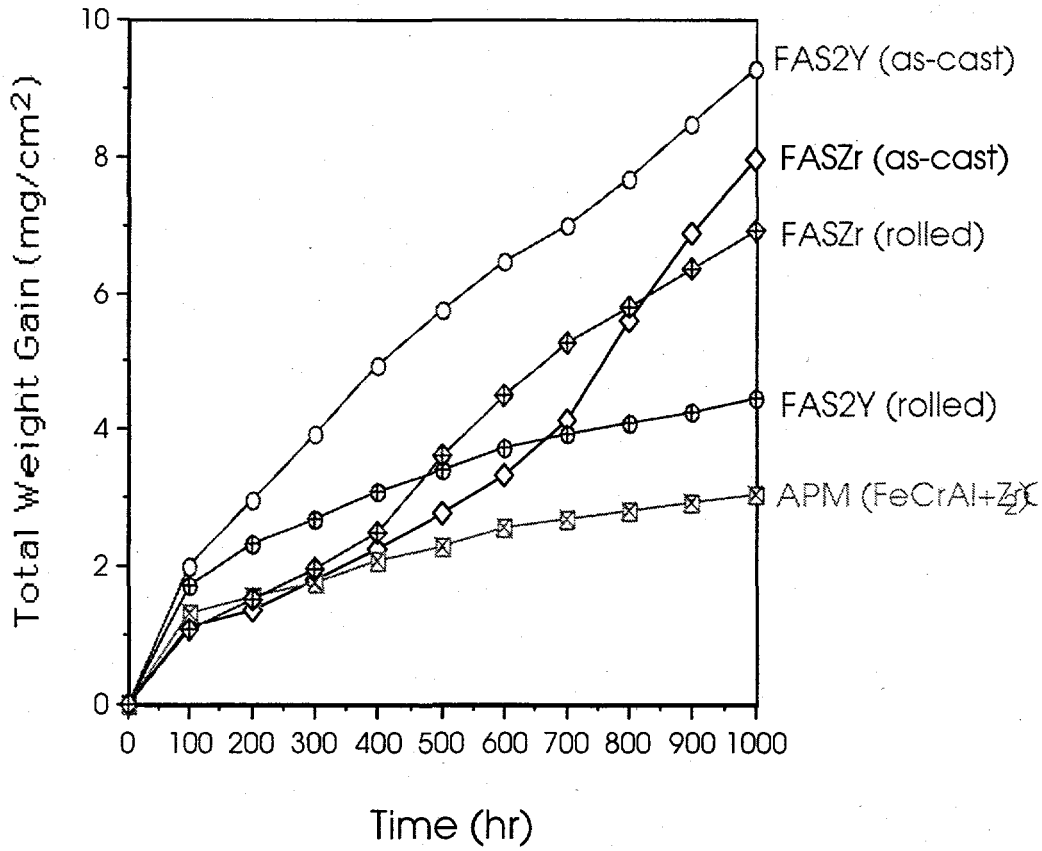

Fig. 3. Total weight gain (specimen + spall) for 100-h cycles at 1200°C in laboratory air.

CORROSION OF IRON-ALUMINIDE WELD OVERLAYS UNDER CONDITIONS SIMULATING FLAME IMPINGEMENT IN LOW-NO_x BOILERS

One possible application for iron-aluminide coatings would be as weld overlays in low NO_x coal boilers. These systems show accelerated attack of boiler tubes, particularly in the areas of flame impingement. Recently, specimens with weld overlays of iron aluminide have been exposed in a waterwall wastage rig at the University of Leeds (United Kingdom). The Leeds rig was constructed as part of an EPRI program and is intended to simulate the flame impingement conditions experienced originally in United Kingdom boilers and recently found in some U. S. boilers that have been retrofitted with low-NO_x burners. The unique feature of the facility is that it burns coal in a controlled manner on a relatively small scale, and has been found to reproduce the rate of corrosion and the corrosion morphologies that are found on the furnace walls of boilers experiencing accelerated attack.[15]

The specimens exposed in the Leeds rig were ground from a Fe- 2.25% Cr-1% Mo plate on which an iron-aluminide weld overlay was deposited on one side. The gas tungsten arc process was used to deposit the coating,[6,7] which had about 25 at.% Al. The specimen configuration is shown in Fig. 4. Note that the sides of the ground specimen were also exposed in the rig such that part of the steel was also in contact with the corrosive environment. This provided a convenient way to compare the corrosion of the coating to that of the substrate. Two weld overlay specimens have now been exposed in the Leeds rig. Exposures conditions are shown in Table 2.

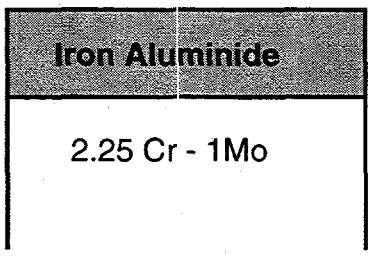

Fig. 4. Schematic depiction of weld-overlay specimen used in flame-impingement rig. Note that top and sides of specimens (including part of 2.25Cr - 1 Mo steel substrate) were exposed.

Table 2. Exposure conditions for iron-aluminide-coated Fe-2.25 Cr-1 Mo steel specimens (47 h)

Spec. No.	Coal	Temp. (°C)	Heat flux (kW/m^2)	Gas composition		
				CO	SO_2 (ppm)	H_2S (ppm)
1	Genco, Low Cl,	460	300	6	1000	600
2	Southern Co., Low Cl	450	280	9	400	800

For specimen 1, the appearance of the exposed surfaces suggested that there had been very little or no corrosion (Fig. 5). Spherical particles of FeS observed on the specimen surface did not appear to be related to the scale beneath them. They were probably pyrite particles deposited from the flame rather than corrosion products. Under the conditions of the test, the substrate steel experienced rapid corrosion with the formation of a mixed oxide-sulfide scale. This is illustrated in Fig. 6, which shows a cross section from the junction of the weld overlay with the bare Fe - 2.25 Cr-1 Mo substrate. This direct comparison clearly shows the superior performance of the iron-aluminide coating vis-à-vis a typical boiler steel under these flame impingement conditions.

A feature of this and other overlay coatings of iron aluminides is the presence of cracks which penetrated almost the full coating thickness.[6,7] During exposure in the Leeds rig, gaseous species and deposits from the flame penetrated along these cracks, but, in no case, did corrosion in the cracks result in further propagation. In service, however, it is possible that alternating stresses experienced by the furnace wall tubes would cause the cracks to propagate, possibly into the base metal, which would not be acceptable from a utility boiler viewpoint. It is possible that changes in the surface profile of these coatings following cracking may have been one reason why a post-test metallographic measurement technique indicated metal loss of 8-10 μm, which is inconsistent with the metallographic analysis summarized above (Figs. 5 and 6). Careful review of the measuring technique suggests that the metal loss for this specimen was probably less than 3-5 μm.

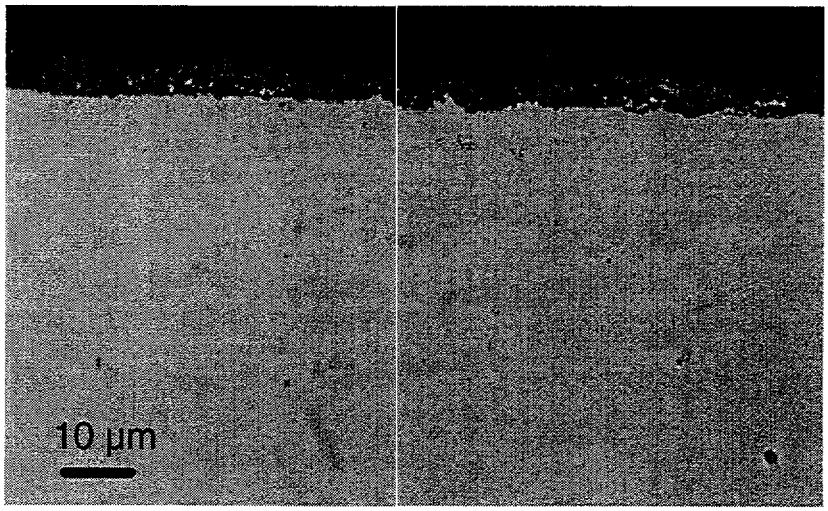

Fig. 5. Polished cross-section of iron-aluminide weld-overlay exposed in flame-impingement rig for 47 h at 450°C. Very little corrosion product was observed

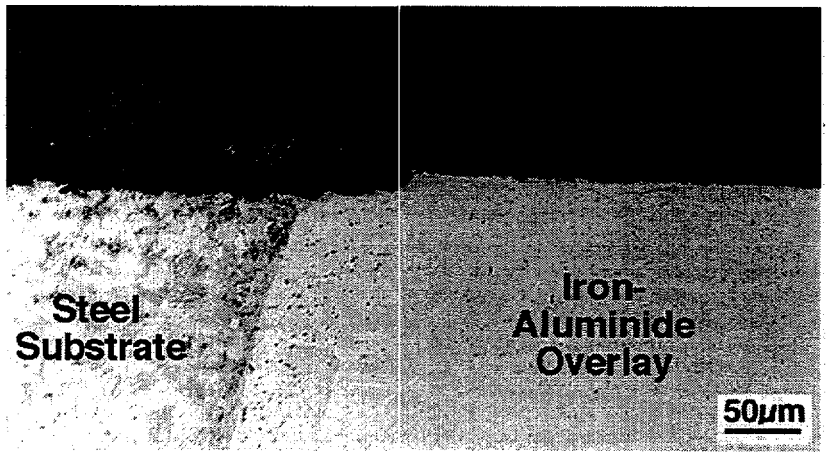

Fig. 6. Polished cross-section of iron-aluminide weld-overlay exposed in flame-impingement rig for 47 h at 450°C showing side of specimen (see Fig. 4). In contrast to the overlay, the 2.25Cr - 1Mo steel substrate showed substantial corrosion product development.

Specimen 2 has not been fully analyzed after its exposure in the Leeds rig (Table 2). Although there was a metal loss of ~4 μm as measured by a metallographic technique, the surface, as with Specimen 1, looked essentially uncorroded. There was a thin (~1 μm) scale and some surface Fe and S were detected. Further characterization is underway, but, again, the Fe and S may be related to deposition of pyrite.

A recent review of the high-temperature corrosion of iron aluminides in many different environments[16] concluded that, while protective alumina is normally considered to be α-Al_2O_3, which is typically not observed below 900°C, other forms of alumina that develop in the various mixed-gas environments at lower temperatures must provide corrosion protection. The present results show good resistance of iron aluminide at a temperature (~ 450°C) where the formation of surface alumina is problematical but match other mixed gas results for iron aluminide alloys in this temperature range.[16] Nevertheless, the rather limited degradation exhibited by the weld overlay material compared to the steel substrate does indicate that some form of slow growing Al-containing product (oxide, sulfide, or an oxysulfide) must be forming to almost the complete exclusion of iron sulfides, which are typically the cause of the rapid corrosion observed in these types of environments.

SUMMARY AND CONCLUSIONS

The oxidation performance of ingot-processed Fe-28 at.% Al-(2-5)% Cr alloys with minor oxygen-active element additions was characterized for long-term exposures in air at 1000 and 1100°C. These alloys have very good cyclic oxidation resistance in air when reactive elements such as Zr, Y, or Hf are present in the appropriate concentrations (~ 0.1 at.%). The most resistant of these matched the performance of a benchmark ZrO_2-dispersed Fe-20% Cr-10% Al alloy. In the absence of a reactive element addition, iron aluminides can show substantially greater oxidation susceptibility in air relative to other alumina formers. This may be due to nitridation that occurs because of the inability of the undoped Fe_3Al alloy to form adherent alumina. Deformation processing can affect the distribution of a RE in overdoped iron-aluminide alloys such that oxidation resistance is improved.

Initial results for iron-aluminide weld overlay coatings exposed in a simulated flame impingement boiler environment at ~ 450°C showed little degradation of the deposit under

conditions that caused significant corrosion of the steel substrate. Cracks in the weld deposit did not compromise corrosion resistance but may be detrimental in the presence of thermal cycling.

ACKNOWLEDGMENTS

The authors thank M. Howell for experimental support. This research was sponsored by the Fossil Energy Advanced Research and Technology Development (AR&TD) Materials Program, U S. Department of Energy, under contract DE-AC05-96OR22464 with Lockheed Martin Energy Research Corporation.

REFERENCES

1. C. G. McKamey, J. H. DeVan, P. F. Tortorelli, and V. K. Sikka, *J. Mater. Res.* 6 (1991) 1779-1805.

2. P. F. Tortorelli and J. H. DeVan, pp. 257-70 in Processing, Properties, and Applications of Iron Aluminides, J. H. Schneibel and M. A. Crimp (eds.), The Minerals, Metals, and Materials Society, Warrendale, PA, 1994.

3. K. Natesan and P. F. Tortorelli, pp. 265-280 in International Symposium on Nickel and Iron Aluminides: Processing, Properties, and Applications, S. C. Deevi, *et al.*, Editors, ASM International, Materials Park, OH, 1997.

4. I. G. Wright, B. A. Pint, E. K. Ohriner, and P. F. Tortorelli, pp. 359-71 in *Proc. Tenth Annual Conf. Fossil Energy Materials*, N. C. Cole and R. R. Judkins (comp.), U. S. Department of Energy, August 1996.

5. I. G. Wright, C. G. McKamey, E. K. Ohriner, and B. A. Pint, "Development of ODS-Fe_3Al Alloys," to be published in *Proc. Twelfth Annual Conf. Fossil Energy Materials,* 1998.

6. G. M. Goodwin, P. J. Maziasz, C. G. McKamey, J. H. DeVan, and V. K. Sikka, pp. 205-10 in *Proc. Eighth Annual Conf. Fossil Energy Materials*, N. C. Cole and R R. Judkins (comp.), CONF-9405143, U. S. Department of Energy, August 1994.

7. G. M. Goodwin, pp. 381-92 in *Proc. Tenth Annual Conf. Fossil Energy Materials*, N. C. Cole and R. R. Judkins (comp.), U. S. Department of Energy, August 1996.

8. P. F. Tortorelli, J. H. DeVan, G. M. Goodwin, and M. Howell, pp. 203-12 in Elevated Temperature Coatings: Science and Technology I, N. B. Dahotre, J. M. Hampikian, and J. J. Stiglich (eds.), The Minerals, Metals, and Materials Society, Warrendale, PA, 1995.

9. K. Natesan and R. N. Johnson, pp. 591-99 in Heat-Resistant Materials II, K. Natesan, P. Ganesan, and G. Lai (eds.), ASM International, August 1995.

10. P. F. Tortorelli, B. A. Pint, and I. G. Wright pp. 235-46 in *Proc. Eleventh Annual Conf. Fossil Energy Materials*, R. R. Judkins (comp.), U. S. Department of Energy, December, 1997.

11. B. A. Pint, A. J. Garratt-Reed, and L. W. Hobbs, *Mater. High Temp.* 13 (1995) 3-16.

12. K. B. Alexander, K. Prüßner, P. F. Tortorelli, and B. A. Pint, "The Role of Microstructure and Microchemistry on the High-Temperature Oxidation Resistance of Alumina-Forming Alloys," to be published in *Proc. Twelfth Annual Conf. Fossil Energy Materials,* 1998.

13. B. A. Pint, *Mater. Sci. Forum* 251-254 (1997) 397-404.
14. B. A. Pint, *Oxid. Met.* 45 (1996) 1-37.
15. R. B. Dooley, EPRI, private communication, 1997.
16. P. F. Tortorelli and K. Natesan, "Critical Factors Affecting the High-Temperature Corrosion Performance of Iron Aluminides", to be published in *Mater. Sci. Eng. A.*

THE ROLE OF MICROSTRUCTURE AND MICROCHEMISTRY ON THE HIGH-TEMPERATURE OXIDATION RESISTANCE OF ALUMINA-FORMING ALLOYS

K. B. Alexander, K. Prüßner, B. A. Pint, and P. F. Tortorelli

Oak Ridge National Laboratory
Oak Ridge, Tennessee, U. S. A.

INTRODUCTION

The mechanical integrity of oxide scales ultimately determines whether they will protect materials from corrosion and other environmental effects at high temperatures. Accordingly, this effort is directed toward improving the high-temperature corrosion resistance of materials of importance for efficient energy production through study of the key factors controlling the chemical and mechanical failure of protective alumina scales. High-spatial-resolution electron microscopy techniques have been used in the microstructural and microchemical characterization of the alumina scale, oxide-metal interface, and substrate for Fe-Al, FeCrAl(Y), and NiCrAlY alloys as well as nickel-based superalloys. These results have been analyzed to provide links between the local microstructure and chemical composition of the scales and relevant interfaces and the associated oxidation performance. Progress to date in improving the understanding of the interplay among reactive-element doping, interfacial segregation, microstructure, scale reliability/failure, and the high-temperature oxidation resistance of alumina-formers suggests that this is a powerful approach for providing quantitative input for alloy and coating design and modification related to maximizing high-temperature corrosion resistance over extended periods of time.

DISCUSSION OF CURRENT ACTIVITIES

MICROSTRUCTURAL CHARACTERIZATION OF REACTIVE ELEMENT SEGREGATION IN ALUMINA SCALES AS RELATED TO OXIDATION PERFORMANCE

Oxide scales consisting mainly of alumina were grown on various model and developmental alloys (Fe-Al, Fe-Cr-Al, and Ni-Cr-Al, with and without reactive-element

dopants) and analyzed in detail by electron microscopy. In general, in all these systems, segregation of the reactive-element (RE) ion was observed at the metal-oxide and oxide-oxide interfaces by analytical electron microscopy of thinned scale cross sections consistent with previous observations related to alumina formers.[1,2,3] The oxidation performance and scale failure modes were also characterized.

As reported for other alumina-forming alloys,[4] the segregation of RE ions to oxide-oxide interfaces tended to alter the morphology of the scale, resulting in a more columnar, slower-growing alumina. The difference in scale structure for a Ni-10%Cr-10%Al alloy with and without a sufficiently high RE (Y) addition is shown in Fig. 1. (All concentrations are in at.%.) High-spatial resolution energy dispersive spectroscopy of thinned scale cross sections showed the Y in the RE-doped alloy was segregated to the boundaries of the thermally grown alumina (Fig. 2). However, the presence of the Y segregant at oxide grain boundaries was not sufficient to ensure improved oxidation performance in every case. For example, while alumina scales on Y-doped Ni-7%Cr-6.5%Al were columnar in nature and well adherent, those on Ni-10%Cr-10%Al-0.041%Y (Figs. 1b and 3) spalled despite the RE doping and columnar grain structure. It was found that the presence of excess RE additions can result in the formation of RE-containing phases at the grain boundaries, which act as sites for enhanced oxidation and, more importantly, for initiation of spallation of the surrounding surface alumina scale. This is illustrated in Fig. 3, which is a top-down view of the remnants of the scale grown on the Ni-10% Cr-10% Al-0.041% Y alloy after 100h at 1200°C. In this case, excess Y results in spallation of the scale (resulting in exposed metal) due to the presence of grain-boundary Y-garnet particles in this alloy, as shown in the inset of Fig. 3. Other recent results have shown that overdoping of a Fe_3Al with Y (albeit at a significantly higher concentration than in the present case) also leads to poorer oxidation performance.[5]

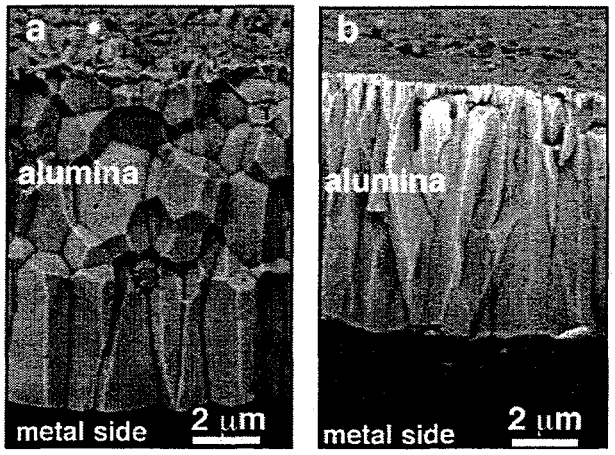

Fig 1. Scanning electron micrographs of cross sections of alumina scales formed on (a) Ni-10%Cr-10%Al-0.006%Y and (b) Ni-10%Cr-10%Al-0.041%Y after 100 h in air at 1200°C.

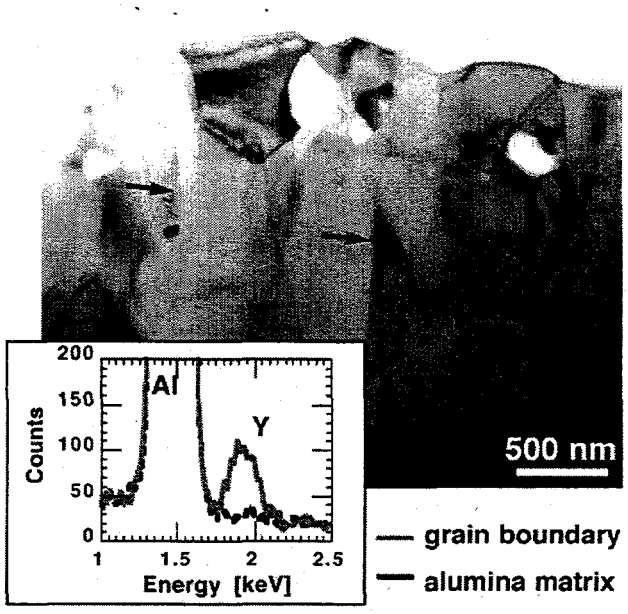

Fig. 2. Transmission electron microscopy of the cross section of an alumina scale formed on Ni-10%Cr-10%Al-0.041%Y after 100 h in air at 1200°C. Preferential yttrium segregation to scale boundaries (indicated by arrows) was detected by use of energy dispersive spectroscopy with high spatial resolution (inset).

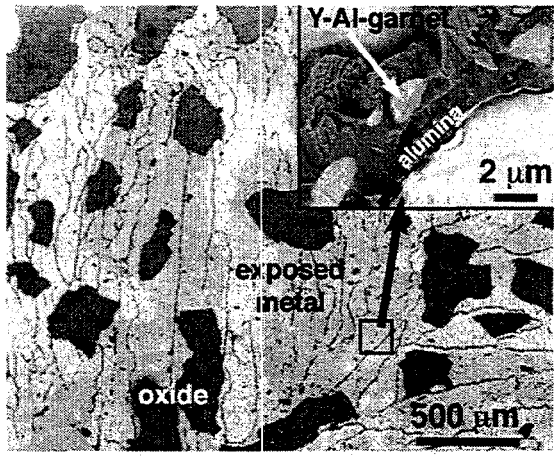

Fig. 3. Scanning electron micrograph showing a top-down view of the surface of Ni-10%Cr-10%Al-0.041%Y after 100 h in air at 1200°C. Exposed metal was visible where parts of the oxide scale spalled during cooling from the oxidation temperature. Yttrium-garnet was found at alloy grain boundaries (inset).

While the RE effect has been known for many years,[1] there have been relatively few detailed electron microscopy studies despite their value in establishing the necessary structure-performance correlations. To this end, the present observations relate the segregation of RE ions at the oxide-metal and oxide-oxide interfaces with scale microstructure and oxidation performance. This and other work indicate that the observations on scale development and failure are applicable to a wide-variety of alloys and coatings that rely on alumina scales for oxidation protection. The results are of relevance for advanced alumina-forming alloys as well as for thermal barrier coating systems in which failure occurs near or at the interface between a metallic bond coat and its thermally grown alumina layer.

EFFECTIVENESS OF REACTIVE ELEMENT IN IMPROVING OXIDATION RESISTANCE OF Fe-Al-Cr ALLOYS IN AIR

Because of previously observed variable oxidation performance and scale failure behavior of Fe_3Al alloys, a series of 96 h experiments were conducted in a variety of gas mixtures to assess the influence of a reactive element on protective alumina formation in the presence of different environmental species. For these experiments, Fe-28%Al-5%Cr (FA186) and Fe-28%Al-5%Cr-0.1%Zr (FAL) were used; it has been shown that the presence of a RE like

Zr results in good scale adherence while FA186 is very susceptible to scale spallation, even after short exposure times.[6,7] Water vapor was added to bottled air and oxygen by bubbling the respective gas through water prior to entering the furnace. A mixed gas of Ar-20%O_2 was used to isolate the effect of nitrogen. The results are summarized in Table 1. At 900°C, there was not much effect of Zr, N or H_2O. At 1000°C, however, FA186 showed twice the weight gain in air compared to Ar-O_2 or O_2. The Zr in FAL consistently reduced the weight gains observed. A similar influence of nitrogen was observed at 1100°C. Microstructural analysis of specimen cross-sections showed some evidence of internal nitridation. At 1200°C, the effect of air versus oxygen was less pronounced, but Zr still consistently reduced the weight gain, indicating a reduction in the alumina growth. Water vapor showed little consistent effect.

The striking effect of nitrogen on the weight change behavior of an Fe-Al-Cr alloy indicates that nitridation can play an important role in explaining the poor oxidation performance of Fe-Al-Cr alloys that do not contain RE additions in the temperature range around 1000-1100°C. However, as shown in Table 1, the addition of 0.1% Zr to FA-186 (to form FAL) eliminates the detrimental effect of nitrogen on the high-temperature corrosion behavior. The present findings therefore underscore the importance of RE dopants in assuring the long-term corrosion resistance of this class of alloys in air by allowing a sound, adherent alumina scale to form and provide protection from substantial reaction with nitrogen.

Table 1. Specimen weight gains after 96 h. All specimens were polished to a 0.3 μm surface finish.

	900°C		1000°C		1100°C		1200°C	
gas:	FA-186	FAL	FA-186	FAL	FA-186	FAL	FA-186	FAL
dry air	0.29	0.41	1.03	0.35	4.56	0.34	2.92	1.47
wet air	0.33	0.36	1.12	0.34	4.50	0.32	2.40	1.35
dry O_2	0.41	0.45	0.55*	0.27*	1.63*	0.39*	3.33*	1.07*
wet O_2	0.43	0.25	0.53	0.30	2.08	0.40	3.11	1.25
Ar-20%O_2	–	–	0.47	0.22	1.25	0.39	11.5	0.96

*average

ACKNOWLEDGMENTS

This research was sponsored by the Fossil Energy Advanced Research and Technology Development (AR&TD) Materials Program and the Division of Materials Sciences, U S. Department of Energy, under contract DE-AC05-96OR22464 with Lockheed Martin Energy Research Corporation.

REFERENCES

1. B. A. Pint, *Oxid. Met.* 45 (1996) 1-37.

2. B. A. Pint, and K. B. Alexander, pp. 153-65 in Microscopy of Oxidation-3, S. B. Newcomb and J. A. Little (eds.), The Institute of Materials, 1997.

3. K. B. Alexander, K. Prübner, and P. F. Tortorelli, pp. 301-12 in *Proc. Eleventh Annual Conf. Fossil Energy Materials*, R. R. Judkins (comp.), U. S. Department of Energy, December, 1997.

4. B. A. Pint, pp. Fundamental Aspects of High Temperature Corrosion, D. A. Shores, R. A. Rapp, and P. Y. Hou, Editors, The Electrochemical Society, Pennington, NJ, 1997.

5. P. F. Tortorelli, B. A. Pint, and I. G. Wright, " High-Temperature Corrosion Behavior of Iron-Aluminide Alloys and Coatings," to be published in *Proc. Twelfth Annual Conf. Fossil Energy Materials,* 1998.

6. P. F. Tortorelli and K. B. Alexander, pp. 247-56 in *Proc. Ninth Annual Conf. Fossil Energy Materials*, N. C. Cole and R. R. Judkins (comp.), U. S. Department of Energy, August 1995.

7. P. Y. Hou, "Kinetics of Sulfur Segregation to Scale-Alloy Interfaces," to be published in *Proc. Symp. on High-Temperature Corrosion and Materials Chemistry*, The Electrochemical Society, 1998.

SOLID-STATE PHASE STABILITIES OF RELEVANCE TO METAL DUSTING IN COAL GASIFIER ENVIRONMENTS

P. F. Tortorelli, J. H. DeVan, R. R. Judkins, and I. G. Wright

INTRODUCTION

The product gas resulting from the partial oxidation of carboniferous materials in a coal gasification system consists predominantly of various proportions of CO, CO_2, H_2, H_2O, CH_4, and, for air-blown units, N_2, at temperatures ranging from about 400 to 1000°C. Depending on the source of the fuel, smaller concentrations of H_2S, COS, and NH_3 can also be present. The gas phase is typically characterized by relatively high carbon and sulfur, but low oxygen, fugacities. Consequently, there are concerns about degradation of gasifier materials by sulfidation or one or more of the several reactions associated with appreciable carbon levels in the environment. These latter processes, which are not necessarily mutually exclusive, include carbon deposition, carburization, metal dusting,[1] and CO disintegration of refractories.[2]

A major materials degradation mechanism associated with CO, CH_4, and the formation of carbon layers is metal dusting.[1] It proceeds by a combination of mechanisms described in detail in references 3-8. Briefly, the high carbon activity in the gas phase provides the driving force for a sequence of processes involving the rapid ingress of carbon into the metallic material leading to supersaturation in the alloy, formation of surface M_3C carbides, and deposition of carbon. The carbon deposition sets the a_c at the metal surface to unity and the carbides (stable only when $a_c > 1$) then decompose to form metal particles and filamentous carbon in the form of a dust that can be carried away by the flowing gas. Pits and holes on affected surfaces often are observed in addition to general metal wastage.

DISCUSSION OF CURRENT ACTIVITIES

Metal dusting for any given material tends to occur in a relatively narrow (100-200°C) segment of the temperature range from 400 to 900°C. The particular temperature window of susceptibility depends on the material, the gas composition, thermodynamic considerations, and kinetics.[1,3,6,7-9] The present work addresses the potential for metal dusting associated with carbon deposition in some typical coal gasification environments using a thermodynamic analysis involving iron-based phase stabilities.

Analysis Procedures

While it is recognized that there are examples of metal dusting phenomena that don't necessarily require formation of a metastable carbide,[3,10] the analysis below assumes that the presence of Fe_3C is a necessary condition for metal dusting of steels. Accordingly, determination of solid-state phase stabilities in different gasifier environments is an important aspect of evaluating the potential for Fe_3C formation and degradation of steels by this process. Equilibrium calculations were performed to determine the phase stabilities of iron-containing reaction products in contact with realistic product gases of air- and oxygen-blown coal gasifiers at 600 and 800°C. The three gas compositions chosen for this analysis are given in Table 1. As will be seen below, the inclusion of two air-blown gas environment cases revealed differences in equilibrium solid-state phase stabilities within the product-gas range covered by this type of gasifier.

Table 1
GAS COMPOSITION AND PRESSURES OF
REFERENCE GASIFIER PRODUCT GASES

	Air-Blown Case I[(a)]	Air-Blown Case II[(b)]	Oxygen-Blown[(c)]
Gas Component		Concentration (vol %)	
CO	23.9	18.0	62.9
CO_2	5.4	8.8	1.3
H_2O	5.5	9.1	0.2
H_2	14.6	16.6	30.8
CH_4	1.4	4.0	0.035
N_2	48.7	42.7	4.4
H_2S	0.03	0.05	0.4
NH_3	0.02	0.3	
Ar/Other	0.6	0.5	
Gas Pressure (bar)	20.3	14.2	28.6

[(a)] Taken from typical product gas specification for M. W. Kellog gasifier (Piñon Pine plant)
[(b)] Taken from typical product gas specification for Foster Wheeler gasifier (Wilsonville plant)
[(c)] Taken from typical product gas specification for a Shell gasifier

The thermochemical calculations were made using HSC Chemistry software (Outokumpu Research, Finland) based on the SOLGASMIX[11] computer program. The program examines essentially all of the possible chemical interactions among the species listed in Table 1 as a function of a given temperature range at the indicated system pressures. The calculations assumed that the mole fractions of the elemental constituents (C, H, O, S, N) composing the reference product gas do not change from point to point in the system (except when carbon deposition occurs), and therefore do not vary with the gas temperature. This assumption appears valid given the typical gasifier conditions of forced convective flow in a closed piping system and limited reaction of the gas with its containment system. For these specific environments, the principal gas-phase chemical reactions that set the relevant elemental fugacities were:

$$2CO\ (g) = CO_2\ (g) + C\ (g) \quad (1)$$

$$CO_2\ (g) + H_2\ (g) = H_2O\ (g) + CO\ (g) \quad (2)$$

$$C\ (s) + 2H_2\ (g) = CH_4\ (g) \quad (3)$$

$$2C\ (s) + O_2\ (g) = 2CO\ (g) \quad (4)$$

$$2H_2\ (g) + O_2\ (g) = 2H_2O\ (g) \quad (5)$$

$$2H_2\ (g) + S_2\ (g) = 2H_2S\ (g) \quad (6)$$

$$N_2\ (g) + 3H_2\ (g) = 2NH_3\ (g) \quad (7)$$

These and all other possible reaction equilibria are considered in determining the levels of stable species. There is a large driving force for carbon deposition; carbon activities significantly greater than 1.0 result when the gasifier products gases (synthesized at higher temperatures) are cooled and equilibrated at 800°C and below.[12]

The solid-state phase stability relationships for iron were initially determined under equilibrium considerations that limited the carbon activity to that of the most stable carbon-containing phase. Since the carbon activity of graphite ($a_c = 1$) is below the equilibrium value in the gas phase necessary for the existence of the most stable iron carbide, Fe_3C, the formation of graphite superseded that of Fe_3C under equilibrium conditions. This is a rather uninteresting case for the present study as Fe_3C-triggered metal dusting would never occur under such circumstances. On the other hand, under conditions where the deposition of solid carbon from the product gas is relatively sluggish, Fe_3C can form, particularly at lower gas temperatures. Accordingly, a second series of calculations focused on phase stabilities when solid carbon formation was suppressed, and this formed the basis for many of the more relevant results shown below.

The H_2S concentrations used in the initial sets of calculations are listed in Table 1 for the given gasifiers. However, the H_2S concentration in a specific gasifier depends on the coal source and hot-gas cleanup system, and such variations will inevitably affect the relative stability of the iron sulfide. Because of this, the solid-state phase stabilities resulting from decreases in the H_2S level from that given in Table 1 for the oxygen-blown case were examined.

The injection of steam into air-blown gasifier environments such as those indicated in Table 1, either as a process requirement or as an attempt to mitigate potential degradation problems, does not eliminate the possibility of carbon deposition but lowers the threshold temperature for solid carbon formation.[12] Such a temperature decrease could prove beneficial by allowing a gasifier to operate above the temperature window for metal dusting of a particular material. However, the point of interest for this paper was to investigate the effect of increasing the steam content of the gas on the phase stability of iron-containing reaction products. This was done by comparing the results for the air-blown Case II vis-à-vis Case I, as the latter environment had a significantly higher H_2O level, as well as by repeating the calculations for Case I when the steam content was doubled.

Results

A thermodynamic driving force for carbon deposition will exist for practically all gasifier systems at some temperature below that attained in the respective partial-oxidation reaction vessels.[12] For all the gas compositions in Table 1, carbon deposition is predicted to occur at about 800°C and below.[12] Therefore, the potential for metal dusting clearly exists for the gas compositions of this study due to the relatively high CO concentrations in the product gases. Based on equilibrium calculations, H_2 will act to offset the extent of carbon deposited through the generation of CH_4 (reaction 3), but this reaction is very sluggish at the temperatures at which carbon deposition occurs.

The stable iron-based reaction products were FeO, $Fe_{0.877}S$ (hereafter denoted in a shorthand manner in the text as FeS), and/or Fe_3C for all the product gas compositions and temperatures examined in this study, and under all the conditions where particular reactions were suppressed based on the assumption of sluggish reaction kinetics (see below). Calculations indicated that nitrogen-containing reaction products with iron would not be expected to form under equilibrium conditions, even under air-blown conditions. The specific results for iron-based phase stabilities under the different conditions defined in Table 1 are presented and discussed below based on whether an air- or oxygen-blown environment was specified.

Air-blown conditions

Under fully equilibrated conditions, phase stability calculations for the two air-blown gasifier cases indicated that FeO was the most stable iron-containing phase at 800°C and both FeS and FeO were stable phases at 600°C - see the first column under "Predominant Phases" in Table 2. When the formation of solid carbon was purposely disallowed (second column under "Predominant Phases"), the results for the air-blown gasifiers were unchanged – FeO and FeS were the principal iron-based phases at 600°C, and FeO alone existed at 800°C. It was only when the reaction to form CH_4 was suppressed along with the one to deposit carbon that the results changed considerably. Referring to the last column in Table 2, at 600°C, Fe_3C and FeS became the predominant phases for the two air-blown cases. At 800°C, however, the phase stabilities differed: Fe_3C was the predominant phase for air-blown Case I, while FeS and FeO were stable for Case II (see Table 2).

Table 2
PREDOMINANT SOLID-STATE PHASES OF IRON WHEN EXPOSED TO REFERENCE PRODUCT GAS COMPOSITIONS

Gasifier System	Temp. (°C)	Predominant Phases		
		Fully Equilibrated	Carbon Deposition Suppressed	Carbon Deposition and CH_4 Formation Suppressed
Air-Blown Case I	600	Graphite, FeO, FeS	FeO, FeS	FeS, Fe_3C
	800	Graphite, FeO	FeO	Fe_3C
Air-Blown Case II	600	Graphite, FeO, FeS	FeO, FeS	FeS, Fe_3C
	800	FeO	FeO	FeO, FeS
Oxygen-Blown	600	Graphite, FeS	FeS	FeS*
	800	Graphite, FeS	FeS	FeS**

* Fe_3C also is stable if $H_2S < 0.2$ vol %
**Fe_3C also is stable if $H_2S < 0.32$ vol %

As noted above, it was of interest to examine the influence of an increased H_2O concentration in the gas phase on the formation of iron-based products for an air-blown gas composition. This was done by including Cases I and II for the air-blown environments as the latter one had a significantly higher H_2O concentration (Table 1). In addition, the H_2O content for the air-blown Case I was increased to 11% without changing any other concentrations. The phase stability calculations, summarized in Table 3, indicated that this increase did not change the results compared to 5.5% H_2O (Table 2) at either 600 or 800°C for the fully equilibrated and carbon-deposition-suppressed conditions. However, when the formation of both solid carbon and CH_4 (reaction 3) was suppressed, increasing the H_2O content changed the stable product at 800°C from Fe_3C to FeO, but had no effect at 600°C, where FeS and Fe_3C co-exist.

Table 3
EFFECT OF WATER VAPOR CONCENTRATION IN AIR-BLOWN CASE I PRODUCT GAS ON THE PREDOMINANT SOLID-STATE PHASES OF IRON

Gasifier System	Temp. (°C)	Predominant Phases		
		Fully Equilibrated	Carbon Deposition Suppressed	Carbon Deposition and CH_4 Formation Suppressed
Air-Blown Case I H_2O = 5.5 vol %	600	Graphite, FeO, FeS	FeO, FeS	FeS, Fe_3C
	800	Graphite, FeO	FeO	Fe_3C
Air-Blown Case I H_2O = 11 vol %	600	Graphite, FeO, FeS	FeO, FeS	FeS, Fe_3C
	800	Graphite, FeO	FeO	FeO

O_2-blown conditions

In the oxygen-blown environment, the oxygen activity is low and the FeS was the only stable iron-based phase regardless of whether the product gas was assumed to be fully equilibrated or the graphite deposition and CH_4 formation reactions were suppressed (bottom two rows, Table 2). The Fe_3C phase was only stable if the H_2S content of the product gas was reduced to below 0.20 vol % at 600°C and 0.32 vol % at 800°C, where, under both conditions, it co-existed with FeS. The iron carbide became the predominant phase at H_2S concentrations below 0.09 vol % and 0.20 vol % at 600 and 800°C, respectively.

Discussion of Results

These thermochemical calculations present a set of boundary conditions under which Fe_3C formation can occur in some representative coal gasifier environments. Given particular assumptions and limitations, a potential does exist for Fe_3C formation. However, a general conclusion based on the present results is that Fe_3C will only form within a rather limited range of environments and temperatures when carbon deposition is suppressed (delayed) and the reaction to form CH_4 (which essentially lowers a_c) is sluggish. Both of these factors are certainly realistic in terms of known kinetic behavior of the product gases as temperature is lowered. Nevertheless, they are not sufficient in all instances. As shown in Table 2, Fe_3C is stable in air-blown gas mixtures under these conditions, but, for Case II, only at lower temperatures (~600°C). Comparison of the air- and oxygen-blown results showed that, even then, Fe_3C will not form when the sulfur activity is above certain levels. Therefore, for gasifier-type environments, the high carbon levels in the gas mixture will not necessarily lead to metal dusting of steel components.

Air-blown conditions - FeO

The results for the air-blown cases indicate that the formation of Fe_3C is precluded thermodynamically under conditions where FeO can exist, a finding that suggests that an oxide scale should be effective in mitigating metal dusting. It is generally known[3,6,7,13,14] that metal dusting can be inhibited by the formation and maintenance of a barrier layer between the gas phase and the reactive solid. Such a barrier would, by definition, be unreactive in the product gas and prevent rapid transport of carbon. While not addressing the carbon-transport properties of FeO, the present results do suggest this oxide would have the necessary thermodynamic stability. The reduction of the oxygen activity of the gas mixture by the relatively high carbon levels that occur when CH_4 formation is suppressed can lead to Fe_3C formation in some instances (Table 2). Oxides of greater thermodynamic stability than that of FeO would, of course, be even better in this regard as they would remain stable to much lower oxygen activities. Indeed, chromia, silica, and alumina appear to have the appropriate thermodynamic (and transport) properties to protect underlying surfaces from reaction with carbon and formation of Fe_3C.[3,6,7,13]

Steam injection could promote the formation of oxide reaction products by increasing the oxygen potential of the gas and may serve to prevent development of Fe_3C. As mentioned above, significant concentrations of water vapor can stabilize FeO rather than Fe_3C on iron or low-alloy steels under gas conditions that normally would lead to formation of the carbide (see the

comparison of Cases I and II in Table 2 and the results in Table 3). This is of particular importance for FeO, which requires a higher partial pressure of oxygen for stability than do the oxides of chromium, silicon, and aluminum. The present results indicate that H_2O additions could provide an overriding effect on Fe_3C formation at higher temperatures (~ 800°C), where the carbon fugacity of the gas is more moderate. However, very large additions would be required at lower temperatures (~ 600°C) to offset the higher carbon levels in the gas that can accrue if solid carbon deposition and CH_4 production fail to keep pace with carbon-forming reactions (such as reaction 1).

O_2-blown conditions - effect of FeS

It is known that the presence of H_2S suppresses the attack of iron and low-alloy steels by metal dusting.[3,6,14,15] The amount of H_2S in the gas phase need not be large – additions on the order of 20-200 ppm can effectively eliminate metal dusting.[3,6,14] This effect is most likely due to an inhibiting effect of H_2S on the carbon deposition rate.[6,8,16,17] However, suppression of the formation of Fe_3C could also play a role. The sulfide reaction product in the air-blown gasifiers was found to co-exist with either the oxide or the carbide (Table 2). In the oxygen-blown case, the oxide was not thermodynamically stable and, because of the relatively high H_2S concentration (1.4 vol %), the FeS existed to the exclusion of Fe_3C. At higher H_2S concentrations, the sulfide effectively supplants the formation of Fe_3C in the same manner as an oxide at higher H_2O concentrations. (Of course, sulfidation can then become the predominant materials degradation problem.) At lower H_2S levels, where FeS co-exists with the carbide, its effectiveness as a barrier to Fe_3C formation will depend on the relative nucleation and growth rates of the products. Because the reaction rate to form iron sulfide is significantly faster than that of iron oxide at 600°C,[18] the stability of iron sulfide in this temperature range could be a significant factor in inhibiting the formation of Fe_3C. Alternatively, sulfur may be incorporated into Fe_3C and effectively stabilize it so that it does not decompose when $a_c = 1$.[3,19]

In light of the discussion of possible effects of sulfide formation, it is interesting to examine the implications of sulfur-removal schemes for solid-state phase stabilities in coal gasification systems. As discussed above, decreasing sulfur levels in the gas mixtures can lead to stabilization of Fe_3C vis-à-vis FeS. A general conclusion from these stability calculations is that removal of H_2S by a hot-gas cleanup system may have less effect on the formation of Fe_3C (and therefore on metal dusting) in air-blown gasifiers than in oxygen ones. The iron oxide phase tended to predominate in the air-blown cases and was less affected by the removal of sulfur,

whereas, in the oxygen-blown gas environment examined here, the iron sulfide phase could provide the only significant barrier to Fe_3C formation.

Summary and Conclusions

Solid-state phase stability calculations for iron-containing products involving some typical gas environments and temperatures of coal gasifiers indicated that FeO, $Fe_{0.877}S$, and/or Fe_3C could form in representative air-blown gasifier systems, while only the sulfide or carbide were stable in the oxygen-blown environment because of the low oxygen activity. Formation of Fe_3C only occurred under limited thermodynamic conditions when certain reactions were suppressed. Assuming Fe_3C is a necessary step in the metal dusting of steels, there are therefore coal gasification systems where this type of carbon-related degradation will not occur, particularly under conditions associated with higher oxygen and sulfur activities such that FeO or $Fe_{0.877}S$ form to the exclusion of the carbide. Such conditions include the use of steam injection to promote the formation of oxide reaction products or high H_2S levels, as determined by the coal source and system design. The removal of H_2S by a hot-gas cleanup system will have less effect on the formation of Fe_3C, and metal dusting, in air-blown gasifiers, where the iron oxide phase exists and is unaffected by the removal of sulfur, than in oxygen-blown environments, where iron sulfide provides the only potential barrier to Fe_3C formation.

ACKNOWLEDGMENTS

The authors thank M. Howell for experimental support. This research was sponsored by the U S. Department of Energy, Office of Fossil Energy, through the Advanced Research and Technology Development (AR&TD) Materials Program under contract DE-AC05-96OR22464 with Lockheed Martin Energy Research Corporation.

REFERENCES

1. R. F. Hochman and J. H. Burson III, "The Fundamentals of Metal Dusting," *API Division of Refining Proc.* 46 (1966) 331-44.
2. J. J. Brown, Jr., "Investigation of Carbon Monoxide Disintegration of Refractories in Coal Gasifiers," Virginia Polytechnic Institute and State University report, VPI/ME-13702-12, July 1984.

3. R. F. Hochman, "Catastrophic Deterioration of High Temperature Alloys in Carbonaceous Atmospheres," *Proc. - Electrochem. Soc.* (1976), Vol. 77-1 (Proc. Symp. Prop. High Temp. Alloys, 1976), pp. 715-32.
4. J. C. Nava Paz and H. J. Grabke, "Metal Dusting," *Oxid. Met.* 39 (1993) 437-56.
5. H. J. Grabke, R. Krajak, and J. C. Nava Paz, "On the Mechanism of Catastrophic Carburization: Metal Dusting," *Corros. Sci.*, 35 (1993) 1141-50.
6. H. J. Grabke, "Metal Dusting of Low- and High-Alloy Steels," Corrosion 51 (1995) 711-20.
7. H. J. Grabke, R. Krajak, and E. M. Mueller-Lorenz, "Metal Dusting of High-Temperature Alloys," *Werkst. Korros.* 44 (1993) 89-97.
8. I. Koszman, "Factors Affecting Catastrophic Carburization and Metal Dusting," pp. 155-67 in High Temp. Gas-Met. React. Mixed Environ., S. A. Jansson and Z. A. Foroulis (eds.), AIME, New York, 1973.
9. L. H. Wolfe, "Laboratory Investigations of High Temperature Alloy Corrosion and Failures," *Mater. Perform.* 17 (1978) 38-44.
10. D. Monceau, E. M. Müller-Lorenz, and H. J. Grabke, "Metal Dusting of Stainless Steels," to be published in Mater. Sci. Forum, 1997
11. T. M. Besmann, "SOLGASMIX-PV, A Computer Program to Calculate Equilibrium Relationships in Complex Chemical Systems," ORNL/TM-5775, Oak Ridge National Laboratory, April 1977.
12. J. H. DeVan, P. F. Tortorelli, R. R. Judkins, and I. G. Wright, "Carbon Formation and Metal Dusting in Advanced Coal Gasification Processes," Oak Ridge National Laboratory report, ORNL/TM-13014, February 1997.
13. D. E. Brown, J. T. K. Clark, A. I. Foster, J. J. McCarroll, and M. L. Sims, "Inhibition of Coke Formation in Ethylene Steam Cracking," pp. 23-44 in Coke Formation on Metal Surfaces, L. F. Albright and R. T. K. Baker, American Chemical Society, 1982.
14. R. A. Perkins, W. C. Coons, and F. J. Radd, "Metal Dusting Corrosion in Coal Gasification Environments," *Proc. - Electrochem. Soc.*, (1976), Vol. 77-1 (Proc. Symp. Prop. High Temp. Alloys, 1976), pp. 733-49.
15. H. J. Grabke, C. B. Bracho-Troconis, and E. M. Mueller-Lorenz, " Metal Dusting of Low Alloy Steels," *Werkst. Korros.* 45 (1994) 215-21.
16. T. F. Berry, R. N. Ames, and R. B. Snow, "Influence of Impurities and Role of Iron Carbides in Deposition of Carbon from Carbon Monoxide," *J. Amer. Ceram. Soc.* 39 (1956) 308-18.
16. T. Kalina and J. A. Kivlen, "Process of Reducing Iron Oxide Ores with Gases Containing Carbon Monoxide," U. S. Patent 3,377,156, April 1968.
17. M. J. Bennett, G. H. Chaffey, B. L. Myatt, and D. R. V. Silvester, "Inhibition by Sulfur Poisoning of the Heterogeneous Decomposition of Acetone," pp. 223-38 in Coke Formation on Metal Surfaces, L. F. Albright and R. T. K. Baker, American Chemical Society, 1982.
18. P. Kofstad, High Temperature Corrosion, Elsevier Applied Science, London, 1988, pp. 428-29.
19. A. Schneider, B. Hüning, G. Inden, and H. J. Grabke, to be published in Mater. and Corr., 1998.

ENVIRONMENTAL ANALYSIS SUPPORT

R. L. Miller

Activities in environmental analysis support included assistance to the Federal Energy Technology Center (FETC) at Morgantown and Pittsburgh in reviewing and preparing documents required by the National Environmental Policy Act (NEPA) for projects selected for the Clean Coal Technology (CCT) Program and for the Low Emission Boiler System (LEBS) Program. An important activity was the preparation of an Environmental Impact Statement (EIS) for a new coal-fired LEBS technology for electric power generation at the proof-of-concept scale adjacent to the Turris Coal Company's existing underground coal mine near Elkhart, Illinois. Another important activity was the initiation of an EIS for a new circulating fluidized bed (CFB) combustor fueled by coal and petroleum coke to repower an existing steam turbine at Jacksonville Electric Authority's (JEA's) Northside Generating Station in Jacksonville, Florida.

ENVIRONMENTAL SUPPORT TO THE LOW EMISSION BOILER SYSTEM PROGRAM

R. L. Miller

Work during this period focused on the preparation for DOE's Federal Energy Technology Center (FETC) of an Environmental Impact Statement (EIS) to evaluate the potential environmental impacts associated with constructing and demonstrating a new coal-fired Low Emission Boiler System (LEBS) for electric power generation at the proof-of-concept scale. The EIS will be used by DOE in making a decision on whether or not to provide cost-shared funding to design, construct, and demonstrate a LEBS technology proposed by a team headed by DB Riley, a private sector participant in the LEBS program. The goal of the LEBS program is to provide the U.S. power industry with a reliable, economic, highly efficient, and environmentally preferred alternative to current coal utilization technologies.

The proposed project would demonstrate the DB Riley technology using a new 80-MW coal-fired power plant to be built adjacent to an existing underground coal mine owned and operated by Turris Coal Company, a member of the project team. The site is situated in central Illinois, about 2 miles southeast of the town of Elkhart and about 17 miles northeast of Springfield. The technology would incorporate the following components: (1) a slagging combustor, which is U-shaped to increase the combustion reaction time; (2) a low-temperature heat-recovery system; (3) low oxides of nitrogen (low-NO_x) burners, staged combustion, and coal reburning (injecting about 10–15% of the coal higher in the combustor) for NO_x control during combustion; (4) a moving-bed, copper-oxide sorption system for sulfur dioxide (SO_2) capture, with ammonia injection for NO_x capture during post-combustion; and (5) a pulse-jet baghouse for particulate removal from the flue gas. The technology is expected to capture over 97% of SO_2 emissions, decrease NO_x emissions by 90%, and remove over 99.7% of particulate matter.

Construction of the proposed facility would begin in late 1998 and continue until mid-2000. The demonstration would be conducted during a 6-month period in late 2000 and early 2001. If the demonstration is successful, commercial operation of the facility would follow immediately; the

lifetime of the plant is projected to be 25 years. The facility would be fueled with coal from the adjacent mine, and electricity generated by the facility would be provided to the mine and to the local power grid. The captured SO_2 would probably be converted to ammonium sulfate which is used to fertilize crops. Other options include converting the sulfur to sulfuric acid or elemental sulfur. Bottom ash is expected to be used by the mine for applications such as construction material.

Potential impacts to environmental resources, including air quality, groundwater, and land availability, that could result from construction and operation of the proposed project were analyzed. Key findings include that emissions from the proposed facility would not exceed National Ambient Air Quality Standards (NAAQS) or Prevention of Significant Deterioration (PSD) increments. For the latter set of standards, the emissions would always be less than 20% of the allowable degradation. The contribution of emissions from the proposed facility to acidic deposition and to global climate change is expected to be negligible.

Initial results indicate that the aquifer may be capable of supporting the additional requirements of groundwater withdrawal during facility operation, but declines in groundwater levels may occur in nearby water supply wells, including the village of Elkhart municipal water well, located approximately 1 mile west of the proposed site. In addition, the relatively large additional consumption could degrade water quality in the aquifer, resulting in increased total dissolved solids, heavy metals, and dissolved minerals. However, the effects of drawdown and groundwater quality degradation can be mitigated somewhat by using multiple wells for groundwater withdrawal with sufficient separation from each other. The DB Riley team currently is evaluating this option. As an alternative, the watershed of a nearby creek could supplement additional groundwater withdrawal.

With the construction of a new coal combustion waste disposal area at the adjacent mine, sufficient disposal capacity would be available to accommodate all solid wastes generated by the proposed facility during its 25-year commercial operation, even if no bottom ash or sulfur by-products are sold or used. If the proposed waste disposal area is not constructed, the Turris Coal Company would have other options to dispose of the material, including (1) reducing the current

level of coal combustion ash received from offsite customers, and (2) transporting solid waste off the site to a permitted landfill.

Impacts to other resource areas would be minor. All onsite water would continue to be recycled for use onsite. Discharges to offsite surface waters would occur only during the infrequent occasions when appreciable rainfall events exceed existing pumping capacities designed to keep all water on the site. Because offsite surface waters would not be used to meet water supply needs, no effects from surface water withdrawal are expected. Flooding at the site is not anticipated, and floodplain encroachment would not occur. There are no significant wetland resources near the proposed site. No appreciable impacts on terrestrial or aquatic ecosystems are expected. There are no historic or archaeological resources known to occur on the project site. Construction and operation of the proposed facility are anticipated to have only minimal impacts on socioeconomic factors in the surrounding area, and no environmental justice impacts are expected. With respect to aesthetic resources, construction of the proposed project would produce slight short-term visual impacts, but visual characteristics would not differ appreciably over the long term from those at the site now. No significant impacts are expected with regard to noise, traffic, land use, and human health including worker safety.

Under the no-action alternative for the LEBS project, no construction activities or changes in operations are expected to occur. There would be no change in current environmental conditions at the site, and the impacts would remain unchanged from the baseline conditions.

ENVIRONMENTAL SUPPORT TO THE CLEAN COAL TECHNOLOGY PROGRAM

R. L. Miller

Also during this period, work began for FETC on an EIS to evaluate the potential environmental impacts associated with constructing and demonstrating a new circulating fluidized bed (CFB) combustor fueled by coal and petroleum coke to repower an existing steam turbine to generate nearly 300 MW of electricity. The EIS will be used by DOE in making a decision on whether or not to provide cost-shared funding to design, construct, and demonstrate the CFB technology under the Clean Coal Technology (CCT) Program. The proposed project would be located at Jacksonville Electric Authority's (JEA's) Northside Generating Station in Jacksonville, Florida, which currently consists of three heavy oil- and natural gas-fired steam generation units and four diesel oil-fired combustion turbine units.

The overall objective of the project is to demonstrate the feasibility of CFB technology at a size that will be attractive for large-scale utility operation. In a CFB combustor, coal and coal/fuel blends, air, and limestone are introduced into the lower portion of the combustor, where initial combustion occurs. As the fuel is reduced in size through combustion and breakage, it is transported higher in the combustor where additional air is introduced. Ash and unburned fuel and limestone pass out of the combustor, collect in a particle separator, and recirculate to the lower portion of the combustor. Sulfur reacts with limestone added in the furnace to form ash that can be marketed as a useful byproduct such as roadbed material. The project is expected to provide JEA with a low-cost, efficient, and environmentally-sound generating resource.

The following issues associated with construction and demonstration of the CFB technology at JEA's Northside Generating Station have been tentatively identified for analysis in the EIS:

(1) Atmospheric Resources: potential air quality impacts resulting from air emissions during current and future operation of Northside Generating Station; potential effects of greenhouse gas emissions on global climate change;

(2) Water Resources and Aquatic Ecology: potential effects on surface water and groundwater resources consumed and discharged; potential effects on estuarine salt marsh ecosystems and aquatic biota resulting from withdrawing and discharging cooling water from the St. Johns River;

(3) Infrastructure and Land Use: potential effects resulting from the transport of coal, petroleum coke, and limestone required for the proposed project, including the development of land for infrastructure, storage, or waste disposal;

(4) Solid Waste: pollution prevention and waste management practices, including solid waste impacts, caused by the generation, treatment, transport, storage, and disposal of solid wastes;

(5) Construction: impacts associated with noise, traffic patterns, and construction-related emissions;

(6) Visual: impacts associated with a new stack that is taller than existing structures at Northside Generating Station;

(7) Floodplains: potential impacts of siting new buildings and infrastructure within floodplain and hurricane storm surge areas;

(8) Wetlands: potential reduction of wetlands due to new construction;

(9) Community Impacts: impacts on public safety related to fire and emergency vehicle access to the Northside community; impacts to local traffic patterns resulting from rail traffic; socioeconomic impacts on public services and infrastructure; noise associated with project operation; environmental justice with respect to the surrounding community; and

(10) Cumulative Impacts: effects of the proposed project added to other past, present, and reasonably foreseeable future actions.

BIOPROCESSING RESEARCH

E. N. Kaufman

This section describes research and development activities performed for the Fossil Energy Bioprocessing Research Program. This program includes fundamental research for coal applications that investigates advanced reactor design for conversion of coal synthesis gas to liquid fuels and investigates how bioprocessing may contribute to CO_2 mitigation options. In addition, the program includes studies on the removal of heteroatoms from heavy oils, renewable hydrogen production, and remediation of oil containing soils. All of these programs apply biological approaches that allow the utilization of our nation's fossil energy reserve in an economical and environmentally more benign manner.

FUNDAMENTAL BIOPROCESSING RESEARCH FOR COAL APPLICATIONS

P. T. Selvaraj and E. N. Kaufman

INTRODUCTION

The purpose of this program is to gain a fundamental understanding and sound scientific technical basis for evaluating the potential roles of innovative bioprocessing concepts for the utilization and conversion of coal. The aim is to explore the numerous ways in which advanced biological processes and techniques can open new opportunities for coal utilization or can replace more conventional techniques by use of milder conditions with less energy consumption or loss.

There are several roles where biotechnology is likely to be important in coal utilization and conversion. These include potential bioprocessing systems such as: conversion of coal synthesis gas to liquid fuels and chemicals, biocatalytic removal of SO_x and NO_x from coal combustion off-gas, environmental control technology for the removal or destruction of hazardous materials in process effluents and/or solid residues, and the removal and utilization of CO_2 from combustion off-gas. Effective bioprocesses for such applications will require detailed knowledge of the biological process mechanisms and advanced bioreactor technology that can be optimized for high productivity, as well as supporting upstream and downstream processes that will allow an effective integrated bioprocess.

DISCUSSION OF CURRENT ACTIVITIES

The efforts in FY 1997-8 have been directed toward 2 primary areas of research: (1) advanced bioprocessing concepts for the **Bioconversion of Coal Synthesis Gas** and (2) **Scoping Analysis Of Biological CO_2 Mitigation Strategies**. These efforts include direct collaboration via subcontracts between ORNL, industry and academia. Progress from these subcontracts is not contained in this report.

Bioconversion of Coal Synthesis Gas

The objective of this task is to study bioreactor concepts for the efficient conversion of coal synthesis gas to liquid fuels and the utilization of coal synthesis gas as a carbon and energy source for bioconversion processes of interest to the coal industry. With large reserves of coal in the United States, coal synthesis gas production will emerge as an important technology in the future. Synthesis gas, primarily a mixture of carbon monoxide (CO), hydrogen (H_2) and carbon dioxide (CO_2) represents an easily obtainable, generic feedstock for the production of fuels and chemicals. Synthesis gas may be obtained directly as a waste gas from many manufacturing processes, or it may be obtained through gasification of any carbonaceous material such as agricultural, municipal, and paper wastes; coal and natural gas; or direct utilization of produced biomass. Conventional processes such as catalytic processes may be used to convert synthesis gas into a variety of fuels and chemicals such methane, methanol and acetic acid. Biological processes have been found to be potentially viable processes and promise to be less costly in producing fuels. In addition, the synthesis gas may also be used as a carbon and energy source for other bioprocessing applications.

A gas mixture containing 36% H_2, 47% CO, 10% CO_2, 5% CH_4 and balance N_2 as a model coal synthesis gas was utilized in these studies. This composition is typical of an oxygen blown, coal fed gasifier. Initially, with development of mixed SRB culture using the syn-gas as sole carbon and energy source, a stirred tank and trickle bed reactors were operated with syn-gas fed as gaseous feed. The mass transfer characteristics were determined under these conditions. Following this, the syn-gas has been fed as microbubbles to enhance the mass transport properties. Due to low solubility of syn-gas in aqueous phase, mass transfer was a key factor in this operation. Therefore, feeding syn-gas as microbubbles was considered to enhance the mass transport properties. The syn-gas microbubbles (50-80 μm, surfactant stabilized) were produced in a microbubbles generator by spinning a disk at 5000 rpm with syn-gas bubbling into a minimal salt medium containing Tween 20 surfactant.

In synthesis gas conversion to liquid fuel, *Clostridium ljungdhalli* have been shown to convert syn-gas to ethanol. In our previous study, with biocatalyst development, a continuously

stirred tank reactor (CSTR) and trickle bed reactors (TBRs) were operated with syn-gas feed stock. Reactor conditions such as pH, temperature, and agitation rate were monitored to obtain maximum ethanol production. Preliminary mass transfer experiments were conducted in these reactors with syn-gas feed as is. Microbubble feed of syn-gas has been considered to improve the mass transport properties. In addition, organic solvent systems were considered to enhance mass transport properties as the syn-gas is more soluble in some organic solvents than aqueous media. Preliminary experiments were conducted in serum bottles with several organic solvents for initial screening for better solubility and biocompatibility. A TBR has been operated with solvent system as a comparative study.

Mass Transfer in Continuous Stirred Tank Reactor (CSTR) with Sulfate Reducing Bacteria (SRB)

The mass transfer study in CSTR for SO_2 reduction using mixed SRB culture with syn-gas fed as is into the reactor was repeated to verify the previous experiment results. The syn-gas feed rate was varied with constant flow rate of SO_2 maintaining at 80% of the reactor's maximum conversion capacity. The syn-gas utilization was determined for each syn-gas flow rate. The mass transfer coefficients for H_2 and CO were 75.5 d^{-1} and 30.3 d^{-1}, respectively, which are very close to the previous values of 74.6 d^{-1} and 30.6 d^{-1}. These values make sense due to the fact that the diffusion coefficient of H_2 is twice that of CO and is directly proportional to mass transfer coefficient. The mass transfer data are valuable to have in terms of process scale up for commercial applications.

In the microbubble-sparged mass transfer study, the system was brought to a maximum productivity of 3 g/(L*d) and maintained for a two days. The microbubble generator replaced the liquid recycle bottle, and the synthesis gas was then added to the reactor as microbubbles. The synthesis gas flow rate to the reactor remained constant at 10 mL/min in order to obtain a maximum productivity using microbubble sparging. The flow rate of SO_2 was incrementally increased over a period of 24 hours until a maximum productivity was obtained with microbubble sparging. The maximum reactor productivity obtained using microbubble sparging is similar to that obtained in our previous work of 3.8 g/(L*d) using a sewage digest medium,

which is considered a soluble substrate. This indicates that at the maximum reactor productivity using microbubble-sparging might no longer be in the mass transfer limited regime. These results also provide more evidence that the CSTR under conventional sparging was in the mass transfer limited regime. By keeping the flowrate of the gaseous substrate constant and only decreasing the average bubble size into the reactor, a 2-fold improvement in the maximum productivity was obtained.

To obtain the mass transfer coefficients using microbubble sparging, the same approach as conventional sparging was used. Due to the difficulty of maintaining long-term (more than 2 or 3 days) high productivity microbubble-sparged fermentations, only two data points have been obtained for the evaluation of K_La values. Using those two data points that were obtained, an estimate of the K_La value for CO was 104 h^{-1} and for H_2 was 190 h^{-1}. These numbers represent a 3.4-fold increase for CO and a 2.6-fold increase for H_2 with a H_2/CO ratio of 1.85. These numbers compare well with the mass transfer coefficient determined by others of 91 h^{-1} for CO in a microbubble-sparged fermentation. They obtained a 6-fold improvement in K_La over conventional sparging at 200 rpm. A comparable 4-fold increase in K_La was obtained in a microbubble-sparged aerobic *Saccharamyces cerevesiae* fermentation. These numbers are comparable, regardless of impeller speed, because the volumetric mass transfer coefficients from microbubbles have been shown to be independent of impeller rate. Microbubbles are created in such a high shear environment, that higher impeller rates would not further increases the breakup of microbubbles.

Microbubbles are ideally suited for use in this type of fermentation, where the cost of power can be a significant portion of manufacturing costs. Since microbubbles are generated in small vessels, the power consumption is small, (0.01 kW/m^3 of fermentation broth to generate microbubbles for a synthesis gas fermentation). Relatively high power inputs are required in large-scale fermentations in conventionally sparged fermentations, but for microbubbles, only enough power to the main reactor is required to provide adequate liquid mixing.

Syn-gas Conversion to Ethanol in a CSTR

The schematic diagram of a CSTR for syn-gas conversion into liquid fuels is shown in Fig. 1. A viable, ethanol-producing strain of *Clostridium ljungdahlii* has been used in stirred tank and trickle bed fermenters. The cultures were grown and maintained on a phosphate-buffered basal salts media with a synthetic syn-gas feedstock. The gas headspace and liquid products were measured using gas chromatography. Biomass was measured using optical density.

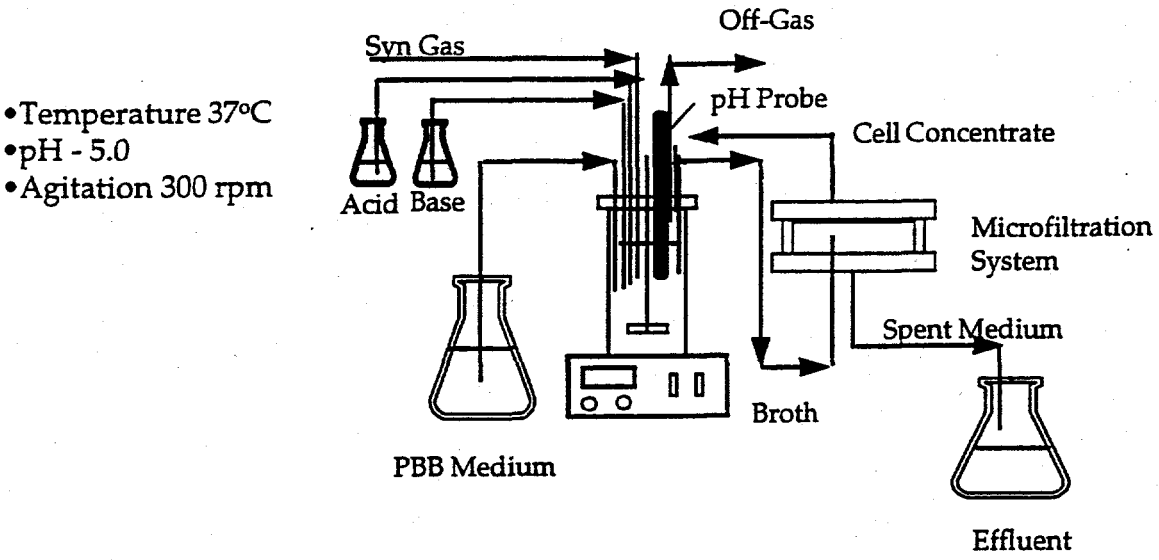

Figure 1: Schematic diagram of a CSTR for syn-gas conversion into liquid fuels

A 1-L continuous stirred tank reactor was started by inoculating 10% by volume of an actively growing serum bottle culture. The reactor was maintained in a fed-batch mode (without nutrient feed) until significant cell concentrations and syn-gas component uptake rates were obtained. The system was then fed a continuous feed of the phosphate buffered basal media which had been enhanced to support higher levels of growth expected to be found in the reactor. A total cell recycle was achieved using a tangential filter. The system was brought to steady-state after several weeks of operation. The liquid and gas retention time in reactor were 83 h and 1.23 h, respectively. Figure 2 shows the reactor performance for that period of time in terms of cell concentration and conversion of syn-gas components.

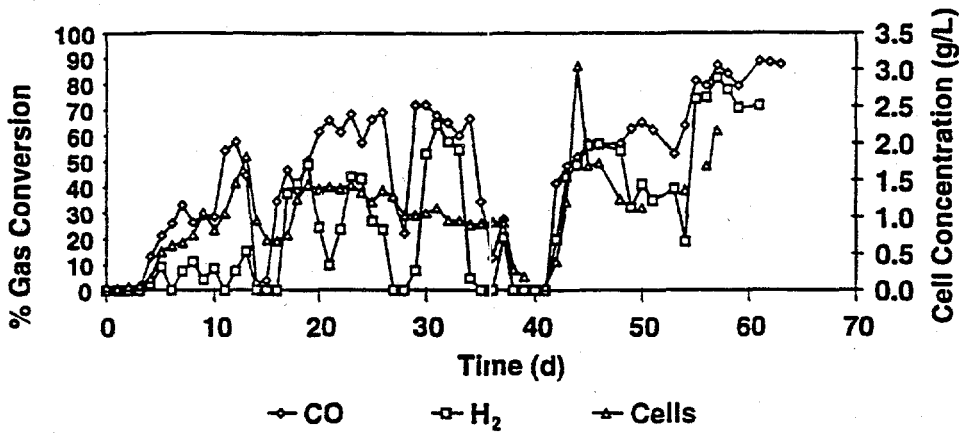

Figure 2: Reactor performance for CSTR

The liquid-phase products varied over time with the maximum ethanol concentration obtained being 6.1g/L with an acetate to ethanol ratio of 2.4. The maximum acetate concentration obtained was 20.5 g/L with an acetate to ethanol ratio of 5.6. The CSTR was run at a pH of 5.1. Volumetric mass transfer coefficients for CO and H_2 have been obtained for the 1 L reactor by varying the inlet gas flow rate and monitoring conversion. The K_La value CO was 64.6 h^{-1} and the K_La value for H_2 was 146.7 h^{-1} at 300 rpm. Though the H_2 is less soluble than CO, the K_La value for H_2 was higher than CO (the H_2/CO ratio for the K_La was 2.27) which might be due to the higher diffusion coefficient of H_2 than CO. The ratio of the diffusion coefficients for H_2/CO is 1.93.

Syn-Gas Conversion to Ethanol in Trickle Bed Reactor

A trickle bed reactor with cell immobilization increases mass transport properties of substrates to biocatalyst and volumetric productivity due to high cell density. A trickle-bed reactor was developed by attaching a packed bed of BIO-SEP beads (50%-80% activated carbon in polyaramid) to a fed-batch stirred tank with an actively growing culture of *C. ljungdahlii*. The cells were allowed to run in trickle flow through the column for a period of three weeks prior to detaching the stirred tank reactor. The columnar reactor with clostridium immobilized in polymeric porous beads was then operated as a trickle bed reactor with liquid phosphate buffered basal (PBB) medium and syn-gas fed concurrently from top of the column (Figure 3).

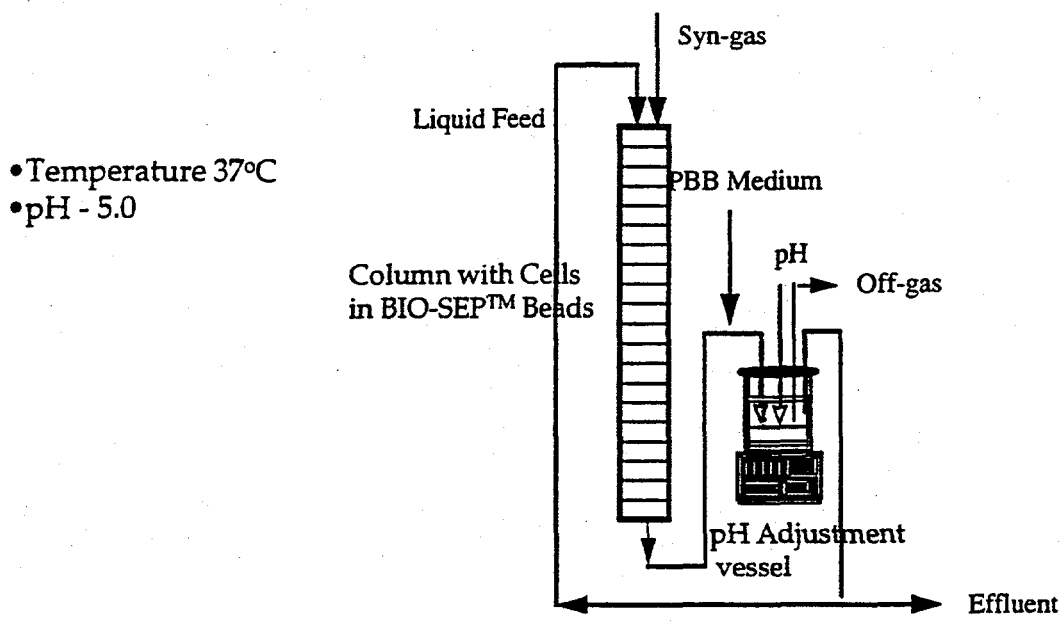

Figure 3: Schematic diagram of a trickle bed reactor for syn-gas conversion into liquid fuels

The effluent from the reactor was pH adjusted to 5.0 and recirculated at 10 mL/min into the column. The liquid and gas residence times in the column were 3.4 h and 0.14 h, respectively. Figure 4 shows the syn-gas utilization in trickle bed reactor.

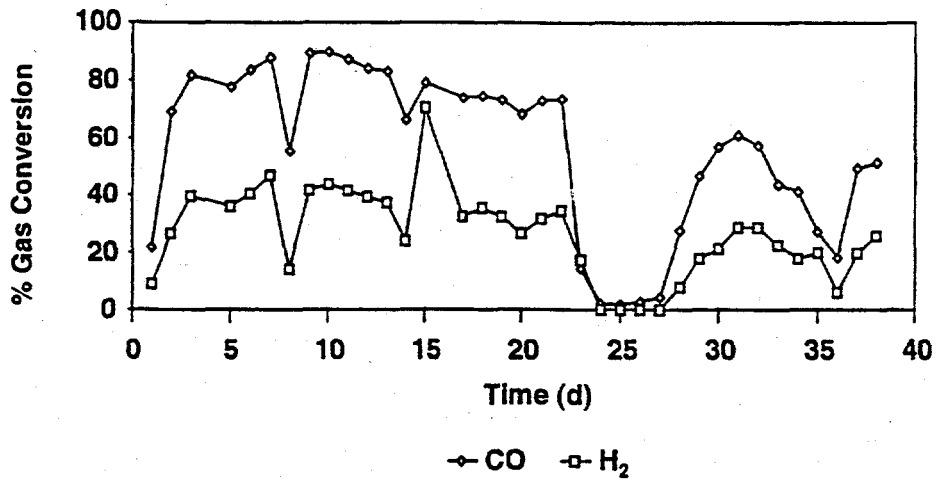

Figure 4: Performance of the TBR

The maximum ethanol concentration obtained in the trickle bed was 2.3 g/L with an acetate to ethanol ratio of 4.8 and the maximum acetate concentration was 12.6 g/L with an acetate to ethanol ratio of 8.3.

The results are summarized in Table 1.

Table 1. Results Summary

Reactor Configuration	LRT (h)	GRT (h)	CO Utilization (%)/(moo/h*L)	H_2 Utiization (%)/(mmol/h*L)	Kla CO (h^{-1})
CSTR with Micrfiltration	83	1.23	65/9.2	50/5.7	58
TBR with BIO-SEP Beads	3.4	0.14	80/46.5	40/17.8	130

Mass Transfer Study in Trickle Bed Reactors

A second trickle bed reactor similar to the first one was set up to study the syn-gas utilization with solvent systems. Prior to the addition of solvent to the reactor, the mass transport characteristics of the two reactors have been determined. The resulting K_La values that were determined for TBR #1 and TBR #2 were 130 h^{-1} and 143 h^{-1}. These numbers indicate a 2.5 fold increase in the volumetric mass transfer coefficient over a stirred tank. The similarity of the two K_La values measured indicate that amount of biomass in the reactor, and subsequently the age of the reactor, was independent of the mass transfer in the system. This shows that the TBR reactors still operate in a mass-transport limited method of operation and can have further advances to increase the mass transfer.

Presently, the second TBR reactor is operated with hexadecane solvent in an effort to study mass transfer enhancement with organic solvent system. The results will be compared with first TBR reactor.

Solvent Systems

Several organic solvents are known to have better solubility for H_2 and CO than water. In our study, several other organic solvents such as Heptane, Decane, Dodecane and Hexadecane

were selected based on syn-gas solubility. Biocompatibility studies for our process culture *Clostridium ljungdahlii* were performed in serum bottles with the above organic solvents. *Clostridium ljungdahlii* was grown in serum bottles containing phosphate-buffered basal salts media. Solvents were used in three different concentrations (v/v): 2.5%, 5.0% and 10.0%. Bottles were sparged with synthesis gas. A 5.0% (v/v) inoculum was used for each bottle. Bottles were incubated at 37°C in an orbital shaker. Synthesis gas component uptake, biomass concentration, and liquid-phase products were monitored. Biocompatibility studies with Heptane, Decane and Dodecane showed that these solvents were inhibitory to the growth of the biocatalyst. There was a very small increase in optical density in the serum bottles containing these solvents when compared to the control bottles. This data correlated with no ethanol production when liquid-phase products were monitored. Also, there was no uptake of synthesis gas by the biocatalyst. Biocompatibility studies with Hexadecane showed promising results for synthesis gas utilization by the biocatalyst. *Clostridium ljungdahlii* has a higher uptake rate of syn-gas in Hexadecane than in the control. This has been supported by increase in liquid products such as ethanol and acetic acid. Higher syn-gas uptake has been observed in 2.5% and 10% C16 serum bottles than in the 5.0% serum bottle. The experiment is being repeated with same cell concentration in all serum bottles to confirm the above results.

Future Work:

Both CSTR and TBR reactors will be operated with microbubble syn-gas feed to enhance the mass transport properties. Solvent system studies will be conducted in detail in serum bottles, batch stirred tank and TBR reactors. Research has been focused to demonstrate the CO_2 utilization by *Clostridium ljungdahlii* culture with an object of controlling CO_2 emission.

Scoping Analysis of Biological CO_2 Mitigation Strategies

In collaboration with our colleagues at Idaho National Engineering and Environmental Laboratory, we are conducting preliminary research into how bioprocessing may affect coal derived CO_2 mitigation. The following topics are being investigated.

Biological Production of Commodity Chemicals and Fuels from Carbon Dioxide: Many commodity chemicals and fuels are manufactured from petroleum feedstocks. There are, however, potential alternative approaches to manufacturing many of these commodity fuels and chemicals through biologically based processes that photosynthetically use the energy from sunlight to split water into hydrogen and oxygen. The hydrogen is then used to provide the reducing power necessary to fix atmospheric carbon dioxide into a desired chemical or fuel.

A number of different products could be potentially made via this type of process. One of the more interesting is the biosynthesis of ethylene using genetically engineered cyanobacteria (i.e. blue-green algae). Preliminary work done in Japan indicates that this process may be feasible. Furthermore, ethylene surpasses all other organic chemicals in the amount produced and sold since it serves as a primary intermediate feedstock for production of dozens of derivative chemicals and fuels such as ethanol. As a result, calculations performed by the authors have demonstrated that up to 5% of the carbon dioxide from coal combustion could be potentially bioconverted to ethylene in the U.S.

Whitings as a Potential Mechanism for Controlling Atmospheric Carbon Dioxide Concentrations: Whitings are biologically-associated formations of white, turbid clouds of fine mud-very fine grained calcium carbonate crystals that have been observed in a variety of shallow salt water seas and large fresh water lakes. It is believed that the White Cliffs of Dover and the Bahama Banks were deposited over geological time as a direct result of this phenomenon. While whitings have been often noted in a variety of locations, they are poorly understood. It has been determined, however, that they are associated with the growth of cyanobacteria (i.e. blue-green algae) such as *Synechocystis*. In addition, carbon and nitrogen concentrations as well as alkalinity and light are apparently important variables contributing to whiting formations. It is believed that under the correct conditions, the cyanobacteria produce an extracellular polymer that serves to enucleate the growth of $CaCO_3$ crystals from bicarbonate dissolved in the sea or lake water. Whitings appear to be self -propagating until a decline in the cyanobacterial population or a change in alkalinity halts the process. Typically, whitings last one to two weeks. Most if not all of the $CaCO_3$ formed during a whiting are believed to precipitate and be trapped in bottom sediments.

Preliminary studies indicate that whitings are capable of sequestering large amounts of atmospheric carbon dioxide. Experimental data have demonstrated that whitings are capable of sequestering approximately 1.2 X 10^5 kg $CaCO_3/km^2$ per day. Based on this information, calculations by the authors have shown that the carbon dioxide from a relatively large coal-fired power plant could be fixed by a whiting sustained over approximately 20 km^2. As a result, a sustained whiting could sequester a large amount of carbon dioxide using a relatively small amount of ocean/lake surface area.

Biological Utilization of "Raffinate" Synthesis Gas in the Conversion of CO_2 to Fuels and Chemicals: Synthesis gas components that are not completely separated by ceramic membranes following the water gas shift reaction at a Vision 21 coal plant (see Figure) could be utilized as a low value energy source in the bioconversion of carbon dioxide fuels and chemicals. The production of ethanol from this waste stream would serve not only to fix a small portion of power plant CO_2, but will also contribute to CO_2 mitigation through the displaced use of gasoline. The stoichiometry of the reaction for the formation of ethanol is:

$$6H_2 + 2CO_2 \rightarrow C_2H_5OH + 3H_2O$$

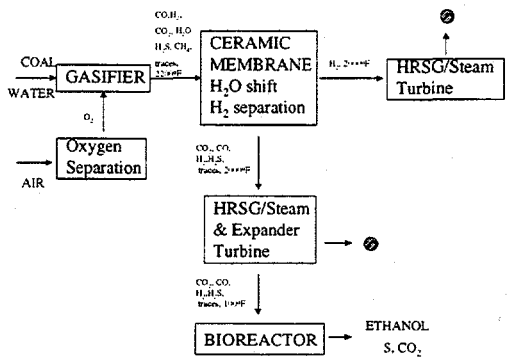

Vision 21 coal plant with integrated biological CO_2 conversion process.

Thus a small, but nevertheless measurable amount of CO_2 would be fixed. While on the surface this may seem like an unacceptable hydrogen cost, the hydrogen may have little other utility due

to its low concentration in the raffinate stream, Assuming a membrane efficiency of 95%, this process could fix 2% of the coal plant CO_2, with a revenue of $135/ton of CO_2 fixed.

Sequestration of Carbon Dioxide by Enhanced Growth of Open Ocean Microalgae: Microalgae grow in shallow, surface zones throughout the world's oceans. They gain their cellular energy from sunlight through photosynthesis and their cellular carbon by fixing (i.e. biochemically reducing) carbon dioxide. There is considerable evidence to show that upon the death of these microalgae, a significant portion of their biomass sinks into the deep ocean. There, the reduced carbon present in the algal biomass apparently undergoes natural cycling into relatively permanent sequestration, possibly, at least in part, in the form of methane hydrates.

Research has shown that in many instances the concentration of microalgae is relatively low in open oceans. More recent research has demonstrated that a primary reason for this sparse density is the lack of nutrients, especially iron. Experiments have shown that when the open ocean is seeded with iron in the form of ferrous sulfate, algae densities increase several fold for 3-4 days after which the newly formed algal biomass sinks from the surface zone, with algal densities re-equilibrating to levels similar to those noted prior to iron seeding.

These observations have led to considerable speculation that algal induced deep ocean sequestration is a major natural mechanism for the removal of carbon dioxide from the atmosphere. Further, it has been hypothesized that this phenomenon may be controlled and enhanced to increase the rates of open ocean algal carbon dioxide fixation and sequestration through the application of iron and other nutrients to open ocean waters.

ACKNOWLEDGMENTS

This work was supported by the Advanced Research and Technology Development Materials Program of the Office of Fossil Energy, U.S. Department of Energy under contract DE-AC05-96OR22464 with Lockheed Martin Energy Research Corp.

REFERENCES

M.D. Bredwell, P.T. Selvaraj, M.H. Little, R.M. Worden and E. N. Kaufman, "Biological Reduction of Sulfur Dioxide with Coal Synthesis Gas as a Feedstock: Improving Reactor Productivity Through Enhanced Mass Transport" 1998, *Biotechnology Progress*. (submitted for publication).

P.T. Selvaraj, M.H. Little, and E.N. Kaufman, "Analysis of immobilized cell bioreactors for desulfurization of flue gases and sulfite/sulfate laden waste water." 1997, *Biodegradation*. **8**: 227-236.

P.T. Selvaraj, M.H. Little, and E.N. Kaufman, "Biodesulfurization of flue gases and other sulfite/sulfate waste streams using immobilized mixed sulfate reducing bacteria." 1997, *Biotechnology Progress*. **13**: 583-589.

P.T. Selvaraj, M.D. Bredwell, M.H. Little, and E.N. Kaufman, "Biodesulfurization of flue gases using synthesis gas delivered as microbubbles." 1997, *American Chemical Society* Division of Fuel Chemistry. **42:** 755-760.

E.N. Kaufman and B.E. Dale, "Emerging Topics in Industrial Biotechnology." 1997, *Applied Biochemistry and Biotechnology*. **63**: 625-626.

E.N. Kaufman, M. H. Little, and P.T. Selvaraj, "A Biological Process for the Reclamation of FGD Gypsum Using Mixed Sulfate-Reducing Bacteria with Inexpensive Carbon Sources." 1997, *Applied Biochemistry and Biotechnology*. **63**: 677-693.

REMOVAL OF HETEROATOMS AND METALS FROM HEAVY OILS BY BIOCONVERSION PROCESSES

A. P. Borole and E. N. Kaufman

INTRODUCTION

Biological removal of organic sulfur from crude oil offers an attractive alternative to conventional thermochemical treatment due to the mild operating conditions afforded by the biocatalyst. In order for biodesulfurization to realize commercial success, reactors must be designed which allow for sufficient liquid/liquid and gas/liquid mass transfer while simultaneously reducing operating costs. To this end, we have investigated the use of electro-spray reactors (Figure 1.) for the desulfurization of the model compound dibenzothiophene (DBT) as well as actual crude oil. The electro-spray reactor (ESR) creates an emulsion of aqueous biocatalyst (5 - 20 μm diameter droplets) in the organic phase by concentrating forces at

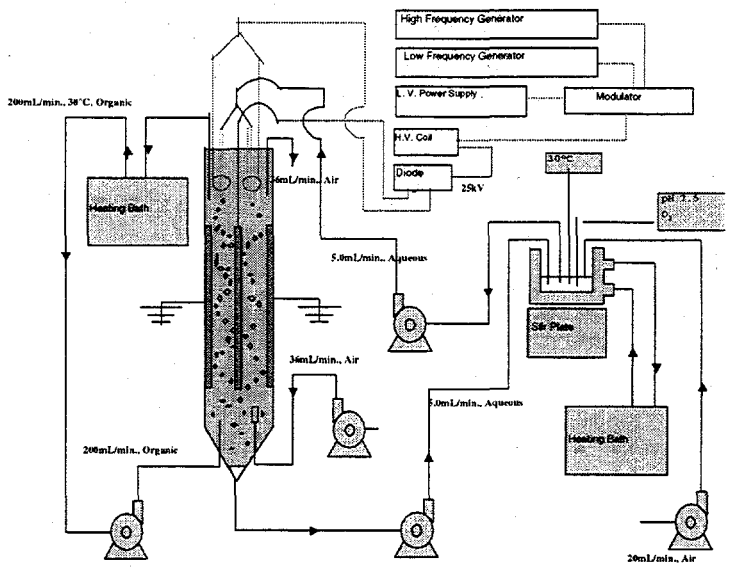

Figure 1. Schematic diagram of the electro-spray reactor and ancillary equipment.

the liquid /liquid interface rather than imparting energy to the bulk solution as is done in impeller mixed reactors. This reactor is being explored for its application in biodesulfurization of crude oils.

This program is a cooperative research and development program with the following companies: Baker Petrolite, Chevron, Energy BioSystems Corporation (EBC), Exxon and Texaco. EBC has provided two biocatalysts including their proprietary biocatalyst UGA41597 and the wild-type *Rhodococcus* species IGTS8 for desulfurization experiments. Exxon has also provided their proprietary biocatalyst, an *E. coli* DH5 alpha host organism carrying dszC gene (similar to that in IGTS8, Figure 2.) capable of converting DBT to DBT sulfone. Texaco has provided analytical support and crude oil for the experiments. Baker Petrolite has provided chemicals and demulsifier kits for studying post-reaction demulsification.

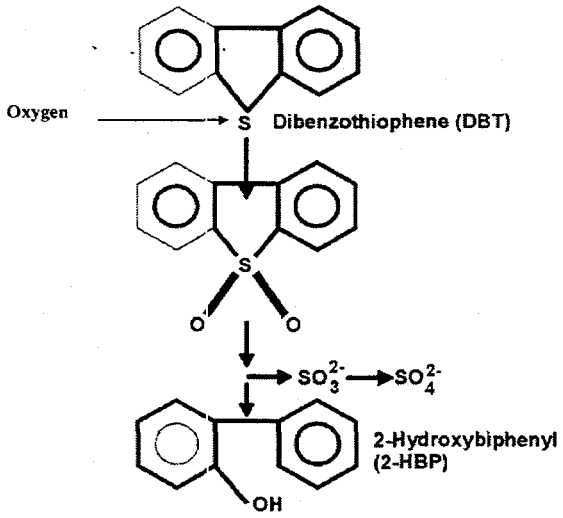

Figure 2. Biochemical mechanism of desulfurization by *Rhodococcus* sp. IGTS8.

DISCUSSION OF CURRENT ACTIVITIES

Biodesulfurization experiments were conducted in the ESR and BSR with UGA41597 biocatalyst to evaluate oxygen mass transfer limitations, effect of organic:aqueous phase ratio and effect of

biocatalyst density on rate of DBT oxidation. It was found that oxygen transport was not a limiting parameter in either the ESR or the BSR. Increasing the biocatalyst density in BSR resulted in lower rates of desulfurization, suggesting a mass transfer limitation. Evaluation of gas-liquid mass transfer at high biocatalyst densities revealed that oxygen mass transfer was not a limiting factor. In order to explore the liquid-liquid mass transfer limitation, experiments were conducted in the ESR, which presumably provides higher surface area than the BSR. Contrary to our expectations, comparison of the ESR with the BSR showed equal rates. In order to determine whether the ESR really provides larger surface area than BSR, emulsions formed in the two reactors were characterized using microscopy techniques. It was found that an equally fine emulsion (~ 5 micron droplets) was formed even in the BSR in the presence of the UGA41597 biocatalyst (Figure 3). Production of biosurfactants has been reported earlier for *Rhodococcus* species in the presence of hexadecane, which was the organic medium used in these experiments. Presence of biosurfactants in the two-phase mixture may have resulted in formation of the fine emulsion observed in the BSR. Additionally, the biocatalyst was found to be extracted into the organic phase, which may be an additional factor why ESR did not show improved performance over BSR. Subsequent experiments with the other EBC biocatalyst, IGTS8, revealed similar observations.

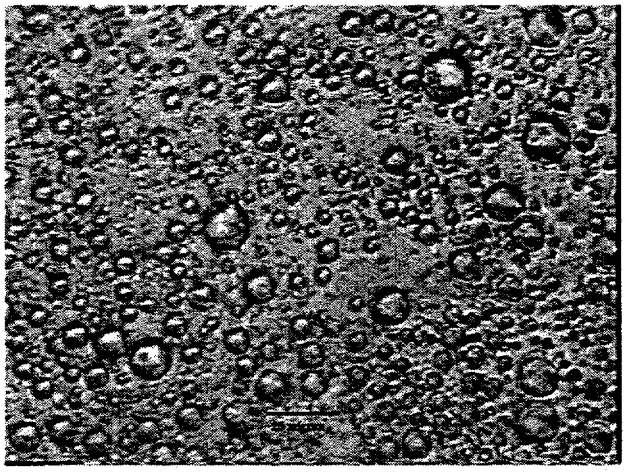

Figure 3. A photomicrograph of an emulsion sample collected from a BSR.

Experiments were also conducted with Exxon's *E. coli* biocatalyst in BSR and ESR. *E.coli* is a gram negative organism which interacts differently with the aqueous and organic phases compared to *Rhodococcus*, a gram positive organism. BSR experiments with *E. coli* showed formation of a coarse emulsion (~ 100 micron droplets) which separated easily once agitation was stopped. The rate of the *E. coli* biocatalyst was, however, lower than that of IGTS8. Due to the low activity of this biocatalyst, rate measurements could not be made in ESR.

Aqueous hold-up measurements were made in the ESR using ultrasonic techniques and Karl Fisher moisture titration. Results indicated 0.3% aqueous hold-up in the plate region of ESR and 1.0% hold-up in the nozzle region, for the hexadecane-aqueous system in the absence of biocatalyst. In crude oil system (API gravity 22°); however, aqueous hold-up ranged from 4.8 to 7.6% with or without biocatalyst present.

An ideal biocatalyst would be capable of high desulfurization rates while enabling easy and fast separation of the biocatalyst and the aqueous phase subsequent to the reaction. Since such a biocatalyst is not presently available, efforts are being focussed on other issues such as development of ESR for processing heavier crude oils. Experiments are also being conducted with the UGA41597 biocatalyst and DBT spiked-crude oils to determine if ESR performs similar to BSR (in terms of desulfurization rates) with actual crude oils as observed in model systems.

Future experiments with heavy crude oils will require good analytical techniques to determine the extent of desulfurization and degradation of complex hydrocarbon molecules. A Gas chromatograph method has been developed to characterize the carbon and sulfur compounds using simultaneous flame ionization and sulfur chemiluminiscence detection, respectively. A sample chromatogram for Sand Flat crude oil is shown in Figure 4. The capability to conduct such analysis in-house will be extremely useful to conduct rapid screening of various biocatalysts for desulfurization as well as upgrading of a range of crude oils.

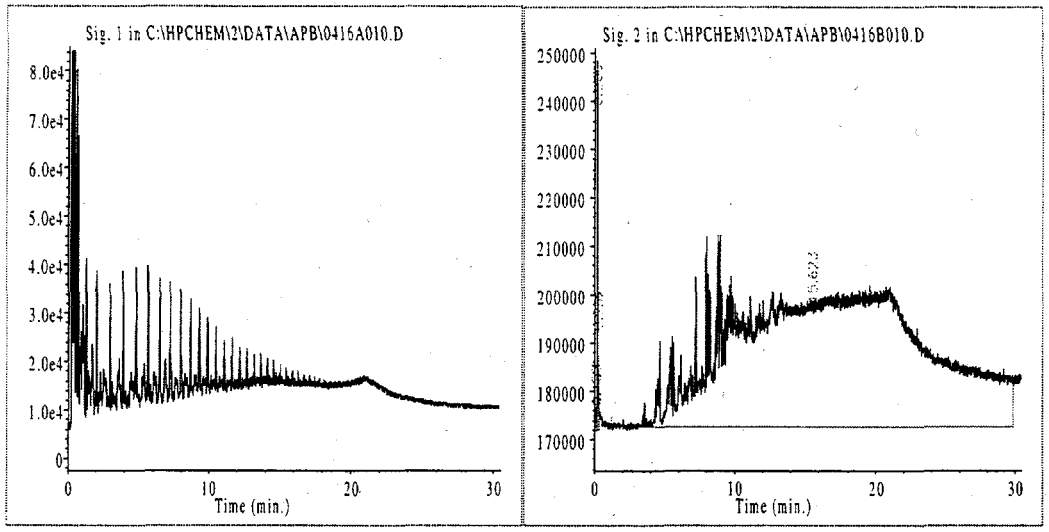

a) carbon compounds (GC_FID), b) sulfur compounds (GC_SCD).

Figure 4. Gas chromatogram of Sand Flat crude oil

ACKNOWLEDGMENTS

This work was supported by the Office of Oil & Gas Processing, U.S. Department of Energy under contract DE-AC05-96OR22464 with Lockheed Martin Energy Research Corp.

REFERENCES

Tsouris, C.; Kaufman, E. N. and Borole, A. P; "Hydrodynamic behavior of an electrically driven bioreactor for oil desulfurization," submitted for publication in *Ind. & Eng. Chem. Res.*

Kaufman, E. N.; Harkins, J. B. and Borole A. P.; 'Comparison of electro-spray and batch stirred reactors for biodesulfurization of dibenzothiophene in crude oil and petroleum feedstocks,' accepted for publication in *Appl. Biochem. Biotech.*

Kaufman, E. N.; Borole, A. P.; Shong, R. G.; Sides, J. L.; and Juengst, C. L.; 'Sulfur specificity in bench-scale biological desulfurization of crude oil by *Rhodococcus IGTS8*,' accepted for publication in *Appl. Microbiol. and Biotech.*

Borole, A. P. and Kaufman E. N.; "Electro-spray vs batch stirred reactors for biodesulfurization of dibenzothiophene in crude oil," a paper was presented at the *American Institute of Chemical Engineers* conference at Los Angeles in November 1997.

Borole, A. P. and Kaufman, E. N.; "Bioreactor Design for Crude Oil Bioprocessing," a poster presented at the *American Chemical Society* conference in San Francisco in May 1997.

RENEWABLE HYDROGEN PRODUCTION FOR FOSSIL FUEL PROCESSING

E. Greenbaum and J. W. Lee

INTRODUCTION

This mission-oriented research project is focused on the production of renewable hydrogen for fossil fuel processing. We have demonstrated (Greenbaum, 1980) that certain unicellular green algae are capable of sustained simultaneous photoproduction of hydrogen and oxygen by light-activated photosynthetic water splitting. It is the goal of this project to develop a practical chemical engineering system for the development of an economic process that can be used to produce renewable hydrogen. There are several fundamental problems that need to be solved before the application of this scientific knowledge can be applied to the development a practical process: (1) maximizing net thermodynamic conversion efficiency of light energy into hydrogen energy, (2) development of oxygen-sensitive hydrogenase-containing mutants, and (3) development of bioreactors that can be used in a real-world chemical engineering process. We are addressing each of these problems here at ORNL and in collaboration with our research colleagues at the National Renewable Energy Laboratory, the University of California, Berkeley, and the University of Hawaii.

CURRENT STATUS OF THE RESEARCH

During the current year, we have made progress in understanding the limiting aspects of the production of molecular hydrogen and oxygen via light-activated microalgal water splitting. We have focused on item 1 above, an investigation of maximizing the net thermodynamic conversion efficiency of light energy into hydrogen energy. In particular, we have focused on the question of how many light reactions are required to split water to molecular hydrogen and oxygen. We recently reported (Greenbaum et al., 1995; Lee et al., 1996) that certain mutants of the green algal *Chlamydomonas reinhardtii* that lack detectable levels of the Photosystem I reaction center were capable of simultaneous photoproduction of molecular hydrogen and oxygen, photoassimilation of atmospheric carbon dioxide and photoautotrophic growth. Although the absence of PS I in mutants B4 and F8 for the data reported in the references was confirmed by physical, biochemical and genetic techniques, subsequent analyses in our own laboratories as well as those of colleagues to whom we have sent the mutants indicate that there is variability in the PS I content of the cultures depending on growth conditions. While some strains retain undetectable levels of P700, others contain variable (0-20%) amounts of wild-type P700. This property of mutants B4 and F8 has been

communicated to the journals in which the results were initially published (Greenbaum et al., 1997a,b).

In his analysis of this work, Boichenko (1996) postulated a "leaky" model of the Z-scheme, illustrated schematically in Fig. 1. According to this model, under continuous high-intensity light PS I turns over with sufficient rapidity to accommodate reductant generated by multiple PS IIs thereby preserving a key requirement of the Z-scheme: only PS I is capable of generating low-potential reductant that can be used for hydrogen evolution or carbon dioxide fixation.

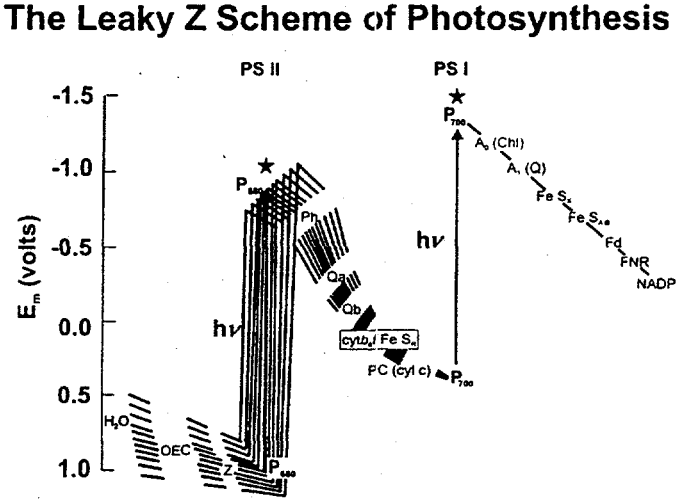

Fig. 1 Schematic illustration of the "leaky" Z-scheme of photosynthesis. It is postulated that under saturating illumination PS I undergoes multiple turnovers such that it can accommodate all output generated by Photosystem II.

We are testing the hypothesis of Fig. 1. In these experiments, mutant Fud26 of the green alga *C. reinhardtii* that had a measurable ratio of Photosystem I to Photosystem II of 0.08 was used for our studies. Table 1 summarizes the properties of this mutant. Our preliminary results with the alga characterized in Table 1 suggests that the Z-scheme is not capable of quantitatively accounting for the pulsed yields of hydrogen and oxygen production or photosynthesis under light-limiting conditions. However, in order to be completely certain that this is the case, we feel that it is necessary to perform the Photosystem I, Photosystem II, and antenna size measurements side-by-side with the oxygen and hydrogen measurements rather than shipping the samples offsite for analysis.

We are in the process of acquiring a spectrometer that will enable us to perform our own measurements of Photosystems I and II. This instrument is scheduled for delivery on June 6, 1998. Acquisition of this capability will enable us to perform all measurements necessary to perform a quantitative test of the Z-scheme. This capability will enable us to address the criticism that perhaps

Table 1. Photosynthetic parameters of mutant Fud26*

Parameter	Value
PSI : PSII Ratio	0.081
PSI Antenna	150
PSII Antenna	320

*Measurements by A. Melis. Frozen samples were pelleted and shipped to the University of California by express courier for analysis.

the Photosystem I measurements in the mutants of our original work were degraded by the process of shipping or freezing the algae.

There is an important practical motivation for determining if evidence can be adduced supporting the possibility that sustained simultaneous photoevolution of hydrogen and oxygen can be driven by a single light reaction because it can, in principle, lead to a doubling of the conversion efficiency of light energy into hydrogen energy. This result, combined with algae that linearize the light saturation curve and possess oxygen-tolerant hydrogenases, would be the appropriate test organisms for development in bioreactors that can be used in chemical engineering development processes.

WORK PLAN FOR FY 1999

It is anticipated that upon receipt of our own spectrometer we will be able to perform, on a side-by-side basis, all the measurements that are necessary for performing a quantitative test of the Z-scheme for hydrogen and oxygen production and carbon dioxide assimilation. We will also address the question of how the accumulation of carbon reserves affects the ability of algae to photoproduce hydrogen by a Photosystem I-mediated reaction. This approach has the advantage of spatial separation of hydrogen and oxygen which avoids the oxygen-tolerance problem of the hydrogenase enzyme. We will also work on the important problem of linearizing the light saturation curve of photosynthesis.

REFERENCES

1. E. Greenbaum, "Simultaneous Photoproduction of Hydrogen and Oxygen by Photosynthesis," *Biotechnol. Bioeng. Symp.* **10**, 1-13 (1980).

2. E. Greenbaum, J. W. Lee, C. V. Tevault, S. L. Blankinship, and L. J. Mets, "CO_2 Fixation and Photoevolution of H_2 and O_2 in a Mutant of *Chlamydomonas* Lacking Photosystem I," *Nature* **376**, 438-411 (1995).

3. J. W. Lee, C. V. Tevault, T. G. Owens, and E. Greenbaum, "Oxygenic Photoautotrophic Growth Without Photosystem I," *Science* **273**, 364-367 (1996).

4. E. Greenbaum, J. W. Lee, C. V. Tevault, S. L. Blankinship, T. G. Owens, and L. J. Mets, "CO_2 Fixation and Photoevolution of H_2 and O_2 in a Mutant of *Chlamydomonas* Lacking Photosystem I," *Nature* **376**, 438-441 (1997a).

5. E. Greenbaum, J. W. Lee, C. V. Tevault, S. L. Blankinship, T. G. Owens, and L. J. Mets, "Photosystem I Measurements in Mutants B4 and F8 of *Chlamydomonas*," *Science* **277**, 167-168 (1997b).

6. V. A. Boichenko, "Can Photosystem I be a Photogenerator of Low Potential Reductant for CO_2 Fixation and H_2 Photoevolution?" *Photosyn. Res.* **47**, 291-292 (1996).

BIOLOGICAL QUALITY OF SOILS CONTAINING HYDROCARBONS AND EFFICACY OF ECOLOGICAL RISK REDUCTION BY BIOREMEDIATION ALTERNATIVES

A. J. Stewart, B. E. Sample, G. W. Suter, II, and L. F. Wicker

INTRODUCTION

This project provides data and technical guidance to Petroleum Environmental Research Forum (PERF), a consortium of petroleum-producing companies, about environmentally acceptable endpoints in relation to ecological risk of petroleum hydrocarbon residuals in soils. Our project focuses on the relationship between 'chemically available' and 'biologically available' measurements of petroleum hydrocarbon compounds in soils, from a risk-based perspective. Clean-up standards for soils contaminated with petroleum hydrocarbon compounds typically are based either on concentrations of total petroleum hydrocarbons (TPH), or on concentrations of particular chemicals of concern (e.g., benzene, benzo[a]pyrene, etc.), as measured in solvent extracts of soil samples. However, various studies indicate that chemicals present in TPH may be able to permeate into soil particles. If this occurs, the particle-embedded hydrocarbons may be extractable by use of organic solvents, and yet be unavailable biologically. This condition clearly would reduce risk to biological receptors, which should be taken into consideration in setting risk-based cleanup standards, or when developing and verifying efficacy of bioremediation clean-up techniques. The ideas summarized above serve as the focus for our studies.

DISCUSSION OF CURRENT ACTIVITIES

Project activities in FY 1997 did not map quite as expected to tasks identified in the Field Work Proposal. For example, we attended six PERF- or Department of Energy Fossil Energy Program related meetings, which exceeded our expectations for travel (Table 1). At each of these meetings, we provided project status reports to petroleum industry representatives. But each of these meetings also was formative, in that we received constructive feedback about industry needs in relation to project activities that we had previously planned or initiated. As a result of this dialog, several tasks that we initially thought to be important declined in priority, and several activities we

Table 1. PERF project-related travel

Meeting location	Meeting date	Meeting purpose
Houston, TX	June 17-19, 1997	DOE, oil technology project review
Salt Lake City, UT	August 4-6, 1997	Biological surveys at a Chevron site
San Francisco, CA	November 4-7, 1997	PERF, 94-06 working group
San Francisco, CA	November 16-20, 1997	Present results of toxicity tests of PERF soils at SETAC[1] meetings
San Francisco, CA	November 30 - December 3, 1997	PERF, 94-06 working group
Denver, CO	January 27-29, 1998	PERF, general administrative
Houston, TX	February 18, 1998	PERF, 97-08 strategy session

[1]Annual meeting for the Society for Environmental Toxicology and Chemistry.

presumed to be of lesser importance increased in priority. Some changes in project priorities were also driven by results of investigations of petroleum-contaminated soils, as a result of studies initiated both by petroleum companies having membership in PERF, and by ORNL scientists, with DOE Fossil Energy Program support. Noteworthy activities in various project task areas are summarized below.

Development of ecological risk assessment tools

In early August, 1997, we used biological survey techniques at a Chevron petroleum-contaminated site in Ogden, Utah, to "ground truth" some of the ideas outlined in an ecological risk assessment framework document that we had developed previously (Suter 1997). The five-acre site contained test plots of alfalfa, fescue and poplar trees that had been established to assess the effectiveness of phytoremediation techniques for lowering the concentrations of petroleum hydrocarbon compounds in soil and shallow groundwater. A walk-over assessment revealed that weedy western plant species indicative of physical disturbance were present over much of the area that was not planted in fescue, alfalfa or poplar trees. The site was used at least intermittently by a few English house sparrows, but we found no evidence of site use by mammals or reptiles. A moderately diverse complement of detritivorous, herbivorous and predatory species of terrestrial invertebrates was present. Working with Chevron research staff, we harvested vegetation samples

from replicate quadrant sampling sites in the alfalfa and fescue plots, and analyzed these samples for percent cover (by species), plant species present, above-ground plant biomass, and litter. We also sampled soil invertebrates in each quadrant, using application of a mustard-water solution to encourage invertebrate evacuation. Relationships among the parameters were explored by correlation and analysis of variance, in association with data on the distribution and concentration of petroleum hydrocarbon compounds in soil at a 1-m depth, obtained previously by Chevron. We found a negative correlation between litter invertebrate abundance and benzene concentration (1-m depth), for fescue and alfalfa plots combined, but the associations between benzene concentrations (1-m depth) and invertebrate biomass, plant biomass, litter biomass, and plant species diversity were not significant. Additionally, none of the associations between total petroleum hydrocarbon (TPH) (1-m depth) and the biological properties that we measured was significant ($R^2 \leq 0.12$). A "lessons learned" report was prepared from observations we made while testing our biological survey methods at this site; the report was distributed to PERF participants. The biological-survey approach for acquiring data that could be used to support an ecological risk assessment was well received by industry representatives. As a result, activities in this task area moved higher on the priority list.

A second area of activity in developing ecological risk assessment tools was that of designing an *in situ* earthworm toxicity test method. The method that we devised was distributed to PERF participant representatives in the form of a Standard Operating Procedure (SOP). Use of the method would permit acquisition of data on earthworm survival and growth, thereby allowing quantification of lethal and sublethal effects of pollutants in soils under environmentally realistic and naturally varying conditions. The Environmental Protection Agency (EPA) has made extensive and effective use of sub-chronic tests for regulating releases of pollutants to surface waters, but does not have widely-accepted sub-chronic test methods that can be used to set risk-based cleanup standards for contaminants in soils. Thus, there seems to be substantial need for economical tests that can be used to provide information about sub-lethal biological risks of pollutants in soils. However, petroleum industry representatives were doubtful that *in situ* tests can ". . . unscramble the keys to toxicity. . ." and so did not rank research on sublethal effects as a research priority. Toxicological benchmarks were the third category of activity in developing ecological risk assessment tools. This task is in progress, and should result in a draft report submitted to PERF participants near the end of this fiscal year (October 1998). Industry representatives support this task.

Assessment of existing bioremediation information

This task was initially delayed and finally terminated due to lack of industry interest. It was felt that most objectives in this task had been addressed sufficiently by the oil industry through American Petroleum Institute (API) studies and various PERF projects. Project resources initially allocated to this task will be redirected to support activities more in line with industry interests.

Field demonstration of risk assessment framework and toxicity testing methodologies

One of our project's goals is that of developing a plan for conducting a demonstration field-scale ecological risk assessment for one or more oil-contaminated sites. In this task, we expected to determine the feasibility of this type of activity; identify the appropriate field and laboratory methods; identify field sites that could be used to support the study; and identify appropriate collaborators among other PERF participants. Several companies have expressed considerable interest in this task, with the understanding that the key objective is to move towards a generic or programmatic risk assessment for various aspects of the upstream oil and gas industry, probably with a focus on screening out sites that either have low ecological risk, and/or those sites that are likely to recover on their own, through natural attenuation. The Gas Research Institute (GRI) and American Petroleum Institute (API) are currently involved with upstream risk-based corrective action studies, some of which may contain activities duplicating those we proposed. We expect to harmonize activities in the studies that we proposed in this task to ongoing and planned activities by GRI, API and PERF; this coordination serves as a key topic for a PERF meeting scheduled for June, in Bartlesville, Oklahoma. The level of engagement by petroleum industry representatives in this task is high. Thus, we expect that this task will move forward successfully, with minor modification. Effective development of this task ultimately must involve incorporation of regulatory and site-management perspectives.

Testing of TPH-contaminated soils for toxicity to earthworms

Earlier in the project, ten soil samples contaminated with petroleum hydrocarbon compounds, and nine non-contaminated reference soils, were tested for acute and chronic toxicity to the earthworm, *Eisenia foetida,* using procedures developed previously (Gibbs et al. 1996). Survival, growth and reproduction data from these 21-day tests were analyzed and submitted to PERF members late in 1996. One significant finding was that earthworm growth varied considerably, even among reference soils, which contained insignificant concentrations of pollutants (Fig. 1).

In 1997, we completed experiments to better understand the source(s) of some of the variation in earthworm growth. These studies involved tests wherein we controlled manipulations of food level and food age; the developmental state of the worms used to initiate the test; hydration conditions used to prepare the worms for testing; and lighting conditions. The results of these experiments showed that the amount and age of the food used in the tests, and the lighting

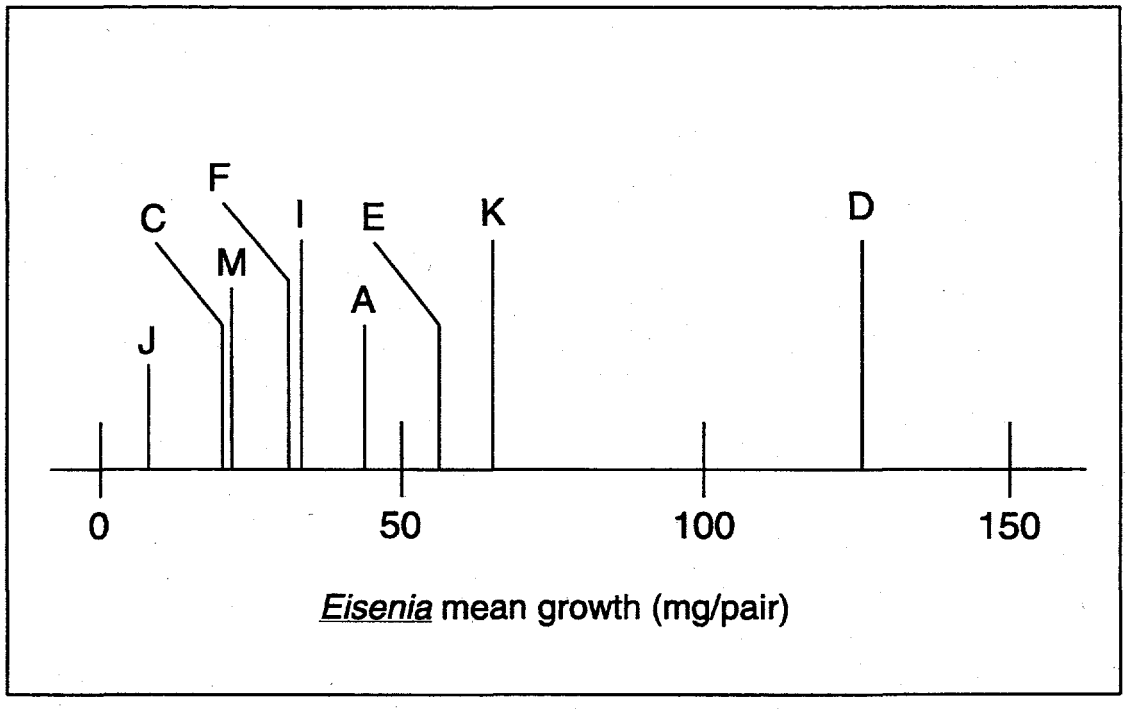

Figure 1. Mean growth rates of earthworms (*Eisenia foetida*) in nine non-contaminated reference soils (standard 21-d test procedures, at 25 °C). Letters are codes designating source of the soils.

conditions, markedly affected earthworm growth. The interaction between soil type and amount of food used in a test was also highly significant: the earthworm growth response to additional food was much smaller in organic-rich soil than it was in soil with little organic matter. Collectively, the results of these experiments demonstrate that it may be difficult to reliably estimate the likelihood of sublethal effects of soil pollutants on *Eisenia*, unless care is taken to appropriately account for the influence of soil organic matter.

Soils containing TPH residuals can be bioremediated *in situ* by discing (to aerate the soil) and adding nitrogenous fertilizer: these manipulations encourage growth of hydrocarbon-metabolizing bacteria. In the autumn of 1997, Chevron began experiments designed to quantify the relationship between loss in TPH and improvement in biological quality of soils, using laboratory "pan tests" involving three PERF soils that were tested previously for toxicity. "Time zero" samples of the three soils have already arrived at ORNL for testing. When bioremediation of the soils used in the "pan tests" is deemed to be complete, "time final" samples will also be sent. In this experiment, our objective is to determine the reduction in toxicity of the soils to earthworms, attributable to bioremediation. We expect to receive the "time final" bioremediated soil samples in late May or early June. The results of the tests will be reported to PERF participants less than 30 days after the "time final" samples have been tested.

Miscellaneous progress

In December, 1997, we submitted a manuscript titled "Characterization of petroleum-contaminated soils by thin-layer chromatography with flame ionization detection" to the *Journal of Soil Contamination*. From a query to the editor of this journal in April 1998, we learned that a decision about this manuscript's publication is expected in late May.

On March 16 and 17, 1998, Brad Sample participated in a peer review of the RISC ecological risk assessment model being developed by Ogden Environmental for BP, as a contribution to PERF. The review involved representatives from BP, Ogden, SAIC, Amoco, ORNL, and the State of Oregon, and focused on the outline and proposed scope of the model. Topics discussed included which media and endpoints should be assessed; what screening values should be used; how data should be incorporated; how bioaccumulation and bioavailability should be considered; and the appropriate spatial and temporal scale for assessments. The general consensus from this review was that a problem formulation component must be explicitly included to facilitate the appropriate use of the model. An early-phase problem formulation component would encourage users of the model

to think through the questions they seek to answer, thereby increasing focus on the data that will be needed to answer the questions. It was decided that the group would meet periodically to review developments as the model progresses.

The US Environmental Protection Agency, in cooperation with the Department of Defense, the Department of Energy, state agencies, and industry, has initiated an effort to develop ecological contaminant screening levels for soils at Superfund sites. Brad Sample has been invited to be a member of the working group for the development of toxicity reference values as part of this effort.

Exxon and Chevron are currently conducting studies on phytoremediation, or the use of plants to help "clean up" soils that contain pollutants. In February, 1998, we submitted a proposal to the ORNL seed-money program, to investigate the influence of a discrete, widely-distributed fungal endophyte (*Neotyphodium*) on the ability of a grass (tall fescue; *Festuca arundinacea*) to deal with pollutants in air and soil. Other studies have shown that this endophyte makes the grass more resistant to grazers, more tolerant of drought, more able to obtain phosphorus from posphorus-poor soil, and more cold-hearty, compared to endophyte-free forms of the grass. We hypothesized that the endophyte might also improve the ability of tall fescue to deal with pollutants, in air or soil, and suggested that the endophyte-grass system could be used as a model system for designing more effective and efficient phytoremediation techniques. The proposal was not funded, despite interest in the proposed work, both by Exxon and Chevron.

In April, 1998, Brad Sample began participating as a contributer and reviewer for the ecotoxicological benchmarks appendix to the American Society for Testing and Materials (ASTM) RBCA-ECO (risk based corrective action, ecological risk) standard. ORNL's participation in this ASTM activity is strongly supported by PERF industry representatives.

REFERENCES

Suter, G. W., II., "A Framework for Assessing Ecological Risks of Petroleum-Derived Materials in Soils", ORNL/TM-13408, Oak Ridge National Laboratory, Oak Ridge, TN, 1997.

Gibbs, M. H., L. F. Wicker and A. J. Stewart, "A method for assessing sublethal effects of contaminants in soils to the earthworm, *Eisenia foetida*," *Environ. Tox. Chem.*, **15**,360-368 (March, 1996).

FOSSIL FUELS SUPPLIES MODELING AND RESEARCH

P. N. Leiby

The fossil fuel supplies modeling and research effort focused on two areas: U.S. Strategic Petroleum Reserve (SPR) planning and management, and transportation fuels and efficiency. Topics covered included new SPR oil valuation models, updating models for SPR risk analysis, and fill-draw planning.

STRATEGIC PETROLEUM RESERVE PLANNING AND MODELING

P. N. Leiby

INTRODUCTION

The Strategic Petroleum Reserve (SPR) is a government-owned stockpile of crude oil intended to serve as a buffer against possible oil market disruptions. The overall purpose of this project is to assist with SPR planning and management, through the development and application of improved models and tools. Current project efforts emphasize developing new modeling tools to explicitly and flexibly portray oil market uncertainty and SPR planning risk.

DISCUSSION OF CURRENT ACTIVITIES

Oak Ridge National Laboratory (ORNL) conducts model development and planning analyses for Strategic Petroleum Reserve (SPR) drawdown, distribution and other management activities, in support of the Office of Management Operations, Petroleum Reserves. The roles and objectives are:

1. to evaluate SPR planning alternatives and roles of SPR;
2. to support development of SPR oil valuation and bid analysis tools;
3. to evaluate potential applications of DIS-Risk model approach to related energy policy issues;
4. to study role and value of risk information in SPR planning;
5. to utilize, maintain, modify, and report on SPR analysis models;
6. to provide analytical support for the SPR office.

Activities This Year

- Analyzed the benefits of alternative enhancements to the SPR draw rate capability.
  The choice of draw rate capability and SPR size is guided by budgetary considerations, general facility performance goals, the need to coordinate with other International Energy Agency members, and engineering cost analyses of the SPR facilities. The ORNL analysis estimates the ranges of economic benefits to the U.S. that could be achieved with alternative maximum drawdown capabilities. Such information can assist in determining the economically preferable draw rate capability for a given SPR size. A report provided results from this ongoing analysis of the benefits of alternative SPR draw rates: "SPR Draw-Rate Capability Benefits Analysis," Paul N. Leiby, David Bowman, and Donald W. Jones, Energy Division, Oak Ridge National Laboratory, October 22, 1997.

- Analyzed the economic consequences of altering SPR stockpile size.
  This analysis so far has focused on the 1 billion barrel reserve size, and its net economic benefit, compared to the current size of 560 million barrels. We considered the economic benefit of a 1 billion barrel reserve, over a wide range of drawdown capabilities. The results are then comparable with those from the ongoing draw-rate study, which focuses on the benefits of the current 560 million barrel reserve for the same range of draw rate capabilities. The SPR size expansion benefits were also estimated for some key sensitivities, notably GNP elasticity, slack (excess) supply capacity, and disruption length. See the technical memorandum "Insights and Preliminary Conclusions on SPR Size From Initial Numerical Results," DRAFT, July 28, 1997.

- Assisted with the evaluation of the proposed Regional Petroleum Product Reserve (RPPR). In a short note, "NOTES ON RPPR EVALUATION," May 27, 1997, our comments discussed four issues salient to this analysis:
  - Estimation of possible macroeconomic losses due to a temporary, regional, product price shock;
  - Accounting for interactions between an RPPR and private inventory behavior;
  - Establishing the duration and geographic scope of product disruptions; and

- RPPR trigger/drawdown rules.

- Maintained and updated the DIS-Risk model to use the latest DOE oil market assumptions, consistent with recent AEO/IEO. This is part of the normal model maintenance tasks required. NEMS modules were used to produce the needed reference data. The model was tested with the aforementioned changes.

ORNL also provided general analytical support to the SPR Office, including:

- Provided comments on the Revised SAVE model (dated 03/10/98).
  ORNL reviewed and offered commentary on the SPR valuation spreadsheet model developed by DOE. Paul Leiby and David Bowman.
- Shared information on recent research on oil price shocks with the SPR Office.
  ORNL summarized the most recent empirical research on the macroeconomic consequences of oil price shocks. We discussed the implications of these empirical insights for SPR planning and evaluation. These empirical results have a bearing on how to assess the benefits of the SPR, and raise some issues on the merits of alternative SPR configurations, such as crude-oil *versus* product storage. For a summary paper on the new research, see "The Findings of the DOE Workshop on Economic Vulnerability to Oil Price Shocks: Summary and Integration with Previous Knowledge," Donald W. Jones, David J. Bjornstad, and Paul N. Leiby, Oak Ridge National Laboratory, September 5, 1997, 2nd DRAFT.

OIL AND GAS PRODUCTION

T. W. Schmidt

Research in oil and gas production at Oak Ridge National Laboratory is represented by activities in three research divisions, Chemical Technology, Compute Science and Mathematics, and Environmental Sciences. The areas of study involve: measurements of wax points in crude oils and petroleum fluids, research on the thermodynamics of brine/oil/rock interfaces and their influence on enhanced oil production in waterfloods, an evaluation of the hydrocarbon potential of part of the Appalachian basin, the application of nuclear fuel reprocessing technology to the separation of petroleum and water downhole in an oilwell, the application of global optimization methods to residual statics in seismic imaging, and the use of neural networks in oilfield parameter estimation.

NATURAL GAS AND OIL TECHNOLOGY PARTNERSHIP SUPPORT

T. W. Schmidt

INTRODUCTION

The Natural Gas and Oil Technology Partnership expedites development and transfer of advanced technologies through technical interactions and collaborations between nine national laboratories and the petroleum industry - majors, independents, service companies, and universities.

The Partnership combines the expertise, equipment, facilities, and technologies of the Department of Energy's national laboratories with those of the US petroleum industry. The laboratories utilize unique capabilities developed through energy and defense R&D including electronics, instrumentation, materials, computer hardware and software, engineering, systems analysis, physics, and expert systems. Industry contributes specialized knowledge and resources and prioritizes Partnership activities.

The areas of technology are:

Diagnostics and Imaging Technology addresses cutting-edge geophysical methods for improved reservoir characterization with a focus on improved borehole hardware and computational efforts for seismic processing and other exploration issues. The Partnership catalyzed formation of a 25-company collaboration which has become the industry focal point for this technology.

Oil and Gas Recovery Technology addresses a broad range of technologies aimed at improving production from existing fields and with specific emphasis on assisting independent producers. The industry interface is an Industry Review Panel consisting of more than 20 individuals representing independents, majors, and the service companies.

Drilling, Completion, and Stimulation Technology aims at better access to the reservoir through improved drilling and completion technologies. Currently, the laboratories participate in several joint industry projects fostered by two industry organizations: the Drilling Engineering Association (DEA) and the Completion engineering Association (CEA).

Environmental Technology addresses new technologies that are needed to produce more oil and gas from mature domestic sources while safeguarding the environment. Key issues to be addressed include: 1. Produced Water, 2. Stationary Source Emissions, 3. Risk Assessment, 4. Tank Bottoms and Sludge, 5. NORM, 6. Soil Remediation, 7. Vapor Recovery, 8. Offshore Structure D&D, and 9. Drilling Wastes.

Downstream Technology is a new area of technology that is being coordinated under the Natural Gas and Oil Technology Partnership for the first time in Fiscal Year 1999. All existing downstream funded projects, largely in the area of heavy oil processing, will be reviewed with industry review panels along with project proposals in the areas of $PM_{2.5}$ and ozone mitigation.

DISCUSSIONS OF CURRENT ACTIVITIES

During 1998 T. W. Schmidt participated in the development of the recommendations for funding of the Partnership Programs on behalf of Oak Ridge National Laboratory. In addition to existing projects in Oil and Gas Recovery Technology and Diagnostics and Imaging Technology, T. W. Schmidt has assisted in the development of two new projects in the Environmental Technology Area and a CRADA with Phillips Petroleum Company on wax point determination. Other activities include program planning with the Partnership, selection of a Partnership Steering Committee, and coordinating all of the national laboratory participation in the Downstream Technology Area.

ADVANCED COMPUTATIONAL TOOLS FOR 3-D SEISMIC DATA FUSION

J. Barhen, D. Reister, E. Oblow, C. Glover, V. Protopopescu

PROJECT OVERVIEW

The development of 3-D structural and stratigraphical models of hydrocarbon reservoirs is crucial for the future ability of the exploration industry to economically discover and produce oil and gas. It requires extensive use of 3-D seismic data. These computational tasks are extremely expensive and new ideas and methods are necessary for making them cost-effective. An important step for the advancement of the state-of-the-art in 3-D seismic technology has been the collaborative 3-D Seismic Modeling Project undertaken by the United States' Society of Exploration Geophysicists (SEG), the European Association of Exploration Geophysicist (EAEG), and U.S. Department of Energy (DOE) under GONII. This international collaboration has designed realistic subsurface models for challenging and relevant exploration plays.

The objective of the present effort is to develop and test advanced computational tools for *data fusion* in 3-D seismic analysis. Research at ORNL's Center for Engineering Science Advanced Research (CESAR) will focus on two tasks: (1) the application of novel global optimization methods to residual statics in seismic imaging; and (2) application of neural networks to oil field parameters estimation. The revolutionary techniques investigated by ORNL provide a unique approach for enhancing the understanding of hydrocarbon reservoirs away from the borehole.

ORNL TASKS

The goal of this project is to develop, test and demonstrate revolutionary computational technologies for data fusion in seismic analysis. It is undertaken as a set of collaborative efforts between a national laboratory (ORNL) and industry. In FY'98, CESAR's efforts have focused on the first of the following two tasks. Partners are specified in parenthesis.

Task 1. ***Global Optimization (ORNL, CogniSeis, Unocal).*** The quality of the solution of many inverse problems, particularly those involving distributed parameters, depends to a great extent

on the availability of good optimization paradigms. CESAR proposes to apply a new fast global optimization technique developed by ORNL to nonlinear parameter estimation (whether by neural nets or by more conventional means) in connection with the industry-provided datasets. As a first typical example we are studying the solution of the long-standing residual statics problem in seismic imaging.

Task 2. ***Neural Networks (ORNL, Western Atlas, BP-USA, Shell, Amoco, Unocal, Texaco).*** Neural networks are adaptive nonlinear dynamical systems that can carry out useful information processing by means of their state response to initial or continuous input. We propose to apply neural network approaches to several specific areas: classification of seismic signatures, nonlinear parameter estimation, data dimensionality reduction, lithology estimation, velocity model estimation, and event tracking. The primary benefit of such paradigms is that they are distribution free, and that they have been shown to produce more accurate classification results than conventional statistical techniques. Further, CESAR's fast "adjoint operator" learning algorithms for processing static and time-dependent information patterns are particularly relevant to large-scale geophysics applications such as distributed parameter estimation and history matching. Finally, neural networks can be efficiently used to reduce the dimensionality of seismic data by providing a nonlinear version of principal component analysis, a technique well established in the realm of linear models.

BENEFITS TO DOE MISSIONS

Since 1974, a core mission for DOE has been to reduce dependence on imported oil. In the "1995 National Assessment of United States Oil and Gas Resources" (USGS Circular 1118) by the U.S. Geological Survey, the total remaining oil in the onshore areas and State waters of the U.S. was estimated at 112.6 BB (Billion Barrels). Of this total, 20 BB are proved reserves, 60 BB are reserve growth in known fields, and 30 BB are undiscovered conventional resources.

The key to oil discovery is to use scientific techniques to find oil structures without having to drill expensive exploratory oil wells. The primary scientific techniques used to find oil structures is 3-D seismic analysis. The goal of this project is to develop advanced computational tools that reduce the cost and increase the precision of 3-D seismic analysis. Thus, it is directly focused on

the DOE mission to reduce oil imports. It will also significantly contribute to the strategic plan issued by the Secretary of Energy (see, e.g., "Fueling a Competitive Economy", April 1994) in the area of Science and Technology.

This project also supports ORNL core competencies. In particular, CESAR's effort corresponds to the programmatic goal of developing and deploying "numerical algorithms for solving large-scale scientific and engineering problems" (see e.g., ORNL R&D Strategic Plan, page 37), and contributes to the building of a world-class program in computational sciences.

MILESTONES

The main results of the ORNL contribution to the overall projects are the development of leading-edge computational capabilities, enabling U.S. oil companies to successfully address some of the most complex issues in exploratory seismic analysis. Codes developed by investigators working on this project will be made available. General results of the project are being presented at public meetings. Participation of companies in each task ensures that knowledge of all work and codes is available to industry as they are developed.

The milestones listed below for Tasks 1 and 2 reflect a project starting date of April 15, 1998

- 05/98 – Complete estimation of ultrafast neural networks learning methodology for seismic parameters.
- 07/98 – Complete application of TRUST global optimization to large-scale residual statics for accurate seismic imaging.
- 09/98 – Implement and demonstrate ultrafast neural learning on actual reservoir parameters.
- 01/99 – Develop a revolutionary method for systematic nonlinear incorporation of uncertainties in reservoir parameters estimation.
- 05/99 – Develop and include stochastic tunneling concepts into TRUST.
- 08/00 – Combine ultrafast neural learning and nonlinear uncertainty analysis; demonstrate on predicting key parameters (porosity and permeability) away from borehole.

These milestones are also assuming full and timely funding of the tasks.

DISCUSSION OF CURRENT ACTIVITIES

In a recent *Science* paper [1], Barhen et al. reported a significant improvement in solving low-dimensional global optimization benchmark problems with a code called TRUST, which employs a descent-tunneling methodology characterized by line search. The essence of this approach is that the optimization problem is broken down into two distinct phases; descent and tunneling (using line search). The descent phase makes use of local derivative information and the wealth of algorithmic experience to find local minima in continuous functions. The search phase utilizes the recent concept of tunneling to find a new region in which to begin to descend again. What makes this combined approach novel and efficient is that by descending into a local minimum before beginning to search for a new descent region, the method avoids repeated descents to the same local minimum. The final solution is thus a single descent interspersed with line searches to find the descent basins of new local minima. Another characteristic of the method, using line search to tunnel to new basins, is an additional attractive feature of this approach, since the ratio of the basin perimeter to its volume favors a line search over a volume search for anything but a hyperspherical basin. Both of these characteristics seem to explain the improvements Barhen reported in benchmark testing using the TRUST methodology.

It is widely recognized that in high-dimensional problems the search phase of any efficient algorithm is the most costly in terms of function evaluations (compared to the descent phase). In order to move from benchmarks to realistic high-dimensional problems, therefore, further improvements must be made in search methodology. The most limiting characterization of search, however, is that local derivative information is of no help in locating a new basin of attraction different from those already found. We therefore must explore what other information can be used to help in this search process. Most recent research indicates that branch and bound approaches address this problem theoretically but are complex and costly to implement in practice. The bounding process allows certain regions of the search space to be eliminated from further functional evaluations.

It is also widely understood that the global optimization problem cannot be solved in general without imposing resolution or probabilistic convergence constraints on its solution. Without such constraints it is impossible to know how to halt an algorithm that has found a lowest-to-date local minimum. Only an exhaustive search is guaranteed to find a global minimum since no local information can ever be used to characterize the current best answer as definitively being the global minimum. From a practical standpoint, probabilistic constraints are easier to implement and we have, therefore, concentrated our efforts in this area. In this approach only a probabilistic guarantee can be given that the best local minimum found is the real global minimum. There is always a chance that another lower minimum will be found, albeit with a predetermined low probability.

The comments above lead one to believe that a stochastic approach to tunneling-search coupled with some limited knowledge of function bounds and Lipschitz-like constants can be made the basis of a powerful yet simple algorithm to improve Barhen's original approach. To make maximum use of such bounding information, a low (or one) dimensional stochastic tunneling approach to covering a high-dimensional space seems to be needed. Since we are committed to a stochastic adaptation of Barhen's method, we must reiterate that only a probabilistic guarantee can be made on deciding whether a global minimum has been found. A halting algorithm which stochastically characterizes the solution is thus our aim. Without stochastic characterization the only other alternative would be to solve the problem within prescribed resolution bounds using a fixed grid and its associated fixed number of function evaluations.

We propose therefore to make use of minimal bounding information in a low-dimensional stochastic algorithm to significantly improve the tunneling phase of our TRUST algorithms. In doing so we will improve an already powerful breakup of the problem into local descent and tunneling. To accomplish this we will adapt Pijavskij's one-dimensional bounding process to higher dimensional problems and produce a stochastic version of Pijavskij's method, called SPT: (S)tocahstic (P)ijavskij (T)unneing, suitable for tunneling-search.

A random multiple square-well global optimization benchmark problem will be used to clearly illustrate the improvements possible with this new method. This benchmark problem is characterized by no derivative information so that emphasis is placed completely on the use of

information that can aid only the search phase of the algorithm proposed. Since optimal descent algorithms are a highly developed research area, this approach will concentrate our efforts on improving the difficult and costly tunneling phase of the algorithm.

We will apply the stochastic improvements developed directly to the combined descent and tunneling TRUST algorithm. This will allow us to revisit the benchmark calculations reported in *Science* to see what improvements can be made in these already good results. We will also solve a new high-dimensional seismic problem, similar to the one reported in the *Science* paper but of even higher dimensionality, to further demonstrate the method's viability.

REFERENCES

[1] Barhen, J., V. Protopopescu, and D. Reister, "TRUST: A Deterministic Algorithm for Global Optimization," *Science*, **276**, 1094-1097 (1997).

DEVELOPMENT OF AN IN-WELL OIL/WATER SEPARATOR FOR IN SITU RECYCLE OF PRODUCED WATER

J. F. Walker, Jr., R. T. Jubin and S. M. Robinson
Oak Ridge National Laboratory

INTRODUCTION

Produced water is the largest generated waste stream by volume in the Gulf Coast region. More than 250 million bbl of produced waster are discharged each year to surface waters in both Texas and Louisiana.[1] Because of the tremendous volume of water generated and the specific constituents typically present, discharge of produced water from oil and gas production operations has been increasingly scrutinized in recent years for potential impacts on sensitive habitats. The maximum concentration of contaminants in produced water that can be discharged will be limited by the latest Environmental Protection Agency (EPA) regulations under the Clean Water Act. These rules are expected to reduce current discharges of toxic pollutants (including arsenic, cadmium, and lead) by more than 200,000 lb/year, conventional pollutants (such as oil, grease, and solids) by 2,800,000 lb/year, and nonconventional pollutants (such as chlorides, ammonia, and aluminum) by about 1,500,000,000 lb/year. Future regulations are likely to be more restrictive and may include zero-discharge standards.[2,3]

This project will extend the application of remotely-operated separations equipment developed for the nuclear industry to in-well recovery of oil generated by enhanced oil recovery techniques. Centrifugal solvent extraction separators, originally developed by the Department of Energy for nuclear fuel reprocessing, have been successfully used for surface treatment of produced water and waste water generated during environmental cleanup operations.[4-8] Centrifugal separator units of 5.5 cm and 8.4 cm rotor diameter have been previously tested at ORNL, and a larger unit has been designed for Costner Industries Nevada, Inc. for these applications. Performance data has shown that centrifugal separators are capable of separating stable emulsions into "single" phase streams with generally less than 1% cross phase contamination. Centrifugal separators, therefore, have the potential to achieve higher capacity and separations efficiencies than traditional oil/water separator equipment.

The goal of this project will be to evaluate (1) the applicability of the centrifugal separator equipment for in-well operations, and (2) the potential for coupling the separations equipment with recently developed horizontal drilling technology to implement in-situ recycle of the produced water. Figure 1 is a conceptual drawing of the Centrifugal Down Hole Separator (CDHS) system. The CDHS is conceptually comprised of three primary components: a centrifugal separator and two pumps. The separator unit itself generates a small hydraulic head, but it will need to be coupled with pumps for deep well applications. The first pump will be used to generate sufficient head pressure to pump the recovered oil to the surface and the second to reinject the recovered water.

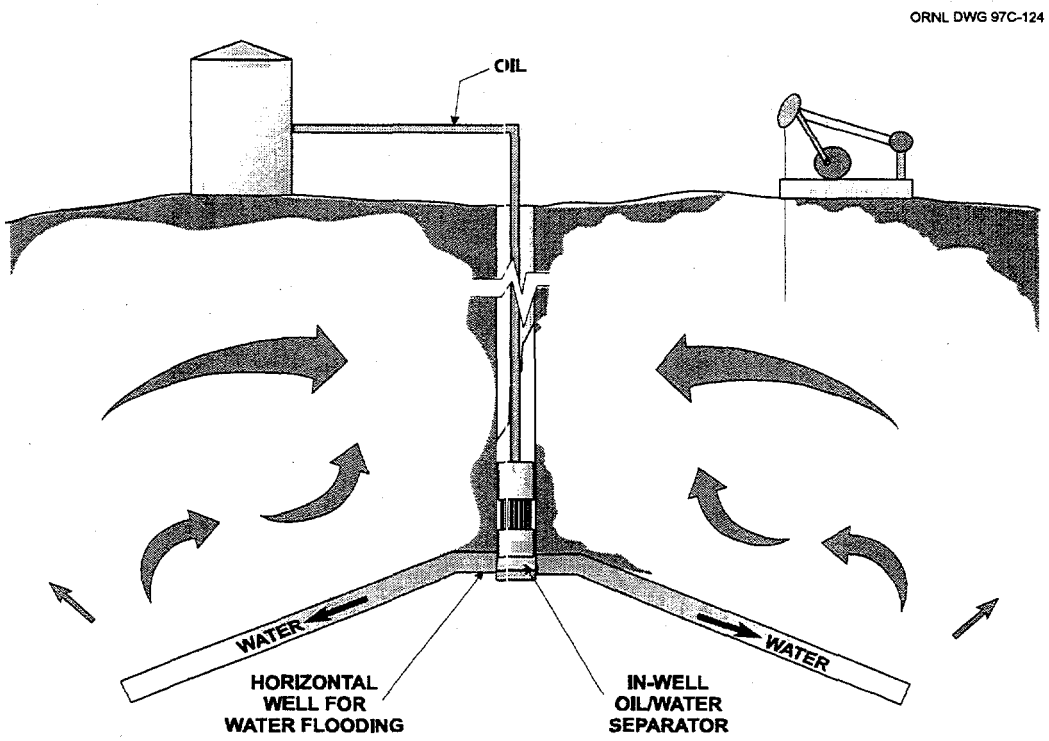

Figure 1. Conceptual drawing of the Centrifugal Down Hole Separator System

Initial testing will be conducted with a bench scale separator to determine the separation efficiency of various crude oils and to provide information necessary to scale up the separator. Information from the bench scale unit will be used in the design of a larger prototype, which will have a much larger height/diameter ratio, and will incorporate some of the components necessary for down hole operations. The prototype separator will be operated in the lab to verify scale up parameters and separation efficiencies, as well as to provide information necessary to design a full

scale demonstration system. Testing of the crudes in the bench scale equipment, as well as design of the larger prototype will be completed in calendar year 1998. Fabrication, installation, and operation of the prototype unit will be completed in calendar year 1999. Fabrication, installation, and operation for the full scale demonstration is planned for calendar year 2000.

CURRENT YEAR LABORATORY RESULTS

Current year progress has occurred in three major areas: (1) setup and operation of a bench scale mixer/settler test system to provide data necessary to design and evaluate a CDHS, (2) procurement and setup of a bench scale centrifugal separator, and (3) operation of the bench scale centrifugal separator.

The primary purpose of the bench scale mixer/settler tests is to determine the dispersion number (N_{Di}), which is a dimensionless number that correlates the time required for an emulsion of two immiscible liquids to break under an accelerational field, of various liquid-liquid mixtures to be separated in the centrifugal separator. The N_{Di} is the key to the overall correlation to the capacity of the centrifugal separator. Since there was little information in the literature regarding the value of N_{Di} for oil-water mixtures, initial mixer/settler tests were conducted with various combinations of tributyl phosphate (TBP) and dodecane (DD) in dilute nitric acid solutions to verify the equipment and procedures prior to conducting tests with emulsions of oil and water. The N_{Di} obtained in these tests, which ranged 2×10^{-3} to 5×10^{-3}, were in the same range as those published in the literature for similar TPB/DD in dilute nitric acid solutions.[9] This indicated that the equipment and procedures were suitable for future testing of oil-water emulsions.

The mixer/settler system was then used to determine the dispersion numbers for various combinations of 30 weight motor oil and water at ambient temperature and pressure. These N_{Di} were used to estimate the capacity of CDHSs with rotor diameters of 3-1/8 or 5-5/8 inches and lengths ranging from 4 to 16 feet. The results are presented in Figure 2. As can be seen, with a 6-5/8 inch diameter rotor which is 16 feet long, the data indicate that flows on the order of 375 gal/min can be expected.

A bench scale centrifugal separator with a rotor diameter of 5 cm (2 inches) was set up to conduct continuous flow studies with various oil-water emulsions. A photograph of the bench scale system are presented in Figure 3. Prior to conducting oil-water emulsion tests it was desirable to test the bench scale unit on emulsions of TBP/DD and dilute nitric acid to verify its operation. In studies by Oak Ridge National Laboratory (ORNL) it has been shown that the dispersion number is constant

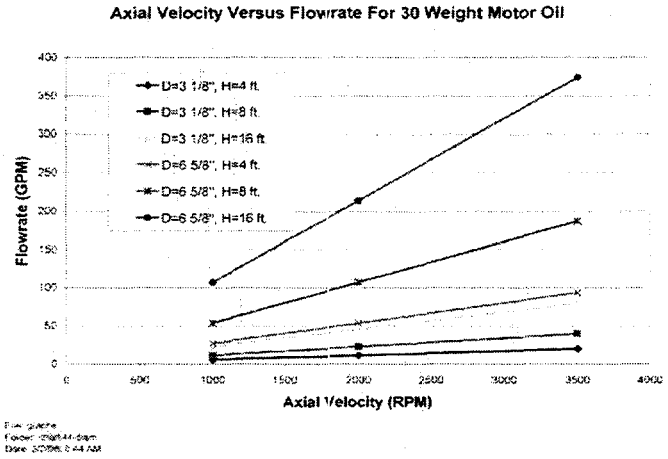

Figure 2. Projected throughput of CDHS as a function of diameter and height.

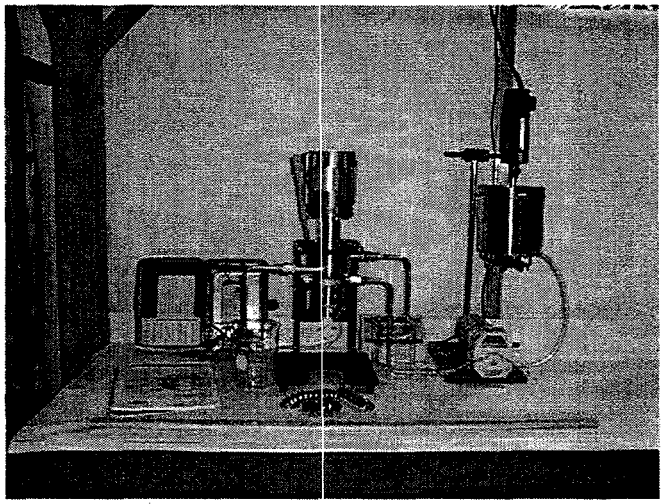

Figure 3. Photograph of the bench scale centrifugal separator system.

for centrifugal separators with rotor diameters ranging from 2 to 25 cm (~0.8 to 9.8 inches) while processing the same concentrations of TBP/DD and dilute nitric acid as those used for the bench scale mixer/settler tests. Therefore, the N_{Di} from the bench scale mixer/settler tests can be used to predict the flow through the 2 inch diameter, bench scale unit (with less than 1% phase crossover in either the aqueous or organic phase). The predicted and actual flows as a function of the

centrifugal acceleration prior to greater than 1% cross phase contamination for the bench scale unit are presented in Figure 4. As can be seen, the actual and predicted flows agree very well for rotors turning at less than 2500 rpm. In the bench scale unit cross phase contamination occurred above 2500 rpm while the model predicted that no cross phase contamination should have occurred at rotor speeds below 3500 rpm. Similar results were obtained with 30 weight motor oil. Tests are currently under way to determine why the cross phase contamination is occurring at lower rotational speeds (and corresponding lower throughput) than predicted for this bench scale unit.

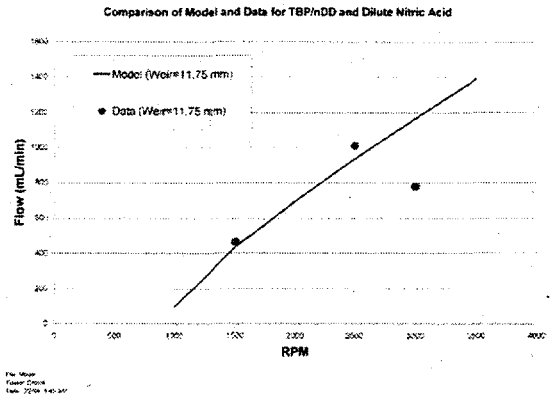

Figure 4. Comparison of the projected and actual flows for the bench scale centrifugal separator.

REFERENCES

1. EYE on Environmental, May 1996.
2. Oil & Gas Journal, November 18, 1996, pg. 22.
3. Oil & Gas Journal, July 15, 1996, pg. 54.
4. Proceedings 74. Annual Convention of the Gas Processors Association, 1995.
5. Scandinavian Oil-Gas Magazine, 21:7/8, 1993, pg. 62.
6. Method for separating disparate components in a fluid stream, Patent 4959158, US Government, 1990.

7. Rotor sleeve for a centrifugal separator, Patent 5571070, Costner Industries Nevada, Inc., 1996.

8. Centrifugal separator, Patent 5591340, Costner Industries Nevada, Inc., 1997.

9. R. T. Jubin, S. F. DeMuth, and S. P. Singh, "Developments in Centrifugal Contactor Technology, ORNL/TM-10768, 1988.

CRUDE OIL COMPOSITION AND OIL RECOVERY

E. P. Robertson, M. R. Ally and N. R. Morrow

INTRODUCTION

Waterflooding is by far the most widely applied method for improved oil recovery and accounts for more than one-half of U.S. domestic oil production; similar proportions hold world wide. Waterflooding is still not well understood and estimation of oil recovery by waterflooding and accurate determination of waterflooding reserves remain serious problems.

The injected brine in a waterflood is obtained from the most convenient source and is usually of different composition than the connate water. Treatment of injected water and modification of its composition are dominated by considerations related to avoiding formation damage, principally fines migration and clay swelling, and mitigation of souring and corrosion. It has generally been believed that composition of the injected brine is immaterial to the efficiency of oil displacement. However, a growing body of laboratory data shows that the brine composition can have a highly significant effect on crude oil/brine/rock (COBR) interactions as evidenced by oil recovery by waterflooding and spontaneous imbibition[1,2,3]. For example, Fig. 1 shows that a change in brine composition can result in waterflood recovery differences of 16% of original oil in place (OOIP); Fig. 2 shows that diluting synthetic reservoir brine results in a systematic increase in oil recovery by up to about 50% OOIP. Although results are strongly dependent on crude oil composition, this trend has been observed for three distinctly different types of crude oil (an asphaltic crude oil, a highly waxy crude, and a crude with extremely low asphaltene content). Changes in oil recovery with cation valency and radius of hydration have also been observed. Crude oil properties (particularly the solvency of high molecular weight polar components) and modest increases in temperature have also been shown to have a major effect on COBR interactions and oil recovery. All of the observed phenomena appear to be dominated by the effect of COBR interactions on wettability. Selection, or adjustment, of injection brine composition in a way that alters wettability to advantage is a novel method of increasing oil recovery at low cost.

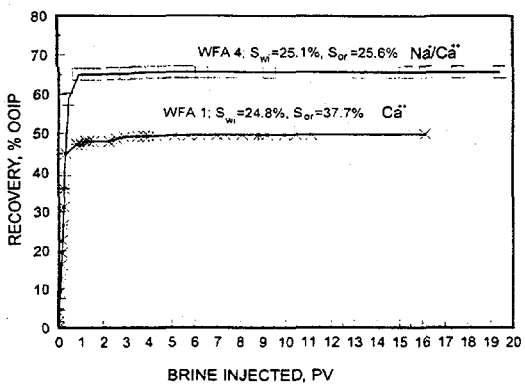

Fig. 1. Effect of brine composition on oil recovery.

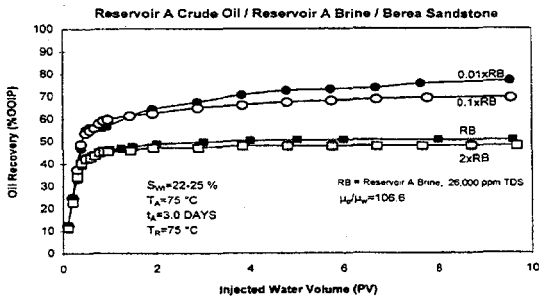

Fig. 2. Effect of brine dilution on oil recovery at reservoir temperature.

The objective of this project is to obtain a more complete understanding of the effects of brine composition, temperature, and crude oil properties on wettability and its effects on oil recovery.

DISCUSSION OF CURRENT ACTIVITIES

Spontaneous imbibition is of special importance to the efficiency of oil recovery from fractured reservoirs. Many factors affect the process of spontaneous imbibition. Investigation of the effect of rock properties and initial water saturation, S_{wi} was undertaken.

In all, 59 imbibition curves were obtained for various types of chalk and sandstone. Final recovery for Berea sandstone expressed as percent of original oil in place (OOIP) showed only a few percent variation with change in S_{wi}. Final recovery for chalk showed much greater variation; for two of the chalk sample sets, oil recovery decreased systematically with increase in S_{wi}. The largest variation was for Rordal chalk; increase in S_{wi} from 7.5 to 51% resulted in decrease in recovery from 67 to 30% OOIP.

Results for very strongly water wet chalk and zero S_{wi} were closely correlated with results for a wide range of other types of porous media. For the chalk cores, there was an overall tendency for imbibition rate to first increase with increase in S_{wi} and then decrease slightly with increase in S_{wi} above about 34%. For Berea sandstone the rate of imbibition decreased with increase in S_{wi} from 0 to 6%, was at a minimum for the range 6 to 15%, and then increased with increase in S_{wi} from 15

to 30%. These changes are ascribed to the net effect of S_{wi} and subsequent increase in water saturation on imbibition capillary pressure and resistance to flow of water and oil.

1. Imbibition rate data for sandstones and chalks with extreme differences in permeability, porosity, pore structure, and for which there was no obvious departure from strongly water wet conditions, were correlated by plots of normalized oil recovery versus dimensionless time with results falling closely to a previously determined reference curve for zero S_{wi}.

2. Imbibition rate for strongly water wet Berea sandstone showed an overall decrease with initial saturation with the rate passing through a minimum.

3. Imbibition rate for four kinds of chalk tended to increase with S_{wi} to a maximum at S_{wi} = 34% and then decrease.

4. Differences in the effect of S_{wi} on rate of imbibition are ascribed to the effect of lowering imbibition capillary pressure relative to the effect of S_{wi} on the change in volumetric displacement and resistance to simultaneous flow of liquids as imbibition progresses.

5. Residual oil saturation for water-wet chalk decreased with increase in S_{wi}. Microscopic displacement efficiency was almost independent of S_{wi} (up to 30%) for Berea sandstone, but tended to decrease with S_{wi} for chalk.

We have shown improved oil recovery with dilution of brine for reservoir crude oil, brine, and rock and that sensitivity of oil recovery to brine composition is small for clean sandstones (low clay content).

The application of the Derjraguin-Landau-Veerwey-Overbeek (DLVO) theory to tailor brines and gauge the effects of potential-determining ions on the surface charge distribution of oil-bearing rocks was investigated. However, this approach requires knowledge of the existence and the magnitude of surface charge on rocks. We have set up the equipment and have the expertise to attempt such measurements on rock samples to be supplied to us by the University of Wyoming.

REFERENCES

1. Zhou, X., Morrow, N.R., and Ma, S.: "Interrelationship of wettability, Initial Water Saturation, Aging Time, and Oil Recovery by Spontaneous Imbibition and Waterflooding," SPE 35436, SPE/DOE Tenth Symposium on Improved Oil Recovery, Tulsa, OK, April 21-24,1996.

2. Buckley, J.S., Liu, Y., Xie, X., and Morrow, N.R.: "Asphaltenes and Crude Oil Wetting--The Effect of Oil Composition," SPE 35366, SPE/DOE Tenth Symposium on Improved Oil Recovery, Tulsa, OK, April 21-24,1996.

3. Yildiz, H.O. and Morrow, N.R.: "Effect of Brine Composition on Recovery of Moutray Crude Oil by Waterflooding," *JPSE,* (in press).

4. Ma, S., Mason, G., and Morrow, N. R., (1996). Effect of contact angle on drainage and imbibition in regular polygonal tubes, *Colloids and Surfaces A: Physicochem. Eng. Aspects* **117**, 273-291.

5. J. S. Buckley, Y. Liu, X. Xie and N. R. Morrow, "Asphaltenes and crude oil wetting - the effect of oil composition," SPECJ, 2, June 1997, 107-119

6. X. Xie, "Application of the dynamic Wilhelmy plate technique to investigation of oil/brine/quartz wetting alteration by adsorption from crude oil," Ph.D. thesis, University of Wyoming, 1996.

DETERMINATION OF ESSENTIAL THERMOPHYSICAL PROPERTIES FOR SUSTAINABLE ENERGY

R. T. Jubin

T. W. Schmidt

INTRODUCTION

This activity is focused on the determination of thermodynamic and thermochemical measurements of hydrocarbon systems. This will include pure components as well as mixtures and spans the range of hydrocarbon mixtures from natural gases to crude oils. One of the major initial focus areas will be wax point determinations. Fiscal year 1998 milestones include obtaining, modifying, and installing an Acoustic Cavity Resonance Spectrometer (ACRS), performing initial measurements to establish the instrument's capabilities, and planning the move of DOE-owned thermophysical property measurement equipment to ORNL. Once the equipment has been returned to operational status, thermophysical and thermochemical measurements on heavy hydrocarbon systems will be resumed. Other specific tasks include critical point measurements for the systems currently being studied in computational molecular chemistry tasks. This task will focus on the validation of computational approaches to predict the measured thermophysical properties for these systems.

The overall objectives of this activity are to conduct research to provide, interpret, and correlate with molecular structure the precise and accurate values of process-engineering properties (thermochemical and thermophysical) of nitrogen-containing, diheteroatom-containing, and polycyclic compounds that occur in or are readily derived from heavy petroleum and to expand fundamental understanding of wax deposition in an effort to provide the data necessary to control unwanted deposition in pipelines and process equipment. The ultimate goal is to be able to rely substantially or entirely on computational results when necessary.

DISCUSSION OF CURRENT ACTIVITIES

As of the information cut-off date for this report, funding had not yet been received in the ORNL Financial Plan for this new task for FY 1998. As such, this report will address planning activities and the development of supporting activities.

Background:

Approaches to sustainable energy encompass a wide variety of technologies that involve both familiar and unfamiliar fluids, often under extreme conditions. These fluids include, but are not limited to, "in-well" crude oils, new "clean" liquid fuels made from petroleum, carbon dioxide that may be used to enhance petroleum production or require sequestration, and new organic products resulting from the conversion of biomass. At present, the ability to rapidly and accurately measure thermophysical properties of these materials over a wide range of conditions is limited, which hampers scientists' understanding of the fundamental mechanisms involved in recovery and separation processes and the chemical reactions involving these fluids. Development of industrial applications involving the fluids is severely hindered. To meet this need, we have proposed a dual-track approach involving state-of-the-art data measurement and advanced computation. First, in order to meet the need for near-term data and provide validation for computed results, an ACRS will be acquired for the experimental measurement of thermophysical properties. The ACRS will complement capabilities of the thermophysical measurement equipment at ORNL as well as other DOE-owned equipment that is to be transferred to ORNL.

The ACRS is a novel instrument (there are currently only three available in industry) that has broad application and provides higher degrees of accuracy over wider ranges of pressure and temperature than conventional methods of determining physical properties. The ACRS can precisely measure many thermophysical properties of materials that are required for recovery, separation, and processing (i.e., heat capacities, dew points, bubble points, vapor pressures, critical points, solubilities, diffusion coefficients, etc.). It can maintain temperatures to within ~0.001 K, pressures to within ~0.005 psia of the setpoint, and system volumes to within 1 μL while operating over a broad range of temperatures and pressures (typically 100–700 K and 0–25000 psia). In addition, the ACRS is much faster and easier to use than more traditional instruments and, hence, is more cost-effective because it can obtain data much more quickly.

Data Needs:

Heavy Crude: Whether it be an East Coast refinery importing crude oil from Nigeria, a Gulf Coast refinery importing from Saudi Arabia, or even a West Coast refinery operating on Alaskan North Slope crude, the quality of the crude oil processed by refineries has declined over the last decade for which records are available (1983–1993). Swain (*Oil & Gas Journals*, January 9, 1995, p. 37) denotes the decline in the quality of crude processed in U.S. refineries in terms of the API gravity, which is stated to have decreased by an average of 0.17° per year in the decade 1983–1993. Furthermore, the decline appears to be accelerating. Measured as a five-year average (1989–1993), the API gravity has declined by 0.22° per year. Swain also denotes the decline in the quality of crude processed in U.S. refineries in terms of the increase in the mass percent of sulfur, which averaged 0.029 mass % per year in the decade 1983–1993. The average sulfur content in crudes refined in the United States in 1993 was 1.16 mass %.

The heavier crudes contain more carbon, oxygen, sulfur, and nitrogen (polycyclic aromatics and heteroatom-containing compounds) than the benchmark West Texas intermediate. These heteroatom-containing compounds are difficult to remove. The processing of crudes that contain increasing levels of oxygen, sulfur, and nitrogen using present-day technology has produced fuels with high heteroatom contents and a tendency toward instability. The refractory nature of the heteroatom-containing compounds is the main reason for an increase in coke production in the last decade. Using heavy oil to make quality transportation fuels requires an understanding of the chemistry and the thermodynamics of adding hydrogen to the feedstocks. One of the major goals of this research project is to aid in that understanding.

Wax Point Determinations: Wax formation and deposition in pipelines and process equipment result in significant operational difficulties for the petroleum industry. The understanding of the crystallization of paraffin deposits from selected crude oils and the relation of paraffin inhibitor structure to performance are essential to developing improved classes of inhibitors to reduce the costs in the early stages of the petroleum production from some deep and ultradeep water wells. Although it is known that the paraffin deposits are formed from long straight-chain alkanes, which can crystallize from the crude under certain conditions of temperature, pressure, composition, and shear rate, conventional molecular simulations have failed to give significant insight into this behavior, mainly because of prohibitive computational costs associated with the large systems that are required for realistic modeling. However, with recent advances in computer hardware (especially massively parallel supercomputers) and computational techniques to study such systems, it is now possible to tackle such problems in a reasonable time period.

Progress:

The scope of this task during the period April 1997 to March 1998 is focused on support activities prior to the receipt of DOE/FE funds. These activities are (1) beginning the acquisition and determining the required modification of the ACRS, (2) preparing laboratory facilities to house the thermophysical measurement equipment, and (3) obtaining key staff. In the upcoming year, thermophysical property measurement equipment will be installed and work will be initiated on the measurement of thermophysical properties for wax point determinations in systems typical of underground petroleum reservoirs. During the second and third years, advanced computational techniques will be used to predict the thermophysical properties measured with the ACRS and other thermophysical property measurement equipment.

We are moving rapidly down a path that will facilitate the transfer of DOE-owned thermophysical property measurement equipment and several key staff members from the National Institute for Petroleum and Energy Research (NIPER) to ORNL. The first staff member has been hired and will begin work at ORNL in May. The equipment is expected to arrive in late CY 1998 or early CY 1999. In addition, we are in the final stages of arrangements to acquire the ACRS from Phillips Petroleum Company. ORNL program development funds have been secured to convert four existing laboratories to a configuration appropriate to house the NIPER thermophysical property measurement equipment and the ACRS.

INTERNAL DISTRIBUTION

1. M. R. Ally
2. J. Barhen
3. T. M. Besmann
4. A. P. Borole
5. R. A. Bradley
6. M. P. Brady
7. T. D. Burchell
8. P. T. Carlson
9. D. F. Craig
10. C. S. Daw
11. R. G. Gilliland
12. G. M. Goodwin
13. E. Greenbaum
14. R. T. Jubin
15–19. R. R. Judkins
20. E. N. Kaufman
21. P. N. Leiby
22. C. T. Liu
23. C. G. McKamey
24. R. L. Miller
25. D. B. Reister
26. P. T. Selvaraj
27. T. W. Schmidt
28. J. H. Schneibel
29. J. Sheffield
30. V. K. Sikka
31. A. J. Stewart
32. D. P. Stinton
33. R. W. Swindeman
34. P. F. Tortorelli
35. J. F. Walker
36. I. G. Wright
37. Central Research Library
38. Laboratory Records, ORNL— RC
39–40. Laboratory Records—OSTI

EXTERNAL DISTRIBUTION

41. C. T. Alsup, U.S. Department of Energy, Federal Energy Technology Center, 3610 Collins Ferry Road, P.O. Box 880, Morgantown, WV 26507-0880
42. W. T. Bakker, Electric Power Research Institute, P.O. Box 10412, 3412 Hillview Avenue, Palo Alto, CA 94303
43. A. L. Baldwin, U.S. Department of Energy, Federal Energy Technology Center, 626 Cochrans Mill Road, P.O. Box 10940, Pittsburgh, PA 15236-0940
44. D. J. Beecy, U.S. Department of Energy, Fossil Energy Office of Advanced Research, FE-72, 19901 Germantown Road, Germantown, MD 20874-1290
45. P. D. Bergman, U.S. Department of Energy, Federal Energy Technology Center, 626 Cochrans Mill Road, P.O. Box 10940, Pittsburgh, PA 15236-0940
46. R. J. Braitsch, Department of Energy, FE-4, 4G-055/FORS, Washington, DC 20545
47. R. A. Carabetta, U.S. Department of Energy, Federal Energy Technology Center, 626 Cochrans Mill Road, P.O. Box 10940, Pittsburgh, PA 15236-0940
48. H. F. Chambers, U.S. Department of Energy, Federal Energy Technology Center, 626 Cochrans Mill Road, P.O. Box 10940, Pittsburgh, PA 15236-0940
49. A. B. Crawley, U.S. Department of Energy, National Petroleum Technology Office, P.O. Box 3628, Tulsa, OK 74101
50. R. A. Dennis, U.S. Department of Energy, Federal Energy Technology Center, 3610 Collins Ferry Road, P.O. Box 880, Morgantown, WV 26507-0880

51. Department of Energy, Deputy Assistant Manager for Energy, Research and Development, Oak Ridge Operations Office, P.O. Box 2008, Oak Ridge, TN 37831-6269
52. H. Feibus, U.S. Department of Energy, FE-23, 19901 Germantown Road, Germantown, MD 20874-1290
53. S. G. Fishman Office of Naval Research, Code 431, 800 N. Quincy Street, Arlington, VA 22217
54. R. D. Furiga, U.S. Department of Energy, FE-40, 3G-024/FORS, Washington, DC 20585
55. F. M. Glaser, U.S. Department of Energy, Office of Fossil Energy, FE-72, 19901 Germantown Road, Germantown, MD 20874-1290
56. P. M. Goldberg, U.S. Department of Energy, Federal Energy Technology Center, 626 Cochrans Mill Road, P.O. Box 10940, Pittsburgh, PA 15236-0940
57. L. E. Graham, U.S. Department of Energy, Federal Energy Technology Center, 3610 Collins Ferry Road, P.O. Box 880, Morgantown, WV 26507-0880
58. J. S. Halow, U.S. Department of Energy, Federal Energy Technology Center, 3610 Collins Ferry Road, P.O. Box 880, Morgantown, WV 26507-0880
59. A. M. Hartstein, U.S. Department of Energy, Office of Fossil Energy, FE-32, D-122/GTN, Washington, D.C. 20585
60. J. L. Hebb, U.S. Department of Energy, Federal Energy Technology Center, 626 Cochrans Mill Road, P.O. Box 10940, Pittsburgh, PA 15236-0940
61. N. T. Holcombe, U.S. Department of Energy, Federal Energy Technology Center, 3610 Collins Ferry Road, P.O. Box 880, Morgantown, WV 26507-0880
62. N. C. Holt, U.S. Department of Energy, National Petroleum Technology Office, P.O. Box 3628, Tulsa, OK 74101
63. C. M. Huang, Tennessee Valley Authority, Energy Demonstration & Technology, MR 2N58A, Chattanooga, TN 37402-2801
64. W. J. Huber, U.S. Department of Energy, Federal Energy Technology Center, 3610 Collins Ferry Road, P.O. Box 880, Morgantown, WV 26507-0880
65. D. S. Jewett, U.S. Department of Energy, Office of Fossil Energy, FE-222, 713/ROSS, Washington, D.C. 20585
66. S. S. Kim, U.S. Department of Energy, Federal Energy Technology Center, 626 Cochrans Mill Road, P.O. Box 10940, Pittsburgh, PA 15236-0940
67. S. R. Lee, U.S. Department of Energy, Federal Energy Technology Center, 626 Cochrans Mill Road, P.O. Box 10940, Pittsburgh, PA 15236-0940
68. R. E. Lemmon, U.S. Department of Energy, National Petroleum Technology Office, P.O. Box 3628, Tulsa, OK 74101
69. Lloyd Lorenzi, Jr., U.S. Department of Energy, Federal Energy Technology Center, 626 Cochrans Mill Road, P.O. Box 10940, Pittsburgh, PA 15236-0940
70. A. M. Manaker, Tennessee Valley Authority, 1101 Market Street, 3A Missionary Ridge, Chattanooga, TN 37402-2801
71. G. V. McGurl, U.S. Department of Energy, Federal Energy Technology Center, 626 Cochrans Mill Road, P.O. Box 10940, Pittsburgh, PA 15236-0940
72. T. J. McMahon, U.S. Department of Energy, Federal Energy Technology Center, 3610 Collins Ferry Road, P.O. Box 880, Morgantown, WV 26507-0880
73. H. S. Meyer, Gas Research Institute, 8600 West Bryn Mawr Avenue, Chicago, IL 60631
74. P. J. Muchunas, U.S. Department of Energy, Office of Fossil Energy, FE-232, 19901 Germantown Road, Germantown, MD 20874-1290

75. P. J. Musser, U.S. Department of Energy, Office of Fossil Energy, FE-232, C-129/GTN, Washington, D.C. 20585
76. H. M. Ness, U.S. Department of Energy, Federal Energy Technology Center, 3610 Collins Ferry Road, P.O. Box 880, Morgantown, WV 26507-0880
77. J. E. Notestein, U.S. Department of Energy, Federal Energy Technology Center, 3610 Collins Ferry Road, P.O. Box 880, Morgantown, WV 26507-0880
78. J. Oakey, British Coal Corporation, Coal Technology Development Division, Stoke Orchard, Cheltenham, Glocestershire, England GL52 4ZG
79. Aksel Olsen, Risoe National Laboratory, P.O. Box 49, DK-4000, Roskilde, Denmark
80. V. U. S. Rao, U.S. Department of Energy, Federal Energy Technology Center, 626 Cochrans Mill Road, P.O. Box 10940, Pittsburgh, PA 15236-0940
81. M. H. Rawlins, Department of Energy, Oak Ridge Operations, P.O. Box 2008, Building 4500N, MS 6269, Oak Ridge, TN 37831
82. S. E. Rogers, U.S. Department of Energy, Federal Energy Technology Center, 626 Cochrans Mill Road, P.O. Box 10940, Pittsburgh, PA 15236-0940
83. L. A. Ruth, U.S. Department of Energy, Federal Energy Technology Center, 626 Cochrans Mill Road, P.O. Box 10940, Pittsburgh, PA 15236-0940
84. T. A. Sarkus, U.S. Department of Energy, Federal Energy Technology Center, 626 Cochrans Mill Road, P.O. Box 10940, Pittsburgh, PA 15236-0940
85. C. E. Schmidt, U.S. Department of Energy, Federal Energy Technology Center, 626 Cochrans Mill Road, P.O. Box 10940, Pittsburgh, PA 15236-0940
86. D. K. Schmidt, U.S. Department of Energy, Federal Energy Technology Center, 3610 Collins Ferry Road, P.O. Box 880, Morgantown, WV 26507-0880
87. J. D. Shages, U.S. Department of Energy, Office of Planning and Financial Management, Petroleum Reserves, FE-432, 3G-052/FORS, Washington, DC 20585
88. T. B. Simpson, U.S. Department of Energy, Office of Fossil Energy, FE-231, 3003/270, 19901 Germantown Road, Germantown, MD 20874-1290
89. Marvin I. Singer, Senior Advisor, Department of Energy, Advanced Research Policy and Planning Team, 4G-052/FORS, Washington, DC 20585
90. W. C. Smith, U.S. Department of Energy, Federal Energy Technology Center, 3610 Collins Ferry Road, P.O. Box 880, Morgantown, WV 26507-0880
91. J. Stringer, Electric Power Research Institute, P.O. Box 10412, 3412 Hillview Avenue, Palo Alto, CA 94303
92. F. D. Sutterfield, U.S. Department of Energy, National Petroleum Technology Office, P.O. Box 3628, Tulsa, OK 74101
93. T. M. Torkos, U.S. Department of Energy, Federal Energy Technology Center, 626 Cochrans Mill Road, P.O. Box 10940, Pittsburgh, PA 15236-0940
94. M. Van de Voorde, European Communities Joint Research Centre, Petten Establishment, P.O. Box 2, 1755 ZG Petten, The Netherlands
95. J. K. Wachter , U.S. Department of Energy, Federal Energy Technology Center, 3610 Collins Ferry Road, P.O. Box 880, Morgantown, WV 26507-0880
96. T. C. Wesson, U.S. Department of Energy, National Petroleum Technology Office, P.O. Box 3628, Tulsa, OK 74101
97. C. M. Zeh, U.S. Department of Energy, Federal Energy Technology Center, 3610 Collins Ferry Road, P.O. Box 880, Morgantown, WV 26507-0880